Structural, electronic and magnetic properties of fulleride materials

ZADIK, RUTH,HELEN

ZADIK, RUTH,HELEN (2015) *Structural, electronic and magnetic properties of fulleride materials*, Durham theses, Durham University. Available at Durham E-Theses Online: http://etheses.dur.ac.uk/11187/

Structural, electronic and magnetic properties of fulleride materials

by

Ruth Helen Zadik

A dissertation submitted to the University of Durham in fulfilment of the requirements for the award of the degree of Doctor of Philosophy.

March 2015

Declaration

I hereby declare that this thesis has not been submitted, either in the same or different form, to this or any other university for a degree.

Signature:

Acknowledgements

I would firstly like to thank my supervisor Prof. Kosmas Prassides for his supervision and patient advice throughout my doctoral studies, and for providing me with the valuable opportunity to work at international facilities such as ISIS, ESRF and SPring-8. I am also grateful to the EPSRC for financial support.

I am indebted to my co-workers in Durham, in particular to Dr. Ross Colman, Dr. Gyöngyi Pergerné Klupp, Esma Okur and Dr. Yasuhiro Takabayashi, for their advice, assistance in data collection and in other technical help. I thank them and other group members, especially Aleš Štefančič and Petra Lavrič, for their valued support and friendship. I am also thankful for the past synthetic efforts of Matthew Williamson, Dominic Myers and Manolis Tzirakis, who made some of the samples for which characterisation is reported herein.

I am grateful to Prof. Denis Arčon and Dr. Anton Potočnik for helpful discussions, advice and guidance about interpreting results. My sincere thanks also go to Prof. Katsumi Tanigaki and to Dr. Satoshi Heguri for the valued opportunity to visit Tohoku University and to attend and present work at the 5th GCOE International Symposium in Sendai, Japan. I am also grateful to Dr. Alexey Ganin and to Prof. Matthew Rosseinsky for the opportunity to visit the University of Liverpool for specialist synthetic training, and for other advice. Furthermore, I would like to extend my thanks to the beamline scientists who have provided support to our group with data collection, in particular Prof. Andy Fitch (ID31, now ID22), Dr. Gaston Garbarino (ID27) and Dr. Yasuo Ohishi (BL10XU).

I thank the staff in the Department of Chemistry at Durham University for their time and assistance, including those of the glassblowing, mechanical and electrical workshops and also Jean Eccleston and Dr. Andrew Hughes for their support, and also those involved in organising the 2012 Powder Diffraction and Rietveld Refinement School.

Last but not least I would like to thank my family (especially my parents Paul and Sarah, and Anne, Liz, Tibor, Sue, Anthony, Tom, Megan, Mary and my cousins and their families – special thanks to Hannah and Kwok), and friends from Sheffield and from my time in Durham, for their invaluable support and encouragement.

Ruth Helen Zadik **Durham University** Degree: PhD

Structural, electronic and magnetic properties of fulleride materials

Abstract

This thesis outlines new research findings into the solid-state properties of selected alkali- and alkaline-earth-intercalated fullerides, focusing on their structural, electronic and magnetic properties at ambient and non-ambient temperatures and pressures, primarily employing synchrotron X-ray powder diffraction and SQUID magnetometry.

Understanding the relationship between superconducting, neighbouring insulating and normal metallic states above T_c in unconventional superconductors is fundamentally important. Highly expanded *fcc* Cs_3C_{60} behaves very differently to underexpanded A_3C_{60} alkali fullerides such as K_3C_{60} and Rb_3C_{60}. Whilst superconductivity in the latter seems well described by conventional Bardeen-Cooper-Schrieffer (BCS) theory, Cs_3C_{60}, a Mott-Jahn-Teller insulator under ambient pressure, exhibits distinctly non-BCS type superconductivity upon pressurisation. The intermediate regime adjacent to the Mott boundary, where strong electronic correlations are prominent, was hitherto only studied through physical pressurisation of Cs_3C_{60} to tune the intermolecular spacing. This thesis reports the solid-state synthesis of *fcc*-rich $Rb_xCs_{3-x}C_{60}$ ($0.25 \leq x \leq 2$) bulk superconducting materials, with excellent stoichiometry control, and the effects on the electronic properties *in situ* of tuning intermolecular separation by varying temperature, physical and chemical pressurisation *via* adjusting the cation dopant ratio. It is shown that the Mott boundary can be traversed at ambient pressure upon cooling, and the metal-insulator crossover temperature tuned by chemical and physical pressurisation.

A15 Cs_3C_{60} orders antiferromagnetically below 46 K. Previous studies found no evidence of symmetry lowering or discontinuous structural changes upon magnetic ordering, despite theoretical predictions to the contrary. This issue is addressed with the first systematic ultrahigh-resolution investigation of its structural evolution with temperature, evidencing a transition to a rhombohedral phase below T_N. The structural properties of A15 Cs_3C_{60} and Ba_3C_{60} *in situ* upon pressurisation are described, extending previous work on A15 Cs_3C_{60}. This first study of the effects of compression on the latter system reveals a pressure-induced structural transition to a hitherto unreported monoclinic phase.

Table of Contents

Chapter 1 – Fullerene C_{60} and fulleride salts

Chapter 2 – Theory, instrumentation and methodology

Chapter 3 – Structural and magnetic studies of $Rb_xCs_{3-x}C_{60}$ *fcc*-rich solid solutions ($0.25 \le x \le 2$)

Chapter 4 – The A15-structured A_3C_{60} (A = Cs, Ba) systems

Chapter 5 – Summary, conclusions and future directions

List of figures

Chapter 1 - Fullerene C_{60} and fulleride salts

1.1. Introduction

The C_{60} molecule, the most stable member of the fullerene family of closed carbon cage molecules, was discovered in 1985,[**1**] through laser vapourisation of a graphite target, whereupon an unusually stable 60 carbon-atom cluster was detected by mass spectrometry. This discovery later led to the 1996 Nobel prize in chemistry being awarded to Curl, Kroto and Smalley. However, an efficient laboratory method to produce bulk fullerenes in the solid state in macroscopic amounts was first described several years later.[**2**] Subsequently, the properties of fullerenes and their derivatives have been intensively researched, with major fields including fullerene chemistry and electrochemistry, and the reductive intercalation of various metals into crystalline C_{60}.

This chapter will firstly summarise some key features of molecular and solid crystalline C_{60} (section 1.2), before outlining the synthesis, structures, characterisation and properties of intercalated fullerides, focusing on the alkali-metal doped A_3C_{60} family, covering early discoveries through to recent progress (section 1.3). Finally, an overview of the thesis contents, showing the relevance of the work to current topical issues in condensed matter science will be presented (section 1.4).

1.2. Molecular and crystal structures of C_{60}

The C_{60} molecule has a truncated icosahedral structure (point group symmetry I_h), with the sixty carbon atoms forming twelve pentagons and twenty hexagons (Fig. 1.1). Two distinct bond lengths are observed, commonly designated 6:6 and 6:5 bonds (i.e. located at hexagon:hexagon and hexagon:pentagon fusions); the average 6:6 and 6:5 reported bond lengths in the solid from powder neutron diffraction are 1.391 Å and 1.455 Å, respectively.[**3**]

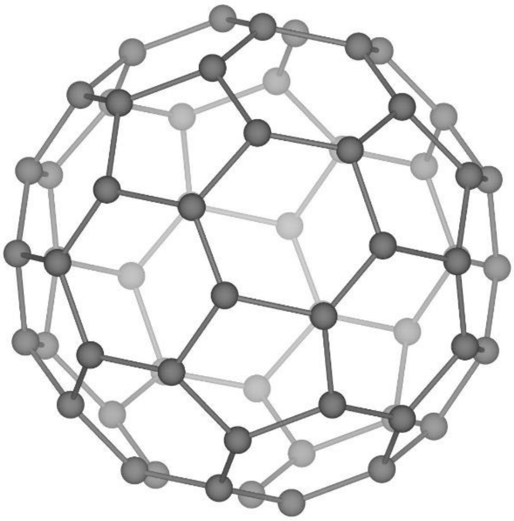

Figure 1.1: The structure of the C_{60} molecule.

Crystalline C_{60} adopts a cubic structure under ambient conditions, assuming an orientationally disordered face-centred cubic structure with almost free C_{60} rotation (space group $Fm\bar{3}m$), albeit with some orientational correlations.[**4**] It undergoes a first-order phase transition upon cooling through 260 K, to a primitive-cubic lower temperature crystal structure described by space group $Pa\bar{3}$.[**5**] The molecules adopt one of two energetically favoured intermolecular contact configurations, interconverting through a pseudo-random sequence of uniaxial reorientations.[**6**] A major fraction (63 %) aligns with electron-rich inter-pentagon 6:6 bonds facing electron-poor pentagon faces of adjacent molecules ('P'), whilst a minor fraction (37 %) orientates with hexagons facing the 6:6 bonds of the adjoining molecules ('H'). Upon cooling between 260 and 90 K, the fraction of molecules in the 'P' orientation continuously increases. A second-order transition occurs at 90 K leading to an orientational glassy phase characterised by lack of rotational motion, with individual C_{60} molecules locked principally into the 'P' configuration, although a small fraction (~16.5 %) is still trapped in the ‘H’ configuration.[**5**]

The close-packed *fcc* C_{60} structure contains large interstitial spaces, where smaller atoms, ions or molecules can be intercalated (see section 1.3). The two high-symmetry cavities comprise a larger cavity with octahedral symmetry (with six closest neighbouring C_{60} molecules), and a smaller cavity with tetrahedral symmetry (four nearest C_{60} neighbours), with radii of 2.06 Å and 1.12 Å, respectively.

Considering the electronic structure of C_{60}, the lowest unoccupied molecular orbital (LUMO) of C_{60} is triply degenerate (t_{1u}) in energy, with a relatively small energy gap between the LUMO and the highest occupied molecular orbital (HOMO) of ~1.9 eV, rendering the molecule a good electron acceptor (Fig. 1.2 a). The next highest unoccupied orbital, termed LUMO+1, is also triply degenerate (t_{1g}), low-lying and accessible. Reduction of C_{60} with up to 12 electrons is, therefore, possible.

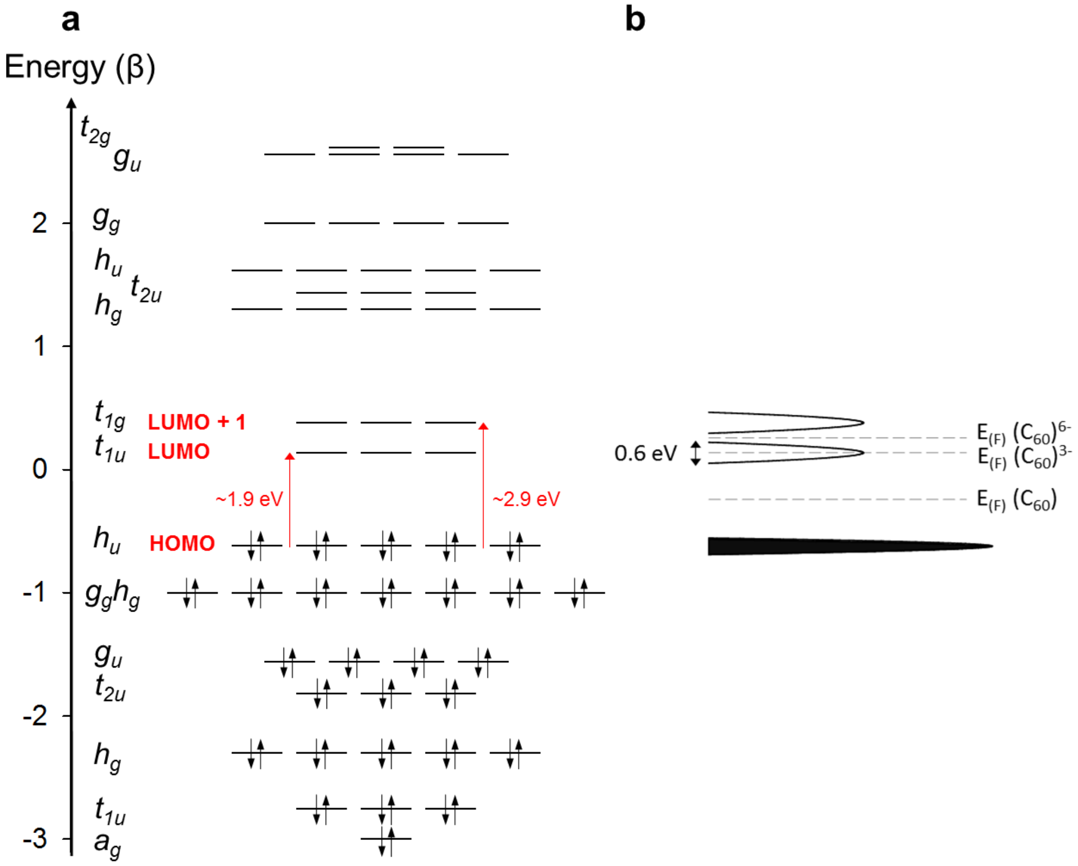

Figure 1.2: (a) Schematic depiction of the C_{60} Hückel molecular orbital diagram, adapted from [**7**]. The energy gaps labelled originate from [**8**]; (b) Representation of the HOMO, LUMO and LUMO+1-derived bands of solid *fcc* C_{60}, with dashed lines depicting the Fermi levels in pristine C_{60}, metallic A_3C_{60} and insulating A_6C_{60}; adapted from [**9**].

In solid C_{60}, a semiconductor, the h_u HOMO and t_{1u} LUMO molecular orbitals overlap, forming bands whose wavefunctions significantly retain the C_{60} molecular features (Fig. 1.2 b). The bandwidths are relatively narrow as characteristic of molecular solids, from relatively small intermolecular overlap. C_{60} has a closed-shell electronic structure, and the cohesion mechanism of solid C_{60} is via weak, van-der-Waals-type interactions, together with weak electrostatic interactions which are significant in determining the ground state crystal structure, promoting well-defined orientational order motifs at low temperatures, as detailed earlier.[**3**]

1.3. Superconductivity in intercalated fullerides

Superconductivity, first observed in alkali-metal-intercalated C_{60} in 1991, has subsequently been confirmed and extensively studied in a wide range of fulleride materials. The superconducting fullerides, which are type II superconductors, fall broadly into two distinct groups in terms of electronic structure. The most studied class of fulleride superconductors posess a half-filled t_{1u} LUMO-derived band (section 1.3.3); these are exemplified by the A_3C_{60} family (A = K, Rb, Cs or a combination thereof) [**10**], with further examples provided by $Na_2A_xC_{60}$ ($x \leq 1$, A = K, Rb, Cs) [**11, 12**], Li_xCsC_{60} [**13**] and ammoniated materials e.g. $(NH_3)_4Na_2CsC_{60}$ [**14**].

Superconductivity has also been reported in higher valence systems, where the t_{1g} LUMO+1 derived band is partially populated. Key examples are $A_{3-x}Ba_xC_{60}$ (A = K, Rb, Cs) [**15**], Ca_xC_{60} ($x \sim 5$) [**16**], AE_4C_{60} (AE = Ba, Sr) [**17, 18**], $A_3Ba_3C_{60}$ (A = K, Rb) [**19, 20**] and $K_2Ba_4C_{60}$ [**21**]. The synthesis, structure and key magnetic and electronic properties of the fulleride superconductors are summarised in the following sections, focusing on the A_3C_{60} and AE_xC_{60} systems as the materials experimentally investigated in this work.

1.3.1. Intercalation into C_{60}

One unique aspect of fullerene solids is their versatility towards doping, with various types of doping possible. The most commonly practiced, exohedral doping, refers here to intercalation of other species into solid crystalline C_{60}, with the dopant occupying interstitial lattice positions within the host crystal structure. Endohedral and substitutional doping of certain species into C_{60}, with the dopant entering the fullerene hollow core or replacing carbon atoms on the fullerene shell, respectively, are also known.[**22**] However, the remaining discussion will refer exclusively to exohedral doping, being the synthetic technique employed in this study.

Exohedrally-doped C_{60}-based materials can be further divided into two categories: charge-transfer compounds and clathrate compounds. In the latter class, molecular species such as O_2, S_8 or solvent molecules intercalate into the C_{60} sublattice with little or no charge transfer; in the former class, foreign atoms e.g. alkali metals donate electrons to C_{60}, forming C_{60}^{n-} molecular anions, producing highly ionic compounds.[**22**] Charge transfer, in particular, can modify the properties of C_{60} in scientifically interesting ways (e.g. inducing superconductivity, see Section 1.3.3), and has thus received most attention.

Experimentally, certain metal species can intercalate into C_{60} forming charge-transfer compounds, whilst others do not. Metals which can be intercalated in this way comprise mainly alkali and alkaline earth metals, but also include certain heavy metals and rare-earth elements. An empirical criterion based on electronic energy arguments has been suggested to explain this distinction,[**23**] where a low cohesive energy of the hypothetical metal-fullerene complex and a low work function for the dopant favour intercalation.

1.3.2. Synthesis of alkali and alkaline earth metal fullerides

Where A is K, Rb or Cs, crystallographic phases where x (in A_xC_{60}) equals 1, 3, 4 and 6 are known, and each alkali atom donates one electron to the solid C_{60} t_{1u} band. With one notable exception (where $x = 1$, low temperature polymeric phases form), the structures of the resulting materials can be rationalised in terms of alkali-metal ions progressively filling the voids of pristine cubic C_{60}. For smaller alkali metals (Na, Li), x can take other values and can exceed 6.

Various methods have been used to intercalate the C_{60} lattice with alkali metals to synthesise A_xC_{60}. All alkali metals react directly with C_{60} on heating, but synthesis is generally more straightforward for the heavier alkali metals (but with some exception, with Cs-rich A_3C_{60} compositions, as explained later), potentially due to higher alkali metal vapour pressure, higher diffusivity of A in solid A_xC_{60}, and lower reactivity with glass. As both alkali metals and A_xC_{60} solids are very air sensitive, reactions must be undertaken in inert oxygen- and water vapour-free atmospheres.

Commonly, solid C_{60} in the form of polycrystalline or crystalline films, microcrystalline powder or single crystals is exposed to alkali metal vapour, which diffuses into the host at a sufficiently high temperature, i.e. from 100 - 200 °C, although higher temperatures are necessary for lighter elements.[**22**] This can be carried out with stoichiometric reagent amounts, or with an excess of alkali metal to synthesise the saturated A_6C_{60} (A = K, Rb, Cs) phase; these A_6C_{60} compounds can also be used as precursors to access other less stable A_xC_{60} fullerides where $x < 6$, by further reaction with C_{60} and sometimes other A_6C_{60} compounds. Vapour transport methods can be used to synthesise A_6C_{60}

phases, with a temperature gradient used to transfer the metal to the C_{60}, then reversed upon cooling to remove any excess unreacted metal.[**24**]

Alkaline earth metal fullerides, AE_xC_{60} (AE = Ca, Sr, Ba) can also be prepared by direct reaction of C_{60} with alkaline earth metal vapour, albeit at a higher temperature than that required for alkali metal intercalation, *i.e.* annealing the typically pelletised reactant mixture between approximately 550 – 740 °C. Solvent routes, e.g. reaction in THF have also, less commonly, been utilised (see [**7**] and references therein).

Various solution routes have also been developed for alkali metal intercalation into C_{60}. Wang and co-workers reported an easily reproducible solution-phase synthesis of an alkali fulleride, synthesising superconducting K_xC_{60} and Rb_xC_{60} from toluene using Schlenk techniques (T_c = 18 K and 29 K, respectively).[**25, 26**] Subsequently, routes to synthesise A_3C_{60} involving other solvents such as ammonia, methylamine, THF, *n*-propylamine and *n*-butylamine have been developed.[**27-30**] Solution routes are typically less time-consuming than directly heating C_{60} with A or A_6C_{60} as described above, and the use of e.g. a liquid ammonia synthesis route to synthesise A_3C_{60} may help avoid the initial formation of stable AC_{60} and A_4C_{60}, which form in higher temperature reactions.[**31**] However, issues with stoichiometry control in $A_xA'_{3-x}C_{60}$ and relatively broad superconducting transition widths, with separate distinct intergrain and intragrain T_cs, have been reported.[**31**] Additionally, where ammonia is used, dynamic pumping and extended heat treatment are typically required to remove residual solvent, to obtain similar T_c values to those obtained by solid-state reactions and achieve good crystallinity.[**32**] Further limitations on the use of ammonia include its low liquid temperature range (−78 to −33 °C) and high vapour pressures for liquid ammonia inside sealed apparatus at higher temperatures, presenting hazards. Alkylamines are solvents for both alkali-metals and C_{60}, and other solvents such as methylamine have a wider liquid temperature range than ammonia (−93 to −6 °C for methylamine).

Several other synthetic routes to produce alkali-metal fullerides have been reported. Douthwaite *et al.* used a microwave-induced argon plasma to synthesise various fullerides from A_6C_{60} and C_{60} (RbC_{60}, CsC_{60}, K_3C_{60}, Rb_3C_{60}, K_4C_{60}, Rb_4C_{60}, Cs_4C_{60}), obtaining only slightly lower phase purities than those using conventional furnace techniques, and significantly reduced reaction times.[**33**] More recently, syntheses of Rb_3C_{60} and K_3C_{60} via self-propagating high-temperature synthesis were reported, with T_c values being in good agreement with existing literature, although no structural characterisation was provided.[**34**] A method involving thermal decomposition of alkali-metal azides as the alkali metal source, more time-efficient than direct doping of C_{60} with metallic vapour, has also been used to produce e.g. K_3C_{60}, Rb_3C_{60}, and $Li_{12}C_{60}$;[**35, 36**] however, this has the disadvantage that it can result in nitrogen co-intercalation. Alkali metal binary alloys (with Hg, Tl, or Bi) can also be used as a metal source,[**37**] although the heavy metals may also co-intercalate into the C_{60} lattice. Na-containing fullerides can be prepared by reactions of NaH or Na_5Hg_2 with C_{60} (and with A_6C_{60} to synthesise mixed fullerides).[**11, 38**] Electrochemical techniques, which previously yielded most superconducting tetrathiafulvalene-derived organic charge transfer salts, have been employed to intercalate Li into C_{60} electrodes.[**39**]

1.3.3. The t_{1u} superconducting fullerides

Metallic behaviour was first observed in alkali-metal doped A_xC_{60} films at 300 K (Rb/C_{60} and K/C_{60} displayed conductivities of 100 S cm^{-1} and 500 S cm^{-1}, respectively)[**40**], with maximum conductivity at $x = 3$ for A = Rb, K.[**41**] Hebard and co-workers then reported superconductivity at $T_c = 18$ K in potassium-doped C_{60}, A_xC_{60};[**10**] the superconducting phase was later identified as face-centred cubic K_3C_{60}.[**42, 43**] Shortly afterwards, superconductivity in rubidium-doped C_{60} at $T_c = 28$ K and 30 K was reported,[**42, 44**] followed by a reported T_c of 33 K for $RbCs_2C_{60}$ from Tanigaki *et al.*[**45**] This was then the highest T_c known for any molecular superconductor, surpassed only at the time by $Ba_{0.6}K_{0.4}BiO_3$ and the cuprate superconductors.

Structural studies on a range of single-phase superconducting A_3C_{60} compounds (Rb_2CsC_{60}, Rb_3C_{60}, Rb_2KC_{60}, $Rb_{1.5}K_{1.5}C_{60}$, K_2RbC_{60}, K_3C_{60}) confirmed that they all adopt the *fcc* cryolite-type structure, with tetrahedral and octahedral interstitial sites fully occupied by the alkali ions.[**46**] The C_{60}^{3-} anions are 'merohedrally' disordered, adopting two different molecular orientations, related by a 90° rotation about the <001> axis or equivalently, by a 44°23' rotation about the <111> crystal axes (with small amplitude librational motion up to 700 K). A neutron pair distribution function study has suggested that the molecular orientation is not completely random, finding local deviations from the merohedral disorder model in Rb_3C_{60}.[**47**] A tendency for nearest neighbour molecules to have the opposite orientation was reported, indicative of short-range 'antiferrorotative' orientational correlations; however, no other experimental studies, using alternative techniques like NMR, have supported these findings.

The A_3C_{60} lattice parameter is larger than that of pristine C_{60} for heavier alkali metals, as K^+, Rb^+ and Cs^+, with ionic radii of 1.38 Å, 1.52 Å and 1.67 Å, respectively, are larger in size than the tetrahedral interstitial site (radius of 1.12 Å) of the pristine *fcc* C_{60} lattice;[**22**] the interfulleride separation relates directly to the size of the cation inserted into the tetrahedral cavity. The occupancy of the larger octahedral cavity (radius = 2.06 Å) has little bearing on the lattice expansion. In contrast, if smaller cations are placed in the tetrahedral sites in A_3C_{60}, as in Na_2CsC_{60}, the C_{60} ions are still able potentially to freely rotate. In analogy to pristine C_{60}, at high temperatures such fullerides exhibit orientational disorder (space group $Fm\overline{3}m$), undergoing an orientational ordering transition upon cooling, yielding a primitive cubic structure ($Pa\overline{3}$).[**48**]

Uniquely amongst the A_3C_{60} materials, the most expanded member, Cs_3C_{60}, is now known to form an A15-structured, body-centred-cubic (*bcc*-) -derived polymorph, with an orientationally ordered simple cubic unit cell,[**49**] in addition to a *fcc* polymorph which is structurally analogous to the less-expanded A_3C_{60} (A = K, Rb, Cs or a mixture) compositions.[**50**] In the *bcc*-based structure, in contrast to the *fcc* lattice packing, the distinction between octahedral and tetrahedral sites is removed; all interstitial sites are equivalent, with distorted tetrahedral symmetry (Fig. 1.3). The orientational ordering in the A15 structure, where the body-centre-site C_{60} is rotated by 90° with respect to C_{60} at the cube corner, is in contrast to the merohedrally disordered *fcc* arrangement of C_{60}^{3-} anions. In addition, the mean C_{60}^{3-}-C_{60}^{3-} near-neighbour contacts are significantly shorter in *fcc* Cs_3C_{60} than in the A15 polymorph (3.59 Å and 3.80 Å, respectively), and the nearest-neighbour C_{60}^{3-}-C_{60}^{3-} contact in *fcc* Cs_3C_{60} is through neighbouring hexagon:pentagon C-C bonds, whereas in A15 Cs_3C_{60}, it is through hexagon:hexagon faces.[**50**]

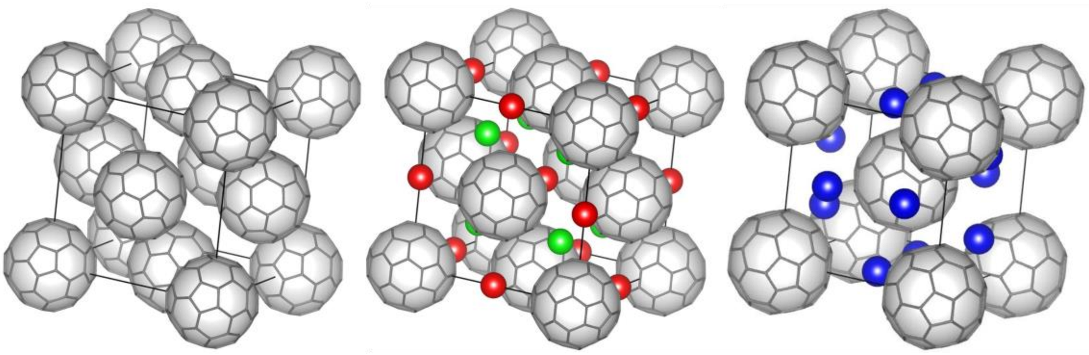

Figure 1.3: (From left to right): Schematic crystal structures of pristine C_{60}, *fcc* A_3C_{60} and A15 Cs_3C_{60}. In the *fcc* structure, only one of the two C_{60} orientations is depicted for visual clarity, and octahedral and tetrahedral cations are shown in red and green, respectively.

1.3.4. Synthetic developments to access more expanded A_3C_{60} lattices

Tanigaki and co-workers used direct doping of solid C_{60} with alkali metals, annealing at 390°C, to synthesise $RbCs_2C_{60}$.[**45**] The thermal azide decomposition route of Bensebaa *et al.* was later employed by other groups to synthesise $RbCs_2C_{60}$, characterised by ^{13}C NMR spectroscopy and magnetisation measurements (the reported T_c of 33 K was identical to that reported in [**45**]).[**51, 52**] However, synthesis of more expanded *fcc* A_3C_{60} fullerides than $RbCs_2C_{60}$, towards the most expanded member Cs_3C_{60}, has presented a greater challenge. This can be attributed to instability towards disproportionation into the stable CsC_{60} and Cs_4C_{60} phases, originating from the size mismatch between the large Cs^+ cation (ionic radius = 1.67 Å) and the *fcc* tetrahedral site (radius = 1.12 Å). For example, Movshovich *et al.* reported superconductivity in a sample of nominal composition $Rb_{0.5}Cs_{2.5}C_{60}$ synthesised by a vapour-phase route involving alloys, but its fractional diamagnetism was low (1-2 %), and the T_c value, with analysis of the compressibility, identified the superconducting phase as Rb_2CsC_{60}; decomposition into this phase, a Cs-rich stable phase (Cs_4C_{60} or Cs_6C_{60}) and pure C_{60} was inferred.[**53**] Dahlke *et al.* synthesised a series of *fcc*-rich samples of overall composition $Rb_xCs_{3-x}C_{60}$, ($0.32 \leq x \leq 1$) with *fcc* phase fractions 79-90%, using a liquid ammonia route, which avoided formation of AC_{60} and A_4C_{60}. This route provided access to a wider compositional range and larger *fcc* phase fractions than synthesis by conventional solid-vapour reaction; attempted solid-vapour preparation of $Rb_{0.3}Cs_{2.7}C_{60}$ resulted only in 13(4)% *fcc* phase fraction, with refined composition $Rb_{0.55(7)}Cs_{2.45(7)}C_{60}$.[**31**] However, reducing the Rb content of $Rb_xCs_{3-x}C_{60}$ to $x < 0.32$ led only to smaller *fcc* phase fractions and no increase in *fcc* unit cell volume, implying a higher fraction of Rb in the *fcc* phase than implied by the nominal stoichiometry, with CsC_{60} and Cs_4C_{60} also forming. A theoretical study of the energetics and structural stability of Cs_3C_{60} had indicated that a low-temperature and high-pressure synthetic route might yield the then-unreported *fcc* Cs_3C_{60} phase, the authors reporting a considerably smaller energy-minimum volume for the *fcc* phase than for the body-centred orthorhombic (*bco*) Cs_3C_{60} ($(Cs_{0.75})_4C_{60}$) and A15 Cs_3C_{60} phases.[**54**]

Trace superconductivity in Cs-doped C_{60} was first reported in 1991, at T_c = 30 K at ambient pressure (Cs_xC_{60}, x = 1.2 – 3),[**55**] and Palstra and coworkers reported superconductivity in nominal Cs_3C_{60} at 40 K under hydrostatic conditions up to 15 kbar,[**56**] but in both cases the shielding fraction was extremely low (<1%); this precluded the identification of the true composition and structure of the putative superconducting phases. In the latter case, whilst Raman spectroscopy indicated a complete charge transfer of 3 electrons per C_{60} unit, X-ray diffraction data signified the presence of two phases, neither of which corresponded to an *fcc*-structured phase. Palstra *et al.* reported that, experimentally, a low temperature synthesis route to Cs_3C_{60} is essential, as at 200 °C the phase segregates into the energetically favourable Cs_1C_{60} and Cs_4C_{60} phases. They utilised a solution route with liquid ammonia, whilst the nominally Cs_3C_{60} samples with T_c = 30 K at ambient pressure reported by Kelty and co-workers were synthesised by reaction of C_{60} with CsM_2 (M = Hg, Tl, Bi) alloys. A *bcc* Cs_3C_{60} phase had been reported as early as 1993, synthesised by reaction of Cs vapour on C_{60},[**57**] and in a later investigation using a liquid ammonia route, a cubic A15 phase was obtained, but no superconductivity was observed up to 10.6 kbar.[**58**] However, before 2008, no bulk superconducting sample of Cs_3C_{60} had been reported, and the identity and characterisation of any superconducting phases remained unresolved.

In 2008, Ganin and co-workers reported the first reproducible synthesis of bulk superconducting Cs_3C_{60} (with a shielding fraction as high as 67% under pressure);[**49**] the superconducting phase was identified as the *bcc* variant A15 phase, which is insulating at ambient pressure but becomes superconducting with a maximum T_c = 38 K under hydrostatic pressure (reaching a broad maximum at ~7 kbar). They synthesised Cs_3C_{60}, containing a high fraction (77.7(6)%) of the A15 superconducting phase, using a low-temperature solution-based route; Cs was reacted stoichiometrically with C_{60} in methylamine at −65°C, followed by solvent removal under dynamic vacuum at ambient temperature and annealing at 180°C for 48 hours.

The *fcc* polymorph of Cs_3C_{60}, identified as a minor component of the phase assemblage in the report of bulk superconducting A15 Cs_3C_{60}, was subsequently isolated in high yield and shown to also become superconducting under pressure (reaching a maximum T_c of 35 K, the highest found in *fcc* A_3C_{60}).[**50**] This modification of the low-temperature synthesis route, using ammonia as solvent, yielded Cs_3C_{60} samples with up to 86% *fcc* phase content. Recently, a solvent route employing THF together with an organometallic salt reducing agent, which prevents the formation of C_{60}^{4-} species, was reported which produced solely C_{60}^{3-} species (Cs_3C_{60} and a solvated analogue) for the first time.[**59**]

1.3.5. The t_{1g} superconducting fullerides

Several crystal structures and phases are known for alkaline earth fullerides, AE_xC_{60} (AE = Ca, Sr, Ba). For AE = Mg, rhombohedral polymeric structures have been reported for several stoichiometries Mg_xC_{60} with $1 < x \leq 6$;[**60, 61**] a metallic phase purportedly exists with stoichiometry $x \sim 5$,[**62**] although this is disputed.[**60**] Whilst the alkali-metal-doped superconducting fullerides have a partially occupied t_{1u}-derived band, the divalent character of alkaline earth metals renders the t_{1u}-derived band in alkaline earth fullerides fully occupied, with occupation of the (LUMO+1) t_{1g}-derived states occurring. Ba- and Sr-doped C_{60} fullerides, AE_xC_{60} (x = 3, 4, 6) generally show similar lattice geometries to their alkali-metal-doped A_xC_{60} equivalents (Fig. 1.4). The insulating AE_3C_{60} materials adopt an A15 bcc-type structure analogous to that of Cs_3C_{60}, with a *fcc*-structured polymorph of Sr_3C_{60} also reported,[**63, 64**] whilst the body-centred-cubic AE_6C_{60} phases are metallic.[**17**] The AE_4C_{60} systems, however, are superconductors, with T_c = 6.7 K and 4.4 K for AE = Ba and Sr, respectively.[**18**]

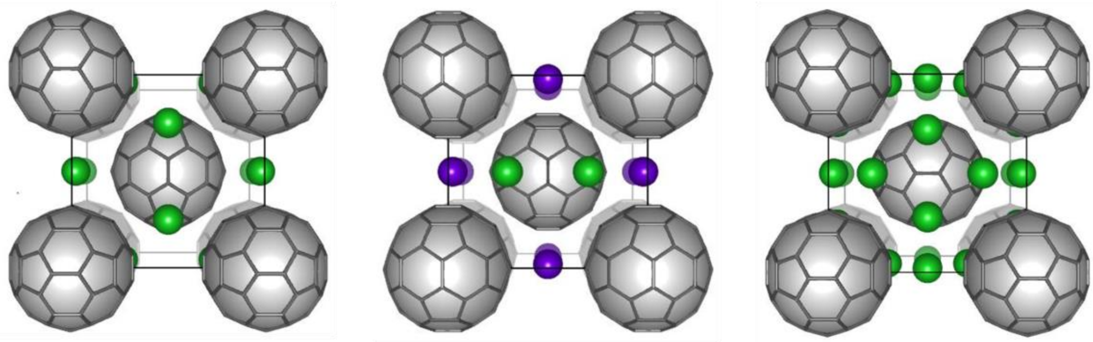

Figure 1.4: (From left to right): Projection views of the Ba_3C_{60}, Ba_4C_{60} and Ba_6C_{60} crystal structures, along the a axes. The inequivalent Ba ions in Ba_4C_{60} are depicted in green and purple.

The body-centred-orthorhombic AE_4C_{60} materials are, excepting A15 Cs_3C_{60}, unique amongst fulleride superconductors in being free from geometric disorder. Additionally, all other fullerene superconductors confirmed thus far have been limited to cubic structures. The stabilisation of metallicity and thus the occurrence of superconductivity in AE_4C_{60} is attributed to a relatively broad t_{1g} conduction band (compared to the t_{1u} conduction band of A_3C_{60} superconductors), arising from hybridisation of Ba 5d and C_{60} t_{1g} orbitals.[**18**]

Besides AE_4C_{60}, with nominal molecular valence C_{60}^{8-}, other 't_{1g}' fulleride superconductors include $A_3Ba_3C_{60}$ (A = K, Rb; T_c = 5.6, 2.0 K)[**19, 20**] and Ca_5C_{60} (T_c = 8.4 K)[**16**], with nominal molecular valences of C_{60}^{9-} and C_{60}^{10-}, respectively; a greater tolerance to molecular valence and structural variety with respect to the occurrence of superconductivity, than in the t_{1u} family, is thus observed. In contrast to behaviour in the t_{1u} superconducting fullerides (Section 1.3.6), in materials such as $A_3Ba_3C_{60}$, with a half-filled t_{1g} band, the density-of-states at the Fermi level, $N_{\varepsilon(F)}$ reportedly decreases with increasing unit cell size; this was attributed to strong hybridisation between alkaline earth d orbitals and C_{60} pπ orbitals.[**20, 21**]

1.3.6. Superconductivity mechanism in A_3C_{60}

The discrete energy levels of molecular C_{60} are only weakly broadened in the solid, resulting in a set of essentially non-overlapping narrow bands with widths of ~0.5 eV.[**65**] In A_3C_{60}, transferred electrons become delocalised due to overlap of C_{60} t_{1u} orbitals between neighbouring molecules. This overlap is not insignificant, as t_{1u} orbitals possess mostly p_z character, radiating out from the C_{60} surface. The t_{1u} band, which can take up to six electrons, is half-full, and the material is metallic.[**40**]

C_{60} has intramolecular vibrations (phonons) with energies up to ~0.2 eV, and the eight with H_g symmetry couple to the t_{1u} electrons.[**65**] It was proposed at an early stage that these phonons are responsible for driving the superconductivity;[**66**] estimates of the electron-phonon interaction fall into the right range to explain experimental T_c values, with other phonon modes (such as librations, intermolecular C_{60}-C_{60} and alkali-C_{60} vibrations) shown to play a minor role.[**65, 67**] Vibrational spectroscopy demonstrated coupling between the conduction electrons and both high-frequency tangential and low-energy radial intramolecular vibrational H_g modes of C_{60}^{3-}.[**68**]

As interfullerene spacing increases, molecular overlap decreases; for a fixed band filling, this smaller spatial overlap between nearest-neighbour t_{1u} orbitals leads to a reduced bandwidth and, thus an increased $N_{\varepsilon(F)}$. This has been used to explain the increase in T_c with interfullerene spacing observed in A_3C_{60}, for instance between K_3C_{60} and Rb_3C_{60},[**44**] using a Bardeen-Cooper-Schrieffer (BCS)-type weak coupling relation:

$$\boldsymbol{T_c} \propto \boldsymbol{\hbar\omega} \, \mathbf{exp}\left[-\frac{\mathbf{1}}{\boldsymbol{V\,N_{\varepsilon(F)}}}\right], \qquad \textbf{Equation 1.1}$$

where $\hbar\omega$ is the frequency of the pairing-mediating excitation, and V the electron-excitation coupling strength.

The range of A_3C_{60} compounds (between K_3C_{60} and Rb_2CsC_{60}) investigated by Fleming *et al*. showed a monotonic increase in T_c with lattice parameter (Fig. 1.5), and extended Hückel band-structure calculations also indicated that $N_{\varepsilon(F)}$ increases monotonically with lattice parameter.[**46**] It was reported that applying pressure to Rb_3C_{60}, reducing the lattice parameter to that of K_3C_{60}, leads to approximately the same T_c for both materials; this suggested that the alkali ions themselves only weakly influence T_c, except for the indirect influence *via* lattice parameter modulation.[**46**] A later study, however, reported some deviation in the lattice parameter dependence of T_c when comparing physical and 'chemical' (*i.e.* K substitution) means of reducing the Rb_3C_{60} lattice parameter.[**69**]

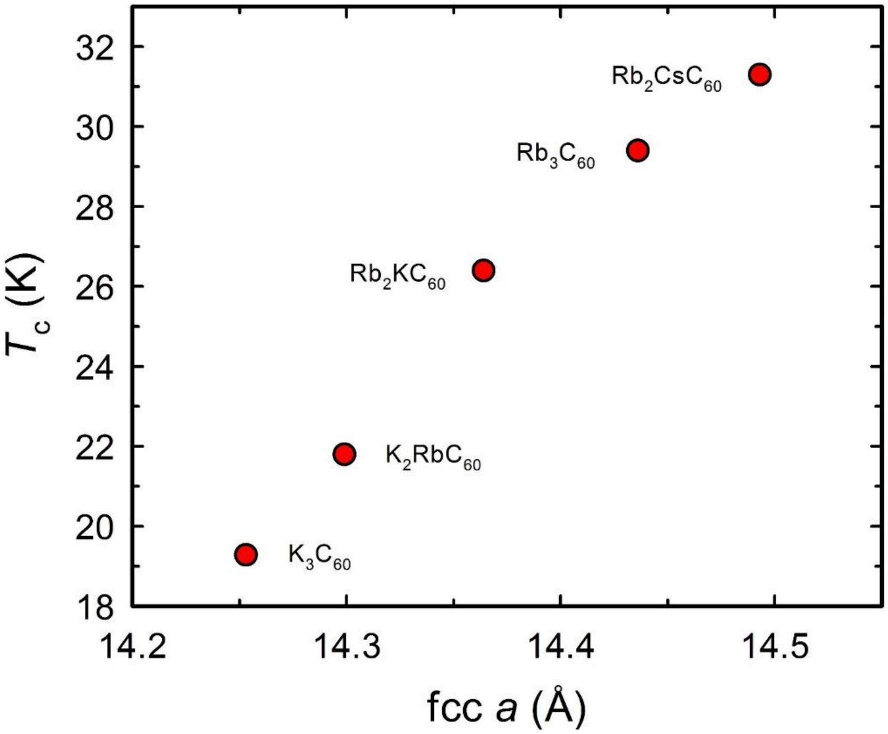

Figure 1.5: The variation of superconducting T_c with *fcc* lattice parameter, *a* for several A_3C_{60} compositions; adapted from [**46**].

A trend of T_c increasing with lattice enlargement was observed earlier in a different class of organic superconductors. The increasing T_c with anion size in *β*-$(ET)_2X$ (where X^- = IBr_2^- and AuI_2^-, ET = bis(ethylenedithio)tetrathiafulvalene) was attributed to lattice softening with respect to translational and/or librational vibrational modes with lattice enlargement, as measured by enhancement of the calculated electron-phonon coupling constant λ.[**70**]

However, Dahlke *et al*., through synthesis and characterisation of several compounds in the series $Rb_xCs_{3-x}C_{60}$ ($0.32 \le x \le 1$), reported that T_c reached a maximum at $x = 1$, then started to decrease with increasing interfullerene separation (Fig. 1.6).[**31**] This ‘chemical pressure’ effect was supported by a more recent study of the effects of physical pressure on T_c in $Rb_xCs_{3-x}C_{60}$ ($0 \leq x \leq 0.62$), showing that T_c initially increases upon pressurisation, up to a maximum, then decreases with further pressure increase, forming ‘dome’-like trajectories (Fig. 1.7).[**71**]

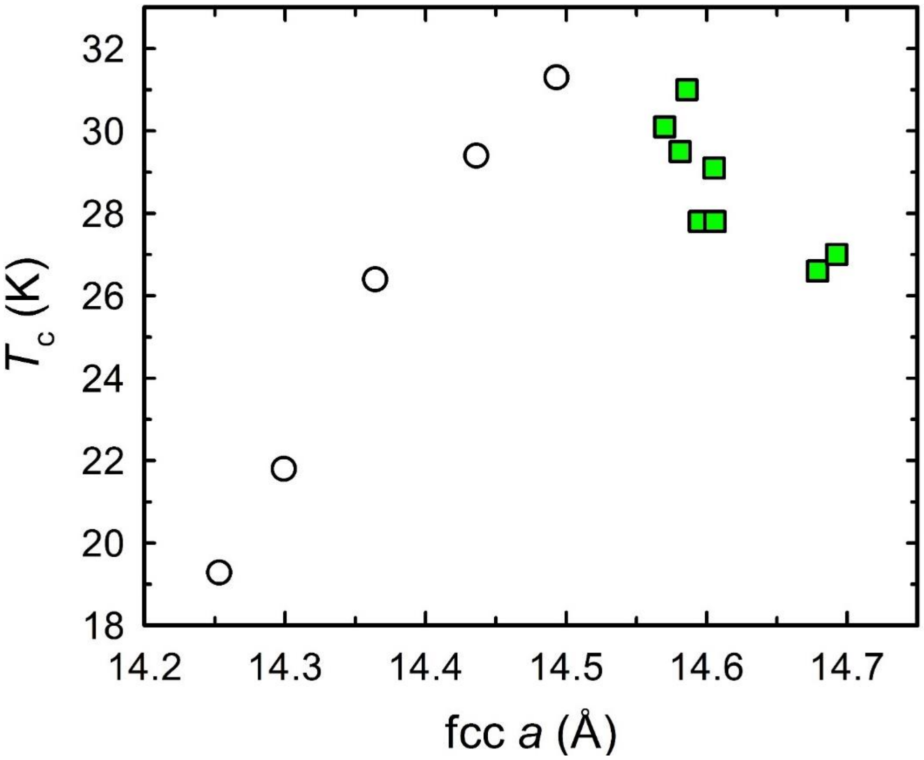

Figure 1.6: The variation of superconducting T_c with *fcc* lattice parameter, *a* for several A_3C_{60} compositions. Unfilled circles represent data from [**46**] (see Fig. 1.5); green squares depict intragrain T_c for $A_xCs_{3-x}C_{60}$ ($0.3 \leq x \leq 1$, x = K, Rb), from [**31**].

The $T_{c(max.)}$ of *fcc* Cs_3C_{60} was recently confirmed as 35 K, under applied pressure.[**50**] This T_c is lower than the ~45 K predicted from the trend in monotonic increase in T_c with lattice parameter established for the less expanded fullerides.[**50, 54**] It is also lower than other T_c predictions from band structure calculations (e.g. 47 K, 68 K).[**72, 73**] Moreover, *fcc* Cs_3C_{60} is an insulator at ambient pressure. This observed decrease in T_c with expansion above a certain limit, and the non-monotonic behaviour of T_c with pressure reported in both Cs_3C_{60} superconducting polymorphs (Fig. 1.7),[**50**] have no apparent explanation within BCS theory unless the electron-phonon coupling strength, V begins to decrease upon further lattice expansion past the volume at $T_{c(max.)}$. However, electron-phonon coupling is a molecular property and such a change in coupling occurring at large separations is thus implausible.

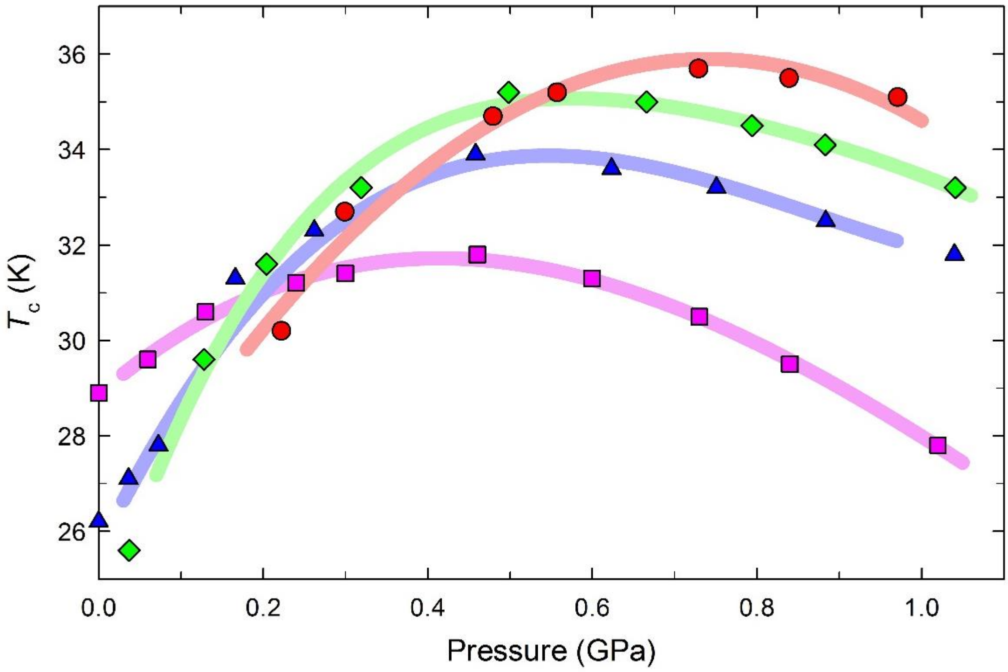

Figure 1.7: Superconducting T_c as a function of pressure for *fcc* $Rb_xCs_{3-x}C_{60}$, where red circles, green diamonds, blue triangles and pink squares represent data for samples with $x = 0, 0.18, 0.37$ and 0.62, respectively; the lines are guides-to-the-eye. Adapted from [**71**].

No uniform behaviour of T_c on the intermolecular spacing is observed for alkaline-earth fulleride superconductors, in contrast to the less expanded A_3C_{60} (A = alkali metal) superconductors. This can be attributed to the varying degree of hybridisation of alkaline-earth s-, d-states and C_{60} pπ-states.[**74**]

Besides the variation of T_c with interfulleride separation, other properties have been investigated, attempting to establish to what extent the BCS model is applicable for the A_3C_{60} superconductors. For instance, extensive measurements of the superconducting gap, Δ, have been carried out, as the BCS model in the weak coupling limit predicts that $2\Delta/k_BT_c = 3.53$, and a substantially larger experimental value would indicate that strong-coupling effects are important. However, values obtained from different experiments and techniques (such as NMR, STM and μSR) have varied substantially, ranging from the BCS value to ~4.2.[**65**] A 'Hebel-Slichter' coherence peak, i.e. a peak in $1/T_1T$ as a function of temperature, just below T_c, when compared with the extrapolated normal state value ($1/T_1$ being the spin-lattice relaxation rate), has been observed in Rb_3C_{60} using μSR;[**75**] this peak is predicted in the Hebel-Slichter theory for a BCS superconductor. Much experimental evidence has indicated that the superconducting pairing is phonon-mediated, with electrons bound in a pair-state of s-wave symmetry, as predicted in the BCS theory;[**65**] other support for the apparent BCS nature of fulleride superconductivity includes specific-heat jumps scaling linearly with T_c, and the magnitude of the normal-phase magnetic susceptibility ([**76**] and references therein).

1.3.7. Mott insulators and strongly correlated superconductivity

Non-BCS mechanisms were, however, also proposed from an early stage, such as an all-electronic pairing mechanism, *i.e.* an effective attractive interaction between electrons from a C_{60} molecule of solely electronic origin.[**77-79**] One early such model considered a Hubbard model of the π-electron system in free C_{60}, with an on-site interaction, U_c, only;[**78**] the resulting estimated effective interaction for C_{60}^{3-} comprised an attractive, quadratic term in U_c, and a repulsive, linear term. For sufficiently large U_c, the effective interaction between two electrons would therefore become attractive. However, the effective Coulomb interaction for free C_{60} is large and repulsive, and such a mechanism could only be viable if this were significantly reduced through metallic screening. The feasability of an electronic mechanism has been debated in many theoretical studies (see [**80**] and references within), but has been gaining additional support through the new advances in the field described later in this thesis.

Based on measurements of the on-site molecular C_{60} Coulomb interaction (U, the Hubbard parameter, is around ~1.6 eV) for solid C_{60}, Lof *et al.* suggested that the ratios of U to the one hole bandwidth (W), U/W, for doped C_{60} are comparable to those of high-T_c cuprates. They concluded that doped C_{60} should be considered as a highly correlated electron system.[**81**]

The Mott transition is a metal-insulator transition without symmetry breaking, similar to a gas-liquid transition. A Mott insulator may form if U exceeds W (for electrons in a solid with ~1 electron per lattice site),[**82**] whereas metallic behaviour is expected where $U/W << 1$. This can lead to a first-order metal-insulator transition at a critical ratio of U/W (Fig. 1.8). An external control parameter, *e.g.* doping or pressure, can thus yield a line of first-order transitions in the pressure-temperature phase diagram, terminating in a second-order critical end point, beyond which a smooth transition from the insulating to the metallic regime can be induced by adjusting pressure and temperature.[**83**] Electrons in a lattice can give rise to a Mott insulating state when electron-electron repulsion prevents their free propagation and the lattice appears as an assembly of molecular ions; correlations lead to an energy gap in their spectrum.[**84**] With a clear separation between the threefold LUMO band and the LUMO +1 and HOMO bands throughout the Brillouin zone in alkali fulleride C_{60}^{n-} crystals, the observed metal-insulator transition in certain materials has been interpreted in terms of electron localisation in the part-filled t_{1u} LUMO band.[**85**]

Whilst the less expanded A_3C_{60} materials are metallic, their relatively high values of U/W would predict that they should be Mott-Hubbard insulators. However, the triple degeneracy of the t_{1u}-derived LUMO band is key here. The critical ratio, $(U/W)_c$ for the metal-insulator transition has been shown to shift to a higher value by a factor of $\sim\sqrt{N}$, where N is the orbital degeneracy;[**86**] conceptually, there are more possibilities in a degenerate band for one electron to 'hop' between sites. In addition, the frustrated nature of the *fcc* lattice shifts this critical ratio to even higher values, *i.e.* $(U/W)_c \approx 2.3$, compared to non-frustrated topologies such as those based on bcc packing, with $(U/W)_c \approx 1.3$.[**87**]

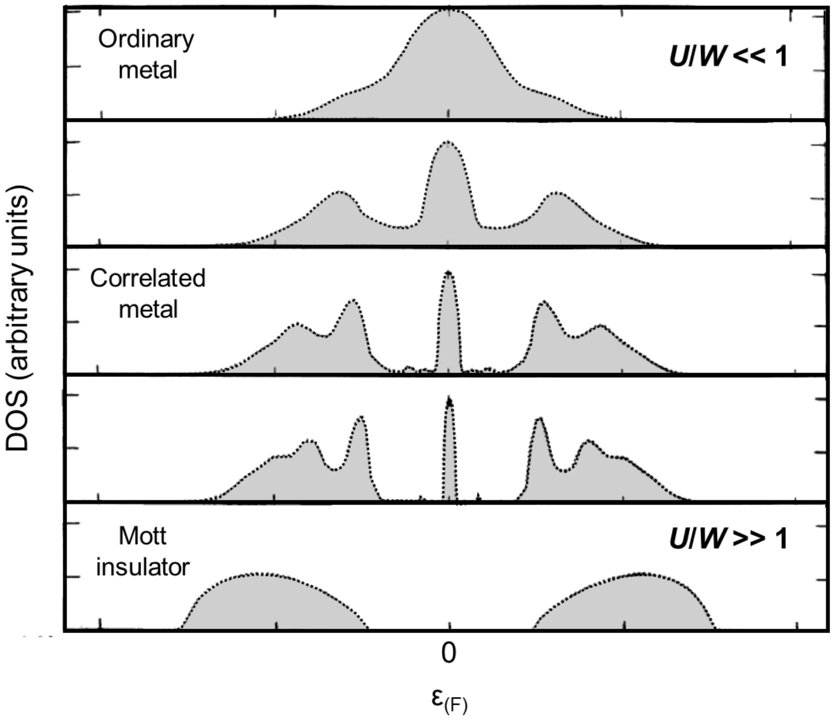

Figure 1.8: Schematic variation of the density-of-states at zero temperature with U/W, obtained through dynamical mean-field theory; adapted from [**88**].

In expanded A_3C_{60} compounds, the importance of strong electron-electron repulsion phenomena has recently been authenticated. Beyond the limit of T_c = 33 K for $RbCs_2C_{60}$, as the unit cell volume increases, superconductivity is destabilised with respect to a Mott insulating state. Following their report of bulk superconductivity at 38 K in A15 Cs_3C_{60},[**49**] Takabayashi and co-workers reported that the superconducting state emerges directly from a localised electron antiferromagnetic Mott-Hubbard insulating state, with T_N = 46 K, upon applying pressure.[**89**]

Emergence of the superconducting state from a Mott-Hubbard insulating state has previously been reported in organic superconductors.[**90**] Superconductivity next to a Mott antiferromagnetic insulating phase as a function of volume change or doping is, indeed, a characteristic indication of strong electron correlations in cuprate and organic superconductors.[**76**] In the high-T_c superconducting cuprates, electron correlations are known to have a favourable effect on superconductivity. Superconductivity emerged in cuprates when Mott insulators were doped with impurities and the antiferromagnetic insulating state is suppressed. Cuprates such as $Bi_2Sr_2CaCu_2O_{8+\delta}$ show a bell-shaped dependence of T_c on doping density;[**91**] the work of Takabayashi *et al.* on A15 Cs_3C_{60} demonstrated that a similar behaviour can be induced in the fullerides by applying pressure.[**89, 92**]

Despite the structural differences between the two cubic Cs_3C_{60} polymorphs, detailed earlier, the synthesis of bulk *fcc* Cs_3C_{60}, showing Mott-Hubbard antiferromagnetic ordering below T_N = 2.2 K (at ambient pressure) and superconductivity under moderate pressures ($T_{c(\max.)}$ = 35 K), has recently demonstrated that the superconductivity in both *fcc*- and *bcc*-based Cs_3C_{60} polymorphs is identical in origin.[**50**] Significantly, it also provided substantiation that seemingly BCS-type superconductivity and the Mott-Hubbard insulating state can occur in the same *fcc* lattice. It revealed that, in both polymorphs of Cs_3C_{60}, T_c scales in a dome-like relationship, independently of structure, in proximity to the Mott metal-insulator transition; this is controlled by the role of electron correlations, which are characteristic of other high-temperature superconducting materials (Fig. 1.9).[**50, 93**] The proximity of the Mott insulating phase strongly suggests that the anomalies of expanded A_3C_{60} superconducting compounds originate from strong repulsive electron correlation in the t_{1u} bands.[**76**] The anomalously low T_N of 2.2 K found for *fcc* Cs_3C_{60}, over one order of magnitude smaller than that of A15 Cs_3C_{60}, was attributed to spin frustration in the *fcc* polymorph, suppressing magnetic ordering.

A theoretical study of the electronic properties of the A15 and *fcc* Cs_3C_{60} polymorphs as a function of unit cell volume, using density functional theory at the LDA level, showed that the A15 polymorph exhibits both a significantly broader t_{1u} bandwidth and a larger density-of-states at the Fermi level. This result was attributed to the differing nature of inter-anion overlap in the two structures.[**87**]

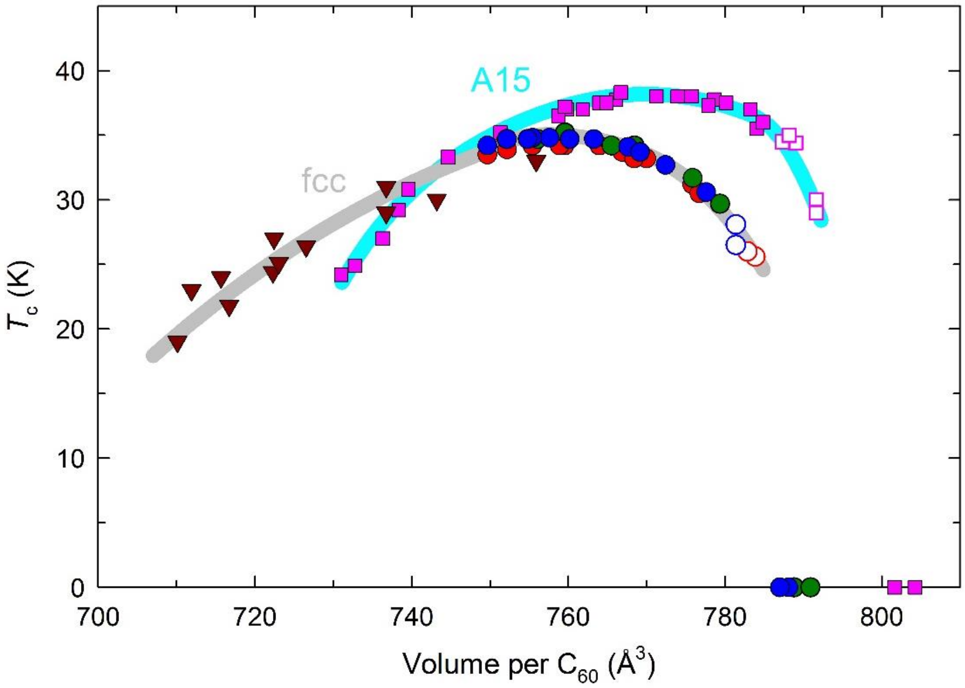

Figure 1.9: Superconducting transition temperature, T_c, as a function of volume occupied per fulleride anion at low temperature, for Cs_3C_{60}. Trace superconductivity is denoted by open symbols. Squares represent A15 Cs_3C_{60}, circles signify *fcc* Cs_3C_{60}, and triangles correspond to ambient pressure T_c values of superconducting *fcc* A_3C_{60} ($Fm\overline{3}m$) materials. Adapted from reference [**50**].

Strong electron-phonon coupling between C_{60} intramolecular phonons and t_{1u} electrons is, from group theory, only plausible for two phonon mode symmetries – the totally symmetric A_g and the five-fold degenerate H_g phonon modes. Only the latter are Jahn-Teller active.

The Jahn-Teller (JT) effect removes orbital degeneracy *via* coupling of the energy levels to symmetry-lowering molecular distortions. It is especially significant in fullerides because of the strong electron-phonon coupling and high (icosohedral) molecular symmetry, resulting in large degeneracies in electronic and phonon levels.[**94**] In a one-electron model, a single spherical C_{60} anion with a partially occupied t_{1u} level is JT unstable against a symmetry-lowering distortion,[**77**] as the triple t_{1u} degeneracy is lifted upon excitation of a vibration of H_g symmetry. Some indirect evidence for the JT effect in C_{60}^{3-} species has been provided by materials such as $NH_3K_3C_{60}$, $(CH_3NH_2)_3K_3C_{60}$ and $Li_3(NH_3)_6C_{60}$, where low-spin $S = ½$ ground states have been reported,[**95-97**] indicating an effective 'inversion' of the effective Hund's rule. However, other effects such as crystal field anisotropy could cause a low-spin state in non-cubic systems like the former systems, and whilst the latter material is cubic, steric effects arising from Li positional disorder could also remove degeneracy.

In a JT-distorted C_{60} molecular ion, tunnelling between equivalent distortions can dynamically re-establish full icosohedral symmetry, forming a dynamic JT state, which can achieve a gap in its electronic spectrum and a maximally-paired electron configuration with no static lattice symmetry breaking.[**77**] Whilst it is well-established that the cubic A_3C_{60} materials show no static JT distortions as evidenced by structural characterisation, the dynamic JT effect has been recently experimentally confirmed in both *fcc* and A15 Cs_3C_{60} polymorphs using infrared spectroscopy; the insulating state of both forms was ascribed to be that of a magnetic Mott-Jahn-Teller insulator.[**98**] Theory indicates that near to the Mott transition in C_{60}^{3-}, JT coupling and Hund's rule terms can virtually 'cancel', yielding a spin ½ state but with a weak on-site spin pairing interaction;[**85**] the recovery of static icosahedral symmetry through the dynamic JT effect would not eliminate splitting of the t_{1u}-derived band. As in the less expanded A_3C_{60} members, the triple degeneracy of the t_{1u}-based conduction band is crucial in enabling metallicity to survive to relatively large values of U/W. The transition to an electron-correlation-driven localised insulating state is accompanied by a loss of the denegeracy through the dynamic JT effect, but whilst locally, individual units are distorted, the interconversion rate between conformations is rapid enough to cause the increased symmetry observed in diffraction.

An attempt to model the unconventional superconducting properties of the expanded A_3C_{60} materials using a Hubbard-type model with the dynamical mean-field theory (DMFT) approximation, widely used in modelling strongly-correlated electron systems,[**82**] has recently been described.[**76**] These calculations confirmed that superconductivity in this system, whilst of *s*-wave symmetry rather than *d*-wave, exhibits many features characteristic of cuprate superconductors. Significantly, a dome-shaped superconducting order parameter region in proximity to the Mott transition, as a function of U/W, was obtained, in good agreement with experimental studies. Of reported theoretical models, DMFT is considered to currently provide the best description of A_3C_{60} experimental results.

1.3.8. Raman spectroscopy of intercalated fullerides

Raman spectroscopy has been widely employed to investigate the doping-induced changes in the vibrational modes of alkali-intercalated fulleride materials, and to probe whether or not the superconducting pairing interaction is mediated by electron-phonon coupling. Despite the rearrangements of fullerene molecules and charge transfer of electrons occuring upon alkali-metal intercalation into pristine C_{60}, the vibrational modes of undoped $C_{60,}$ which has ten Raman-active modes (two of A_g and eight of H_g symmetry), are largely preserved in A_3C_{60}, due to very weak coupling between A^+ and C_{60} molecular ions.[**22**] However, a new subclass of intermolecular modes involving the relative motion of the cation with respect to the molecular anion sublattice must also be considered. As the symmetry considerations for intramolecular coupling permit only A_g and H_g phonons to couple to t_{1u} conduction electrons, the applicability of Raman spectroscopy to studying these modes is thus evident. Whilst coupling to the A_g modes is thought to be weak because of an efficient screening effect, coupling to the H_g modes is stronger because it permits the JT mechanism.

Doping C_{60} with alkali metals transfers electrons to the C_{60} π electron orbitals, elongating the 6:6 C-C bonds and shifting the intramolecular tangential modes to lower wavenumber. In particular, the downshift of the ~1469 cm^{-1} tangential $A_g(2)$ mode upon alkali-metal doping is conveniently used to ascertain the stoichiometry x of A_xC_{60} materials. This mode, the most intense feature in an A_xC_{60} Raman spectrum, which corresponds to a symmetric stretch of C=C double bonds joining two pentagons, softens by ~6 cm^{-1} per alkali atom.[**99**]

The H_g modes in C_{60} broaden or even disappear upon alkali-metal doping to yield A_3C_{60} (A = K, Rb), ascribed to coupling between the phonons and a low-energy continuum, and possibly from the effects of Jahn-Teller distortion;[**22, 100**] due to electron-phonon coupling, phonon decay into an electron-hole pair is known to contribute to phonon width in A_3C_{60}, with the width therefore providing a measure of electron-phonon coupling.[**65**] Coupling between phonons and a low-energy continuum in A_3C_{60} further yields a modified Raman lineshape for H_g-derived modes, where Breit-Wigner-Fano modifications to the lineshape are observed, as opposed to a Lorentzian lineshape in insulating pristine C_{60}.[**22, 101**]

1.4. Outline of Thesis

This work aimed to systematically investigate the structural, electronic and magnetic properties of several key alkali and alkaline-earth fullerides under ambient and non-ambient temperature and pressure conditions, furthering our understanding of their physical behaviour as the interfulleride spacing is tuned *via* temperature, hydrostatic pressure and 'chemical' pressure application, through adjusting the alkali stoichiometry. In Chapter 2, the experimental characterisation and modelling techniques used are outlined, with a main focus on synchrotron X-ray powder diffraction and SQUID magnetometry techniques together with relevant theoretical background.

Chapter 3 focuses on a series of *fcc*-rich $Rb_xCs_{3-x}C_{60}$ ($0.25 \leq x \leq 2$) materials prepared *via* solid state synthesis, describing the evolution of their structural and magnetic properties at ambient and at elevated pressures and providing new insight into the strongly correlated, highly expanded regime of the A_3C_{60} phase diagram close to the Mott insulator boundary. Following from the complete *fcc* A_3C_{60} phase diagram, three regions are designated here; the 'underexpanded' region, spanning up to around a unit cell volume V_{max} of ~760 Å^3 per C_{60}, the 'optimally expanded' region around V_{max}, where T_c is highest, and the 'overexpanded' regime, for unit cell volumes larger than V_{max}.

Chapter 4 describes the structural properties of the A15-structured fullerides Cs_3C_{60} and Ba_3C_{60}, and their evolution with temperature and pressure. These samples were prepared at the University of Durham in our laboratory by Dr. Manolis Tzirakis and Mr. Dominic Myers, and the presently reported structural analysis was undertaken by the candidate. For the first time, the temperature evolution of A15 Cs_3C_{60} and the pressure evolution of Ba_3C_{60} have been studied in detail, and previous studies of the structural properties of A15 Cs_3C_{60} upon compression have been extended to higher pressures on high quality materials.

Lastly, Chapter 5 summarises the key results and contributions to knowledge arising from the present work, and proposes future directions in which these investigations could be extended.

Chapter 2 - Theory, instrumentation and methodology

2.1. Introduction

The objective of this chapter is to outline and describe the analytical procedures employed. The powder X-ray diffraction technique was extensively used to investigate the structural properties of various fulleride compounds as a function of temperature and of pressure, using high-resolution diffractometers at synchrotron X-ray radiation facilities. Magnetic properties were also investigated using a SQUID magnetometer, at both ambient and high pressures. This chapter focuses on the characterisation techniques employed, whilst including some relevant theoretical background to provide context. The synthetic aspects of this study are dealt with in the subsequent chapters.

2.2. Powder X-ray Diffraction

The structure of crystalline materials is widely studied through the diffraction of photons, neutrons and electrons. In this study, powder X-ray diffraction techniques have been widely used, and the following sections will focus on this technique, after first introducing some key concepts relating to crystal lattices and diffraction physics.

X-rays, a type of electromagnetic radiation, were first detected in 1895 by W. C. Röntgen, whilst studying the effects of high tension electrical discharges in sealed tubes under vacuum. X-rays used in diffraction experiments have wavelengths of ~0.1 – 5 Å, comparable with the distances between lattice planes in crystals, and corresponding to energies of ~125 keV – 2.5 keV.[**102**]

Powder X-ray diffraction (PXRD) is a powerful structural characterisation technique in solid-state chemistry, typically used when single crystals are not available. A powder defines a polycrystalline material in which all possible orientations of the crystals are present. Most materials only become practical or useful in the form of polycrystalline powders or ceramics; in the case of fullerenes, uniform phase-pure intercalation reactions of single crystals are experimentally difficult.

2.2.1. Unit cell and unit cell symmetry

A lattice is a mathematical array of points, related by the lattice translation operator $\mathbf{T} = u_1\mathbf{a}_1 + u_2\mathbf{a}_2 + u_3\mathbf{a}_3$, with u_1, u_2 and u_3 being integers and $\mathbf{a}_1$, $\mathbf{a}_2$ and $\mathbf{a}_3$ representing the crystal axes. If an identical basis comprised of s atoms at the positions $\mathbf{r}_j = x_j\mathbf{a}_1 + y_j\mathbf{a}_2 + z_j\mathbf{a}_3$ (where $j = 1, 2, \ldots, s$) is attached to each lattice point, this forms a crystal; x, y and z are typically chosen to take values between 0 and 1.[**103**]

A primitive unit cell is a minimum-volume cell, containing one lattice point, which will fill all space by the repetition of appropriate crystal translation operations.[**103**] Crystal lattices can be mapped into themselves by lattice translations, and also by various other symmetry operations. This additional symmetry allows the unit cell, and thus the entire structure, to be built from just a minimal section of the unit cell, termed the asymmetric unit.

A lattice point group refers to the group of symmetry operations which map the lattice into itself when applied about a lattice point. In three dimensions, the point symmetry groups define 14 separate lattice types, or Bravais lattices. They are grouped into systems classified according to seven cell types, termed triclinic, monoclinic, orthorhombic, tetragonal, cubic, trigonal and hexagonal, with further distinctions arising from the type of lattice centering, which may be primitive, body-centred, face-centred or base-centered (depending on cell type – for instance, only primitive centering is found in triclinic, trigonal and hexagonal lattices).[**103**]

Symmetry elements present in a crystal structure may include lattice translations, mirror planes, proper/improper rotation axes (including a centre of symmetry), screw axes and glide planes. As not every combination of lattice type and symmmetry element(s) is compatible, 230 unique ways to combine symmetry elements in a 3D lattice result, defined by 230 space groups. The presence of certain symmetry elements cause specific reflections to be missing from diffraction patterns, termed systematic absences, which are vital in identifying the symmetry of a given material.

2.2.2. Bragg's Law and the reciprocal lattice

W. L. Bragg presented a simple explanation of beam diffraction from a crystal, which, whilst straightforward, experimentally reproduces the correct result. The so-called Bragg Law, when considering two lattice planes separated by a distance *d*, with incoming X-ray radiation of wavelength λ at angle of incidence θ, defines when constructive interference occurs. It is expressed as follows:

$$n\lambda = 2d\sin\theta, \qquad \textbf{Equation 2.1}$$

where *n*, an integer, denotes the order of the diffraction (although typically, as the unit cell geometry may not always be known, *n* is set to 1 and peak positions are reported as a spacing *d*, which may not necessarily correspond to a real separation of equivalent atomic planes in the crystal structure).[**104**] The derivation assumes specular (mirror-like) reflection of incident waves from the parallel atomic planes, meaning the angle of incidence equals the angle of reflection, and elastic scattering, in which the energy of the X-ray is not changed on reflection.[**103**] The derivation of the Bragg law is depicted schematically in Fig. 2.1.

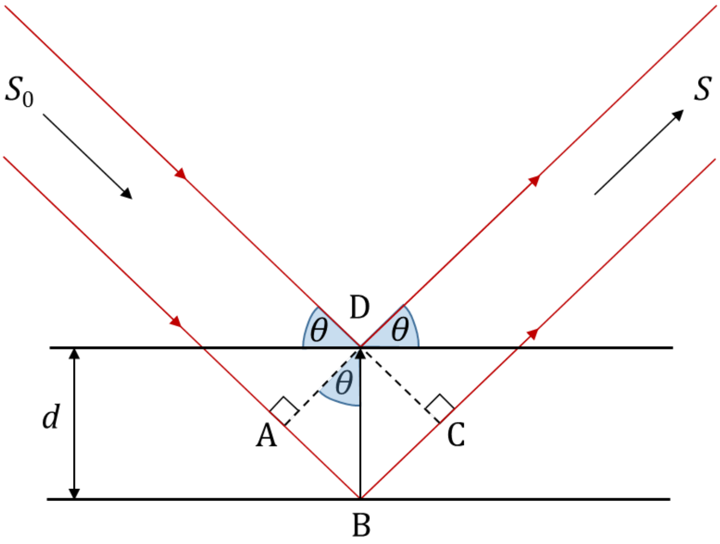

Figure 2.1 Schematic depiction of reflection of X-rays from two lattice planes from a family with indices *h*, *k*, *l* (with no common integer factor higher than unity). S_0 and S signify the directions of propagation of the primary X-ray beam and the wave scattered by the family of planes, respectively. The difference in 'path' between waves scattered at B and D equals AB + BC = $2d \sin \theta$; if this is a multiple of λ, the two waves may combine with maximum positive interference.

Whilst the Bragg equation is purely a consequence of lattice periodicity, the basis composition defines the relative intensity of the various orders of diffraction from a particular set of parallel planes. The interplanar spacing for a particular set of planes, d_{hkl}, relates in turn to the unit cell parameters, e.g. as follows (for a cubic unit cell with lattice parameter a):

$$\frac{1}{(d_{hkl})^2} = \frac{(h^2 + k^2 + l^2)}{a^2}, \qquad \textbf{Equation 2.2}$$

where *h*, *k* and *l* denote the so-called Miller indices, which define crystal lattice planes.

The reciprocal lattice is used to conveniently represent the diffraction physics of crystals. It is defined as a 'second' lattice, with unit cell parameters of a*, b*, c*, α*, β*, γ*, with the same origin as the 'standard' crystal lattice, and related to the latter as follows, where lattice parameters are defined as vectors:

$$\mathbf{a} \cdot \mathbf{b}^* = \mathbf{a} \cdot \mathbf{c}^* = \mathbf{b} \cdot \mathbf{c}^* = \mathbf{a}^* \cdot \mathbf{b} = \mathbf{a}^* \cdot \mathbf{c} = \mathbf{b}^* \cdot \mathbf{c} = 0 \qquad \textbf{Equation 2.3}$$

$$\mathbf{a} \cdot \mathbf{a}^* = \mathbf{b} \cdot \mathbf{b}^* = \mathbf{c} \cdot \mathbf{c}^* = 1 \qquad \textbf{Equation 2.4}$$

The reciprocal lattice vector **a***, for example, is perpendicular to the (100) planes, and equal in magnitude to the inverse of the interplanar spacing d_{100}. More generally, each reciprocal lattice vector $\mathbf{r}_{hkl}^* = h\mathbf{a}^* + k\mathbf{b}^* + l\mathbf{c}^*$ is associated with a family of direct lattice planes, to which it is perpendicular.

The 'Ewald sphere' construction represents in reciprocal space every possible point where planes, or reflection, could satisfy the Bragg equation, leading to its derivation. In Fig. 2.2, where this concept is depicted schematically, basic trigonometry dictates that $\sin\theta = OX / 2r$. If r, the sphere radius, is equal to $1/\lambda$, i.e. the inverse of the experimental wavelength, O is defined as the (0, 0, 0) reciprocal lattice point and X is a general reciprocal lattice point (h, k, l), the reciprocal lattice vector OX becomes $1/d_{hkl}$. Therefore, $\sin\theta = (1/d_{hkl})/(2/\lambda)$, yielding the Bragg equation upon rearrangement.

Diffraction can only occur when the scattering vector equals a reciprocal lattice vector. If an incoming beam is in the YO direction, and a detector is positioned on the general reciprocal lattice point, a diffraction 'spot' can be measured. If the crystal orientation is changed, the reciprocal lattice will be reoriented, with different reciprocal lattice points brought to the Ewald sphere surface.

In an ideal polycrystalline sample, individual crystallites should orientate in all possible directions, represented with equal probability; all reciprocal lattice points 'smear out' onto spherical shells, with the origin of reciprocal space at the centre. The circular intersection of these shells with the Ewald sphere produces co-axial 'Debye-Scherrer' cones of diffracted X-rays.[**105**]

Intensity is isotropic around the rings from an ideal powder, and conventional measurements usually take one-dimensional cuts through the rings, but various detectors can be employed, including two-dimensional detectors (discussed in Section 2.4.1). PXRD data consist of a set of intensity values, measured at a set of specific momentum transfer (Q) values, normally stated as 2θ settings, although diffraction measurements can also be collected with fixed 2θ whilst varying wavelength, in time-of-flight or energy-dispersive diffraction.

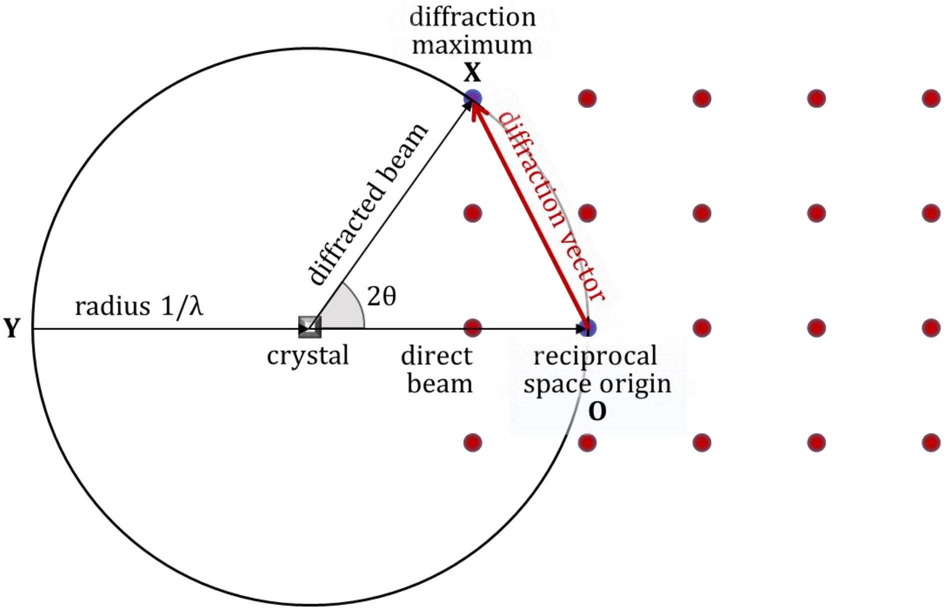

Figure 2.2 Schematic two-dimensional representation of the Ewald sphere construction.

2.2.3. X-ray diffraction from crystals

A single electron scatters as a point source, with scattering amplitude equal in all directions, the magnitude of which is described in units relative to scattering from a single electron. Intensity, the quantity measured by the diffraction apparatus, is given by the magnitude of the amplitude squared. If an atom is considered a point source of scattering (neglecting partially destructive interference between scattering of electrons within the atoms), at a diffraction angle of 0°, all scattering is in phase, hence the scattering amplitude, f_0, equals the number of electrons in the atom. In general, the scattering magnitude of an atom is approximately proportional to the atomic number when sinθ / λ is small; at higher angles, f_0 decreases in accordance with functions of the electronic structure.[**104**]

Atoms in a crystal structure are not immobile in space, as thermal effects produce vibration about their average positions; a given atom is thus symbolised by a 3D triaxial ellipsoid scattering distribution. At temperatures $T > 0$ K, scattering amplitude decreases monotonically at higher diffraction angles. The necessary correction to values of f_0 to account for these effects can be described using the Debye-Waller equation:[**104**]

$$f = f_0\, e^{\left(\frac{-B\, sin^2 \theta}{\lambda^2}\right)}, \qquad \textbf{Equation 2.5}$$

f being the scattering factor under experimental conditions, f_0 representing the scattering factor at 0 K, and B, the Debye-Waller factor, is a quantity relating to the mean vibration amplitude normal to the diffraction direction for which f is implemented.[**104**] B is defined as $B = 8\pi^2\langle u^2\rangle$, with $\langle u^2\rangle$ being the mean square amplitude of displacement.

As electrons are bound to the nucleus by forces depending on the atomic field strength and the electron's quantum state, they can be regarded as oscillators with natural frequencies. If the frequency of the primary beam is close to these frequencies, resonance can take place. Scattering occuring under these conditions is termed anomalous, and f_0, as defined above, is substituted by a complex quantity given by the sum of $f_0 + f' + if''$, with f' and f'' defined as the real and imaginary dispersion corrections.[**106**]

The intensity of a diffracted X-ray beam, I_{hkl}, is related to the 'structure factor', F_{hkl}, as follows:

$$I_{\mathrm{hkl}} \propto |\, F_{\mathrm{hkl}} \,|^2. \qquad \textbf{Equation 2.6}$$

The structure factor describes the scattering amplitude from the unit cell in the direction θ, in a plane perpendicular to the atomic plane *hkl*.[**104**] It is evaluated by summing over all atoms in the crystal:

$$F_{\mathrm{hkl}} = \Sigma_{\mathrm{i}}\, f_i\, e^{2\pi \mathrm{i}(\mathrm{hx_i} + \mathrm{ky_i} + \mathrm{lz_i})}, \qquad \textbf{Equation 2.7}$$

with f_i signifying the scattering power of an atom under experimental conditions (after correction for the effects of thermal vibration and anomalous scattering, as described earlier).

Other factors between I and F which affect the measured intensity are the Lorentz factor, absorption, polarisation, the multiplicity (*i.e.* the number of symmetry equivalent reflections) and the scale factor. These values depend on the particular sample and experimental conditions employed, including the incident beam intensity and X-ray wavelength, the detector slit height, the sample-to-detector distance, the unit cell volume, and the volume of sample irradiated by the beam; the sample may also be multiphasic.

2.2.4. Radiation sources

In a standard laboratory diffractometer, X-rays are produced in a sealed-tube source, through the bombardment of a metal anode by electrons accelerated using a potential difference. The resulting electronic transitions in the atoms of the target material result in the emission of electromagnetic radiation as electrons return to lower energy states. A continuous energy spectrum of X-rays, termed white radiation, is obtained through multiple collision events with the target atoms which result in gradual electron energy loss. However, when the energy of the accelerated electrons exceeds a certain threshold, a second, discontinuous spectrum is also obtained, called the characteristic radiation. This spectrum consists of discrete peaks, their wavelength determined only by the target metal employed, and results from the ejection of electrons from inner electron shells of the metal atom. Higher energy electrons then drop to the vacant levels, emitting X-ray photons, with wavelengths defined by the energy difference between the two levels. The characteristic K_α line is that of highest intensity, and therefore that normally used for X-ray diffraction experiments.[**102, 106**]

Common target elements, selected as good heat and electricity conductors with high melting points, are Cu and Mo, with Cr, Fe, Ag, Co and W employed for specialist purposes. Elements heavier than Cu may be used for total scattering and pair-distribution-function (PDF) studies, although their wavelengths are too short for many practical laboratory uses, whilst lighter element targets may circumvent problems with fluorescence encountered with a Cu target in certain materials such as steels (disadvantages include higher sample absorption and air scatter, and fewer available Bragg reflections).[**102**] Copper is a good thermal conductor, enabling a reasonably large power to be applied to the target. Where a Cu target is used, CuK_β radiation (λ = 1.392 Å) is typically strongly attenuated using a Ni filter in the beam path, with the threshold energy of the Ni K absorption edge at λ = 1.488 Å, to more selectively obtain the desired CuK_α X-rays, with λ = 1.542 Å.[**102**]

Samples are commonly measured using one of two types of instrument geometries, termed reflection and transmission. In reflection geometry, also often referred to as 'Bragg-Brentano', a flat plate sample is measured, with the divergent incident X-ray beam reflected from the sample surface and converging at a defined radius from the sample at a receiving slit, before reaching the detector. Typically, the sample is spun around an axis normal to the plate, and a diffracted-beam monochromator crystal is placed between the sample and the detector, and the source is normally fixed whilst the monochromator and detector arm rotate to vary 2θ. In transmission geometry, used to measure capillary or thin foil samples, a pre-sample monochromator is typically used to focus the divergent X-ray beam onto the 2θ measuring circle of the detector. Samples are also spun (*i.e.* about the capillary axis), to improve the powder average being measured.[**102**]

X-rays, along with other types of electromagnetic radiation, can also be generated at synchrotron radiation facilities, which are a type of particle accelerator. Synchrotron X-ray radiation, first observed at a synchrotron in 1947, is produced when charged particles moving at relativistic speeds change velocity. X-ray beams of ~100-10000 times higher intensity than X-ray tube $K_{\alpha 1}$ emission can be generated. Electrons, moving at relativistic velocities close to the speed of light, are restricted to travel in near-circular paths in a 'storage ring', using magnets located at intervals around the ring. Straight sections of the ring alternate with curved sections, where electrons are steered via a bending magnet into the next straight section. Synchrotron radiation, arising from the continuous inward radial acceleration of the electrons, is emitted with a continuous spectrum tangentially from the ring in the curved sections,[**107**] where the electrons encounter a bending magnet. It is also emitted at undulator or wiggler insertion devices, consisting of rows of magnets with alternating polarity and located in a straight part of the electron orbit; the former emit ultra-bright quasi-monochromatic radiation, and the latter result in a bright and spectrally continuous electron beam with short wavelengths. The main features of a synchrotron facility are illustrated schematically in Fig. 2.3.

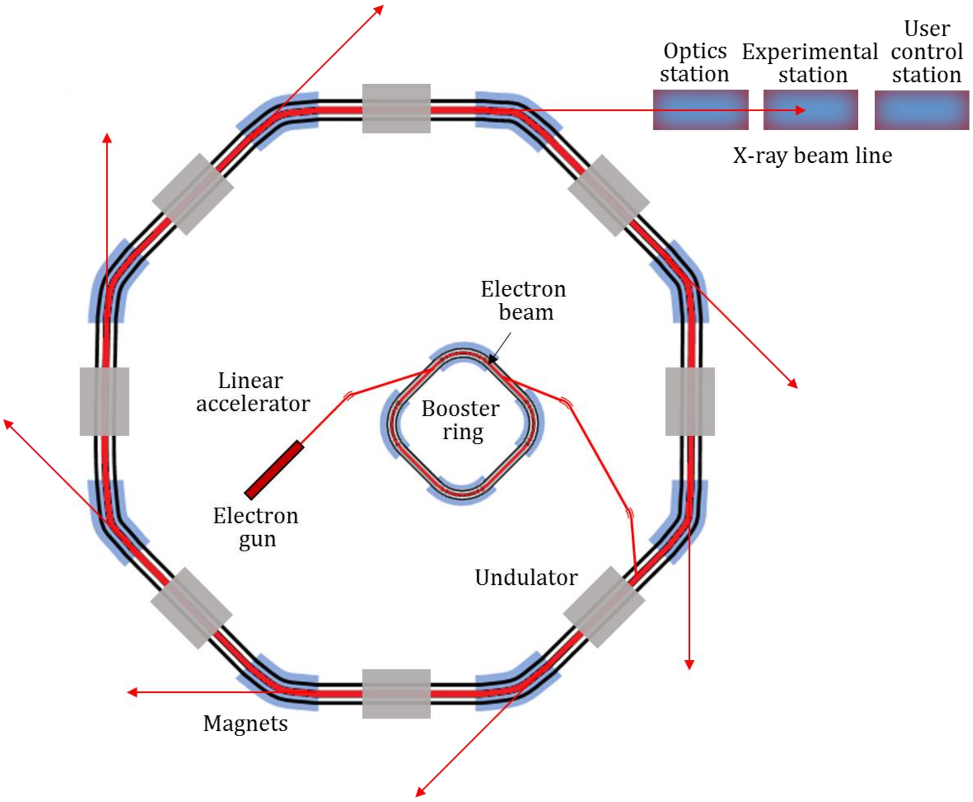

Figure 2.3 Schematic illustration of key features of a synchrotron facility (not to scale).

The wavelengths of synchrotron radiation span from infrared to very short X-ray wavelengths, and a particular wavelength can be selected using a crystal monochromator, which can be set to reflect only a desired wavelength; this illustrates a main advantage of synchrotron radiation, besides higher intensity, over X-ray tubes where the wavelength cannot be varied. An X-ray wavelength may be chosen of energy well away from the absorption edge of a heavy element in a sample to minimise absorption effects, or, conversely, close to an absorption edge, exploited in techniques such as extended X-ray absorption fine structure, and to enhance contrast between elements for probing cation distribution or even oxidation state using anomalous scattering techniques. Selection of an x-ray wavelength entails a compromise between improved peak separation but fewer accessible reflections (which cannot then offset the many structural parameters to refine) obtained using a longer wavelength, and gaining more accessible peaks, but with severe overlap, resulting from a shorter wavelength.

The incident monochromatic beam of synchrotron radiation is also highly vertically collimated, allowing instruments with much higher 2θ resolution than an X-ray tube source to be created. This high collimation, however, may exacerbate problems with highly crystalline samples in which there is insufficient sampling of grains appropriately oriented for diffraction, thus rendering rotation or rocking of the sample during data collection essential.[**108**] Beam lines at synchrotron radiation facilities have a wide variety of sample environments routinely available, *e.g.* experiments may be performed under non-ambient conditions of temperature or pressure.

2.2.5. The diamond-anvil cell (DAC)

Pressure is a key thermodynamic parameter, allowing an increase of matter density by reducing volume; this results in an overall reduction of interatomic and intermolecular distances over a much greater range than can be accessed by varying temperature, and allows atomic and molecular interactions to be investigated in detail.

The diamond-anvil cell (DAC) is the most versatile tool for pressure generation in X-ray diffraction, and also widely used in many other experimental techniques of condensed-matter physics (including X-ray absorption, Mössbauer, Raman, infrared spectroscopies, electrical and magnetic measurements). In this work, several experiments have been undertaken using DACs for structural investigations of polycrystalline fulleride materials at low and at ambient temperatures. A DAC comprises two opposed anvils formed by two high-quality diamonds, each presenting two plane surfaces: the table, with a large area (~4 mm diameter), and the culet, with a small area (50 – 500 μm diameter);[**109**] a schematic diagram of a DAC is shown in Fig. 2.4.

Utilising diamond as an anvil material confers the advantages of mechanical hardness and transparency for electromagnetic radiation. The anvils are mounted on seats which transmit force from the cell body to the diamond tables; whilst pressure is generated axially, it is normally transmitted to the sample quasi-hydrostatically, utilising the Pascal principle, *i.e.* that pressure is transmitted equally to all parts of a fluid in equilibrium.

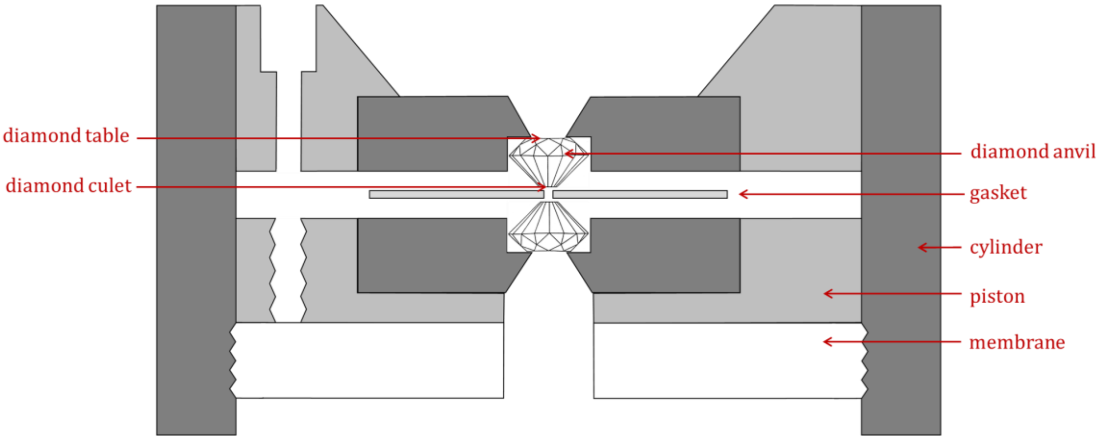

Figure 2.4 A schematic cross-section of a membrane DAC used for powder X-ray diffraction.

Between the diamonds, a pre-indented metal gasket, typically stainless steel or beryllium of ~0.2 mm thickness, guarantees lateral support for the diamond's conical faces close to the tips. A hole drilled at the centre provides containment for the sample, pressure medium required for quasi-hydrostatic pressure transmission to the sample, and pressure sensor. When force is applied by the parallel oriented diamond tips, generated through screws or gas membranes, the gasket deforms plastically, transferring pressure to the sample (*via* the pressure medium) resulting from the volume reduction.[**110**]

Whilst the small beam diameters of 30 μm or less typical of a synchrotron source allow selective measurement of the area close to the centre of the DAC, where pressure gradients are minor, to improve the resulting powder average, the DAC is typically oscillated during measurement. The utilisation of two-dimensional (2D) imaging plate detectors also helps to minimise problems associated with reduced powder average, as 2D images are converted into one-dimensional data (intensity *vs.* diffraction angle) prior to analysis by azimuthal integration of the intensities.[**110**]

The ruby fluorescence method, the most commonly used to ascertain pressure in DAC measurements, is based on the shift in energy (~3.6 Å/GPa) observed in a pair of electronic transitions in Cr^{3+} dopants in Al_2O_3 upon lattice compression. This technique was used throughout this work to obtain accurate values for pressure at the sample, with crystal ruby chips placed on one diamond face prior to sample loading. Whilst the high sensitivity of the fluorescence wavelength to temperature changes and to non-hydrostatic stresses is disadvantageous, measurement of optical fluorescence is relatively fast and can yield pressures as precise as 0.1 GPa. A blue laser was employed to monitor the pressure dependence of the R_1 luminescence line wavelength (λ), with pressure calibrated using the following formula:[**111**]

$$P = \frac{B_0}{B'}\left(\left(\frac{\lambda}{\lambda_0}\right)^{\mathrm{B}'} - 1\right),$$

Equation 2.8

using B_0 = 1904 GPa and B' = 7.665. The R_1 line wavelength at ambient pressure, λ_0, is ~694 nm, but the precise value depends on the ruby quality and is calibrated at the beginning of each experiment.

2.3. Radiation Facilities (Instrumentation)

2.3.1. European Synchrotron Radiation Facility (ESRF)

The ESRF, the most powerful synchrotron radiation source in Europe, is situated in Grenoble, France. At the ESRF, where user operation commenced in 1994, electrons are first accelerated using a 16-metre-long linear accelerator, then pass into a booster accelerator. Upon attaining their maximum speed, with an energy of 6 GeV, the electrons are injected into the vacuum tube of the 844-metre-long storage ring, where they are steered on their orbital path by magnets, also passing through undulator insertion devices. Synchrotron X-ray beams leave the main storage ring a few metres after each undulator, entering 41 different 'beamlines' around the storage ring; each beamline is specialised for differing scientific fields, and X-ray optical equipment is used to prepare the beam appropriately for experiments, prior to its arrival at each experimental station.[**112**] In this study, experimental work was undertaken at ESRF beamlines ID27 and ID31.

2.3.2. ID31 – High-resolution X-ray powder diffraction

The high-resolution X-ray powder diffraction beamline ID31, now decomissioned prior to the opening of an upgraded powder diffraction beamline, ID22, was utilised for structural studies of the materials in this work at ambient and at variable temperatures. Three 11-mm-gap ex-vacuum undulator insertion devices produced the X-rays; these had their magnetic field in the vertical direction, resulting in horizontal electron deflection, and linearly polarised radiation with the electric component in the plane of the synchrotron orbit is generated. X-ray wavelengths tunable between 0.21 Å – 2.48 Å could be generated. The magnetic field varied sinusoidally, and every oscillation of the electrons supplied tangential bursts of X-ray radiation. Interference between radiation from different oscillations collimated the beam in the horizontal plane, concentrating the radiation into a central on-axis cone enclosed by weaker rings, and resulting in a high flux density reaching the sample. Undulators produced a succession of peaks at integer multiples of a fundamental energy, determined by the magnetic field strength, and the energy of the fundamental and its harmonics could be adjusted by changing the vertical gap separating the array of magnets.[**102**]

A double-crystal monochromator utilising Si (111) crystals then ensured that the generated polychromatic X-ray beam was monochromatic before reaching the sample. A perfectly aligned double-crystal arrangement preserved the direction of the incident beam, and cryogenic cooling maintained the temperature stability of monochromator crystals, under the heat load from incoming X-rays.

For the data collection at beamline ID31 presented throughout this work, samples were loaded into 0.5 mm diameter glass capillaries (sealed under Ar or He gas, the latter for low-temperature studies). Each capillary was mounted on a goniometer head that was spun about the capillary axis at a frequency of ~20 Hz, to reduce aberrations arising from the powder specimen (*e.g.* improve powder average, reduce any preferred orientation effects). Flat plate specimens could also be measured on ID31. A multianalyser stage containing a bank of 9 detectors, each preceded by a Si (111) analyser crystal and separated by ~ 2° in 2θ, was scanned in an arc about the specimen to record diffracted intensity as a function of 2θ (Fig. 2.5). Such a setup, utilising multiple crystals operating in parallel both increases detection efficiency, and allows rapid measurement of a relative large angular range, useful for e.g. dynamic measurements or where samples are particularly X-ray sensitive. The independent high-resolution diffraction patterns collected in parallel using the multianalyser stage were summed into single data sets, using the program 'id31sum'. [**113**]

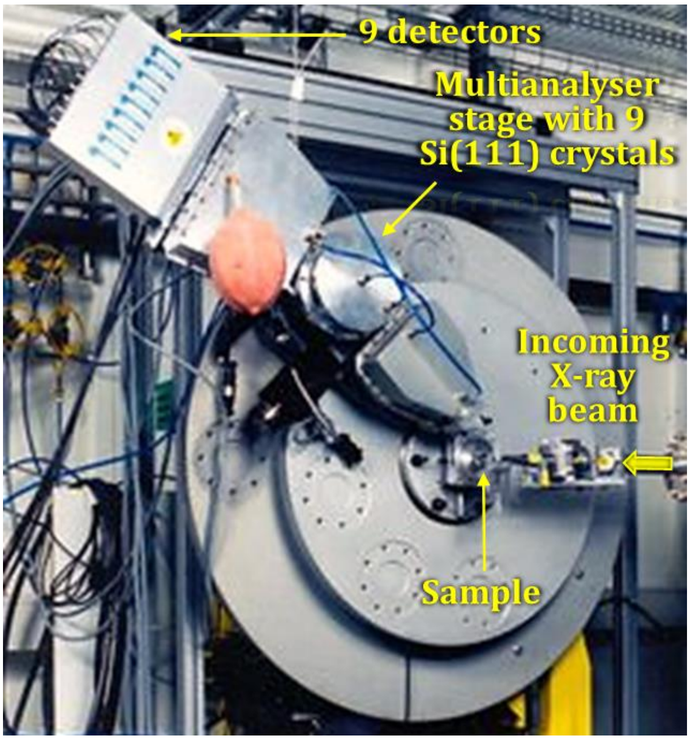

Figure 2.5 The diffractometer setup on beamline ID31, ESRF (adapted from [**102**]).

Various ancillary equipment for measurements under a wide range of conditions was available. In this work, a liquid-helium-cooled cryostat (Janis INC., USA) was utilised for low temperature data collection; within the cryostat, sample measurement of a spinning capillary, albeit at a reduced spinning rate than the standard goniometer spinner allows, could be achieved down to 4 K. A nitrogen gas cryostream, hot-air blower and mirror furnace were also available (maximum achievable temperature 1500 °C), along with an automatic sample changer and cells for gas loading.

2.3.3. ID27 – High pressure beamline

The high pressure beamline ID27 was employed for structural studies as a function of pressure at low and at ambient temperatures in this work. The X-ray source consists of two small-gap in-vacuum undulators of period 23 mm, which can be operated simultaneously with a minimum magnetic gap of 6 mm. The monochromatic beam is selected with a nitrogen-cooled Si (111) monochromator, optimised to select X-ray energies of 6 keV – 90 keV (corresponding to wavelengths of 2 Å – 0.14 Å). A pair of multilayer mirrors in the 'Kirkpatrick-Baez' geometry then focus the X-ray beam on the sample. In one dedicated experimental hutch, optimised for DAC experiments, DACs are mounted on a high-precision two-circle goniometer. A second experimental hutch is available for large-volume-cell experiments using *e.g.* a Paris-Edinburgh cell.[**114**]

In this study, powder samples were loaded inside an argon glovebox into a helium-gas-driven membrane diamond-anvil-cell (MDAC), which was placed inside a closed-cycle helium refrigerator for low-temperature data collection. Helium gas loaded in the MDAC was used as a pressure medium. The applied pressure was increased at the fixed temperature chosen for the experiment by controlling the He gas pressure on the MDAC diaphragm. The MDAC was rotated (oscillated) slightly during data collection, by ±5-8°, to improve the powder average.

Diffraction patterns were collected with a monochromatic X-ray beam (λ = 0.3738 Å) focused to 3×3 μm^2, and images of the Debye-Scherrer rings were recorded using a MARCCD detector (165 mm diameter, 79.012 μm pixel size). Imaging plate data were converted into one-dimensional intensity *vs*. diffraction angle data by azimuthal integration, using the program FIT2D.[**115**]

2.3.4. SPring-8 Synchrotron Radiation Facility

The synchrotron radiation facility 'SPring-8', formally the Large-scale Synchrotron Radiation Facility, located in Hyogo Prefecture, Japan, delivers the most powerful synchrotron radiation presently available, and opened for users in 1997. As at the ESRF, high-energy (8 GeV) electrons accelerated to relativistic speeds are injected into a storage ring, of 1436 m circumference. 62 beamlines, specialised for differing applications, are available. In this work, beamline BL10XU was utilised to perform X-ray diffraction structural analysis under high-pressure.

2.3.5. BL10XU – High pressure beamline

Beamline BL10XU at SPring-8, utilised for structural studies of the materials in this research at low and at ambient temperatures as a function of pressure, is optimised for X-ray diffraction experiments using DACs at high pressure and low or high temperature.[**116**] Samples were measured in an MDAC, loaded as described in Section 2.3.3; the MDACs were oscillated by ±1-2° during data collection.

A high-resolution monochromatic angle-dispersive X-ray diffraction technique is employed. The radiation source is an in-vacuum X-ray undulator, with a short period providing higher brilliance in the 20-50 keV range, selected because of the limited opening angle of DACs for X-ray scattering and their highly absorbing diamond windows, although a tunable X-ray energy range from 7 to 90 keV is accessible. A Si(111) double-crystal monochromator is installed in the optics hutch, generating a monochromatic X-ray beam passed through transport channels to the experimental hutch for diffraction experiments. The X-ray beam had wavelength $\lambda \sim 0.41$ Å (details are presented in Sections 3.3 and 5.3) and was focused to 40×40 μm^2.

Pressures of up to 300 GPa can be generated, with accessible temperatures ranging from 10 K – 300 K and from 1000 - 3000 K, utilising a cryostat or a double-sided laser heating system, respectively. Both flat imaging plate (Rigaku R-AXIS IV, 300×300 mm^2 area, 0.100 mm pixel size) and X-ray CCD (Bruker) detector systems are available, with the former used in this work to record images of the Debye-Scherrer rings. Imaging plate data were converted into one-dimensional intensity *vs*. diffraction angle data by azimuthal integration, using the program WinPIP.[**117**]

2.4. Data Analysis – Diffraction

2.4.1. Integration of two-dimensional powder X-ray diffraction data

All powder X-ray diffraction data collected at elevated pressures described in this work were collected using an imaging plate (IP) detector. To process these data, converting them into tables of scattered intensities *vs.* scattering angle 2θ requires software such as the aforementioned FIT2D [**115**] and WinPIP [**117**].

The diffracted intensity is observed on a set of Debye-Scherrer cones; intersection of the cones with the detection plane of an IP detector, if aligned perpendicular to the cones' axes, results in a series of concentric rings (termed Debye-Scherrer rings) on the detection plane. A representative data set from the IP detector is shown in Fig. 2.6. Whilst ideally intensity on each ring is homogeneous, in practice the small sample volume in the

DAC renders real powder rings spotty or discontinuous to some extent, a fundamental problem with data quality from high pressure PXRD experiments. The intensity as a function of ring radius is thus most reliably extracted by averaging over numerous radial scans taken along different azimuthal directions, or over larger unbroken segments of the Debye-Scherrer rings. Ideally, data are integrated along circles around the centre of the Debye-Scherrer rings, with radii ranging from zero up to the detector border.

Four geometric parameters must be known prior to integration, although can be determined purely using information present on the diffraction images, to obtain data of intensity *vs.* effective radius. These are the x_0 and y_0 coordinates defining the position of the centre of the Debye-Scherrer rings on the image, and, as the detector is not normally aligned perfectly perpendicularly to the incident beam, the integration must be made along curves representing the elliptical shape of the resulting rings; two parameters, the tilt plane rotation angle and the tilt angle, define the shape and orientation of the integration ellipses. To convert these data into data of intensity *vs.* 2θ for structural refinement, the incident X-ray wavelength and the sample-to-detector distance must also be known, requiring knowledge of the lattice parameters of the measured compound, and typically determined by calibration with an external standard. Decreasing the sample-to-detector distance increases the angular range and thus the total number of Debye-Scherrer rings in an image, but the spatial resolution of the IP detector imposes a minimum distance.[**118**]

Certain areas of the IP recording must be excluded from subsequent data reduction steps, prior to integration. An overlay for an image is defined using masking tools, with pixels underneath the overlay excluded from subsequent data processing, without changing the image itself. These areas may include shadows cast on the detection area from diffracted radiation hitting the beam stop assembly or the DAC, or overexposed spots, where the photomultiplier(s) measuring the intensity of luminescence radiation emitted from each particular pixel(s) become saturated.

Contributions from the crystalline diamond anvils and the ruby (or other) pressure calibration standard, and if desirable, identifiable and non-overlapping, rings from impurity phases in the sample, are also typically excluded or ‘masked’ before data integration. Other minor phenomena which may yield incorrect intensities on the IP recording include radiation scattered from the beam stop hitting the detection area, dust on the diamond anvil or on the image plate, or an image plate defect.[**118**] The integrated data, *i.e.* diffraction angles or d-spacing and intensities (usually after straightforward conversion to a file format native to the Rietveld refinement program of choice), can then be analysed using *e.g.* the Rietveld method.

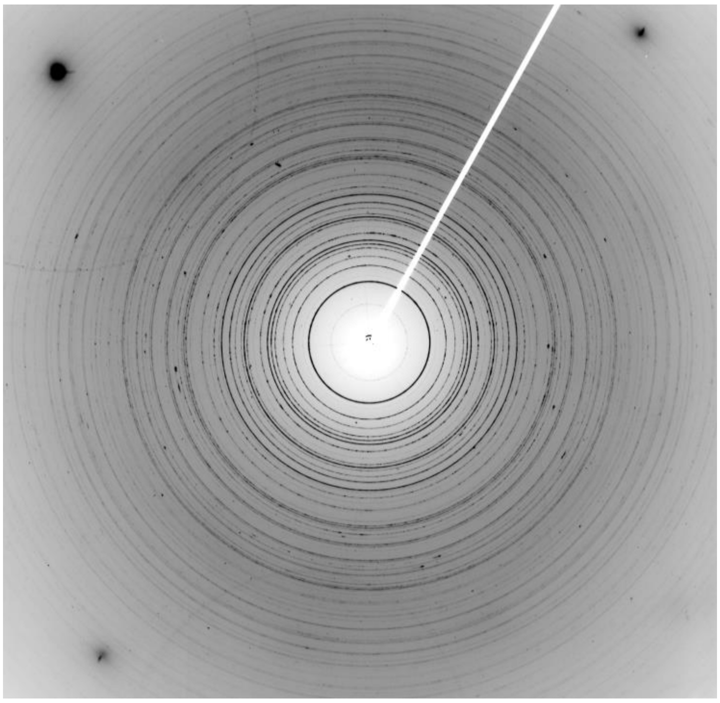

Figure 2.6 X-ray powder diffraction data of Ba_3C_{60}, contained in a MDAC, at 1.13 GPa and at ambient temperature, recorded with a Rigaku R-AXIS IV IP detector (X-ray wavelength = 0.41261 Å). The light grey area in the top right quadrant is a shadow cast by the beam stop assembly. The large black spots near the corners, attributed to diamond single crystal reflections, are excluded from data reduction using an overlay (along with the beam stop shadow and various smaller abberations), which is not shown.

2.4.2. The Rietveld method

The Rietveld method for structural analysis of powder diffraction data was first described by Hugo Rietveld in 1969.[**119**] It enables both phase-pure samples and separate crystalline phases in multiphase samples to be analysed with their relative volume fractions determined quantitatively, through refinement of a starting structural model. In a Rietveld refinement, least-squares refinements of an overall model are undertaken until the best achievable fit is obtained between the entire observed powder diffraction pattern and the entire calculated pattern; the latter is based on simulataneously refined models for the crystal structure(s), diffraction optics effects, instrumental factors and other sample characteristics as desired and permitted by the data quality.[**120**]

A powder diffraction pattern of a crystalline material can be considered as a combination of individual reflection peaks, with individual peak heights, positions, and breadths, and tails decaying gradually with distance from the peak position. The integrated area of each peak profile is proportional to its Bragg intensity, I_K (K represents the Miller indices), which in turn is proportional to $|F_K|^2$. In most cases, individual peak profiles are not completely resolved, partially overlapping one another to varying degrees. In the Rietveld method, no attempt is made to resolve overlapped reflections prior to structure refinement, and thus, a reasonably good starting model is required.[**120**]

Besides a starting model for atomic positional and thermal parameters, several other requirements are fundamental to the success of the Rietveld method; in general, diffractometer geometry, the quality of instrumental alignment and calibration, the most appropriate radiation type and wavelength, suitable sample preparation, slit sizes and the counting time required need all be considered prior to data collection.[**108**] Sample crystallites should be of approximately equal size, around 1-5 μm, and randomly distributed, with preferred orientations minimised (an empirical correction function can be used to correct the intensities, and rotation of a horizontally mounted capillary can effectively remove preferred-orientation effects), and corrections for instrumental aberrations should be made.[**106, 108**] In Bragg-Brentano geometries, a constant-volume condition must be ensured, with the incident beam kept on the sample at all angles (irradiation of the sample holder at low angles can result in too-low intensities) and sample transparency issues, which light element samples are particularly prone to, avoided, by *e.g.* the use of transmission geometry. Transmission geometry may be problematic for highly absorbing samples, if the incident beam cannot penetrate the entire samples, which may require dilution with a light-element material or measurement in reflection geometry. To optimise counting statistics throughout an X-ray powder diffraction pattern, more time is generally required for data collection at higher angles where intensities are lower. The step size should be around a fifth to a tenth of the full-width at half-maximum (FWHM) of each peak, and the highest 2θ should be selected to yield the maximum useful data.[**108**]

The best fit entails finding the minimum S_y (residual) satisfying the following equation:

$$S_y = \Sigma_i w_i (y_i - y_{ci})^2,$$ **Equation 2.9**

where y_i represents the observed numerical intensity value at increment i in the pattern, i.e. the observations measured at independent variable setting x_i, y_{ci} signifies the calculated intensity, *i.e.* the model – a function predicting the intensity at increment i, and w_i, the weight, is defined as follows:

$$w_{\mathrm{i}} = [\frac{1}{\sigma(y_{\mathrm{i}})}]^2, \qquad \textbf{Equation 2.10}$$

where σ is the standard uncertainty on y_i.[**120**]

As previously discussed, the diffracted intensity is proportional to the square of the structure factor, F_{hkl}; this leads to the following expression used to calculate the model intensities at any arbitrary position in the diffractogram, i, which also accounts for other factors affecting the diffracted intensity:[**120**]

$$y_{\mathrm{ci}} = s\,\Sigma_{\mathrm{K}}\,L_{\mathrm{K}}\,|F_{\mathrm{hkl}}|^2\,\phi\,(2\theta_{\mathrm{i}} - 2\theta_{\mathrm{K}})\,P_{\mathrm{K}}\,A\; +\; y_{\mathrm{bi}}, \qquad \textbf{Equation 2.11}$$

with s representing the scale factor, K signifying the Miller indices, *hkl*, for each Bragg reflection, L_K comprising the polarisation, Lorentz and multiplicity factors, and F_{hkl} denoting the structure factor for the *K*th Bragg reflection. The terms ϕ, P_K and A represent a reflection profile function, a preferred orientation function and an absorption factor, respectively, and y_{bi} represents the background intensity, typically obtained from a refinable background function.[**120**]

The Rietveld refinement procedure modifies the refinable parameters until the residual is minimised, *i.e.* a 'best fit' of the whole calculated pattern to the entire observed pattern is attained, but the particular 'best fit' achievable depends on the satisfactoriness of the model, and on whether a global minimum, as opposed to a local, 'false' minimum, has been reached; various criteria of fit are required to make such judgements.[**120**] In addition to the 'chemical reasonableness' of the model and graphical analysis of the fit, so-called Rietveld error indices are a common criterion used to judge the quality of Rietveld fits.

The most straightforward discrepancy index, the weighted profile R-factor, R_{wp}, derives from the square root of the quantity minimised, scaled by the weighted intensities, and is defined as follows:[**121**]

$$R_{\mathrm{wp}}^2 = \frac{\Sigma_{\mathrm{i}} w_{\mathrm{i}} [y_{\mathrm{i}} - y_{\mathrm{ci}}]^2}{\Sigma_{\mathrm{i}} w_{\mathrm{i}} [{y_{\mathrm{i}}}^2]} \qquad \textbf{Equation 2.12}$$

In a theoretical, ideal model, the average value of $[y_\mathrm{i} - y_\mathrm{ci})]^2$ will equal $\sigma^2(y_\mathrm{i})$, and thus, from Equations 2.10 and 2.12, $w_\mathrm{i}[y_\mathrm{i} - y_\mathrm{ci}]^2$ should equal one. Therefore, the 'best possible' R_wp, termed the expected R factor, R_exp, is described as follows:

$$R^2_\mathrm{exp} = \frac{N}{\Sigma_\mathrm{i} w_\mathrm{i}[y_\mathrm{i}{}^2]}, \qquad \textbf{Equation 2.13}$$

N being the number of data points, with the number of refinable parameters subtracted (less the number of constraints used), although in practice the number of data points is sufficiently larger than the number of refining parameters such that subtracting the latter should produce a negligible effect. Values of R_wp and R_exp quoted in this thesis are as fitted (*i.e.* not after background subtraction).

A related statistical criterion of fit, χ^2, is commonly employed:

$$\chi^2 = (\frac{R_\mathrm{wp}}{R_\mathrm{exp}})^2 \qquad \textbf{Equation 2.14}$$

Alternatively, it can be defined as the average of the weighted sums of squared differences:

$$\chi^2 = (1/N)\, \Sigma_\mathrm{i} w_\mathrm{i}[y_\mathrm{i} - y_\mathrm{ci}]^2 \qquad \textbf{Equation 2.15}$$

Another useful measure of refinement quality, R_F2 has, unlike R_wp, R_exp and χ^2, no statistical basis. In single-crystal diffraction, R factors are calculated from the observed and computed structure factors (denoted $F_\mathrm{O,hkl}$ and $F_\mathrm{C,hkl}$), but the former cannot be measured using powder diffraction, due to the superposition of multiple reflections into single peaks.[**121**] However, the Rietveld method includes a procedure to estimate $F_\mathrm{O,hkl}$ values, by apportioning intensity between contributing reflections at each point in the diffratogram according to the ratio of how the $F_\mathrm{C,hkl}$ contribute to the calculated pattern. [**119**]. R_F2, built from $F_\mathrm{O,hkl}$ and $F_\mathrm{C,hkl}$ is hence defined as follows:

$$R_{\mathrm{F}^2} = \frac{\Sigma_\mathrm{hkl}\left(F^2{}_\mathrm{O,hkl} - F^2{}_\mathrm{C,hkl}\right)}{\Sigma_\mathrm{hkl} F^2{}_\mathrm{O,hkl}} \qquad \textbf{Equation 2.16}$$

Parameters which may be refined simulateously for each phase present include the three positional coordinates for each atom, a Debye-Waller temperature factor, and the site occupancy multiplier for each individual atom, and overall, a scale factor, sample profile breadth parameters, lattice parameters, preferred orientation correction terms, and crystallite size and microstrain profile broadening parameters. Further, global parameters in the model which can be refined include 2θ-zero shift, instrumental profile, profile asymmetry, background, wavelength, sample displacement and transparency, and absorption.[**120**]

The observed peak shapes in PXRD are a function of both the sample, where factors include domain size, stress/strain and defects, and of the instrument, where the radiation source, geometry and slit sizes contribute. They change as a function of 2θ and may also possess a *hkl* indices dependence, resulting *e.g.* from anisotropic strain or a pattern of defects, like stacking faults.[**108**] A combination of Gaussian and Lorentzian functions is needed to describe the observed peak shapes; the ideal description is a convolution of the two function types, *i.e.* a Voigt function, but for reasons of computational practicality, a 'pseudo-Voigt' function, *i.e.* a linear combination of Gaussian and Lorentzian profiles, is typically implemented.

2.4.3. The Le Bail method

The Rietveld method, described in the preceding section, is termed a whole powder pattern fitting method, with the structure used to calculate peak intensities. An alternative approach to fitting a model to powder diffraction data, where in contrast the structure is not used (only the indexing and cell parameters are required), is to employ a whole powder pattern decomposition (WPPD) method, such as Le Bail fitting.[**122**] Whilst Le Bail fitting is not the only WPPD approach in use (*i.e.* the Pawley technique), the Le Bail method was employed in this work. One key application of the Le Bail technique, derived from the Rietveld method, is reliable peak intensity extraction for *ab initio* structure solution.

In the Le Bail method, the intensities of individual peaks are not treated as least-squares parameters (unlike in the Rietveld method), and are not refined. In Hugo Rietveld's intensity extraction algorithm, crucial for apportioning intensity between overlapped reflections, peaks are separated according to the calculated values of integrated intensities. The fractions of computed intensity originating from each reflection at a particular point are assumed to be the same as a percentage of the observed intensity, permitting reflection intensity to be estimated.

Initially, in the Le Bail method, calculated structure factors $F_{C,hkl}$ are set to 1, the Rietveld algorithm is employed to generate $F_{O,hkl}$ values, then better $F_{C,hkl}$ values can be set from the extracted $F_{O,hkl}$. The $F_{O,hkl}$ extraction is then repeated, in an iterative procedure. Besides unit cell parameters, the background and profile function terms can also be refined.

2.4.4. Structural refinement software: GSAS and EXPGUI

GSAS (General Structure Analysis System),[**123**] a comprehensive group of over fifty individual programs written in the FORTRAN language, is widely utilised for fitting crystallographic and magnetic structural models to single crystal and powder diffraction data, which may be neutron or x-ray diffraction data. It can be used with both time-of-flight and constant-wavelength neutron powder diffraction data, and laboratory, synchrotron constant-wavelength and energy-dispersive X-ray powder diffraction datasets. Up to nine distinct crystallographic phases can be simultaneously included in the model, thus datasets from multiphase samples can be successfully treated.

Rietveld and Le Bail analysis of powder X-ray diffraction data throughout this work was undertaken using GSAS, in conjunction with the graphical user interface EXPGUI,[**124**] a shell used to directly modify the GSAS experiment file and to invoke the various programs within GSAS, with some additional features. Whilst EXPGUI does not contain all the functionality within GSAS, it provides a user-friendly GUI alternative to the dialogue options of EXPEDT (the experiment editor central to GSAS), avoiding the need to transcend six or more dialogue menus to reach a particular option, and enables easier viewing of various options and refinement parameters in the experiment file simultaneously.

GSAS requires two input files, one being a diffraction data file, termed ‘histogram’, containing intensities and 2θ (or equivalent), and the second, an instrument parameter file, defining the data type, including *e.g.* X-ray wavelength and expected profile shape parameters. However, multiple ‘histograms’ (<100) may be added and modelled simutaneously to determine a single structural model, rendering *e.g.* combined X-ray and neutron refinements possible. Besides structural determination using the Rietveld method, as described in this study, GSAS is also employed for lattice-constant determination, even where structures are not known, and for creating simulations of powder diffraction data.[**124**]

2.4.5. Modelling thermal expansivity and compressibility behaviour

Rietveld analysis of powder X-ray diffraction data collected under non-ambient conditions permits the extraction of changes in unit cell volume, amongst other information about structural changes, as a function of external stimuli, *e.g.* temperature or pressure, for a particular material. This provides a useful means of comparing materials, allowing information about their physical properties to be inferred, and enables changes in electronic and magnetic properties as a function of temperature or pressure obtained through other techniques to be parameterised in terms of unit cell volume. In superconductivity research, extraction of the T_c dependence on unit cell volume has helped identify the pairing mechanism and test theoretical models in molecular superconductors. Evidence for phase transitions in materials occuring as a function of external stimuli may also be detected.

When a force per unit area, or pressure P, acts on a volume, V, the work done, W, is described by the expression $W = -P\,\Delta V$. As both pressure and work are positive, ΔV must be negative in all materials under compression. The magnitude of ΔV is directly related to interatomic forces, which may thus be investigated through analysing structural changes in a material with pressure.[**125**]

The compressibility behaviour of solids can conveniently be described using 'equations of state' (EoS), providing a useful method to compare the properties of different materials. The variation of the volume of a solid with pressure, at constant temperature, can be described by the bulk modulus, K, expressed as follows:

$$K = -\frac{V\delta P}{\delta V}$$ **Equation 2.17**

Measured EoS are usually parameterised in terms of the bulk modulus, and its pressure derivatives, defined at zero pressure.[**126**] There is no absolute thermodynamic basis for stipulating the correct form of the EoS of solids; all commonly used EoS are constructed on various assumptions, the validity of which can only be evaluated by considering whether the EoS reproduces experimental data.[**126**]

The Murnaghan EoS, based on the supposition that K varies linearly with pressure,[**127**] is described as follows (at constant temperature):

$$P = \frac{K_0}{K'_0}\left[\left(\frac{V_0}{V}\right)^{K'_0} - 1\right],$$ **Equation 2.18**

where V_0 refers to the 'zero-pressure' volume, K_0 is the isothermal bulk modulus at zero pressure, and K'_0 is the pressure derivative of K_0, i.e. $K = K_0 + K'_0P$. Whilst the Murnaghan EoS has the advantage of algebraic simplicity, it can be less effective at reproducing experimental data at high compressions.

Other commonly used EoS include the Birch-Murnaghan, natural strain and Vinet EoS models. The Birch-Murnaghan EoS [**128**] is derived from the approximation that the strain energy of a solid undergoing compression can be described by a Taylor series in the Eulerian finite strain, f_E, defined as follows:

$$f_\mathrm{E} = \frac{(V_0/V)^{\frac{2}{3}} - 1}{2}$$ **Equation 2.19**

Truncation at third order in the strain yields the following EoS:

$$P = 3K_0 f_\mathrm{E}(1 + 2f_\mathrm{E})^{\frac{5}{2}}\left[1 + \frac{3}{2}(K'_0 - 4)f_\mathrm{E}\right]$$ **Equation 2.20**

An EoS model can be fitted to experimental data, such as that obtained from a high-pressure PXRD experiment, with volumes obtained from structural analysis; these results can be combined with those from other experimental techniques (*e.g.* the measurement of magnetic properties as a function of pressure), to extract further significant results, *e.g.* the variation of superconducting T_c with unit cell volume.

The addition of heat to an ionic crystal increases the crystal's energy, principally in the form of lattice vibrations, or phonons. In the harmonic approximation, where the potential energy of atoms is modelled using terms quadratic in the interatomic displacements, consequences include zero thermal expansion of a crystal, as its equilibrium size does not depend on the temperature. The principal calculated effect of temperature is just increased vibration amplitude, leading to bond breakage at high temperature. However, in real crystals, anharmonic (higher than quadratic) terms in the interatomic displacements are significant, and thermal expansion is typically observed.[**103**] The thermal expansion behaviour of solid crystals often presents pertinent information for understanding how physical properties evolve; thermal expansion and specific heat are indeed correlated with one another.[**125**] Powder X-ray diffraction has been used in this study to investigate the thermal expansion behaviour of $Rb_xCs_{3-x}C_{60}$ systems; unlike other techniques commonly used to investigate thermal expansion such as capacitance dilatometry, it enables the behaviour of each crystallographic phase to be examined separately in multiphasic samples.

Sayetat and coworkers described a simple method to interpolate the thermal variation of lattice parameters, which combines the early methodology of the Debye model for specific heat and the Grüneisen theory of the thermal expansion of solids.[**129**] This treatment permits the Debye temperature, θ_D, the Grüneisen parameter, γ, and extrapolated lattice parameters at 0 K to be extracted through least-squares fitting to thermal expansivity data. A similar approach was earlier referred to by Fei,[**130**] requiring four parameters to be defined through least squares fitting, but the method from Sayetat *et al.* was used in this work. Any thermal anomalies, such as those which may arise from a phase transition, may be highlighted, and the modelled phonon contributions can be extracted from the thermal expansion curves, revealing any extra contributions to the thermal expansion, e.g. magnetic or electronic.[**129**] In this work, where this model was applied, lattice parameters (and unit cell volumes) were obtained through Rietveld analysis of PXRD data, collected as a function of temperature.

The Debye model is used to estimate the phonon contribution to the specific heat in a solid. Debye recognised that there is a maximum number of vibrational modes in a solid. The Debye temperature defines the temperature of a crystal's highest normal mode of vibration, and is related to the Debye frequency, ω_D, the maximum allowed phonon frequency in the approximation, as follows:

$$\theta_{\mathrm{D}} = \frac{\hbar\omega_{\mathrm{D}}}{k_{\mathrm{B}}},$$ **Equation 2.21**

k_B and $\hbar$ representing the Boltzmann and reduced Planck's constants, respectively.

Debye's elementary model of the lattice specific heat at constant volume, C_V^{lat}, yields the following expression for the variation of C_V^{lat} with temperature, T:

$$C_{\mathrm{V}}^{\mathrm{lat}} = (\delta/\delta T)\left[9k_{\mathrm{B}}NrT(T/\theta_{\mathrm{D}})^3 \int_0^{\theta_{\mathrm{D}/T}} \frac{x^3}{e^{\mathrm{x}}-1}\,dx\right],$$ **Equation 2.22**

where N is the number of primitive cells in the crystal, and r signifies the number of atoms in the polyatomic basis.

The Grüneisen parameter describes the effect that changing a crystal lattice's volume, V has on its vibrational characteristics. In the Debye approximation, the parameter can be defined as follows:

$$\gamma = -\left(\frac{\delta \ln \omega_{\mathrm{D}}}{\delta \ln V}\right)$$ **Equation 2.23**

Through Grüneisen's empirical law, which describes the relationship between the thermal expansion coefficient α, the isothermal compressibility, K, and the specific heat at constant volume, C_{v}, an expression yielding V as a function of $C_{\mathrm{v}}^{\mathrm{lat}}$ can be obtained (assuming the phonons are the only contribution to C_{v}, termed $C_{\mathrm{v}}^{\mathrm{lat}}$)[**129**]:

$$V \simeq V_0\left(1 + \frac{K\gamma}{V_0}\int_0^T C_{\mathrm{V}}^{\mathrm{lat}}\,\mathrm{d}T\right),$$ **Equation 2.24**

where V_0 is the crystal volume at 0 K. Combining Equations 2.22 and 2.24, the volume can now be parameterised in terms of temperature, and finally reduced to a more basic form (K and γ, weakly temperature-dependent, are assumed constant and combined with other constants as 'I_{v}'), providing the simplest theoretical description of the lattice thermal expansion:[**129**]

$$V \simeq V_0 + I_{\mathrm{V}} T \varphi\left(\frac{\theta_{\mathrm{D}}}{T}\right),$$ **Equation 2.25**

where $I_{\mathrm{V}} = 3k_{\mathrm{B}}rK\gamma$, and φ represents a straightforward polynomial, Thacher's function, of (θ_{D}/T), which is a good approximation replacing the 'exact' function (containing an integral, and thus less straightforward to fit), except at very low temperature ($T < \theta_{\mathrm{D}}/10$). The coefficients of the function φ, expanded to the fourth power in T, are tabulated in Sayetat *et al.*[**129**]

2.5. Magnetism

2.5.1. Common types of magnetic behaviour

All materials display some type of magnetic behaviour, the designation 'magnetism' describing their response on a microscopic level upon being placed in an external field. A sample's magnetisation, M, the magnetic moment per unit of volume (or mass, mole *etc.*) of solid, *i.e.* the vector field reflecting the density of permanent or induced magnetic dipole moments in the material, changes with temperature, T, and with the size of the applied magnetic field, H. Measuring $M(T)$ and $M(H)$ allows the type of magnetism in the material, e.g. paramagnetism, ferromagnetism, antiferromagnetism or diamagnetism, and important related parameters, to be established. Another key definition, the magnetic susceptibility χ, is a constant indicating the degree of magnetisation in response to an applied field, H, expressed as follows:

$$\chi = M/H. \qquad \textbf{Equation 2.26}$$

Paramagnetism, a magnetic behaviour typically observed in atoms and molecules with an odd number of electrons, enables the atomic magnetic moments of atoms to be studied practically in isolation, as it is not a cooperative phenomenon unlike *e.g.* ferromagnetism. A typical paramagnetic material shows a linear $M(H)$ behaviour at constant temperature, other than at very high fields, with the line intersecting zero. The magnetisation is reversible, following the same curve upon reducing the field as when increasing it. The magnitude and the temperature dependence of χ can indicate the origin of the paramagnetism. For instance, where atoms with unpaired electrons are present (Curie-type paramagnetism), the following temperature dependence is expected:

$$\chi(T) = \frac{C}{T}, \qquad \textbf{Equation 2.27}$$

where C represents the Curie constant, a material-dependent property which is proportional to the square of the sample's effective magnetic moment. In a Curie-Weiss paramagnet, meanwhile, an additional interaction between the spins on neighbouring atoms is present (exchange interaction); its susceptibility is described by:

$$\chi(T) = \frac{C}{T - \Theta}, \qquad \textbf{Equation 2.28}$$

where Θ, the Weiss temperature, is related to the interaction strength between moments, its sign indicating whether the interaction acts to align adjacent moments in the same (positive Θ) or in opposite direction (negative Θ) (Fig. 2.7). Other types of paramagnetism include Pauli paramagnetism, found in metals and resulting from alignment of the conduction electrons' magnetic moments with an applied field, producing a small, almost temperature-independent χ, and van Vleck paramagnetism, associated with thermal excitations to low-lying states, and also typically small in magnitude and nearly temperature-independent.

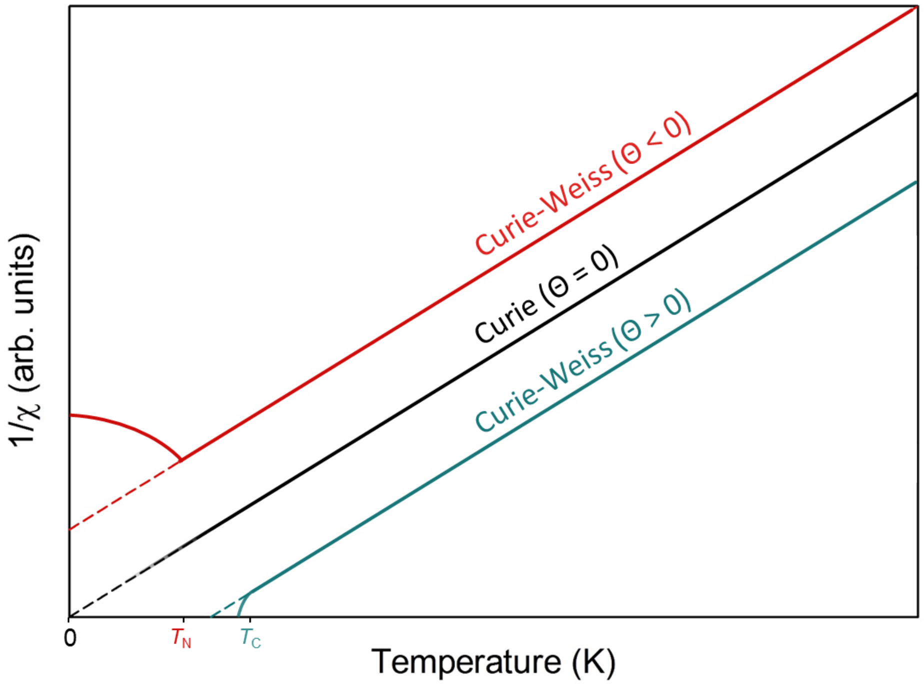

Figure 2.7: Schematic variation of $1/\chi$ with temperature for systems demonstrating Curie and Curie-Weiss paramagnetic behaviour, and ferromagnetic and antiferromagnetic behaviour.

Diamagnetism, another type of magnetic behaviour, manifests as negative χ (a $M(H)$ plot should be linear and reversible but with a negative slope). A diamagnetic contribution arises from paired electrons in most cases, typically of small magnitude. However, superconductivity, an important state of matter, can produce the largest possible value of diamagnetism, and is discussed in the next section.

Ferromagnetism, the strongest type of magnetism found in materials, is characterised by a non-linear $M(H)$ curve which is not reversible (*i.e.* magnetic hysteresis is found). χ is field and history-dependent, hence other parameters such as the saturation magnetisation, as an intrinsic property, tend to be more useful to describe the properties.

Below a Curie temperature (above which, a ferromagnet is paramagnetic), a ferromagnetic material displays long range magnetic order, in contrast to paramagnetic materials in which the moments are randomly oriented.

Antiferromagnets, meanwhile, also display long-range magnetic ordering, but have magnetic moments ordered such that adjacent moments are aligned in opposite direction to one another. As the moments on neighbouring atoms cancel one another, the resulting χ is fairly small. Above a characteristic Néel temperature T_N, an antiferromagnet is typically paramagnetic demonstrating Curie-Weiss behaviour, but below this temperature, antiferromagnetic long-range ordering is found. The order-disorder transition at T_N is characterised by a 'cusp' in $\chi(T)$. Below T_N, $M(H)$ curves are linear. Finally, in a ferrimagnet, adjacent magnetic moments are aligned in opposite directions, as in an antiferromagnet, but the non-equal magnitudes of these moments, where the larger moment tends to align with an applied field, produces a large net moment aligned with the magnetic field.[**131**]

2.5.2. Superconductivity

The superconducting state, first observed in mercury in 1911, is a phase in a material for which, below a critical temperature T_c, the material's dc electrical resistance drops abruptly to zero in the absence of an applied magnetic field. Superconductors have long been of technological interest, particularly since type II superconductors capable of carrying high current densities in the presence of high magnetic fields were discovered, as large amounts of electrical current can be transmitted without dissipating energy as heat. Superconducting magnets provide a relatively inexpensive way to achieve high magnetic fields for experimental work, and applications requiring large magnetic fields such as medical Magnetic Resonance Imaging (MRI) are thus rendered practical to implement.[**132**]

One fundamental property of superconductors, the Meissner effect, expresses that inside a superconductor, magnetic flux density is zero. From the following fundamental relation, a superconductor subjected to a positive magnetic field acquires a negative magnetisation:

$$B = \mu_0(H + M), \qquad \textbf{Equation 2.29}$$

where B is magnetic induction or flux density, μ_0 represents the magnetic permeability of vacuum, H is the applied magnetic field strength, and M denotes magnetisation (in SI notation). This effect arises from a real electric current flowing, without resistance, in a thin shell over the external surface of the superconductor, indistinguishable from a magnetic moment by external meaurements. It is therefore customary to ascribe a magnetisation to a superconductor in a magnetic field.[**132**]

When an ideal superconductor is cooled through its T_c with a small field applied, known as field-cooled (FC) measurement, the magnetic field is completely expelled from the materials' interior at T_c, demonstrating the Meissner effect, and often used to determine T_c. An alternative measurement, termed magnetic shielding or screening, is typically made by first cooling the sample to low temperature below T_c, then applying a field, thus called a zero-field-cooled (ZFC) measurement. The changing magnetic field induces currents which flow as long as the sample remains superconducting.

Most elemental superconductors and some alloy superconductors display so-called 'type I' behaviour. In an ideal specimen with demagnetising factor $N = 0$, the negative magnetisation increases linearly with field up to a critical field, H_c, then with further increase in field, magnetisation falls abruptly to zero, as the superconducting state is destroyed, and normal conductivity ensues. A negative applied field results in a positive magnetisation. The Silsbee rule, stating that the maximum current which can be carried in a superconductor is that which produces the critical field at the surface, relates the critical field to a corresponding critical current in the rod. Up to H_c, surface currents completely screen the inside of the sample from the applied magnetic field. In a sample with a non-zero demagnetising factor, whilst H_c is reached at the same value of magnetisation, increasing the field above a certain threshold (below H_c) yields an intermediate state (a mixture of superconducting and normal regions) where magnetisation decreases with increasing field, becoming zero at H_c.[**132**] H_c is a function of the temperature, and is zero at T_c.

In a 'type II' superconductor, the surface energy of the superconducting/normal interface is negative, in contrast to 'type I' materials. These tend to be alloys or transition metals with high electrical resistivity in the normal state. Whilst both types display a negative magnetisation, produced by a surface current, upon applying field, in a type II superconductor this is only the case up to a lower critical field, H_{c1}. At this field, magnetic flux enters the sample, forming individual flux lines or vortices, and the sample is described as being in the mixed state. The flux lines may move freely, or, more practically for engineering applications, be pinned by interactions with structural defects. Flux creep, due to motion of flux lines, appears as a resistance, and thus the production of heat, in a superconducting coil. The introduction of such defects, normally through appropriate sample preparation and processing, results in the $M(H)$ curve becoming irreversible (hysteretic), although it is reversible for an 'ideal' type II superconductor, as illustrated in Fig. 2.8. Above an upper critical field, H_{c2}, the material enters the normal state.[**131, 132**]

In the superconducting state, characteristically (although not universally) the superconducting electrons are separated from 'normal' electrons by an energy gap, $E_g \approx 4k_BT_c$, which can be detected by various techniques including heat capacity, infrared absorption and tunnelling.[**103**] Superconductors have a characteristic quantity λ_L, termed the London penetration depth, which measures the depth of penetration of the magnetic field. An independent length, the coherence length ξ, provides a measure of the distance within which the superconducting electron concentration cannot significantly vary in a spatially-varying magnetic field. If the ratio λ/ξ, defining the Ginzburg-Landau parameter κ, is less than 1, the superconductor will be type I, whilst it will otherwise be type II; λ refers to the actual penetration depth, not precisely described by λ_L alone.[**103**]

If measuring a sample with a large magnetisation value, applying a 'demagnetisation' correction can be important. This is associated with the dependence of the field inside the sample on sample shape. The demagnetisation effect is normally quantified in terms of an additional magnetic field, a demagnetisation field H_d. The total field inside the sample, H, is thus described by $H = H_0 + H_d$, where H_0 is the applied magnetic field. Whilst H_d is zero for a long, thin sample in a field parallel to its long axis, the demagnetisation correction can be huge for e.g. a short, flat sample in a perpendicular field.[**131**]

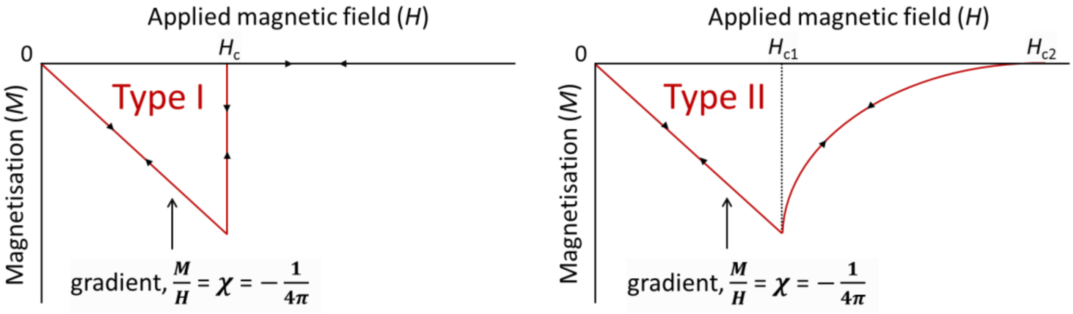

Figure 2.8 The variation of magnetisation with field for a type I superconductor (left), and an ideal type II superconductor (right).

2.5.3. BCS theory of superconductivity and its extensions

The superconducting state is an ordered state of the conduction electrons of the metal, in forming loosely associated electron pairs, occuring only at temperatures below T_c. The basis of a quantum theory of superconductivity, explaining the nature and origin of the electron ordering into so-called 'Cooper pairs', was described by Bardeen, Cooper and Schrieffer in 1957 (later awarded with the Nobel Prize in Physics), and is known as the 'BCS' theory of superconductivity.

A so-called 'BCS wavefunction' composed of particle pairs, when treated by the BCS theory, describes standard electronic superconductivity as observed in *e.g.* elemental metals, known as *s*-wave pairing. Its attributes include describing how an attractive interaction between electrons can yield a ground state separated from excited states by an energy gap, the consequences of which include the critical field, thermal properties and most electromagnetic properties of superconductors. The gap results from an electron-phonon interaction, whereby an electron, interacting with the lattice, deforms it, whilst a second electron, 'seeing' the deformation, adjusts itself to take advantage of the deformation to lower its energy. The Coulomb repulsion between electrons opposes pair formation, but does not suppress superconductivity as it is sufficiently attenuated through screening.

In addition, the penetration depth and the coherence lengths arise naturally from the theory, and T_c can be predicted from the electron density of orbitals of one spin at the Fermi level, $N(\varepsilon_F)$, the attractive electron-lattice interaction, V, and the Debye temperature, θ_D:

$$T_c = 1.14\,\theta_D\, exp^{\left[\frac{-1}{VN(\varepsilon_F)}\right]}, \qquad \textbf{Equation 2.30}$$

applicable when $V\,N(\varepsilon_F) \ll 1$. [**103**]

Various extensions to the BCS theory have been formulated. In one key example, the Migdal-Eliashberg theory, which renders the BCS theory more applicable to strongly-coupled superconductors, the typical phonon frequency is approximated as being significantly smaller than the Fermi energy; interelectron repulsion lowers, rather than enhances, T_c. An empirical parameter, μ^*, can then be used to describe Coulomb electronic interactions. [**133**] T_c is expressed as a function of the electron-phonon and Coulomb interaction coupling constants, through the McMillan equation:

$$T_{\mathrm{c}} = \left(\frac{\theta_{\mathrm{D}}}{1.45}\right) exp\left[\frac{-1.04(1+\lambda)}{\lambda - \mu^{*}(1+0.62\lambda)}\right], \qquad \textbf{Equation 2.31}$$

where λ represents the dimensionless electron-phonon coupling constant, and μ* is the Coulomb pseudopotential. For this approach to be applicable, $\hbar\omega_D$ must be significantly smaller than the Fermi energy ε_F, but in A_3C_{60}, the phonons, Jahn-Teller distortion and the Fermi energies have the same order of magnitude.[**134**]

The DMFT approximation, a new theoretical framework for treating strongly correlated electron systems,[**82**] is now considered to provide the best available description of A_3C_{60} experimental results, as discussed in Section 1.3.7. A quantitative description of DMFT is beyond the scope of this thesis; qualitatively, the full lattice of atoms and electrons is replaced with a single impurity atom supposed to exist in a bath of electrons. The electron dynamics on a central atom can be captured as it fluctuates between different atomic configurations, with a hybridisation function representing the ability of an electron to enter or leave an atom on a particular time scale. The many-body lattice problem is thus reduced to a single-site problem, with effective parameters.[**135**] There is no need to assume a hierarchy between energy scales (weak to strong coupling can be treated), and the dynamical information obtained can be used for comparison with experimental results, from *e.g.* angle-resolved photoemission spectroscopy.

2.5.4. SQUID magnetometry

SQUID (superconducting quantum interference device) magnetometers enable the high sensitivity detection of the magnetic moment of a sample, over a wide temperature range (generally ~2 – 400 K), and in applied magnetic fields to 7 T. Superconductivity plays a critical role, enabling both the production of large, very stable magnetic fields and the ability to measure changes in those fields of 14 orders of magnitude smaller. For the magnetic properties measurements presented in this work, a Magnetic Properties Measurement System (MPMS XL) magnetometer from Quantum Design was employed, with a maximum available applied field of 5 T. All data were collected using direct-current (DC) magnetometry.

The system contains several superconducting components, including a magnet (to generate large magnetic fields), a detection coil which couples inductively to the sample, a SQUID connected to the detection coil, and a superconducting magnetic shield surrounding the SQUID. A schematic representation of the components surrounding the sample is shown in Fig. 2.9. In a measurement, a sample is moved through the superconducting detection coils, inducing an electric current in the detection coils, changing the current in the detection circuit. The detection coils, connecting wires and the SQUID input coil comprise a closed superconducting loop. The SQUID functions as an extremely linear current-to-voltage convertor. Therefore, and crucially, any changes in persistant current in the detection circuit, proportional to changes in magnetic flux, produce corresponding variations in the SQUID output voltage, directly proportional to the magnetic moment of the sample (in a fully calibrated system).[**131**]

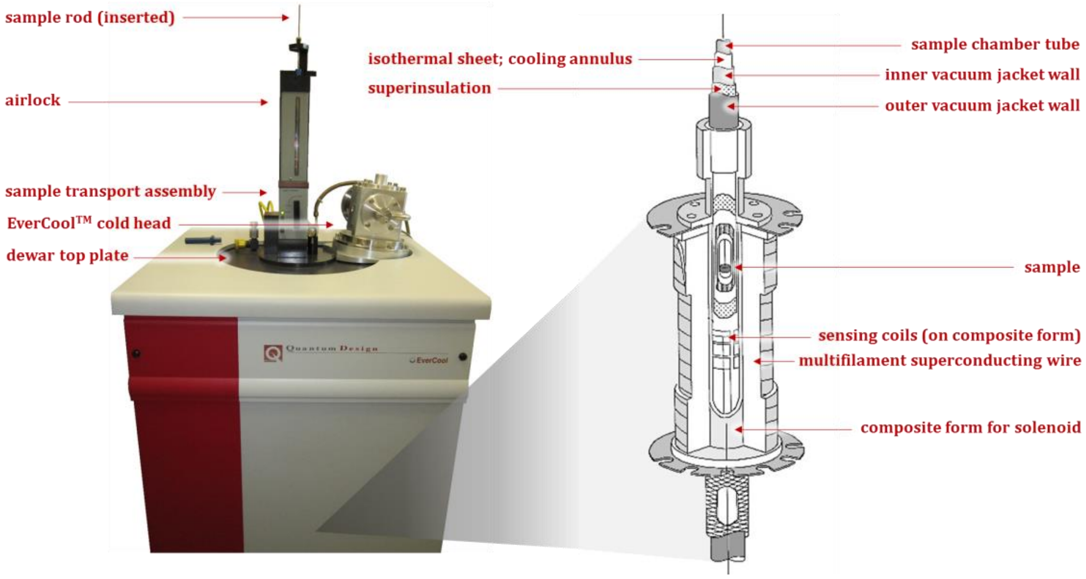

Figure 2.9 (left): Exterior view of an MPMS XL SQUID magnetometer, fitted with EverCool™ dewar to minimise helium loss; (right): schematic representation of the MPMS magnet and surrounding components, adapted from [**136**].

SQUIDs combine the physical phenomena of flux quantisation, requiring that magnetic flux enclosed by a superconducting loop is quantised in units of the flux quantum Φ_0, and Josephson tunnelling, which comprises the coherent tunnelling of Cooper pairs through a thin barrier separating two superconductors. A voltage appears across the junction only when currents exceed a critical value. In a dc SQUID, such as that employed in this work, two parallel Josephson junctions are connected in a superconducting loop, which is operated in the voltage state with a current bias. When the loop flux increases, the voltage oscillates with period Φ_0, and by detecting a slight change in voltage, a change in flux characteristically as small as $10^{-6}\ \Phi_0$ can be ascertained.[**137**]

During a normal measurement, the sample is moved in discrete steps over a specified scan length, and several readings of the SQUID voltage are collected and averaged at each position. If the sample is well-centered in the detection coil, the area under the SQUID voltage versus position curve (Fig. 2.10) is proportional to the magnetic moment, and various fitting options are available in the software MPMS MultiVu™ to determine the moment (reported in emu) from the SQUID output signal. In this work, the iterative regression method was used to analyse the SQUID output signal (the theoretical signal of a dipole moving through a second-order gradiometer is fitted to the actual SQUID output signal).[**131**]

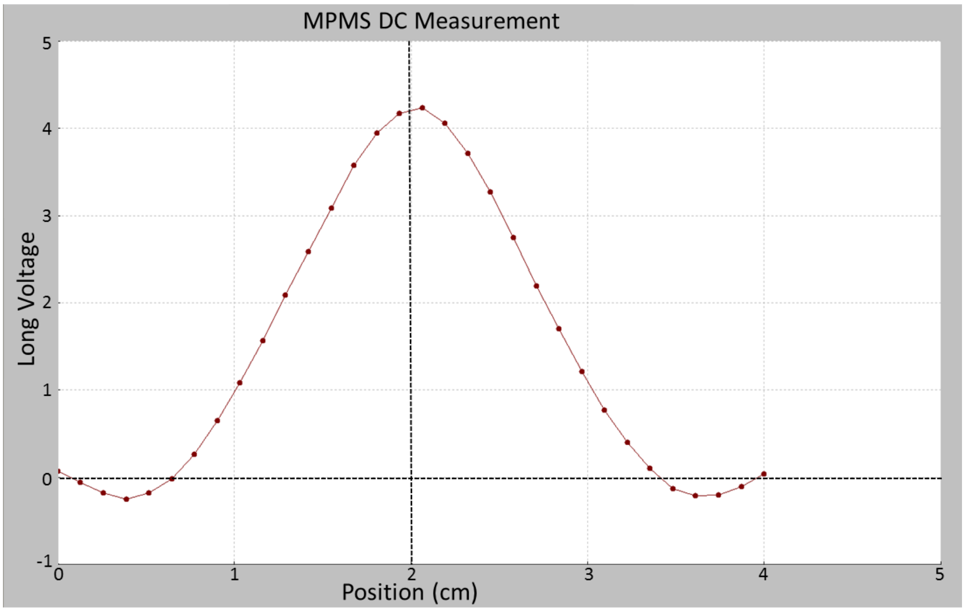

Figure 2.10 Representative output of the MPMS XL SQUID (for a sample with positive magnetic moment, in the ideal case a point-source magnetic dipole) as the sample is moved through the second-order gradiometer superconducting detection coil. The vertical axis corresponds to an output voltage; the horizontal axis indicates the sample position as it is moved stepwise through the scan length.

The characterisation of superconductors with magnetic measurements in the MPMS, as undertaken in this work, has certain advantages over performing direct resistance measurements; magnetic measurements do not require voltage and current leads to be attached to the sample, and whilst resistance measurements require samples with reasonably long lengths and small, uniform cross-sections, magnetic measurements can be executed on small pellets of differing shape.[**132**]

2.5.5. Ambient pressure SQUID magnetometry measurements

Low-field magnetisation measurements are often useful in studying superconductors, as they provide information on T_c approaching the condition $H = 0$, $J = 0$; T_c decreases as H is increased. Such characterisation was undertaken for all fulleride samples in this work, along with high-field magnetisation measurements, in order to investigate the magnetic susceptibility behaviour in the normal, paramagnetic state. All samples measured at ambient pressure in the MPMS in this work were sealed inside Suprasil high-purity quartz ampoules, due to their air-sensitivity, and attached to a sample rod using a plastic straw and Kapton tape, which is non-magnetic and resistant to low temperatures.

In this work, the relative superconducting shielding fraction in different samples has been compared using magnetic shielding (ZFC) low-field measurements. Whilst a 100 % Meissner fraction determined from a FC measurement, corresponding to $\chi = -1/4\pi$, can be a legitimate measure of an entirely superconducting sample, any values less than 100% could simply indicate the presence of flux pinning. Although the shielding measurement could also produce a misguiding result if *e.g.* a specimen had a thin superconducting surface with a non-superconducting centre, samples in this study were well ground prior to measurement to maximise homogeneity.

Estimated shielding fractions quoted in this study are derived from the ZFC magnetic moment, as measured at the temperature for which shielding fraction is defined, as follows:

$$shielding\ fraction\ (\%) = \left(\frac{4\pi Md}{Hm}\right) \times 100, \qquad \textbf{Equation 2.32}$$

where M represents magnetic moment in emu, d is density in g cm^{-3}, H signifies applied field in Oe, and m denotes the sample mass, in grams.

In contrast to any ferromagnetic impurities present, superconducting materials do not have a saturation magnetisation; in a fully superconducting state, the magnetisation is a function of the total field, which strictly comprises the applied field plus the demagnetising field.

2.5.6. High pressure SQUID magnetometry measurements

The magnetic properties of the materials in this work were investigated under applied pressures of up to ~6.9 MPa, using a 'Mcell 10' piston cylinder high-pressure cell (easyLab), designed for use in the MPMS. The labelled cell and its components are shown in Fig. 2.11.

Inside an argon-filled glovebox, each powder sample of ~20-25 mg was loaded into a deformable, single-use PTFE capsule with a PTFE lid. Mineral oil (easyLab), with a weak dependence of pressure on temperature, was used as a pressure-transmitting medium, dispensed into the capsule using a needle and syringe.

A ~5 mm long piece of 0.25 mm diameter high purity Sn wire (easyLab), placed at the within the PTFE capsule prior to sample loading, is used as an *in situ* manometer in each experiment for accurate pressure determination.[**138**] Whilst the pressure applied at room temperature may be accurately known, corrections for relaxation of the clamp when locking in the pressure, effects of differential thermal contraction and changes in elastic contents, *etc.*, are significant, resulting in a different final internal pressure at low temperatures. Internal hydrostatic pressures of up to ~10 kbar could be achieved. The tin superconducting transition shift was utilised to determine the internal pressure. If $M(T)$ of Sn is measured under consistent conditions (*e.g.* using the same applied field), the Sn superconducting T_c decreases upon increasing pressure, according to the following function, allowing *in-situ* pressure to be determined if T_c at ambient pressure is known:[**139**]

$$P = (5.041489 \times [T_c(0) - T_c(P)]^2) + (17.81287 \times [T_c(0) - T_c(P)]), \qquad \textbf{Equation 2.33}$$

where P represents pressure in kbar, and T_c is in units of K. The estimated error in pressure determination is ~0.2-0.3 kbar. Other elemental superconductors with T_c adequately sensitive to pressure which may be used as manometers include lead and indium.[**139**] The *in-situ* pressure tends to remain constant below ~200 K, the solidification temperature of the pressure medium.

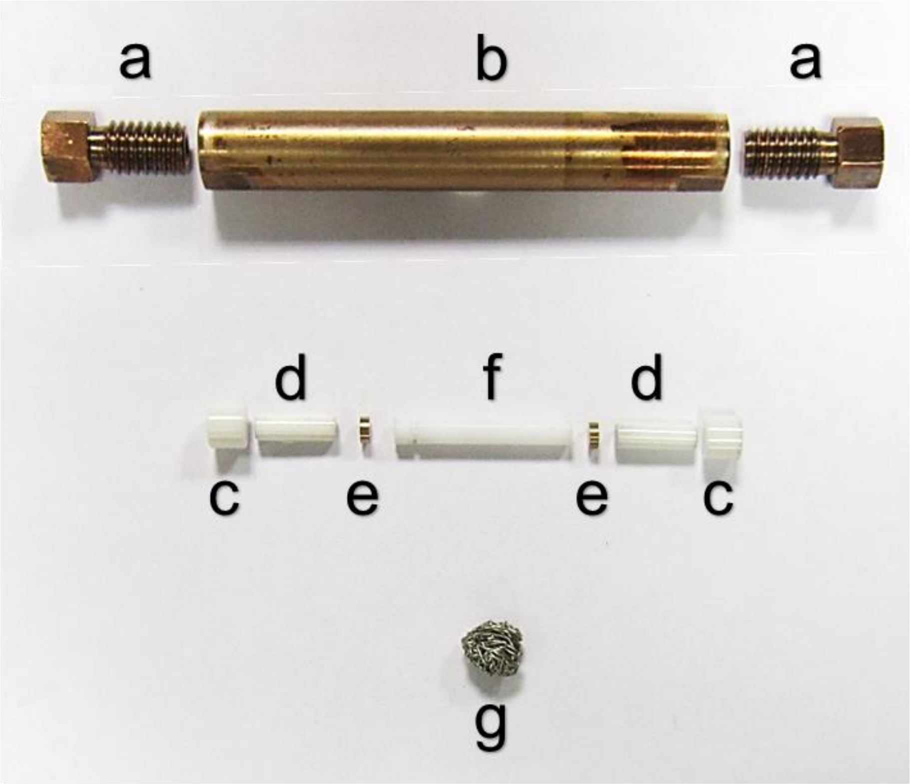

Figure 2.11 The Mcell 10 and its components; (a) upper and lower locking nuts, (b) Mcell body, (c) ceramic piston caps, (d) ceramic pistons, (e) copper anti-extrusion disks, (f) PTFE cell and cap for sample containment, (g) Sn wire supplied by EasyLab, of which a ~5 mm long piece is placed inside the PTFE cell, for use as a manometer.

The closed PTFE capsule is inserted into the Mcell, which can then be fully assembled. A polyether ether ketone interfacing holder is used to attach the Mcell to a MPMS sample rod, prior to its insertion into the MPMS. Whilst the initial internal cell pressure, after tightening the upper locking nut by hand to complete its assembly, is typically 0.3-0.5 kbar, further pressure is applied by means of a hydraulic press ram, the Mpress. During pressurisation, a tungsten carbide piston transmits the applied pressure to the cell contents, and a spanner then used to tighten the upper locking nut of the cell, to retain the applied pressure. The cell pressure may also be decreased in a very similar manner. Measurement of the distance between the upper locking nut head and the main cell body using a Vernier calliper after each pressurisation enables certain potential problems to be identified (*e.g.* insufficient pressure medium) and overpressurisation, which could destroy the cell, to be avoided.

In order to remove the large magnetic contribution associated with the Mcell and its components, background measurements are collected with the Mcell assembled as standard but with the PTFE capsule containing mineral oil only, using an identical measurement protocol to that later used for the sample (*e.g.* applied field, cooling history and temperature steps). These raw data are then subtracted from a combined (sample + Mcell) measurement, prior to fitting the raw data in the MultiVu software, using the Automated Background Subtraction (ABS) feature. Background measurements were collected using PTFE capsules of two different lengths, to best emulate the backgroumd contribution of the cell at low and high pressures.

Centering the loaded sample under weak fields can be challenging. In order to ensure a consistent positioning of the sample in the coils at the mean place, centering of the transport mechanism is first carried out with the MPMS at ambient temperature, using a ferromagnetic Ni sphere (easyLab), prior to insertion of the Mcell into the MPMS with the rod length accurately adjusted accordingly.

2.6. Raman spectroscopy

2.6.1. Introduction to Raman spectroscopy

Raman spectroscopy is a non-destructive technique used to study vibrational, rotational and other low-frequency modes in a system, based on inelastic scattering of light. In the spontaneous Raman effect, upon irradiation of a sample with monochromatic laser light, incident photons scatter with either increased or decreased frequency, termed anti-Stokes and Stokes Raman scattering processes, respectively. The photons induce transitions in the sample, resulting in energy gain or loss of the scattered radiation.

Considering a Raman spectrum of a solid, each peak corresponds to a particular vibrational mode, which, to be Raman-active, must have a non-zero first derivative of the polarisability with respect to the vibrational normal coordinate. In a Raman experiment, the intensity of the scattered light is measured as a function of the frequency shift of the photons, termed the Raman shift (cm^{-1}).

2.6.2. Experimental setup for Raman spectroscopy

A Horiba Jobin-Yvon LabRam HR confocal scanning microscope, in backscattering geometry, was employed for collection of the Raman spectroscopy data presented in this thesis. A 532 nm Nd-YAG laser was used, with a 10 % filter to avoid photo-damage of the investigated samples, resulting in an estimated 2 mW power at the sample. The spectrometer was calibrated to the 520 cm^{-1} signal of Si prior to data collection. A microscope objective of ×50 magnification was used. A 1800 lines/mm grating was used for highest resolution, and a CCD detector recorded the intensity of scattered light. The spectrometer control program LabSpec was used to control instrument functions and data acquisition.

In this study, ~2-4 mg fulleride samples were measured (although only minute fractions of each sample were irradiated for measurement), contained in 0.5 mm diameter special glass capillaries and sealed under Ar atmosphere. Data were collected over a wavenumber range of 1400-1520 cm^{-1}. The capillaries were mounted on a glass slide, and samples measured at ambient temperature, with ten or twenty 10 second acquisitions accumulated for each measurement (no signal deterioration was observed during this time). Data were collected at 3-5 different positions for each sample, to confirm good measurement reproducibility and sample homogeneity, with the most intense spectrum for each sample used for further analysis.

Chapter 3 - Structural and magnetic studies of $Rb_xCs_{3-x}C_{60}$ *fcc*-rich solid solutions ($0.25 \leq x \leq 2$)

3.1. Introduction

3.1.1. The *fcc* $A_xCs_{3-x}C_{60}$ systems

Following the earlier discovery of superconductivity in A_3C_{60} (A = K, Rb), superconducting *fcc* $RbCs_2C_{60}$, with a superconducting T_c of 33 K (the highest ambient pressure T_c of any A_3C_{60} material), was reported in 1991.[**45**] This material is consistent with the well-established trend in the less expanded A_3C_{60} series, where T_c increases monotonically with unit cell volume.[**46**] However, intrinstic synthetic difficulties in increasing the Cs fraction in the structure beyond this point rendered the behaviour of potentially more expanded A_3C_{60} materials unknown for considerable time.

A significant breakthrough was achieved by Dahlke and coworkers, who utilised solution synthesis to obtain $Rb_xCs_{3-x}C_{60}$ and $K_xCs_{3-x}C_{60}$ materials with the most expanded *fcc* lattice volumes reported at the time in the cubic A_3C_{60} series.[**31**] Their results showed that increasing the *fcc* lattice parameter beyond 14.555 Å (corresponding to $RbCs_2C_{60}$) fundamentally altered the dependence of the electronic properties on inter-fulleride separation; at larger expansion, in contrast to the less expanded A_3C_{60} materials reported up to then, increasing inter-fulleride separation resulted in a decreasing superconducting T_c (whilst the density-of-states at the Fermi level continued to increase with unit cell volume). This breakdown of a monotonic increase in T_c with unit cell volume, well-established in the underexpanded A_3C_{60} systems, was attributed to increasing significance of interelectron repulsion as the Mott-Hubbard transition is approached upon expansion.[**31**] However, the most expanded sample which could be made had a refined *fcc* phase composition of $Rb_{0.35(2)}Cs_{2.65(2)}C_{60}$, and *fcc* Rb content from structural analysis was generally significantly higher than that nominally introduced.

In 2010, subsequently to the bulk synthesis and characterisation of the A15 superconducting polymorph of Cs_3C_{60},[**49**] the first successful bulk synthesis of *fcc* Cs_3C_{60} was reported.[**140**] In contrast to all other reported *fcc* A_3C_{60} materials (A = K, Rb, or a combination including Cs), *fcc* Cs_3C_{60} is a magnetic insulator at ambient pressure, becoming superconducting under applied pressure. The superconducting T_c initially increases with pressure, reaching a maximum of 35 K (the highest found in the *fcc* A_3C_{60} series); this contrasts sharply with the BCS theory description conventionally applied to explain the unit cell volume-T_c dependence in the underexpanded A_3C_{60} materials.

Martin McDonald and colleagues also extended the previous work on $Rb_xCs_{3-x}C_{60}$, developing the liquid ammonia synthetic route further to synthesise and characterise high-quality superconducting samples covering the compositional range ($0 \leq x \leq 0.5$).[**71**] The dependence of superconducting T_c upon pressure in each of these systems was found to form distinctive 'dome' shapes, showing that physical pressure has an analogous effect to chemical pressure in this overexpanded regime, with T_c initially increasing with pressure up to a maximum. The superconducting fraction for all samples was reported to increase monotonically with pressure, eventually saturating.

NMR investigations of both Cs_3C_{60} superconducting polymorphs showed that at pressures far greater than the insulator-to-superconductor transition pressure, the $1/T_1T$ behaviour as a function of temperature in the normal state (where T_1 is the spin-lattice relaxation rate) displays metallic-like Korringa constant values, close to those reported for other A_3C_{60} compositions. Closer to the Mott transition boundary, at lower pressures, $1/T_1T$ became significantly higher than expected from Korringa values predicted if the BCS theory were fully applicable, underlining the importance of correlations near to the Mott transition.[**141**] Likewise, under moderate hydrostatic pressure (~ 7 kbar) the *s*-wave superconducting gap in *fcc* Cs_3C_{60} approaches the value expected for a weakly-coupled BCS superconductor, $2\Delta_0/k_BT_c \sim 3.5$, but this value increases to ~5.3 at lower pressure close to the metal-insulator transition, evidencing the increased significance of electronic correlations for the pairing interaction.[**142**]

3.1.2. Purpose of present study

The insulator-to-metal transition in Cs_3C_{60} is traversed through applying hydrostatic pressure, which reduces interfullerene separation.[**140**] The underexpanded metallic fullerides such as Rb_3C_{60}, far from the Mott insulator boundary have been well studied, but limited experimental studies have been carried out for the overexpanded regime in proximity to the Mott boundary, where marked deviation from BCS-type behaviour is observed. The compositional series $Rb_xCs_{3-x}C_{60}$ ($x \leq 1$) is significant as at a certain point it must traverse the insulator-metal boundary, and should permit this key region to be studied at ambient pressure.

Whilst previous studies were key in demonstrating that overexpanded $Rb_xCs_{3-x}C_{60}$ ($x < 1$) could be synthetically accessed,[**31, 71**] and showed the contrasting trend in $T_c(V)$ found at higher expansivities from application of both hydrostatic and 'chemical' pressure, further investigation of these systems is warranted. Previous work has not addressed the nature of the normal state magnetic and electronic properties of these materials, and the structural response of the overexpanded *fcc* lattices to variable temperatures and pressures has not been probed, save for the insulating Cs_3C_{60}.[**140**] Furthermore, compositional ranges probed in the earlier studies were relatively limited, and the liquid ammonia synthetic routes gave rise to broad superconducting transition widths. Issues with stoichiometry control were also reported, and shielding fractions in the McDonald study were low (samples of nominal Rb_x = 0.5, 0.25 had refined x values of 0.62 and 0.37, and estimated shielding fractions of 20 % and 3 %, respectively). The liquid ammonia route also involves certain inherent issues, *e.g.* a significant hazard is posed due to the high ammonia vapour pressure at ambient temperature, and extended evacuation of products is required to effectively remove solvent.

This study aimed to synthesise a wide compositional range of $Rb_xCs_{3-x}C_{60}$ materials, ranging from conventional underexpanded materials such as Rb_2CsC_{60} through to overexpanded, unconventional systems close to the Mott insulator boundary; this series must have high *fcc* phase fractions, good stoichiometry control and be highly crystalline, becoming bulk superconductors with high shielding fractions at low temperature. Reproducibility is of high importance, with large homogeneous batches of materials (> 1 g) eventually needed to enable further novel characterisation of these systems to gain further physical insight from techniques such as μSR and powder neutron diffraction. With solid-state synthesis the choice of synthetic route, long known to be a successful route to high-quality conventional less expanded A_3C_{60} materials, this study aimed to push the boundaries of the solid-state route towards materials with highest possible expansion. Developing improved solid-state routes to access highly expanded *fcc* A_3C_{60} could circumvent disadvantages inherent within the reported solution routes.[**31, 71, 140**]

High-resolution synchrotron X-ray diffraction will be used to finely probe the structural evolution of these materials upon reduction of interfullerene spacing, both by varying temperature and applying hydrostatic pressure. Complementary studies of the structural and magnetic properties using various techniques will allow these results to be combined, mapping out a full electronic phase diagram of critical temperature as a function of interfullerene spacing (or unit cell volume), through both ambient pressure and high pressure techniques. The effects of applying hydrostatic and ‘chemical’ pressure (through fine adjustment of the Rb^+/Cs^+ ratio in the *fcc* lattice), on magnetic and structural properties will be compared.

Additional characterisation is also planned, *e.g.* Raman spectroscopy will provide an additional check of sample quality. A key target, external collaboration with other groups with expertise in other complementary characterisation methods such as NMR, IR, and specific heat, will allow further elucidation of the physics of these unconventional strongly correlated superconductors.

3.2. Experimental methods

All samples in this study were synthesised by the candidate, with the exception of two underexpanded *fcc*-rich samples ($Rb_{1.5}Cs_{1.5}C_{60}$ sample I, Rb_2CsC_{60} sample I), prepared by project student M. J. Williamson in the Prof. Prassides laboratory using the 'standard' protocol described below.

For nominal stoichiometries $Rb_xCs_{3-x}C_{60}$ (x = 0.25, 0.35, 0.5, 0.75 and 1), one *fcc*-rich sample of each composition was used for all characterisation described in this Chapter. However, for x = 1.5 and x = 2, two and three samples, respectively, were used, as new samples became available with higher *fcc* phase fractions during the study; individual samples are differentiated using the following form: 'x = 1.5 (sample II)'.

3.2.1. Preparation of $Rb_xCs_{3-x}C_{60}$ ($0.25 \leq x \leq 2$) by solid state synthesis

All samples synthesised are very air sensitive, so care was taken to ensure the sample environment was extremely clean, dry and air free. All sample manipulations were carried out inside an MBraun MB 200B Ar-filled glove box with low O_2/H_2O levels (H_2O < 0.3 p.p.m., O_2 < 0.1 p.p.m.), with equipment thoroughly dried in an oven at ~85°C before transfer to the glove box. Prior to synthesis, C_{60} (99.9%, MER Corp.) was sublimed for higher purity, as follows: 500-600 mg of pristine C_{60} was ground with a mortar and pestle, degassed for 3-4 hours in a 12 mm-diameter quartz ampoule with striction to 10^{-4}-10^{-5} mbar, then sublimed using a tube furnace (ramp from ambient temperature to 550°C, dwell for 16 hrs, under dynamic vacuum); thereafter, the furnace was removed directly, the tube was sealed with a Young's tap and adaptor with Swagelok connector and transferred to the glove box, where sublimed material above the striction was removed with a long spatula and ground again.

Reaction mixtures of Rb, Cs (>99.6% Aldrich/Acros, used as supplied) and ground, sublimed C_{60} were placed in a 5 mm diameter open tantalum cell in stoichiometric quantities, inside a larger tantalum cell with closable screw ends. Typically, 200-300 mg total of reactants were used for each synthesis. The tantalum cell and contents were placed in a 15 mm diameter Pyrex glass ampoule, closed with a high-vacuum Swagelok fitting with J. Young tap, and removed from the glove box. The ampoules were evacuated to $\sim 1\times10^{-4}$ mbar using a glass high-vacuum manifold setup with a Leybold vacuum

PT70B turbopump for 15 minutes, filled with a small He gas pressure (typically 400 mbar) and sealed.

The samples were annealed inside a chamber furnace as follows: ramp at 5°C/min from RT to 150°C, dwell 1 hr, ramp at 10°C/min to 200°C, dwell 12 hrs, ramp at 10°C/min to 300 °C, dwell 12 hrs, ramp at 5°C/min to RT. Inside the glove box, the sample then was ground with a mortar and pestle, pelletised, and loaded back into the larger tantalum cell.

For the 'standard' synthetic procedure, used to synthesise all *fcc*-rich $Rb_xCs_{3-x}C_{60}$ ($0.35 \leq x \leq 2$) samples described herein, after evacuation and sealing under He as before each sample was placed directly in a chamber furnace at 430°C. It was held for 2-5 weeks, with 1-3 intermediate grindings and pelletisations as before to improve crystallinity. At each intermediate grinding stage, the sample was removed directly from the 430°C furnace and allowed to cool in air. Upon opening in the glove box and grinding with an agate pestle and mortar, a 0.5 mm-diameter special glass capillary was filled in the glove box and the sample quality monitored using powder X-ray diffraction (PXRD), with Siemens D5000 and Bruker d8 Advance X-ray powder diffractometers. At the final stage after annealing was complete, each sample was structurally characterised using high-resolution synchrotron PXRD (Section 3.3), along with magnetic (Section 3.4) and other characterisation techniques (Sections 3.5, 3.7).

Extensive characterisation of an *fcc*-rich sample with nominal composition $Rb_{0.25}Cs_{2.75}C_{60}$ is also reported in subsequent sections. This sample was also prepared by a solid-state route, with the pelletised sample annealed at the same temperatures (identical initial stepped protocol to 300 °C, with two subsequent annealings at 430°C). However, different cooling protocols were used, with the sample drop quenched from 430°C into cryogen baths, rather than allowing to cool in air. Overall, various changes to the 'standard' cooling protocol were tested, focusing on compositions of $x < 0.35$, aiming for improved synthesis of *fcc*-rich materials with highly-expanded *fcc* lattices. These tests, along with the detailed synthetic protocol for this sample, are detailed later in Section 3.6.

3.3. Synchrotron X-ray diffraction studies of $Rb_xCs_{3-x}C_{60}$ ($0.25 \leq x \leq 2$)

In the following sections, structural characterisation with synchrotron PXRD, employing Rietveld and Le Bail analysis, is described for the *fcc*-rich $Rb_xCs_{3-x}C_{60}$ series, under both ambient conditions and under variable temperature and elevated pressures. Firstly, a summary of all experimental procedures is provided (section 3.3.1).

Whilst the candidate was actively involved in all data collection, devising the best refinement technique and treatment of the results, solely for reasons of time and practicality (given the very large number of datasets collected), Dr. Yasuhiro Takabayashi carried out certain Rietveld analysis presented here: variable temperature refinements for samples with $Rb_x = 0.35$ and $x = 0.75$ and low-temperature high-pressure refinements for $Rb_x = 0.35$, 0.5 and 1. Dr. Ross Colman was also involved, undertaking low-temperature high-pressure refinements for $x = 1.5$ and the final, Si-calibrated refinements extended to high temperature for $x = 1.5$ and 2. However, it is necessary to include all the data together here to provide the best overall description of the system.

Besides the remaining variable temperature and low-temperature high pressure refinements, significant work from the candidate includes the ambient-temperature high-pressure analysis for $Rb_{0.5}Cs_{2.5}C_{60}$ (section 3.3.6). Furthermore, the remaining subsections in this chapter (magnetic characterisation, Raman spectroscopy and variable cooling rate experiments with structural characterisation) represent work carried out and directed by the candidate.

3.3.1. Experimental procedures

High-resolution synchrotron PXRD data were collected as a function of temperature between 300 and 5 K (or 10 K) on beamline ID31 at the European Synchrotron Radiation Facility (ESRF), Grenoble, for samples of nominal composition $Rb_xCs_{3-x}C_{60}$ ($0.25 \leq x \leq 2$). The overall setup was outlined in Section 2.3.2. Samples were sealed under ~300 mbar He in 0.5-mm diameter special glass capillaries. Two scans over an angular range of $2\theta = 2\text{-}30°$ were collected at each temperature, with typically 2-4 extra scans of the higher angle region ($2\theta = 15\text{-}30°$) collected at the lowest and highest temperatures, for more accurate definition of structural parameters. X-ray wavelengths of $\lambda \sim 0.4$ Å were used (Table 3.2), and data were binned with a step size of 0.003° in 2θ. For $Rb_{1.5}Cs_{1.5}C_{60}$ (sample II) and Rb_2CsC_{60} (sample III), additional data were collected upon heating to 570 K using a hot-air blower. For calibration purposes, enabling these data to be reliably combined with data collected at lower temperature with the He cryostat, finely ground Si (~15 wt.%) was mixed with specimens of these ground samples before filling and sealing the capillaries. The variation of Si lattice parameter with temperature obtained from structural analysis enabled the precise temperature at the sample to be extracted (using the method detailed in ref. [**143**]).

Ambient-temperature synchrotron PXRD data were collected for *fcc*-rich $Rb_{0.5}Cs_{2.5}C_{60}$ as a function of pressure, between 0.1 – 14.7 GPa, at beamline ID27, ESRF (X-ray wavelength = 0.3738 Å); the specimen was that whose characteristion is described throughout this chapter. The general experimental setup and details of the 2D image integration to yield 2θ *vs.* intensity data were described in Section 2.3. The MDAC had a diamond culet diameter of 600 μm, and was equipped with a stainless steel gasket with a hole 70 μm deep, 330 μm in diameter. The monochromatic X-ray beam was focused to 3×3 μm^2. Pressure was carefully increased in small steps ($\delta P \sim 0.05$ GPa) in the low pressure range to finely monitor the structural compression and correlate it with the corresponding temperature response at ambient pressure. Data were binned with a step size of 0.0081° in 2θ.

High pressure synchrotron PXRD measurements were also undertaken at low temperature in the superconducting regime for several compositions, at beamlines ID27 and BL10XU. As above, experimental and 2D image integration details were provided in section 2.3. Data were binned with step size 0.01° in 2θ. At BL10XU, diffraction patterns were collected at 7 K for samples $Rb_{0.35}Cs_{2.65}C_{60}$ (λ = 0.41305 Å, $P \leq 11$ GPa), $Rb_{1.5}Cs_{1.5}C_{60}$ (sample I, λ = 0.41238 Å, $P \leq 10$ GPa), and Rb_2CsC_{60} (sample II, λ = 0.41238 Å, $P \leq 12$ GPa). MDAC diamond culet diameters were 500 μm, with samples introduced in 90- or 100-μm-deep, 200-μm-diameter gasket holes. At ID27, diffraction data were collected at 20 K for $Rb_{0.5}Cs_{2.5}C_{60}$ ($P \leq 10$ GPa, diamond culet diameter 350 μm, gasket hole 40-μm deep, 190 μm in diameter) and $RbCs_2C_{60}$ ($P \leq 13$ GPa, diamond culet diameter 600 μm, gasket hole 60-μm deep, 330 μm in diameter).

3.3.2. Structural results at ambient temperature

Rietveld analysis was undertaken for synchrotron PXRD data collected under ambient conditions, for each sample in the study; a description of the model and refinement method now follows. A maximum of three crystallographic phases were included in the model where their contributions were visually evident: a majority *fcc* phase, with minority Cs_4C_{60} and CsC_{60} phases, although several samples (x = 1, 2) had >98 % *fcc* content. A pseudo-Voigt profile function was used (continuous wavelength profile function '3' within GSAS); profile shape coefficients GU, GV, GW, LX, LY and L_{ij} (i, j = 1-3) were allowed to refine for the majority *fcc* phase. Low-angle peak asymmetry from axial divergence was modelled with coefficients S/L = 0.001, H/L = 0.0005.[**144**] A Chebyschev polynomial function (~18 terms) was used to fit the background. The anomalous contributions to the X-ray form factors of all atoms, f' and f'' corrections to f, were calculated using the program DISPANO [**145**] for input into GSAS. A cylindrical absorption correction was applied (values of μr, i.e. linear absorption coefficient×sample radius, were 0.10-0.13).

For each phase, the C_{60} radii and C-C bond distances were kept fixed, with fractional coordinates rescaled to the refined lattice metrics. For the *fcc* phase, C-C bond distances were fixed to 1.42 Å, using C_{60} coordinates originally determined for Rb_3C_{60}.[**146**] This approach was adopted as the resulting fits were of excellent quality. For Cs_4C_{60}, a body-centred-orthorhombic model [**140**] (space group *Immm* [**147**]) was employed, whilst for CsC_{60} a structural model with space group *Pmnn* was used, extremely similar to that confirmed for KC_{60}. Whilst CsC_{60} was earlier also thought to take an orthorhombic structure at ambient temperature,[**148**] its true structure is monoclinic ($I2/m$), albeit with α = 89.8° (40 K, [**149**]). However, in these diffraction data, CsC_{60} contributions are relatively broad and highly overlapped with the *fcc* phase, and only comprise typically ~7 wt.%; it is therefore desirable to limit the number of variables for this phase, and the orthorhombic *Pmnn* model was found to prove a satisfactory approximate model.

Isotropic thermal displacement parameters were allowed to refine for all atoms in the majority *fcc* phase, but U_{iso} for the three inequivalent C atoms was constrained to take the same value, as was U_{iso} for the Rb^+ and Cs^+ distributed at the tetrahedral interstitial site. Modelling of thermal displacment as isotropic was deemed reasonable due to the high symmetry of the cubic structure and the weak scattering of X-rays by carbon; furthermore, a detailed PXRD study of *fcc* Rb_3C_{60} found that, if Rb was displaced stepwise away from the centre of the octahedral interstice (e.g. ½+δ, 0, 0), U_{iso} smoothly decreased with the direction of displacement having no effect on this behaviour (or on R_{wp}).[**150**]

In the present investigation, the Rb-Cs *fcc* phase stoichiometry was allowed to refine in the model to the best statistics dataset, typically at 5 K or 10 K, then kept fixed at these values in the models to the higher temperature datasets; structural studies to low temperature are discussed later in Section 3.3.3, with refined *fcc* phase stoichiometries presented there in Table 3.3. Adopting the successful approach of a recent investigation which comprehensively tested different PXRD models of cation distribution in *fcc*-rich $Rb_xCs_{3-x}C_{60}$,[**71**] and concluded that Rb likely resides exclusively in the *fcc* phase, the octahedral interstice was modelled as occupied entirely by Cs^+. Tests for one $Rb_{0.5}Cs_{2.5}C_{60}$ dataset indicated that if the Rb^+/Cs^+ distribution is allowed to vary in both tetrahedral and octahedral sites, the octahedral Rb^+ occupancy becomes negative. An assumption of negligible cation vacancy concentration in the *fcc* phase and modelling the occupancy of the tetrahedral cavity by a disordered Rb^+/Cs^+ mixture, with total occupancy fixed to 1.0 and relative ratio allowed to refine, led to excellent fits to the PXRD data for the $Rb_xCs_{3-x}C_{60}$ series. However, for Rb_2CsC_{60}, full occupancy of the tetrahedral and octahedral interstices by Rb and Cs, respectively, was assumed in accordance with recent complementary ^{133}Cs and ^{87}Rb NMR experiments.[**151**]

For two representative Rietveld fits, to the ambient temperature PXRD data for samples with nominal x = 0.5 and 1, the *fcc* phase structural model and the observed, calculated and distance profiles are presented in Table 3.1 and Fig. 3.1, respectively. Analogous data for the remaining compositions in the study (x = 0.25, 0.35, 0.75, 1.5 and 2) are presented in the Appendix.

Table 3.1: Refined *fcc* phase structural parameters for $Rb_xCs_{3-x}C_{60}$ samples with nominal $x = 0.5$ and 1, from Rietveld analysis of synchrotron PXRD data collected at 300 K. The fractional cation occupancies, N of the tetrahedral interstitial site were fixed to values refined from low temperature higher statistics data, described later (section 3.3.3); values in parentheses are statistical errors from the least-squares fitting.

$Rb_x = 0.5$	x/a	y/b	z/c	N	B_{iso} (Å^2)
Rb	0.25	0.25	0.25	0.213	1.66(2)
Cs(1)	0.25	0.25	0.25	0.787	1.66(2)
Cs(2)	0.5	0.5	0.5	1.0	8.85(6)
C(1)	0	0.04845	0.23495	0.5	0.81(6)
C(2)	0.20507	0.07831	0.09669	0.5	0.81(6)
C(3)	0.17500	0.15647	0.04845	0.5	0.81(6)

$Rb_x = 1$	x/a	y/b	z/c	N	B_{iso} (Å^2)
Rb	0.25	0.25	0.25	0.486	1.70(1)
Cs(1)	0.25	0.25	0.25	0.514	1.70(1)
Cs(2)	0.5	0.5	0.5	1.0	7.67(4)
C(1)	0	0.04871	0.23620	0.5	0.81(4)
C(2)	0.20616	0.07873	0.09720	0.5	0.81(4)
C(3)	0.17593	0.15730	0.04871	0.5	0.81(4)

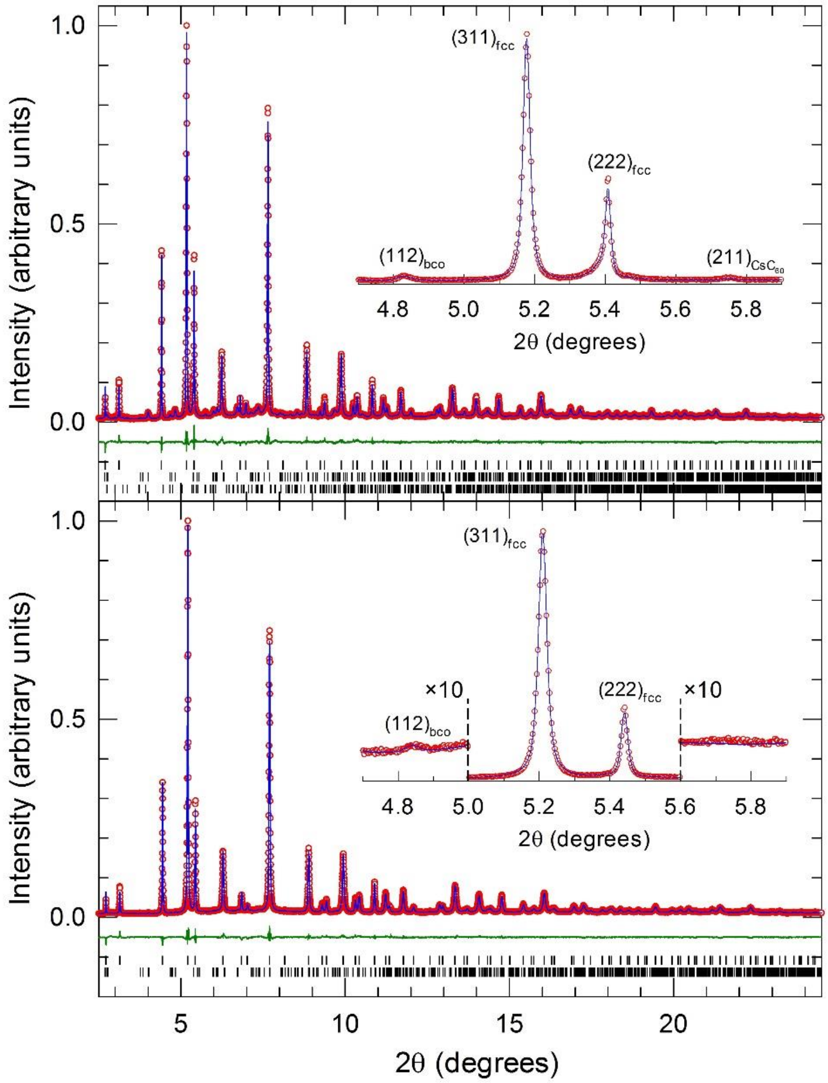

Figure 3.1: Rietveld fits to synchrotron PXRD data collected at ambient temperature, for *fcc*-rich $Rb_{0.5}Cs_{2.5}C_{60}$ (upper panel, λ = 0.39989 Å) and $RbCs_2C_{60}$ (lower panel, λ = 0.40006 Å). Red circles, blue lines and green lines represent the observed, calculated and difference profiles. Bars mark the reflection positions, from top-to-bottom, of co-existing *fcc*, body-centered-orthorhombic (*bco*) and CsC_{60} (observable in x = 0.5 only) phases. Both insets display expanded regions of the respective diffraction profiles; observed Bragg peaks are labelled by their (*hkl*) Miller indices.

The resulting *fcc* lattice parameters at ambient temperature and X-ray wavelengths employed for data collection on each sample are collected in Table 3.2. Significantly, the *fcc* lattice parameter, *a* varies linearly with refined Rb_x (Fig. 3.2), implying excellent stoichiometry control in the series of samples in this study; the deviation of refined *fcc* phase Rb_x from overall nominal Rb_x is minimal throughout.

Table 3.2: The *fcc* lattice parameter at ambient temperature for *fcc*-rich $Rb_xCs_{3-x}C_{60}$ ($0.25 \leq x \leq 2$). Statistical errors from Rietveld analysis are shown in parentheses. The X-ray wavelength, λ, used in PXRD data collection for each sample is also shown.

Nominal x_{Rb}	X-ray λ (Å)	a_{fcc} (RT) (Å)	Nominal x_{Rb}	X-ray λ (Å)	a_{fcc} (RT) (Å)
0.25	0.39984	14.71345(5)	1.5 (sample I)	0.40006	14.50815(4)
0.35	0.40006	14.70780(9)	1.5 (sample II)	0.39996	14.51470(6)
0.5	0.39989	14.67951(5)	2 (sample I)	0.39620	14.45329(8)
0.75	0.40006	14.64113(6)	2 (sample II)	0.40006	14.45373(7)
1	0.40006	14.60211(5)	2 (sample III)	0.39996	14.45169(9)

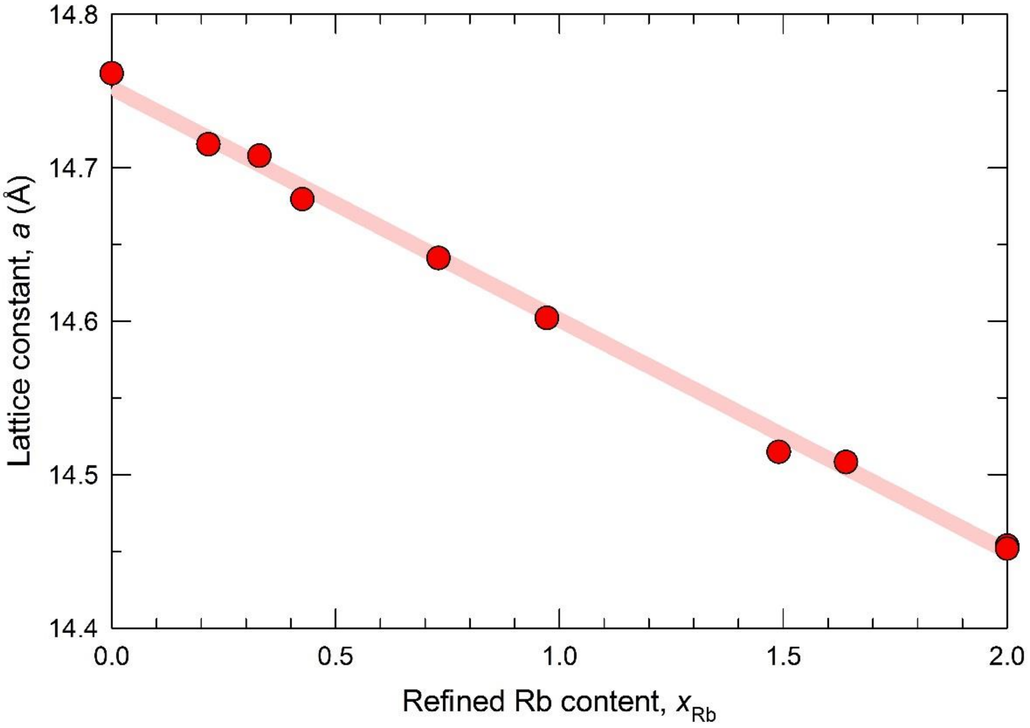

Figure 3.2: Variation of the ambient temperature *fcc* lattice constant of $Rb_xCs_{3-x}C_{60}$ ($0 \leq x \leq 2$), with refined Rb content, x_{Rb}, from analysis of high-resolution synchrotron PXRD data. The $x = 0$ lattice constant is from ref. [**140**]; the solid line through the data points is a linear fit, yielding a value of $da/dx_{Rb} = -0.151(3)$ Å.

These experimental results regarding the cation distribution in *fcc* $Rb_xCs_{3-x}C_{60}$ ($x = 1, 2$) are in good agreement with earlier literature reports, both experimentally from *e.g.* ^{133}Cs NMR spectroscopy studies,[**152**] X-ray diffraction,[**153**] and from a theoretical study, based on minimising the free energy when configuration entropy is considered;[**154**] Saito *et al*. predicted that 99 % of the octahedral sites in Rb_2CsC_{60} should be occupied by Cs, and that in $RbCs_2C_{60}$, the octahedral interstitial Rb occupation should be significantly lower still. Their calculations also showed that, under normal synthetic conditions, the $Fm\bar{3}m$ space group (from random occupation of the two tetrahedral sites by Rb and Cs) should be experimentally observed for $RbCs_2C_{60}$, as in the known Rb_3C_{60} and Cs_3C_{60}. The feasible alternative, $F\bar{4}3m$, would result from ordered tetrahedral site occupation, with a loss of inversion symmetry.[**154**]

Anisotropic microstrain broadening was included in the profile function, by refining the profile parameters L_{11}, L_{22}, L_{33}, L_{12}, L_{13} and L_{23} in the fit to the highest statistics data set (4 K) and fixing the parameters to these values over all higher temperatures. An earlier PXRD investigation of Rb_3C_{60} found that diffraction peak width was not purely a function of 2θ, reporting a continuous progression from the sharpest peaks in the (hhh) direction to the broadest along $(h00)$;[**155**] ascribed to strain broadening rendered by increased rigidity of crystallites along the body diagonal than in other directions, this effect could only be effectively modelled using a profile function incorporating anisotropic profile broadening parameters. A large thermal factor at the octahedral site in *fcc* A_3C_{60} materials, as found experimentally here, has invariably been observed in previous literature PXRD studies.[**156**]

3.3.3. Structural results to low temperatures

Further to the structural characterisation of *fcc* $Rb_xCs_{3-x}C_{60}$ $(0.25 \le x \le 2)$ at ambient temperatures, the temperature evolution of structural properties of this series, investigated using high-resolution synchrotron PXRD, will now be discussed.

As at ambient temperature, the same fixed C_{60} geometry was employed for each phase (with *fcc* C-C bond distances of 1.42 Å), and rescaled to the refined lattice dimensions at each temperature. This approach was adopted as, given the available data quality, refinement of C_{60} coordinates at each temperature would not have produced physically meaningful results, and with reference to previous literature approaches: a previous variable-temperature powder X-ray diffraction study of Rb_3C_{60} found no variation within error in C_{60} radius between 20 and 295 K.[**150**] The same study also found no significant variation in the fractional cation occupancy of Rb_3C_{60} in the tetrahedral or octahedral sites between 20 – 295 K. In this work, *fcc* interstitial Rb^+/Cs^+ distribution was allowed to refine for the best statistics data set only (usually collected at 5 or 10 K), then fixed to these values at all other temperatures, in the same manner as the relative phase fractions.

Rietveld fits to the highest statistics PXRD data collected for $Rb_{0.5}Cs_{2.5}C_{60}$ and $RbCs_2C_{60}$, at 5 and 10 K respectively, are displayed in Fig. 3.3. Table 3.3 summarises the refined *fcc* phase stoichiometry and phase fractions for each $Rb_xCs_{3-x}C_{60}$ sample, defined from the highest statistics dataset available.

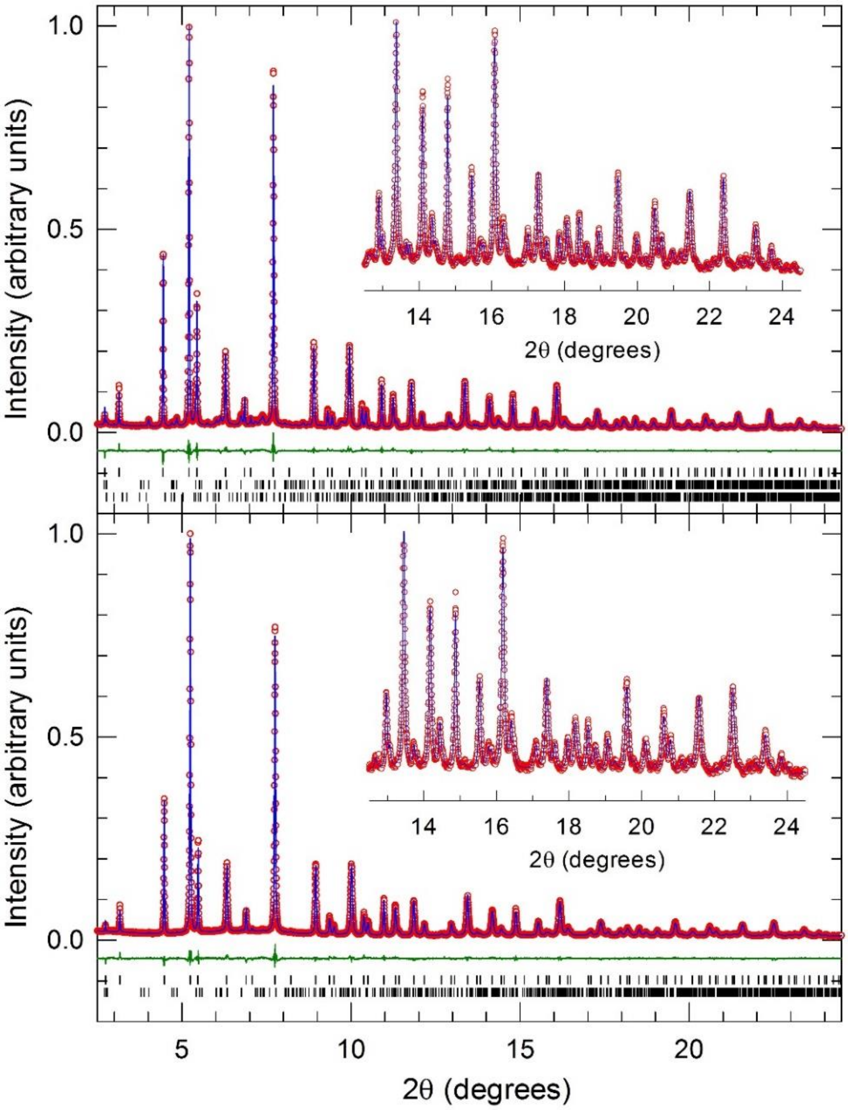

Figure 3.3: Rietveld fits to synchrotron PXRD data collected at 5 K for *fcc*-rich $Rb_{0.5}Cs_{2.5}C_{60}$ (upper panel, λ = 0.39989 Å), and at 10 K for $RbCs_2C_{60}$ (lower panel, λ = 0.40006 Å). Red circles, blue lines and green lines represent the observed, calculated and difference profiles. Bars mark the reflection positions, from top-to-bottom, of co-existing *fcc*, body-centered-orthorhombic (bco) and CsC_{60} (observable in *x* = 0.5 only) phases. Both insets display expanded regions of the respective diffraction profiles at high Bragg angles.

Table 3.3: Summary of refined *fcc* phase stoichiometries and phase fractions for *fcc*-rich $Rb_xCs_{3-x}C_{60}$ ($0.25 \leq x \leq 2$), obtained from the highest statistics PXRD data sets available, collected at (*) ambient temperature, (**) 10 K or (***) 5 K. Statistical errors from Rietveld analysis are shown in parentheses. For the $x = 2$ composition, the Rb^+/Cs^+ occupancy ratio in the tetrahedral site was fixed according to the nominal stoichiometry.

Nominal x_{Rb}	Refined *fcc* x_{Rb}	*fcc* phase (%)	bco phase (%)	CsC_{60} phase (%)
0.25	0.22(1)**	83.28(5)**	7.36(7)**	9.4(2)**
0.35	0.33(2)**	76.48(7)**	10.1(1)**	13.5(3)**
0.5	0.426(8)***	83.23(3)***	13.16(7)***	3.6(1)***
0.75	0.73(1)*	94.30(1)*	-	5.7(1)*
1	0.972(8)**	98.994(2)**	1.01(4)**	-
1.5 (sample I)	1.64(1)**	94.04(1)**	-	6.0(1)**
1.5 (sample II)	1.49(1)*	93.98(2)*	-	6.0(2)*
2 (sample I)	2*	91.71(2)*	-	8.3(2)*
2 (sample II)	2*	98.184(4)*	-	1.8(1)*
2 (sample III)	2*	99.137(2)*	-	0.9(2)*

Whilst no signs of symmetry changes upon cooling are visually evident from diffraction profiles (Fig. 3.3), for $Rb_xCs_{3-x}C_{60}$ ($0.25 \leq x \leq 1.5$), the variation of lattice metrics with temperature appears strikingly discontinuous. This is exemplified by the evolution of *fcc* unit cell parameter with temperature (Fig. 3.4). Upon cooling, each sample undergoes a distinct isosymmetric collapse in unit cell volume, at a certain temperature which varies systematically with the nominal stoichiometry. This appears to represent a transition to a lower volume phase upon cooling, which we ascribe to a Mott insulator-metal transition; this hypothesis is corroborated by evidence from other techniques *e.g.* SQUID magnetometry and solid-state NMR spectroscopy, discussed later in Sections 3.4.3 and 3.6. The lattice collapse onset temperature increases with decreasing unit cell size, through increasing Rb^+ substitution into the *fcc* lattice (Table 3.5), and the transition extends over a broader temperature range. In stark contrast, the temperature evolution of *fcc* Rb_2CsC_{60} and Cs_3C_{60} [**140**] unit cell volumes appear typical of thermal contraction of solids upon cooling to low temperature, with no anomalies evident.

The thermal expansivity of the *fcc* lattice can be parameterised using a Debye-Grüneisen model, such as that proposed by Sayetat and co-workers and applied here (described in Section 2.4.5).[**129**] The function in Equation 2.25 is fitted to the temperature variation of unit cell volume, $V(T)$ by least-squares fitting.

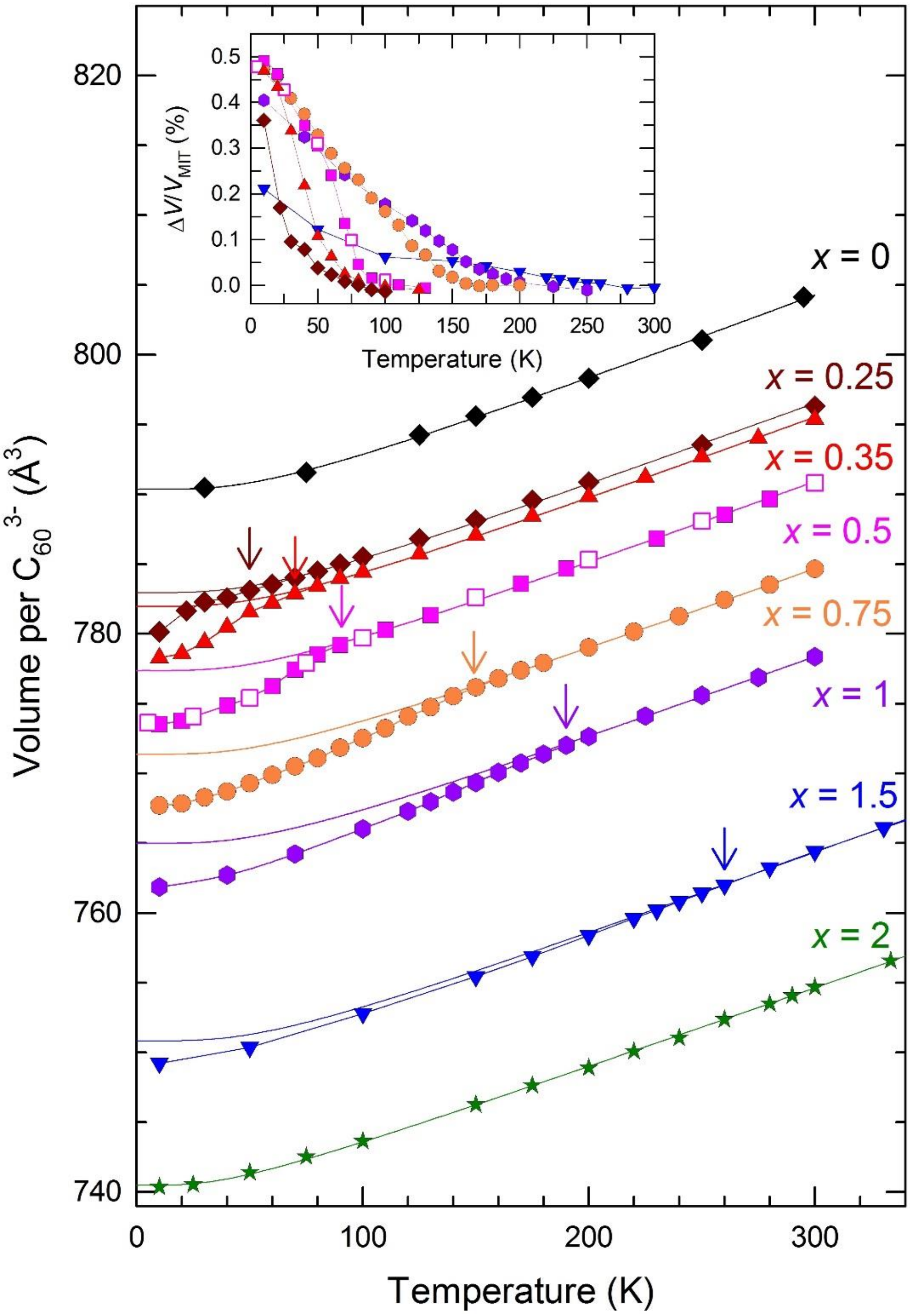

Figure 3.4: The variation of unit cell volume, V, occupied per C_{60}^{3-} anion for *fcc* $Rb_xCs_{3-x}C_{60}$ ($0 \le x \le 2$); for x = 1.5 and 2, samples II and III, respectively, were measured. Open symbols for x = 0.5 represent results from a repeat experiment; data for x = 0 are reproduced from ref. [**140**]. Arrows mark the onset temperatures of the change in lattice response, denoted T_{MIT}, where observed. Solid lines at $T > T_{MIT}$ (or over all T for x = 0 and 2) display the results of Debye-Grüneisen fits, but at $T < T_{MIT}$ are guides to the eye. Inset: Temperature evolution of the normalised volume change, $\Delta V/V_{MIT}$, for $Rb_xCs_{3-x}C_{60}$ ($0.25 \le x \le 1.5$).

However, because of the distinctive anomalies in the $V(T)$ evolution of $Rb_xCs_{3-x}C_{60}$ ($0.25 \leq x \leq 1.5$), data from the full temperature range cannot be modelled with one fit. The following approach was therefore undertaken to characterise the expansivity behaviour and best define the onset temperatures of volume collapse: firstly, the *fcc* Cs_3C_{60} data,[**140**] insulating over the full temperature range, were fitted using this Debye-Grüneisen model; parameters from this and subsequent fits are presented in Table 3.4. The Debye temperature, Θ_D is largely determined by the shape of the low temperature data. Assuming that the high-temperature phase of $Rb_xCs_{3-x}C_{60}$ ($0.25 \leq x \leq 1.5$) is similar in character to *fcc* Cs_3C_{60}, fits were next undertaken for the former compositions, with data collected at temperatures above the volume collapse included only and Θ_D fixed at the value obtained for Cs_3C_{60}. This provides a best estimate for the hypothetical $V(T)$ trajectory for the insulating phase in each sample to 0 K, if no lattice collapse were observed. Finally, data for the full temperature range were included for a fit to Rb_2CsC_{60} (with no anomaly evident), providing estimated expansivity parameters for a $Rb_xCs_{3-x}C_{60}$ system known to be metallic throughout the experimental temperature range.

Table 3.4: Derived parameters from the fits to the thermal expansion data of *fcc* $Rb_xCs_{3-x}C_{60}$ ($0 \leq x \leq 2$), after ref. [**129**]. The fit for *fcc* Cs_3C_{60} is to data from reference **[140]**; fits for x = 1.5 and 2 are to data for samples II and III, respectively. Statistical errors from least-squares fitting are in parentheses; the symbol '*' indicates the parameter was fixed.

Nominal x_{Rb}	Fitted T range (K)	V_0 (Å^3)	Θ_D (K)	I_V (Å^3 K^{-1})
0	30 – 295	3161.4(7)	218(22)	0.246(7)
0.25	50 - 300	3131.8(3)	218*	0.240(3)
0.35	70 – 300	3127.8(2)	218*	0.240(2)
0.5	90 – 300	3109.4(2)	218*	0.240(2)
0.75	160 – 300	3085.5(1)	218*	0.235(7)
1	200 – 300	3059.9(6)	218*	0.237(3)
1.5	280 – 516	3003.3(5)	218*	0.2388(8)
2	10 – 570	2962.0(3)	152(6)	0.2293(9)

The normalised volume change below T_{MIT} for $Rb_xCs_{3-x}C_{60}$ ($0.25 \leq x \leq 1.5$), $\Delta V/V_{MIT}$ (with ΔV the difference between the hypothetical V/C_{60}^{3-} derived from the Debye-Grüneisen model extrapolated below T_{MIT}, and the 'true' experimental volume extracted from Rietveld analysis), is shown in Fig. 3.4 (inset); this appears to approach the same value of ~0.5% for all overexpanded compositions, although the transition becomes smeared out with increasing Rb_x.

Comparing literature data to the present results, EXAFS measurements yielded Θ_D values of 163(10) K, 167(10) K (Rb_2CsC_{60}, Rb_3C_{60} [**157**]), in excellent agreement with the present estimate of Θ_D = 152(6) K for Rb_2CsC_{60} from the $V(T)$ data. Using a similar approach to the present study (variable temperature PXRD), Θ_D = 208 K has been estimated for Rb_3C_{60}.[**158**] Specific heat measurements of Θ_D have generally produced lower estimates (70 K, 54 K for K_3C_{60}, A15 Cs_3C_{60} [**159, 160**]). A discontinuity in the thermal expansivity of K_3C_{60} and Rb_3C_{60} at $T \sim T_c$ has been reported;[**161**] if such a discontinuity exists in overexpanded $Rb_xCs_{3-x}C_{60}$, although not ascertainable from the $V(T)$ data presented here because of the large temperature steps, this may result in slightly overestimed Θ_D estimates. However, this effect is believed to be relatively minor.

Table 3.5: Summary of the onset of expansivity anomalies in $V(T)$, attributed to insulator-to-metal transitions and designated 'T_{MIT}', for *fcc* $Rb_xCs_{3-x}C_{60}$ (0.25 ≤ x ≤ 1.5); data for x = 1.5 are from sample II. Values of T_{MIT} are defined as the first point of deviation, on cooling, between V from experiment and V calculated for the high-temperature insulating phase (assuming no transition with concurrent volume collapse). Statistical uncertainties (Rietveld analysis, neglecting error in T_{MIT}) are in parentheses, but the 'true' error in T_{MIT} is estimated at ±5 K, corresponding to uncertainty in $V(T_{MIT})$ of the order ~ ±0.4 Å^3.

Nominal x_{Rb}	T_{MIT} from PXRD (K)	V per C_{60} at T_{MIT} (Å^3)
0.25	50	783.126(8)
0.35	70	782.89(1)
0.5	90	779.211(7)
0.75	150	776.16(1)
1	190	772.015(7)
1.5	260	762.01(5)

The variation in U_{iso} with temperature for the octahedral and tetrahedral intercalants (Fig. 3.5) reveals an overall reduction in U_{iso} with increasing Rb_x, particularly for the octahedral site, and that the trend in octahedral U_{iso} with temperature closely mimics the $V(T)$ behaviour; a similar trend is not clearly observed in tetrahedral U_{iso}, although the values are significantly smaller in magnitude and there is more scatter.

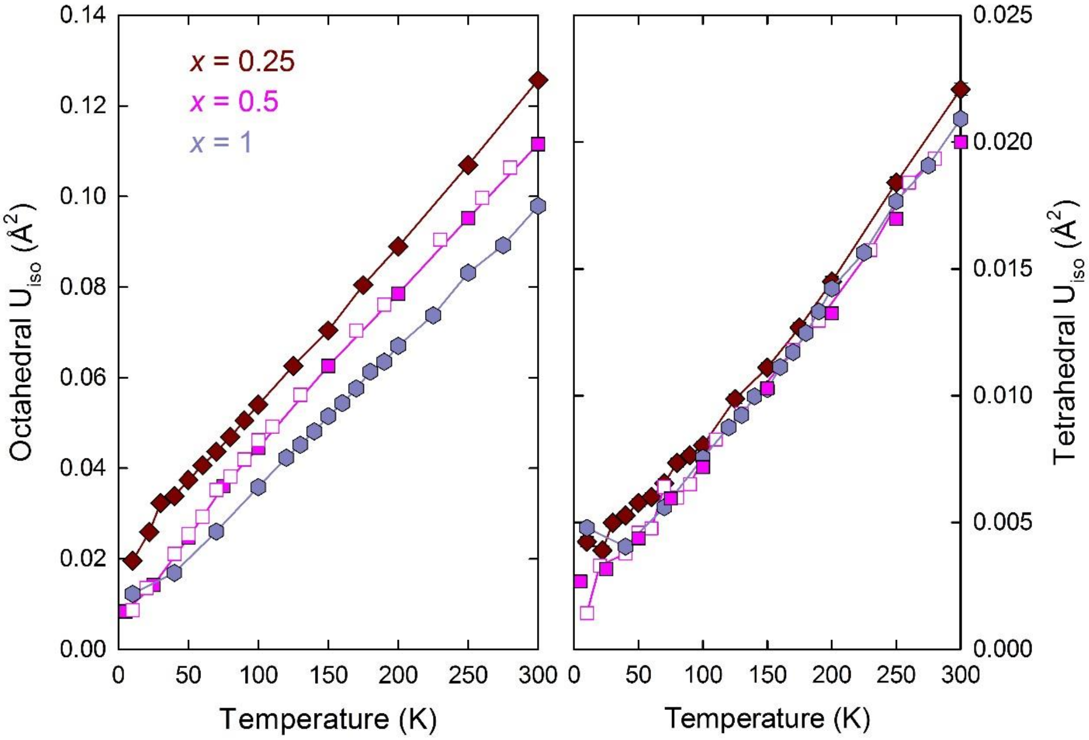

Figure 3.5: The evolution of U_{iso} at the octahedral (left panel) and tetrahedral (right panel) interstitial sites in *fcc* $Rb_xCs_{3-x}C_{60}$ (x = 0.25, 0.5, 1).

Examining the temperature variation of peak width for two relatively intense and isolated *fcc* reflections from two overexpanded compositions (x = 0.25, 0.5), there is very little variation over the experimental temperature range ~5–300 K (Fig. 3.6). Significantly, no changes at T_{MIT} are evident; this further lack of evidence for any symmetry-lowering transition over the temperature range investigated indicates that the MIT is isosymmetric. It must be concluded that the space group $Fm\bar{3}m$ is preserved to low temperatures. Furthermore, no evidence for phase coexistence is observed, which, if present, would be anticipated to result in diffraction peak broadening across the MIT; such a behaviour is not observed experimentally.

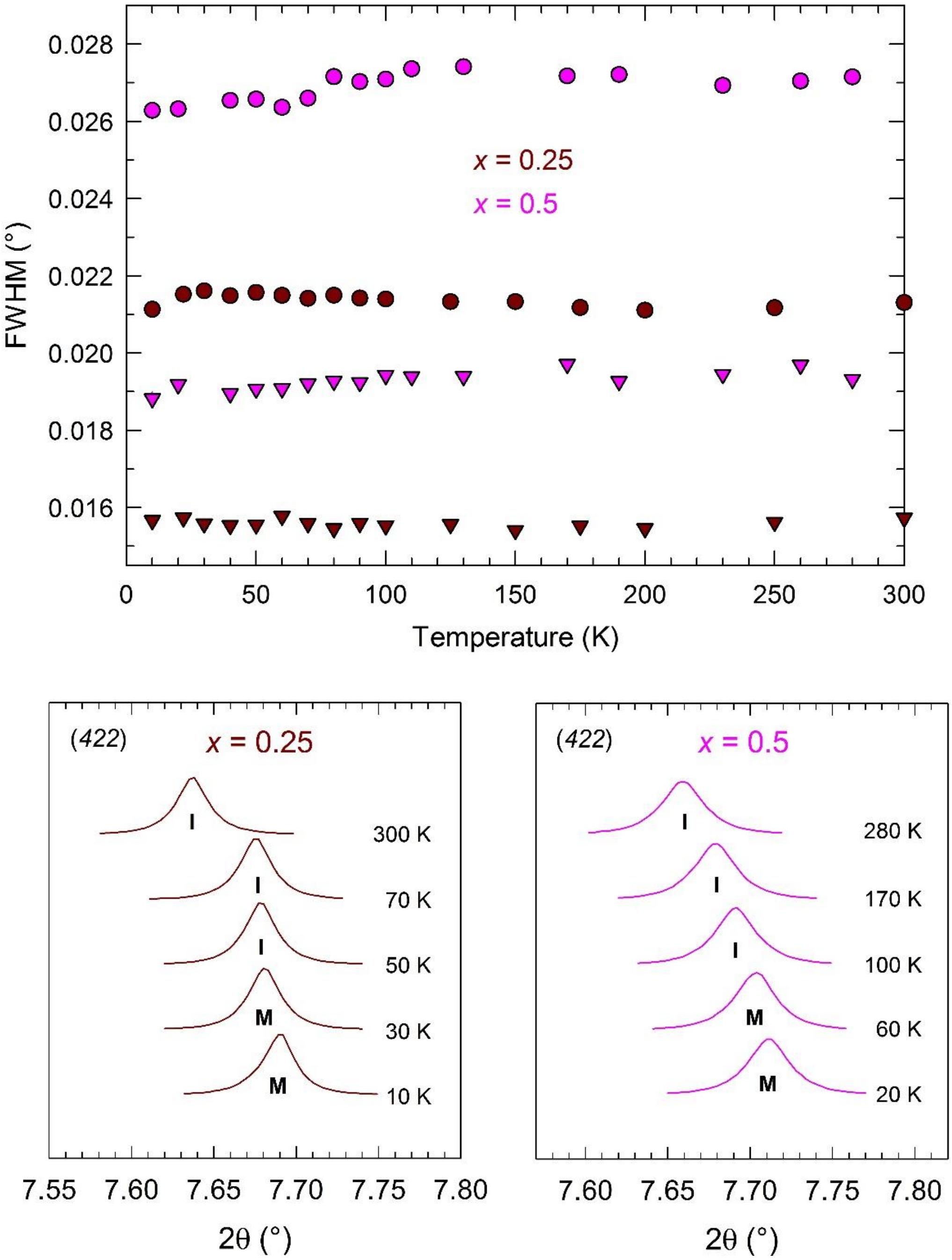

Figure 3.6: Upper panel: The evolution of full-width-at-half-maximum (FWHM) with temperature for the *311* (circles) and *220* (triangles) reflections of *fcc* $Rb_xCs_{3-x}C_{60}$ (x = 0.25, 0.5). For x = 0.5, data from one of two experimental runs only are plotted. Values of FWHM were extracted through least-squares one-peak fits using the software WinPLOTR (FullProf), with a pseudo-Voigt peak shape function. Eta (Lorentzian/Gaussian mixing parameter) was refined at 10 K and fixed over all temperatures, whilst FWHM was allowed to refine (statistical uncertainties are smaller than data points). Lower panels: the evolution of peak profile with temperature for the *422* reflection of *fcc* $Rb_xCs_{3-x}C_{60}$ (x = 0.25, 0.5); 'I' and 'M' label the insulating and metallic phases, respectively.

3.3.4. Summary of structural properties at ambient pressure

The PXRD analysis of *fcc*-rich $Rb_xCs_{3-x}C_{60}$ ($0.25 \leq x \leq 2$) under ambient conditions showed that the volume of the *fcc* phases increases monotonically with decreasing Rb_x (nominal or refined), up to the literature value for *fcc* Cs_3C_{60},[**140**] indicative of good *fcc* phase stoichiometry control. Whilst the $x = 0$ analogue contracts smoothly with temperature with no evidence of anomalies, structural analysis to low temperatures for the overexpanded compositions ($0.25 \leq x \leq 1$) revealed distinctive volume collapses upon cooling; the normalised volume change is approximately the same for all compositions. The onset temperature of volume collapse is tuneable with chemical pressure, increasing with increasing Rb_x. No evidence for peak broadening or any change in lattice symmetry is found upon cooling to low temperature. The transition must thus be classed as isostructural from the data presently available; in addition, no evidence for phase co-existence across the transition has been found, as shown by the absence of diffraction peak splittings and of any peak broadening.

3.3.5. Compressibility behaviour in the superconducting regime

The results of low-temperature, high-pressure synchrotron X-ray powder diffraction investigations of *fcc*-rich $Rb_xCs_{3-x}C_{60}$ ($0.35 \leq x \leq 2$), undertaken to investigate evolution of structural properties with pressure in these systems in the superconducting regime, will now be presented.

The structural model employed was identical to that used to model the ambient pressure data. There were, however, certain differences in the Rietveld model used: C_{60} temperature factors were modelled as isotropic, fixed equal to one another and fixed over all pressures; in general, pressure typically has only a small effect on isotropic temperature factors,[**162**] and the effect of any change would be difficult to model meaningfully due to significant pressure-induced peak broadening. Furthermore, given that the resolution and statistics for the ambient pressure data were higher, *fcc* phase cation stoichiometries in these high pressure data refinements were set to those obtained in the highest statistics ambient pressure data (Section 3.3.3), and fixed over all pressures. No absorption correction was used, in contrast to the ambient pressure data. For samples with $x = 0.5$ and $x = 1$, with data collected at ID27 (ESRF), the background from the cryostat was significant with large features, which could not be simply modelled with a background function, so a 'background' profile had to be subtracted from the sample profile (*i.e.* data collected by irradiating at a part of the DAC where there is no sample, at a similar pressure to that at which the sample profile was collected).

The evolution of the PXRD profiles with pressure over the full pressure range is illustrated for the two compositions Rb_2CsC_{60} and $Rb_{0.35}Cs_{2.65}C_{60}$ in Fig 3.7. (corresponding data for $Rb_{0.5}Cs_{2.5}C_{60}$, $RbCs_2C_{60}$ and $Rb_{1.5}Cs_{1.5}C_{60}$ are shown in the Appendix). Representative observed, calculated and difference diffraction profiles from Rietveld analysis at low and high pressure are shown in Fig. 3.8 and Fig. 3.9, for Rb_2CsC_{60} and $Rb_{0.35}Cs_{2.65}C_{60}$, respectively. The corresponding fractional atomic coordinates, site occupancies and thermal parameters for the majority *fcc* phase from these four refinements are contained in Table 3.6.

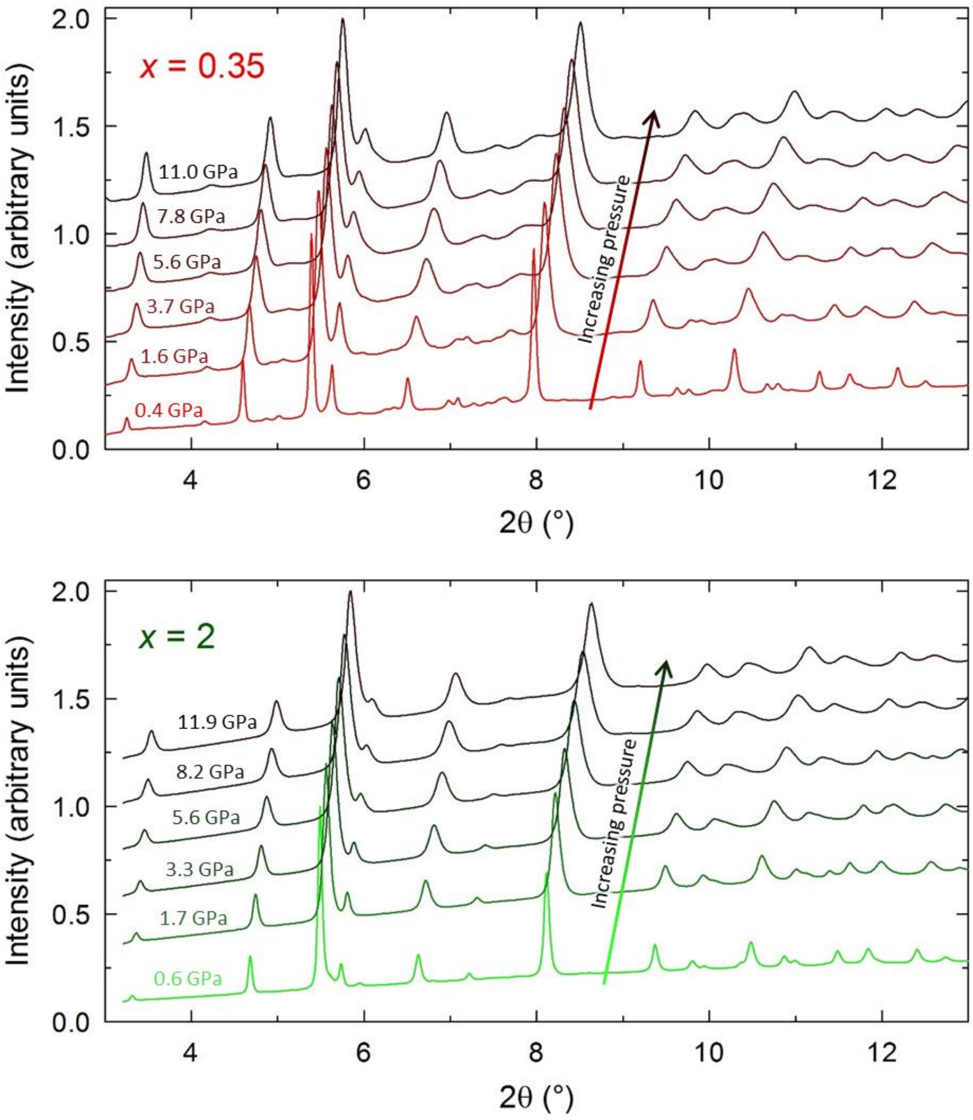

Figure 3.7: The evolution of synchrotron PXRD profiles with pressure, collected at 7 K, for *fcc*-rich $Rb_{0.35}Cs_{2.65}C_{60}$ (upper panel, λ = 0.41305 Å) and for *fcc*-rich Rb_2CsC_{60} (lower panel, sample II, λ = 0.41238 Å). Intensities are normalised and offset for visual clarity.

With unit cell volume at each pressure, V, extracted from Rietveld refinements, the $V(P)$ trends for each sample were modelled using the Murnaghan EoS (Equation 2.18), yielding excellent fits to the data over the experimental pressure range. However, prior to fitting, a small uniform pressure shift, ΔP, was applied to all pressures in each particular experiment, in order to render the high pressure $V(P)$ data fully consistent with the V at ambient pressure and equivalent low temperature. The latter data (Fig. 3.4) are considered more accurate as they were collected at the same beamline, ID31, with higher statistics and over a larger *d*-spacing range than the high pressure data; peak widths are also narrower due to less strain broadening, absence of pressure inhomogeneity effects, etc. The ΔP factor is largely required as high-pressure data were collected at two different beamlines, with slightly different setups and wavelength calibration techniques (Section 2.3); it is consistent in magnitude, negative for data collected at BL10XU, but positive for data collected at ID27 (Table 3.7). The ΔP is defined for each sample as the P shift required such that a linear fit to the lowest P data points (typically < 0.8 GPa) intersects the ambient P data point (collected at equivalent low temperature).

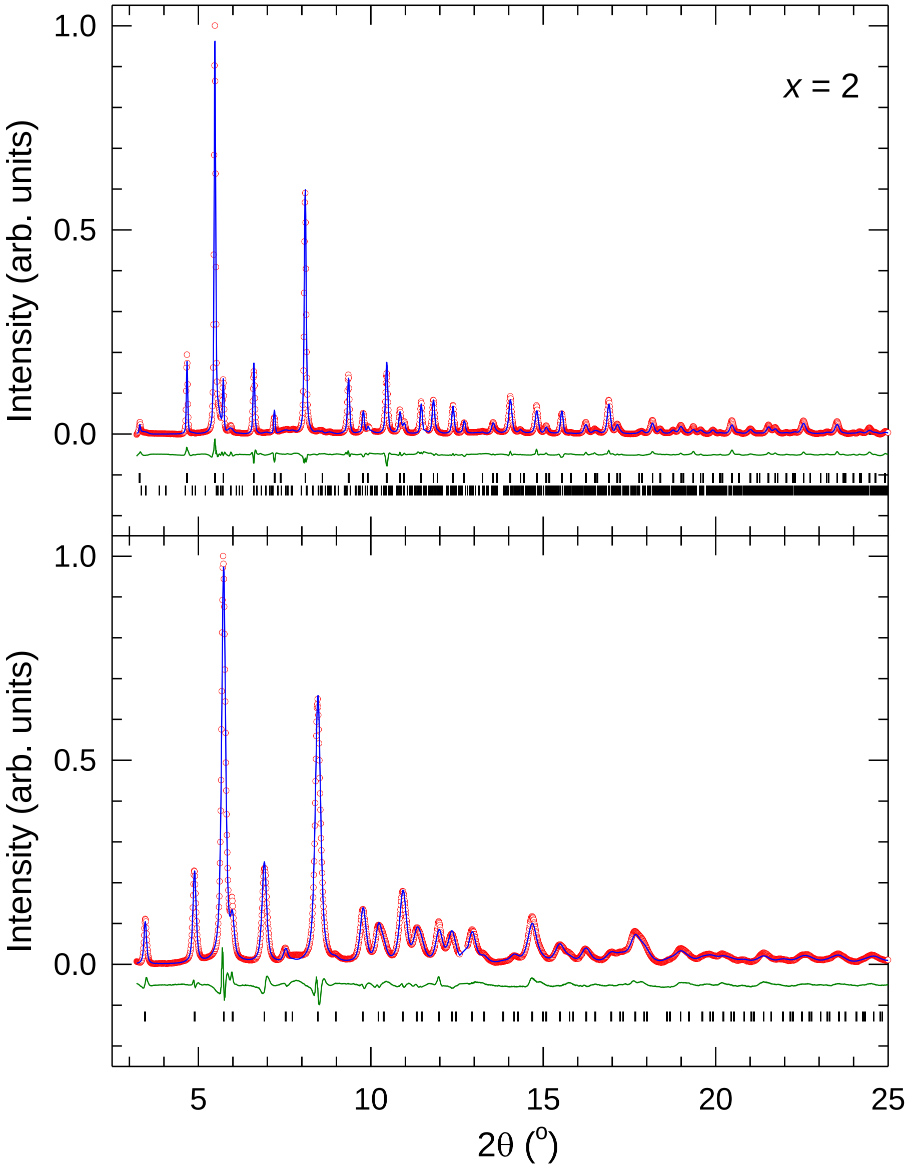

Figure 3.8: High-pressure synchrotron X-ray powder diffraction for Rb_2CsC_{60} (sample II, 7 K). Final observed (o) and calculated (blue line) diffraction profiles (λ = 0.41238 Å) at 0.41 GPa (upper panel) and 6.05 GPa (lower panel). The lower green lines show the difference profiles, and bars mark the reflection positions of the *fcc* (top) and CsC_{60} (bottom) phases; above 1.45 GPa, no peaks from CsC_{60} were visible, so *fcc* phase only was used in fits to the higher pressure data. The fitted background contribution has been subtracted, for visual clarity.

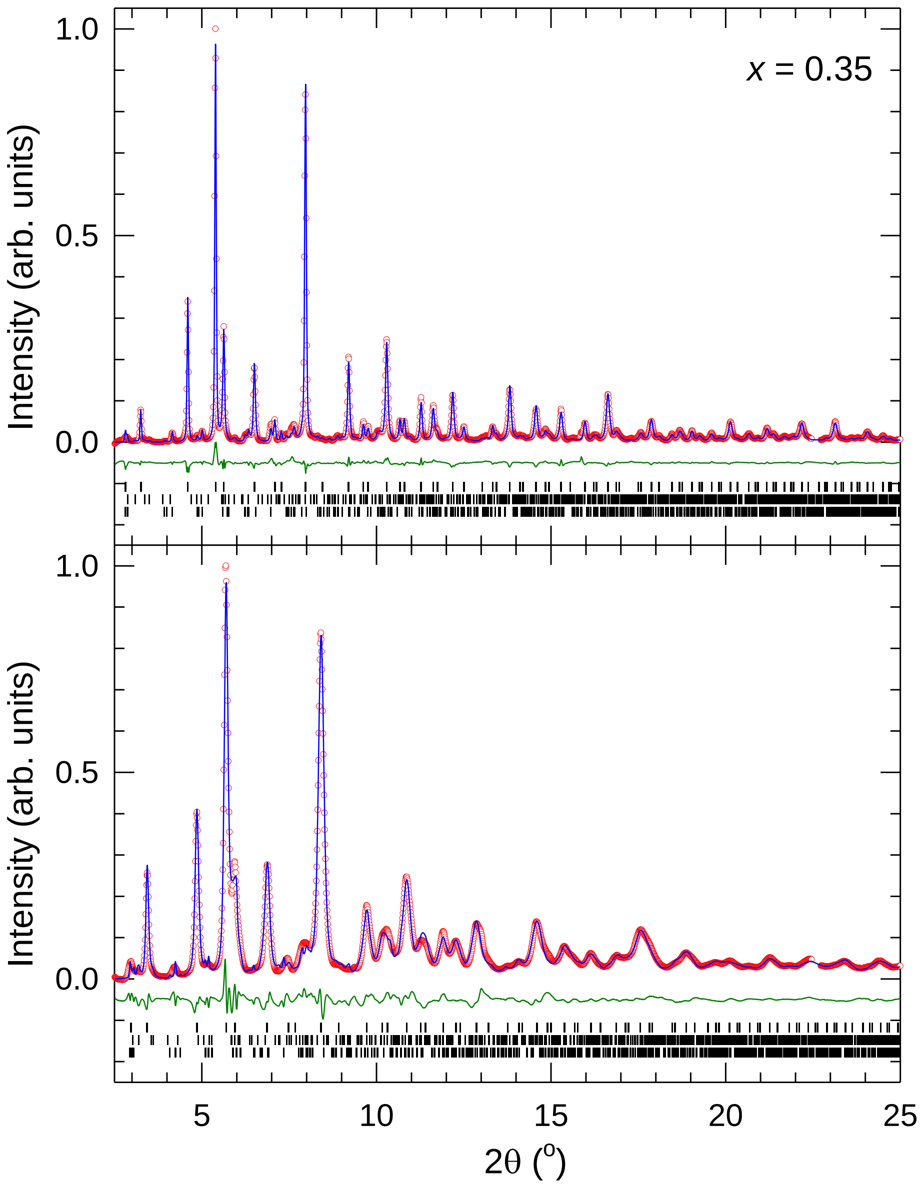

Figure 3.9: High-pressure synchrotron X-ray powder diffraction for $Rb_{0.35}Cs_{2.65}C_{60}$ (7 K). Final observed (o) and calculated (blue line) diffraction profiles (λ = 0.41305 Å) at 0.41 GPa (upper panel) and 7.82 GPa (lower panel). The lower green lines show the difference profiles, and bars mark the reflection positions of the *fcc* (top), CsC_{60} (middle) and Cs_4C_{60} (bottom) phases. The fitted background contribution has been subtracted, for visual clarity.

In the final Murnaghan EoS fits to $V(P + \Delta P)$, the ambient pressure data point is included in the fit with the shifted high pressure data, and the V_0 fixed to the ambient pressure V, so K_0 and K_0' only are refined. The $V(P + \Delta P)$ data for each sample together with the EoS fits are presented in Fig. 3.10, and the EoS fit parameters are shown in Table 3.7.

Table 3.6: Structural parameters for the majority *fcc* ($Fm\bar{3}m$) phases of $Rb_xCs_{3-x}C_{60}$ samples (x = 0.35 and 2, sample II), used in Rietveld analysis of synchrotron PXRD data collected at 7 K under applied hydrostatic pressure. The fractional cation occupancies, N of the tetrahedral interstitial site were fixed to values refined from low temperature ambient pressure higher statistics data, described earlier (section 3.3.3). For x = 0.35, more multiphasic in character and thus affected more by *fcc* peak overlap with minority phases, B_{iso} values of the alkali metal cations were fixed over all pressures (analogously to the carbon B_{iso} values). Where values were refined, statistical uncertainties are shown in parentheses.

$Rb_{0.35}Cs_{2.65}C_{60}$

P = 0.41 GPa	x/a	y/b	z/c	N	B_{iso} (Å^2)
Rb	0.25	0.25	0.25	0.163	0.22
Cs(1)	0.25	0.25	0.25	0.837	0.22
Cs(2)	0.5	0.5	0.5	1.0	1.18
C(1)	0	0.04884	0.23683	0.5	0.03
C(2)	0.20672	0.07894	0.09746	0.5	0.03
C(3)	0.17640	0.15772	0.04884	0.5	0.03

$Rb_{0.35}Cs_{2.65}C_{60}$

P = 7.82 GPa	x/a	y/b	z/c	N	B_{iso} (Å^2)
Rb	0.25	0.25	0.25	0.163	0.22
Cs(1)	0.25	0.25	0.25	0.837	0.22
Cs(2)	0.5	0.5	0.5	1.0	1.18
C(1)	0	0.05153	0.24990	0.5	0.03
C(2)	0.21812	0.08330	0.10284	0.5	0.03
C(3)	0.18614	0.16642	0.05153	0.5	0.03

Rb_2CsC_{60}

P = 0.41 GPa	x/a	y/b	z/c	N	B_{iso} (Å^2)
Rb	0.25	0.25	0.25	1	1.28(7)
Cs	0.5	0.5	0.5	1	3.2(1)
C(1)	0	0.04971	0.24106	0.5	0.03
C(2)	0.21041	0.08035	0.09921	0.5	0.03
C(3)	0.17956	0.16054	0.04971	0.5	0.03

Rb_2CsC_{60}					
P = 6.05 GPa	x/a	y/b	z/c	N	B_{iso} (Å^2)
Rb	0.25	0.25	0.25	1	1.35(7)
Cs	0.5	0.5	0.5	1	3.3(1)
C(1)	0	0.05191	0.25174	0.5	0.03
C(2)	0.21973	0.08391	0.10360	0.5	0.03
C(3)	0.18751	0.16765	0.05191	0.5	0.03

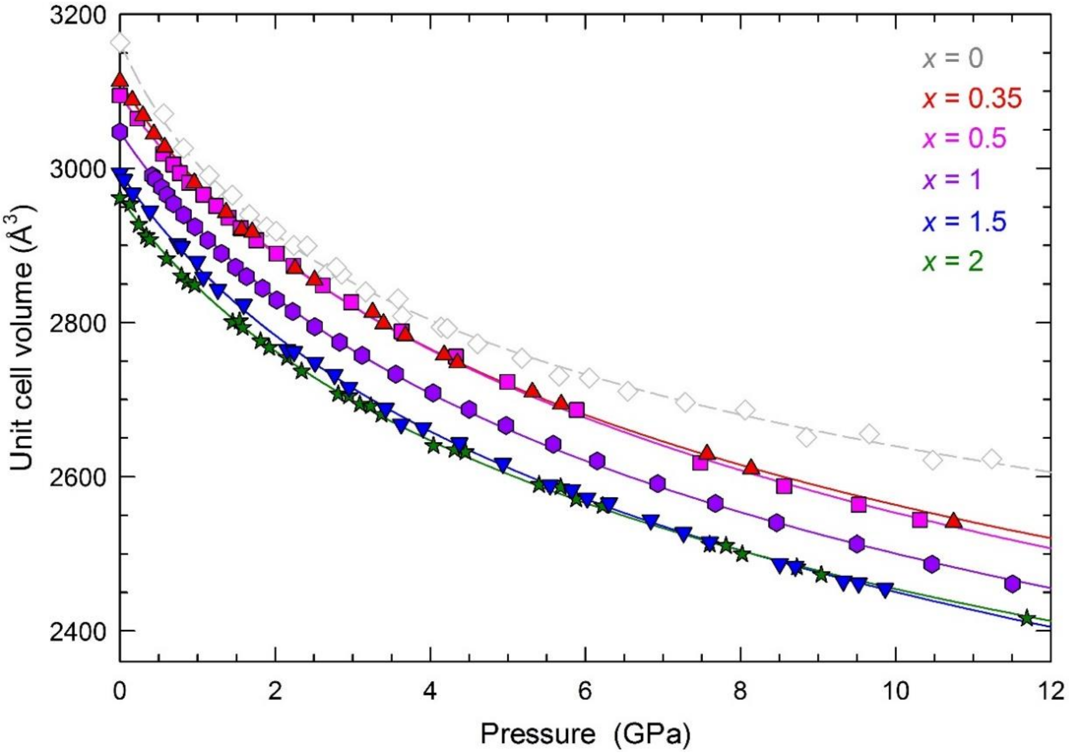

Figure 3.10: The evolution of *fcc* unit cell volume with pressure at low temperature, for $Rb_xCs_{3-x}C_{60}$ ($0.35 \le x \le 2$). Data for *fcc* Cs_3C_{60} (dashed line), from ref. [**140**], are also presented for comparison. The lines through the data points show results from least-squares fits to second-order Murnaghan EoS (see Table 3.7 for details). Data for x = 1.5, 2 were collected for samples I and II, respectively. Statistical errors in V from Rietveld analysis are smaller than the data point size.

Table 3.7: Details of the Murnaghan EoS fits to low-temperature $V(P)$ data for *fcc* $Rb_xCs_{3-x}C_{60}$ ($0.35 \leq x \leq 2$). Numbers in parentheses indicate statistical errors from the least-squares-fitting. Data for $x = 0$ are also included for comparison (in italics), taken from ref. [**140**]. Data for $x = 1.5$, 2 refer to samples I and II, respectively.

Nominal x_{Rb}	Data collection temperature (K)	K_0 (GPa)	K_0'	V_0 (Å^3)	ΔP (GPa)
0	*15*	*13.7(3)*	*13.0(3)*	*3163.6*	*n/a*
0.35	7	19.0(2)	9.0(1)	3113.2	-0.2535
0.5	20	21.9(3)	8.0(2)	3094.5	0.1427
1	20	20.0(1)	8.26(8)	3047.4	0.2611
1.5	7	20.3(2)	8.0(2)	2993.9	-0.1675
2	7	20.9(3)	8.8(2)	2961.9	-0.1687

Consistent with previous work on *fcc* A_3C_{60} (A = Rb, Cs),[**140, 163**] *fcc* $Rb_xCs_{3-x}C_{60}$ is found to be stable at elevated pressures (up to at least 11 GPa); smooth compressibility behaviour is observed, with no evidence of any phase transformations evident.

The $V(P)$ evolution of *fcc* Cs_3C_{60} differs slightly from the Rb-substituted analogues. The relatively lower compressibility in the former at higher pressures may arise from its larger average cation radius in the *fcc* tetrahedral interstice. In addition, for *fcc* Cs_3C_{60}, data from two experiments were combined, and there are few data points available at very low P, a region sensitively affecting the resulting K' and K_0' from EoS fitting (and therefore affected by the method of calibration to ambient P data; in ref. [**140**], a volume normalisation, rather than ΔP shift, was employed).

The values of K_0', at 8-9, are somewhat larger than the $K_0' = 4$ obtained from second-order truncation of the Birch-Murnaghan EoS (in mineralogical databases, K_0' is frequently fixed to 4 to obtain a two-parameter Murnaghan EoS). However, the values of K', K'_0 found here experimentally are not atypical for *fcc* A_3C_{60}; a study of the compressibility of *fcc* Rb_3C_{60} at ambient temperature, also undertaken with a gaseous pressure medium (Ar) and over a similar pressure range (P_{max} = 13 GPa), reported $K_0 = 14(1)$, $K' = 10.0(3)$.[**163**] These materials should be less compressible at the low temperatures in the present study, and with a higher average tetrahedral cation radius (*i.e.* increasing K_0).

In these molecular crystalline systems, the C_{60} molecules are expected to be effectively incompressible (in the pressure range under investigation). One approach adopted in studying the compressibility of Rb_3C_{60}, for which a standard EoS was deemed inadequate to describe the compression properties, was to use a modified EoS where the volume of the incompressible molecules had been subtracted; this yielded K_0 = 20.5 GPa for the compressible part of the crystal, as opposed to K_0 ~27 GPa for the crystal itself.[**164**] However, in the present investigation such an approach was not required, as the Murnaghan EoS could model the low temperature $V(P)$ data for *fcc* $Rb_xCs_{3-x}C_{60}$ $(0.35 \leq x \leq 2)$ well.

3.3.6. Pressure-induced structural transition in overexpanded $Rb_{0.5}Cs_{2.5}C_{60}$

In light of the distinct isosymmetric volume collapses induced through reducing interfullerene spacing in $Rb_xCs_{3-x}C_{60}$ $(0.25 \leq x \leq 1.5)$ through cooling, attributed to insulator-to-metal transitions (Section 3.3.3), it is of interest to investigate whether an analogous transition may also be induced through pressurisation alone. Accordingly, high-pressure synchrotron PXRD data were collected for *fcc* $Rb_{0.5}Cs_{2.5}C_{60}$ at ambient temperature (see Section 3.3.1 for experimental details), to probe whether any compressibility anomalies are evident.

The powder X-ray diffraction profiles could be modelled well up to ~1 GPa using Rietveld analysis with a two-phase fit. As for the low-temperature high-pressure data, an identical structural model was used to that described at ambient pressures. In the final set of refinements, the zero shift was fixed over all pressures (to a mean value, determined through allowing zero point to refine with pressure in a preliminary set of refinements). The *fcc* phase stoichiometry was also fixed to that determined from refinement of the higher statistics ambient pressure data for the same sample. Phase fractions were allowed to vary with pressure, together with lattice parameters, *fcc* octahedral site U_{iso}, 18 background function terms and Gaussian and Lorentzian *fcc* profile broadening parameters (*GU*, *GW* and *LY*); no absorption correction was employed.

The sample comprised 70.61(9)% *fcc* $Rb_{0.5}Cs_{2.5}C_{60}$ at the lowest pressure (0.14 GPa) and 29.4(1)% CsC_{60}; no other phases, *e.g.* Cs_4C_{60} (found in the ambient pressure PXRD data for the same specimen), could be discerned (Fig. 3.11, top). The minority CsC_{60} was modelled with the same *Pmnn* model, as described in Section 3.3.2, over all pressures.

Although a pressure-induced phase transition has been found to take place in CsC_{60} above 3.3 GPa,[**165**] characterised by an increase in unit cell angle in the strictly $I2/m$ unit cell, we aimed to minimise the number of refinable parameters for the minority, broadened and severely overlapped CsC_{60} phase. The $Pmnn$ model provides a satisfactory fit over the pressure range; the latter study stated that their data resolution and angular range "…(did) not allow the distinction between the two structural models (orthorhombic $Pmnn$ and monoclinic $I2/m$)".[**165**]

At higher pressures, an experimental effect, which could be pressure-induced increased crystallinity, led to some deviation from a true powder average being sampled and concurrent saturated regions appearing on the detector; it must be emphasised that no evidence of symmetry breaking is evident, and that such an effect was not observed in our low-temperature high pressure structural studies of $Rb_xCs_{3-x}C_{60}$ (Section 3.3.3). Le Bail analysis for the *fcc* phase was therefore employed above 1 GPa to reliably extract the pressure-dependent unit cell volume (Fig. 3.11, bottom). The minority CsC_{60} phase was modelled with the Rietveld technique in the same fit.

The extracted pressure evolution of *fcc* $Rb_{0.5}Cs_{2.5}C_{60}$ unit cell volume at ambient temperature is presented in Fig. 3.12. As for the low-temperature $V(P)$ data presented earlier in Fig. 3.10, a small offset between high pressure and ambient pressure V is anticipated because of differences in experimental set up, and the data in Fig. 3.12 are also presented as $V(P+\Delta P)$. The compressibility shows no evidence of sharp discontinuity to 14.7 GPa; however, at the lowest pressures ($P \leq 0.5$ GPa), a gradual upturn in the compressibility is revealed. This low-pressure anomaly prevents us from using a linear fit at low pressures to best estimate a value of ΔP, so the final correction used, $\Delta P = -0.02$ GPa, was selected carefully through comparing the effects of varying ΔP for a so-called F_E-f_E plot (explained below), and selecting the ΔP providing the least anomalous curvature away from linearity, as the latter can indicate an incorrect selection of ΔP (or V_0 for an F_E-f_E plot).

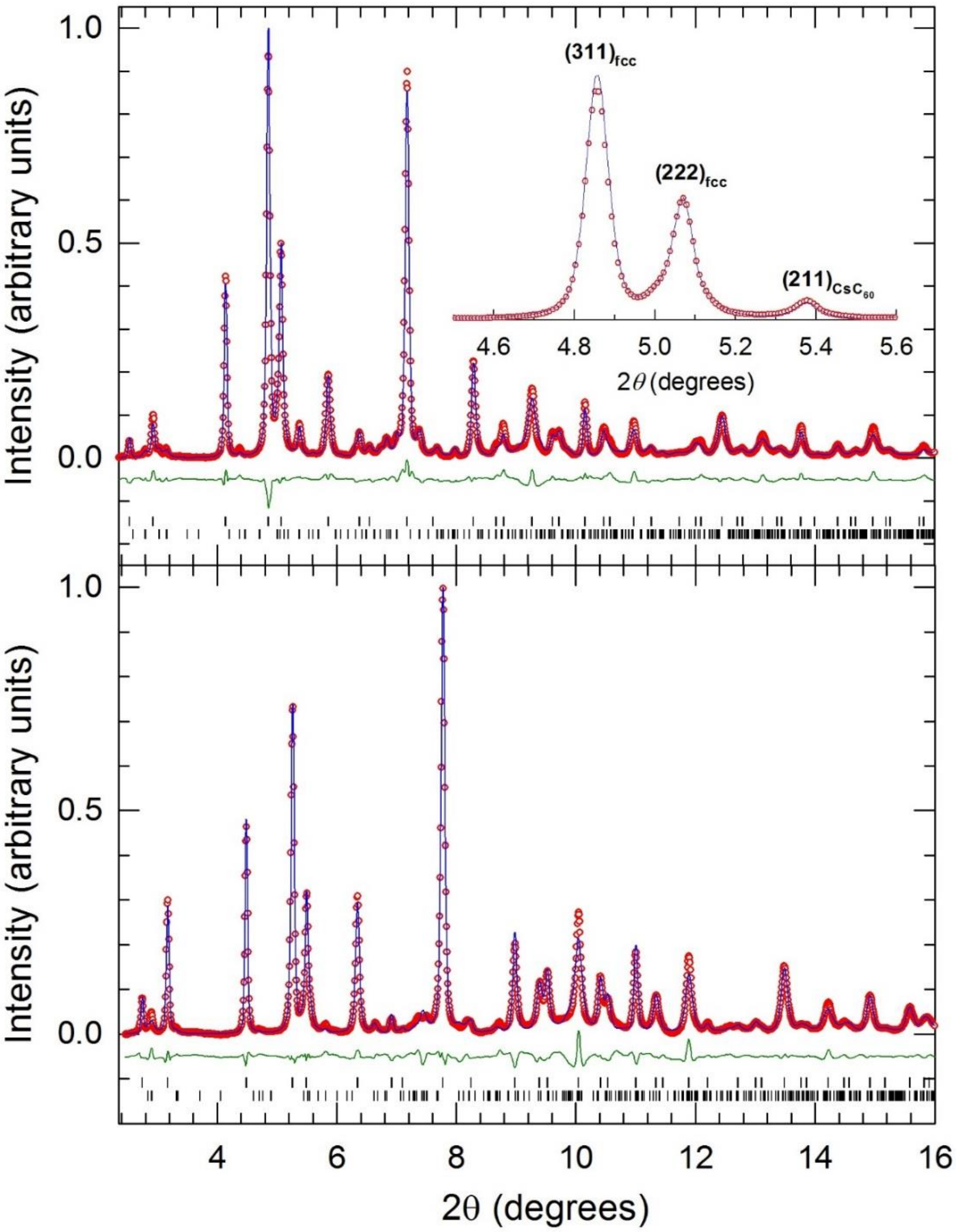

Figure 3.11: Ambient-temperature high-pressure synchrotron X-ray powder diffraction for $Rb_{0.5}Cs_{2.5}C_{60}$ (λ = 0.3738 Å). Final observed (o) and calculated (blue line) diffraction profiles at 0.14 GPa from Rietveld refinement (top) and at 12.1 GPa from Le Bail refinement (bottom). Green lines show the difference profiles, with bars representing reflection positions from *fcc* $Rb_{0.5}Cs_{2.5}C_{60}$ (upper) and CsC_{60} (lower). Inset (top): expanded region of observed and calculated profiles at 0.14 GPa.

The low-pressure anomaly is further illustrated by a least-squares fit to the data with the Birch-Murnaghan EoS (Equation 2.20, Fig. 3.12).[**128**] Data in the pressure range 0.6 - 14.7 GPa only are included in the fit to this model. A zero-pressure isothermal bulk modulus, K_0 = 15.5(3), and its pressure derivative, K'_0 = 11.2(2) are obtained; for comparison, K_0 and K_0' for the same sample at 20 K, extracted from the Murnaghan EoS model, are 21.9(3) GPa and 8.0(2) (Table 3.7). A distinct deviation between the fit and experimental volumes at low pressures is evident (Fig. 3.12, inset).

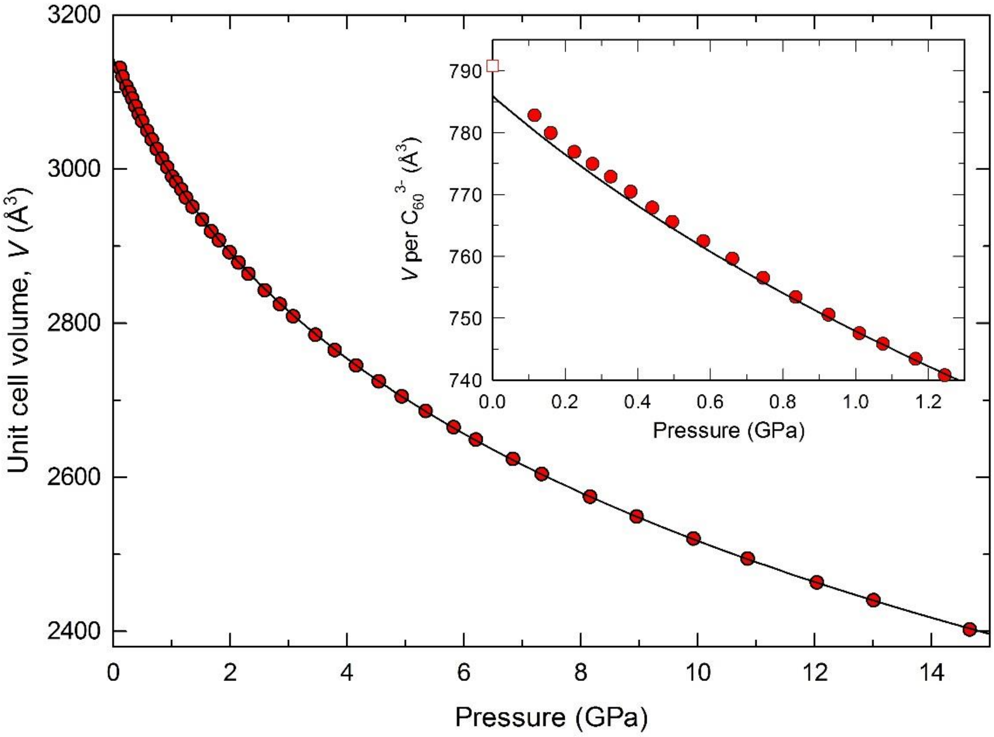

Figure 3.12: Pressure evolution of the *fcc* unit cell volume (circles), *V*, of $Rb_{0.5}Cs_{2.5}C_{60}$, at ambient temperature, up to an applied pressure of 14.7 GPa. The solid line is a fit to the third-order Birch-Murnaghan EoS in the range 0.6 to 14.7 GPa. Statistical uncertainties in *V* from structural analysis are smaller than the data point size. The extrapolated ambient pressure volume, V_0 = 3144(2) Å^3, is distinctly smaller than that measured experimentally at 300 K (3163.28(3)Å^3, Fig. 3.4). Inset: expanded view of the low-pressure data, showing V/C_{60}^{3-} as a function of *P*; the square symbol in inset represents *V* from data collected at 300 K and ambient pressure (Fig. 3.4).

Significantly, approaching ambient *P*, the *fcc* unit cell volume tends towards that measured at ambient *P* at 300 K (Fig. 3.4), corroborating these results. With a striking unit cell volume collapse clearly marking the MIT at ambient *P* (Section 3.3.3), these data indicate that an analogous volume collapse, in addition to the volume contraction expected upon applying pressure through reduction of inter-fullerene spacing, is occurring upon pressurisation alone, and that the MIT boundary may be traversed without necessitating low temperatures. The volume collapses at the pressure-induced and temperature-induced transitions in *fcc* $Rb_{0.5}Cs_{2.5}C_{60}$ are similar in magnitude (Fig. 3.13).

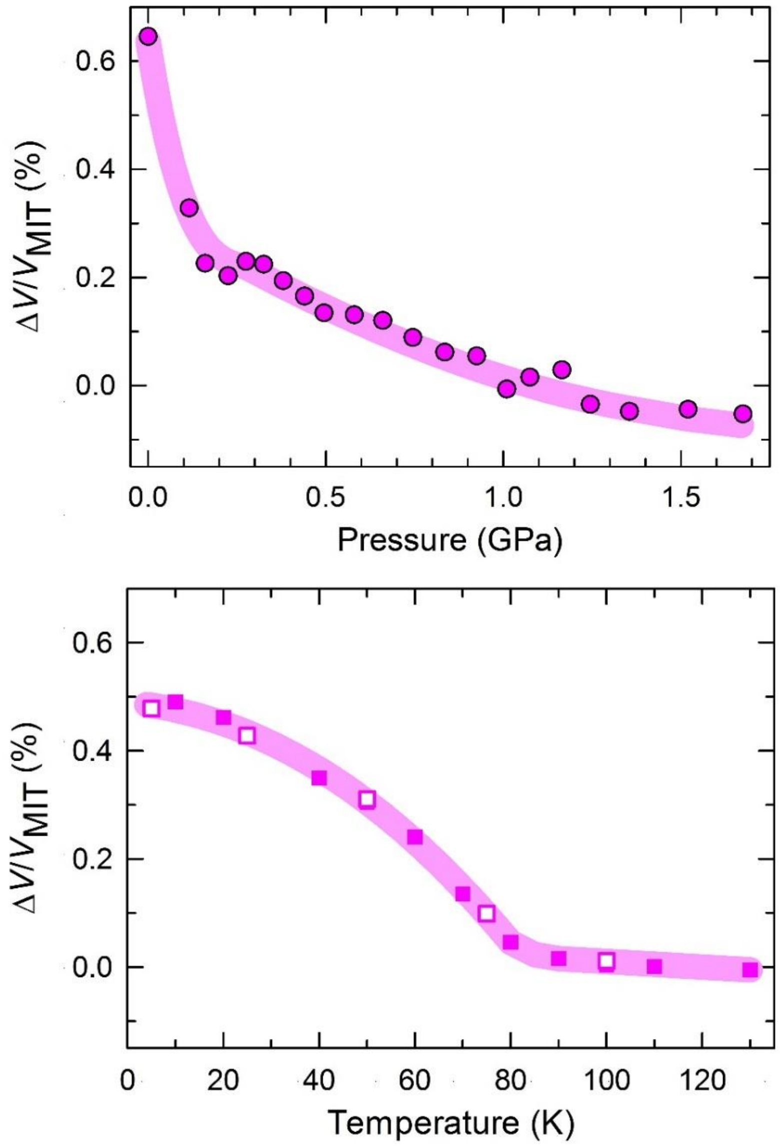

Figure 3.13: The normalised volume change, $\Delta V/V_{\mathrm{MIT}}$, for *fcc* $Rb_{0.5}Cs_{2.5}C_{60}$, as a function of pressure (upper panel) and of temperature (lower panel, Fig. 3.4 inset). ΔV represents, respectively, the difference between the unit cell volume from structural analysis and that estimated for the hypothetical low pressure metallic phase, simulated through fitting the data between 0.6 – 14.7 GPa to the Birch-Murnaghan equation (upper, fit shown in Fig. 3.12), and the difference between the unit cell volume of the hypothetical insulating phase at low temperature (simulated with a Debye model as described in Section 3.3.3) and the unit cell volume from Rietveld analysis (lower). Solid lines are guides to the eye, and statistical uncertainties in $\Delta V/V_{\mathrm{MIT}}$ from structural analysis are smaller than the data points.

A useful visual assessment of fit quality for EoS based on finite strain is provided by the so-called F_E-f_E plot, which can highlight any subtle anomaly in the volume compressibility not immediately evident in the V vs P representation. For the Birch-Murnaghan EoS, where f_E is Eulerian finite strain ($f_E = ½[(V_0/V)^{2/3} - 1]$), a normalised stress, F_E, can be defined as follows: $F_E = P/[3f_E\ (1 + 2f_E)^{5/2}]$.[**126**] In the absence of any transition, F_E should be a linear function of f_E (except in rare cases, where higher-order terms not included in the third-order EoS truncation become significant, then a parabolic curve may be observed). The F_E axis intercept is K_0, whilst, if the data are adequately described by a third-order truncation of the Birch-Murnaghan EoS, the gradient equals $\frac{3}{2}K_0(K'_0 - 4)$.[**126**]

Such analysis was undertaken for the pressure dependence of the ambient T *fcc* volume of $Rb_{0.5}Cs_{2.5}C_{60}$. The V_0 used was that obtained from the Birch-Murnaghan EoS fit depicted in Fig. 3.12, *i.e.* V_0 defined by the metallic regime. In the resulting F_E *vs* f_E plot (Fig. 3.14), a clear deviation from linearity in F_E is indeed observed below $f_E \sim 0.009$ ($P \sim 0.5$ GPa) implying the occurrence of a pressure-induced isosymmetric transition at ~765 Å^3/C_{60}^{3-}, somewhat lower in volume than the ambient P lattice volume of $Rb_{0.5}Cs_{2.5}C_{60}$ at 90 K, 779 Å^3/C_{60}^{3-}.

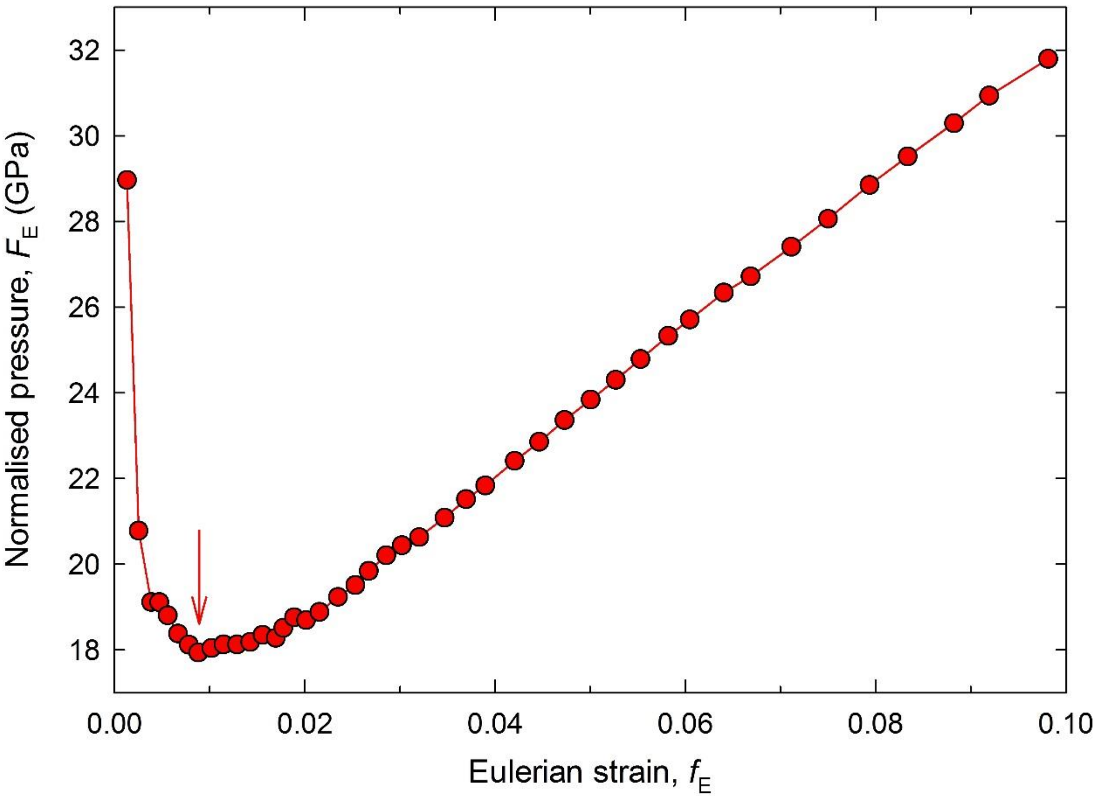

Figure 3.14: The normalised pressure, F_E *vs.* Eulerian finite strain, $f_E = ½[(V_0/V)^{2/3} - 1]$, for *fcc* $Rb_{0.5}Cs_{2.5}C_{60}$ at ambient temperature. The arrow marks the onset of a notable change in gradient, at ~765 Å^3/C_{60}^{3-}.

However, a more subtle deviation from linearity is also observed below $f_E \sim 0.017$ ($P \sim 1.0$ GPa). Whilst the precise cause is not established, even in a 'perfect' dataset from a material with no pressure-induced transitions, using a V_0 (which must be known *a-priori*) slightly away from the 'correct' value, e.g. $0.9995 \times V_0$, results in anomalous curvature at low pressures;[**126**] here, there is no 'correct' value of V_0 reflecting the entire dataset, due to the high probability of a low-pressure phase transition. We can distinguish the deviation at ~0.5 GPa as there is a clear, abrupt gradient change, as opposed to gradual curvature. The slight deviation from strict linearity at high pressure (above ~10 GPa) is anticipated, as the approximation that the second derivative of K_0 (K_0'') is zero, as assumed in the third-order Birch-Murnaghan EoS, is not strictly true.

3.3.7. Summary of structural properties at high pressures

Whilst we have established the presence of a temperature-induced MIT in overexpanded $Rb_xCs_{3-x}C_{60}$ ($0.25 \le x \le 1$), the MIT can also be traversed purely through applying external pressure, at ambient temperature (T), in *fcc* $Rb_{0.5}Cs_{2.5}C_{60}$, with interfullerene spacing the critical parameter controlling the MIT onset in these expanded cubic materials. Significantly, the unit cell volume at the transition onset, ~765 Å^3/C_{60}^{3-}, is entirely consistent with the global MIT boundary we obtain for $Rb_xCs_{3-x}C_{60}$ (in a $V(T)$ electronic phase diagram, with MIT defined from multiple structural and magnetic investigations at ambient and elevated pressures), discussed later in Section 3.4.8. Meanwhile, at low temperatures in the superconducting regime, smooth compressibility behaviour upon applying pressure is observed for *fcc* $Rb_xCs_{3-x}C_{60}$ ($0.35 \leq x \leq 2$).

3.4. Magnetic properties of $Rb_xCs_{3-x}C_{60}$ ($0.25 \leq x \leq 2$)

Ambient pressure SQUID magnetisation measurements were performed on ~20-25 mg powder samples, contained in thin-walled 5 mm-diameter Suprasil® quartz glass ampoules, sealed under a reduced pressure of He(g) (~ 400 mbar). However, larger masses (58 and 68 mg) were used for the determination of Pauli susceptibility and estimation of the density-of-states at the Fermi level for underexpanded $Rb_{1.5}Cs_{1.5}C_{60}$ and Rb_2CsC_{60}, for improved accuracy.

To investigate the superconducting properties of this series, magnetisation data were collected under ZFC and FC protocols under small applied magnetic fields of 10-20 Oe, chosen to give a sufficiently strong signal but to remain well below the H_{c1} of these materials (Section 3.4.2). Ambient pressure SQUID magnetisation measurements were also undertaken at high applied fields, with samples prepared exactly as described above. Data were collected at temperatures between 1.8 K and 300 K, at 3 T and at 5 T, under field-cooled (FC) protocols. The field-dependence of magnetisation in the normal and superconducting states was investigated through ramping the applied field between 0 and 5 T, with samples held at 295 K and at 5 K.

Magnetisation measurements at elevated pressures were also performed on ~20-25 mg samples of *fcc*-rich $Rb_xCs_{3-x}C_{60}$ ($0.35 \leq x \leq 2$), as a function of temperature. The experimental setup, employing an EasyLab MCell 10 high pressure cell, was described in detail in Section 2.5.6. Data were collected at temperatures between 1.8-50 K, under applied fields of 20 Oe and with ZFC protocols, at pressures between ~0.3-10.5 kbar. Additional magnetic susceptibility measurements at elevated pressures were undertaken for $Rb_{0.5}Cs_{2.5}C_{60}$ (26 mg specimen). Data were collected at temperatures between 30-300 K, at 3 T and at 5 T under FC protocols, at pressures of 0.54 kbar and 1.64 kbar.

3.4.1. Ambient pressure, low-field magnetisation measurements

The temperature dependence of magnetisation, $M(T)$ for $Rb_xCs_{3-x}C_{60}$ ($0.25 \leq x \leq 2$), collected under a ZFC protocol, is overplotted for all samples in Fig. 3.15., whilst Fig. 3.16 displays $M(T)$ collected under both ZFC and FC protocols for several individual compositions. Diamagnetic shielding is evident below ~26-33 K in the ZFC data, signalling the onset of bulk superconductivity. No kink in $M(T)$ below T_c in the ZFC and FC data, attributed to granular shielding and observed in previous low field magnetisation measurements of A_3C_{60},[**31, 161**] is seen in this data, indicative of the high sample quality. The small FC signal magnitude, close to the zero magnetisation line, indicates that pinning in the samples is extremely strong, with virtually no magnetic field expulsion (*i.e.* vortex lines are fixed by crystal structure defects). Shielding fractions have been estimated from ZFC measurements, but a quantitative evaluation of superconducting fractions would be difficult, as the field inside the superconducting fraction must be corrected for the demagnetisation effect. In practice this would be difficult for these samples, with irregular particle shapes, and therefore not undertaken.

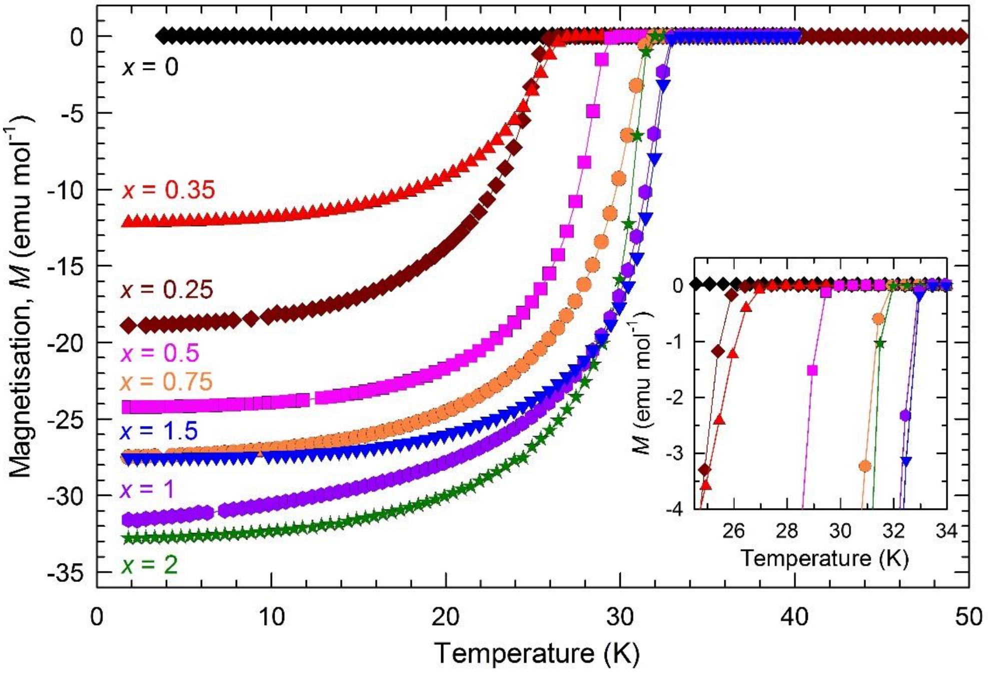

Figure 3.15: Temperature dependence of the magnetisation, M (ZFC protocol), for *fcc*-rich $Rb_xCs_{3-x}C_{60}$ ($0.25 \leq x \leq 2$), divided by the applied measurement field (10 Oe for $x = 0.25$, 20 Oe for other samples). For $x = 1.5$ and 2, data are for samples II and III, respectively.

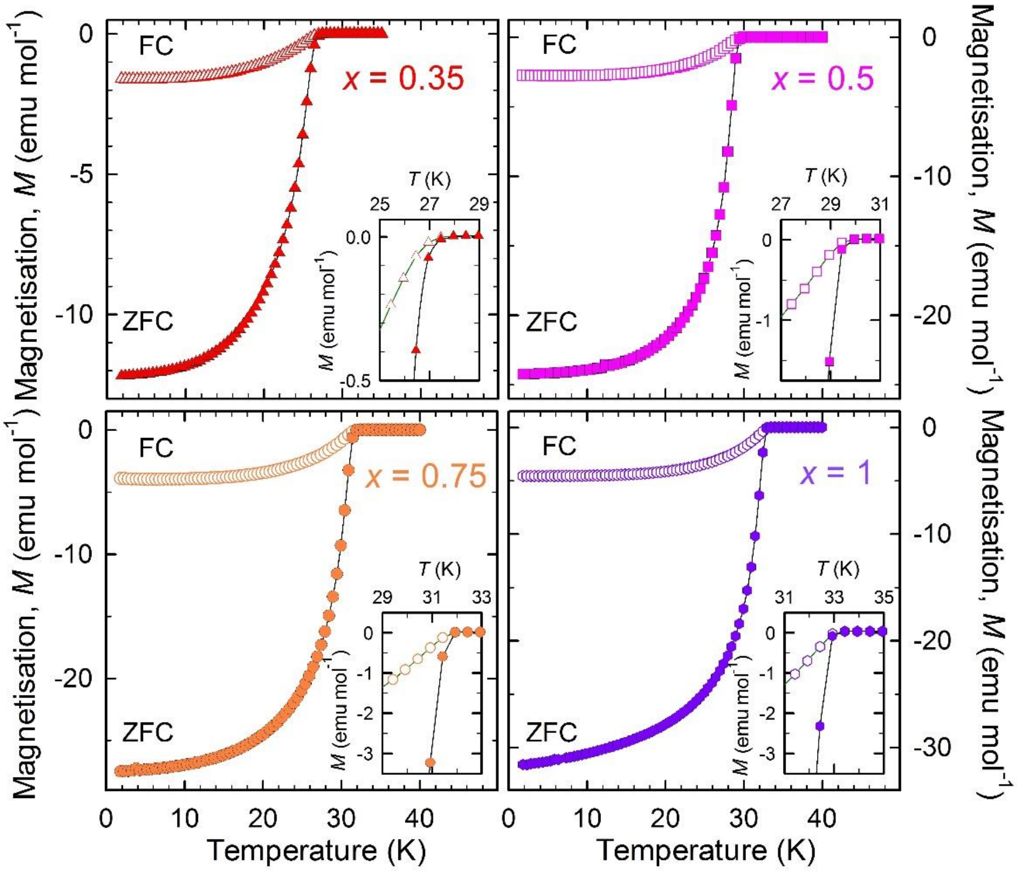

Figure 3.16: Temperature evolution of magnetisation, M (ZFC and FC protocols, divided by the applied measurement field of 20 Oe) for *fcc*-rich $Rb_xCs_{3-x}C_{60}$ ($0.35 \le x \le 1$). Insets show expanded regions near the superconducting T_c.

Estimated shielding fractions range from 32-91 %, for $x = 0.35$ and $x = 2$ respectively. The T_c values and estimated shielding fractions are collected in Table 3.8. Previous studies of *fcc*-rich $Rb_xCs_{3-x}C_{60}$ synthesised using liquid ammonia solution techniques, reported shielding fractions from ZFC magnetisation measurements of 25-60 % ($0.32 \le x \le 1$ [**31**]) and 3-20 % ($x = 0.25, 0.5$ [**71**]). These results indicate that, in contrast to the consensus existing prior to this work, solid-state annealing techniques can be used to synthesise high-quality overexpanded A_3C_{60} materials close to the Mott insulator boundary, with high *fcc* phase content and shielding fractions at least as high as equivalent studies using solution techniques. The superconducting transitions in the present study are also sharper in breadth than those reported earlier in refs. [**31**] and [**71**].

Table 3.8: Superconducting transition temperatures (T_c) and estimated shielding fractions (SF) at ambient pressure for *fcc* $Rb_xCs_{3-x}C_{60}$ ($0.25 \leq x \leq 2$).

Nominal x_{Rb}	T_c (K)	SF (%)
0.25	25.9	50
0.35	26.9	32
0.5	29.4	64
0.75	31.6	74
1	32.9	85

Nominal x_{Rb}	T_c (K)	SF (%)
1.5 (sample I)	32.7	45
1.5 (sample II)	32.8	75
2 (sample I)	31.7	37
2 (sample II)	31.8	72
2 (sample III)	31.8	91

The ambient pressure T_c values of all samples in the study, derived from the first point of deviation of the ZFC and FC datasets, are plotted as functions of unit cell volume and nominal Rb_x in Fig. 1.9. The $T_c(V)$ and $T_c(x)$ form distinct 'dome' shapes, reminiscent of the pressure-induced $T_c(V)$ behaviour in both superconducting Cs_3C_{60} polymorphs,[**140**] and in contrast to the monotonic increase in T_c with V observed in the underexpanded A_3C_{60} materials. Whilst the decreasing T_c with V observed in highly expanded $A_xCs_{3-x}C_{60}$ was reported earlier,[**31, 71**] this work is the first to systematically and extensively characterise a wide range of compositions, from underexpanded metallic Rb_2CsC_{60} through to $Rb_{0.25}Cs_{2.75}C_{60}$, close to the Mott insulator boundary. The *fcc* phase stoichiometry here was finely and reliably controlled through varying the Rb/Cs ratio in the reaction mixture; several samples with the same nominal stoichiometry (x = 1.5, 2) have very consistent *fcc* volumes and ambient pressure T_c values (Fig. 1.9).

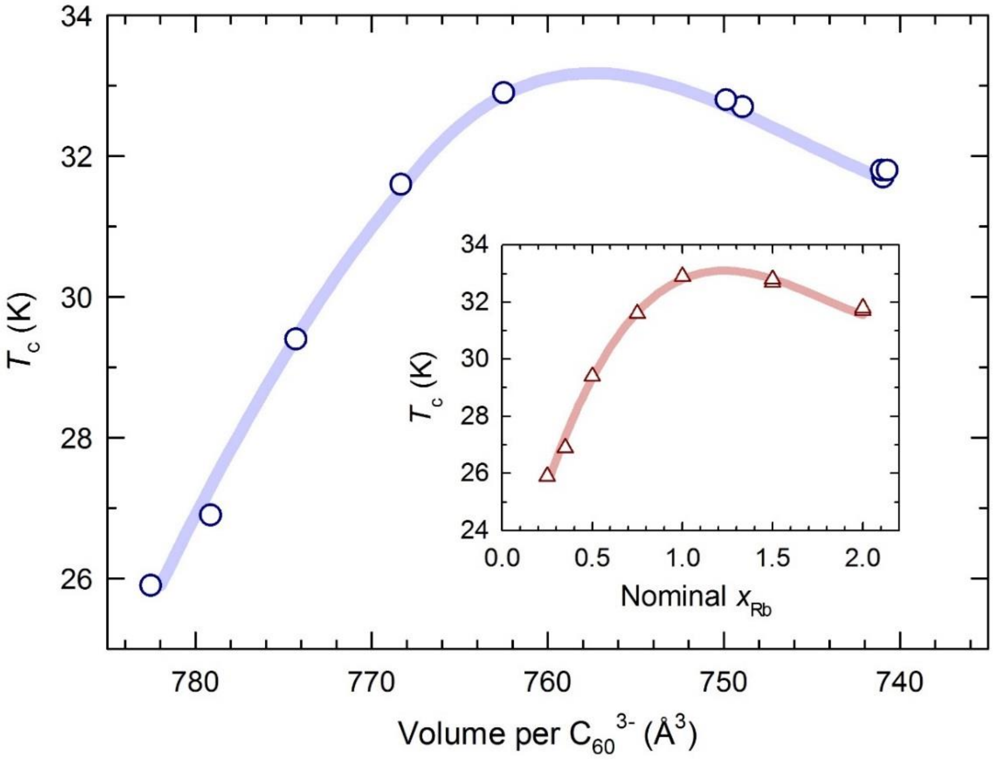

Figure 3.17: The dependence of superconducting T_c at ambient pressure on *fcc* unit cell volume at $T = T_c$ for *fcc*-rich $Rb_xCs_{3-x}C_{60}$ ($0.25 \leq x \leq 2$). Best estimates for unit cell volume at T_c are obtained through extrapolation of the values obtained by Rietveld analysis of data collected at low temperature (Section 3.3.3). The inset shows how T_c varies as a function of nominal x. Solid lines are guides-to-the-eye.

3.4.2. Ambient pressure $M(H)$ in the superconducting state

Measurements of the lower critical field, H_{c1}, are important in characterising superconductors, as this quantity is directly related to the the coherence length ξ and penetration depth λ, from Ginzburg-Landau theory. Previous measurements of H_{c1} in the overexpanded *fcc* $Rb_xCs_{3-x}C_{60}$ systems are few; estimates of H_{c1} (0 K) include 55-81 Oe in $RbCs_2C_{60}$ [**51**] and 75 Oe for $Rb_{0.32}Cs_{2.68}C_{60}$ [**31**]. These studies estimated H_{c1} as the field at which a deviation from linearity in $M(H)$, measured in the superconducting regime, first appears; this definition method, and others, have been evaluated *e.g.* by Buntar and Weber [**166**]. The value of H_{c1} (0 K) may then be estimated as follows: $H_{c1}(T) = H_{c1}\,(0\ \mathrm{K})\,[1 - (T/T_c)^2]$. However, some non-linearity in $M(H)$ behaviour at fields even below H_{c1} has been reported in A_3C_{60} materials, attributed to intergranular flux penetration and the large penetration depth being close to the average grain size, leading to flux penetration and pinning at fields below H_{c1}.[**51**]

The field-dependent magnetisation has been measured at 5 K for two *fcc*-rich $Rb_xCs_{3-x}C_{60}$ samples, towards the overexpanded and underexpanded limits of the compositions studied (x = 0.35, 2), at applied fields between 20-2000 Oe (Fig. 3.18). For better visual comparison between the samples and to highlight the onset of deviation from linearity upon increasing the applied field, magnetisation has also been plotted as $\Delta M = M_{\text{linear}} - M_{\text{exp}}$ (Fig. 3.19); M_{linear} is the calculated magnetisation at each applied field from a least-squares linear fit to $M(H)$ at low fields (~20-140 Oe), and M_{exp} is the measured magnetisation, with no corrections made.

Although some non-linearity indeed perisists down to low fields in the $M(H)$ trends, H_{c1} (5 K) for x = 0.35, 2 can be estimated as 100-120 Oe and 120-140 Oe, respectively. For comparison, literature values of H_{c1} at 5 K from the $M(H)$ deviation method were ~50 Oe and ~170 Oe, for x = 0.32 and x = 1 respectively;[**31, 51**] these are consistent in magnitude with the data presented here and suggest the same qualitative trend in decreased H_{c1} (5 K) in more expanded *fcc* $Rb_xCs_{3-x}C_{60}$ compositions.

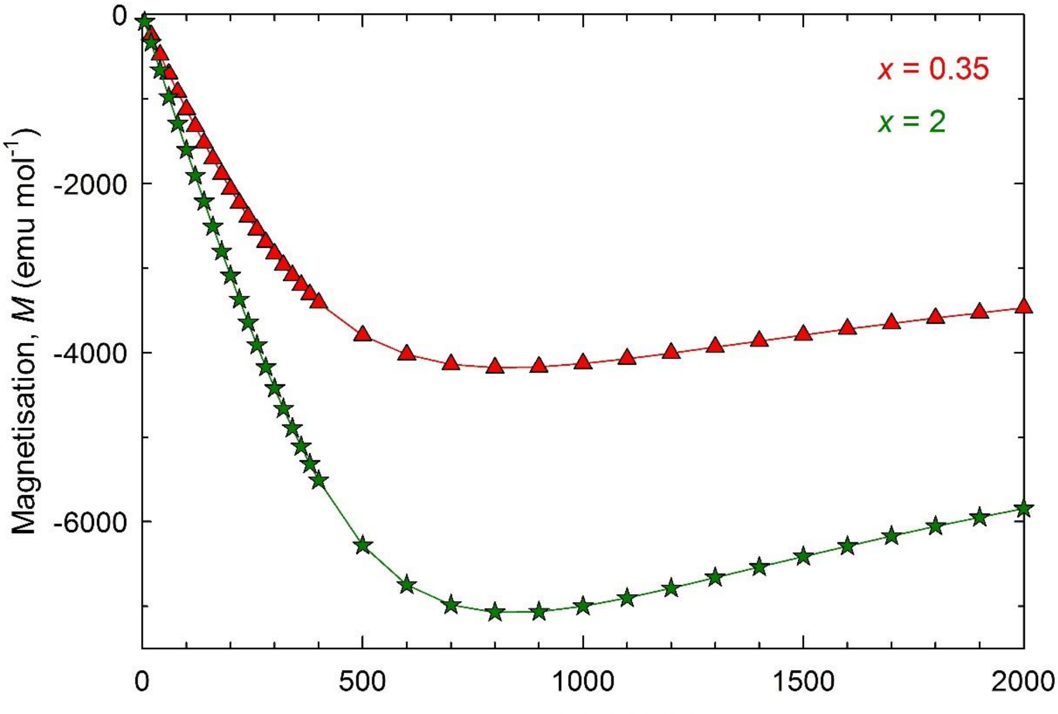

Figure 3.18: The variation of magnetisation, M, with applied field, H, at 5 K, for $Rb_{0.35}Cs_{2.65}C_{60}$ and Rb_2CsC_{60} sample I (*fcc* phase fractions are 76.48(7) % and 91.71(2) %, respectively).

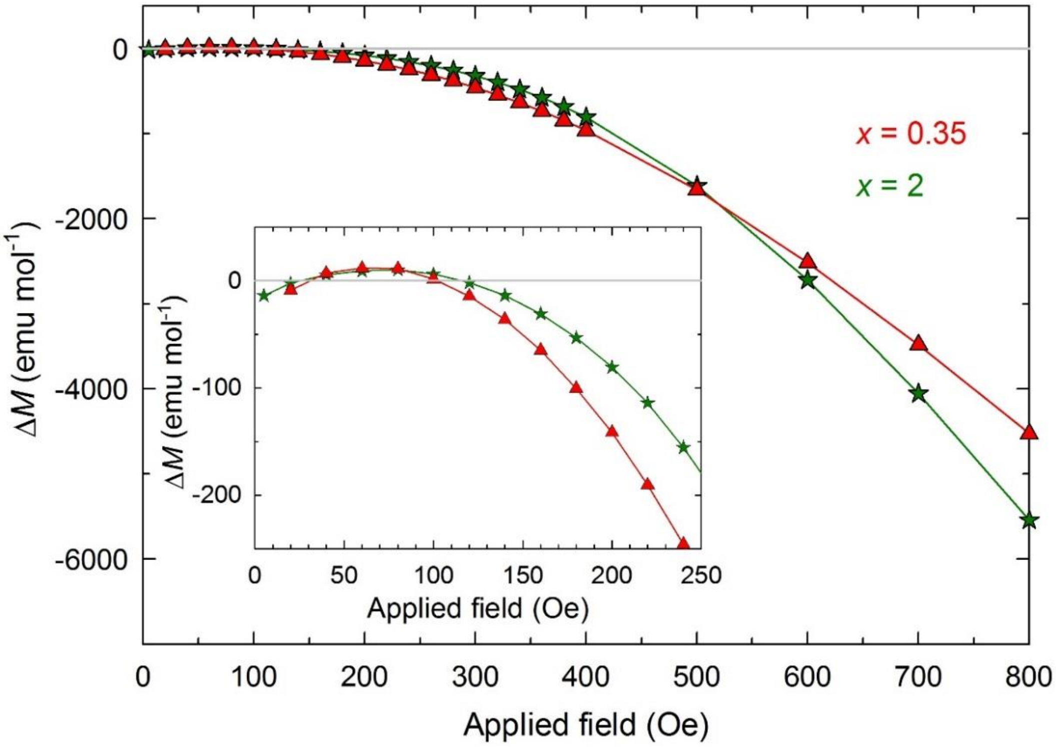

Figure 3.19: The variation of ΔM with applied field, H, at 5 K, for $Rb_{0.35}Cs_{2.65}C_{60}$ and Rb_2CsC_{60} sample I (*fcc* phase fractions are 76.48(7) % and 91.71(2) %, respectively), where $\Delta M = M_{\text{linear}} - M_{\text{exp}}$ (M_{linear} is the calculated magnetisation at each applied field from a least-squares linear fit to $M(H)$ at low fields, i.e. ~20-140 Oe, and M_{exp} is the measured magnetisation).

3.4.3. Ambient pressure, high-field magnetic susceptibility measurements

The temperature dependence of the magnetic susceptibility, $\chi(T)$ for several $Rb_xCs_{3-x}C_{60}$ ($0.25 \leq x \leq 1$) samples is shown in Fig. 3.20. For comparison, representative data for *fcc*-rich Cs_3C_{60} are also included, with data collection undertaken in the same manner as for the Rb-containing series. These data, taken from [**140**], are plotted as $\chi(5\text{T} - 3\text{T}) - \chi_{\text{core}}$, and further sample characterisation is detailed therein (sample 5, 86.71(1) % *fcc* phase fraction).

The $\chi(T)$ was obtained from the difference of values collected at 5T and 3T in field-cooled protocols, to subtract out the contribution of ferromagnetic impurities (χ_{FM}), and is hereafter termed $\chi(5\text{T} - 3\text{T})$. These fields were selected as the magnetisation of any ferromagnetic impurities is experimentally found to saturate at applied fields of H << 3T, and 5T was the highest experimentally available applied field. Further corrections, detailed below, were then undertaken to $\chi(5\text{T} - 3\text{T})$ to subtract the core diamagnetic susceptibility and small impurity contributions (*e.g.* from minor phases).

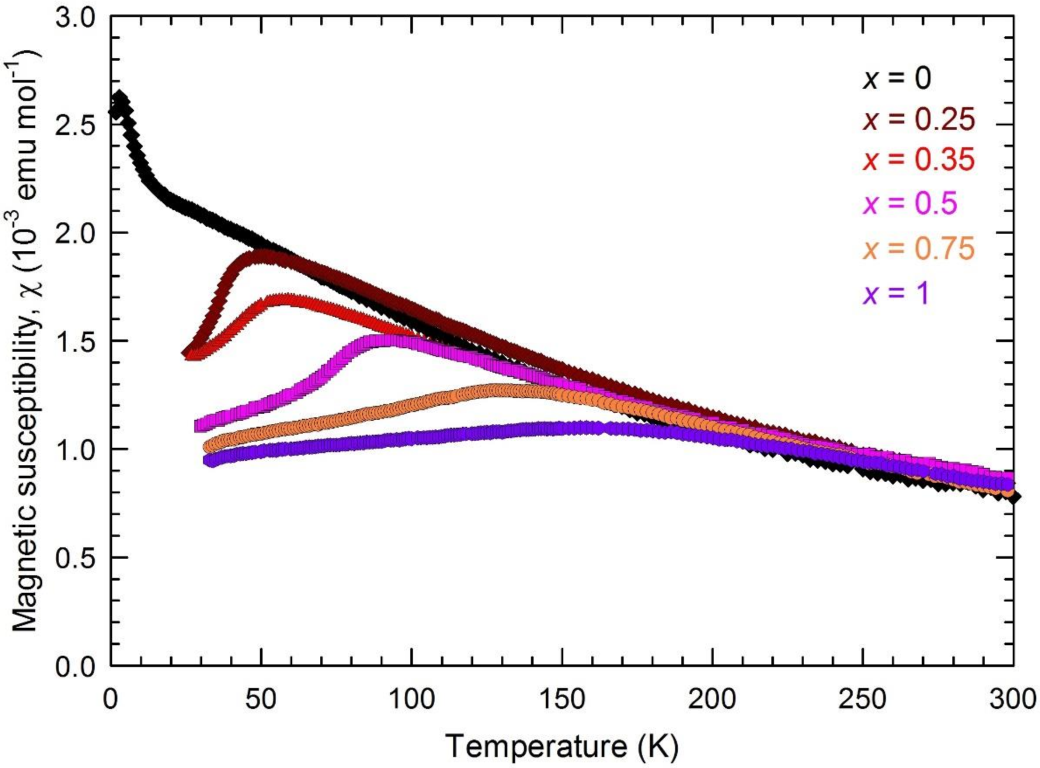

Figure 3.20: Temperature dependence of the magnetic susceptibility, $\chi(T)$, of several *fcc*-rich compositions $Rb_xCs_{3-x}C_{60}$ ($0 \leq x \leq 1$).

Whilst the parent material *fcc* Cs_3C_{60} is insulating to low temperatures, we see distinctly different behaviour emerging upon 'chemically pressurising' via Rb substitution into the *fcc* phase, illustrated in the $\chi(T)$ trends. At high temperatures, the $\chi(T)$ behaviour of the $Rb_xCs_{3-x}C_{60}$ ($0 \leq x \leq 1$) materials can be well described by the Curie-Weiss law. Firstly, a correction for the core diamagnetic susceptibility of $Rb_xCs_{3-x}C_{60}$, χ_{core}, has been subtracted from the data, which was estimated using literature values for pristine C_{60} (-2.43×10^{-4} emu mol^{-1}),**[167]** Rb^+ and Cs^+ (-22.5×10^{-6} and -35.0×10^{-6}, respectively).[**168**]

For each sample, a least-squares fit using the Curie-Weiss law to the quantity $[\,\chi(5\text{T} - 3\text{T}) - \chi_{\text{core}}\,]$, with a temperature-independent contribution included, has next been undertaken using the following form:

$$\chi(5\mathrm{T}-3\mathrm{T})-\chi_{\mathrm{core}}=\frac{C}{T-\Theta}+\chi_0,$$ **Equation 3.1**

where C is the Curie constant, T corresponds to temperature, Θ stands for the Weiss temperature, and χ_0 signifies a term representing impurity contributions to the susceptibility which are effectively temperature-independent. The refinable term χ_0 should comprise contributions to the magnetic susceptibility from any minor impurity phases, (*e.g.* non-magnetic Cs_4C_{60}), approximated here as temperature-independent.

The refined parameters from the Curie-Weiss fits are presented in Table 3.9. The term χ_0 was not refined in certain cases; for $Rb_{0.25}Cs_{2.75}C_{60}$, χ_0 was small and poorly defined, with an excellent fit achievable omitting this term. For samples with x = 0.75 and 1, relatively small temperature ranges were available for fitting in the insulating regime; therefore, χ_0 were fixed in the final fits to best refined values obtained from earlier fit iterations (where two of the three variables were refined in turn, starting from fixed C from *fcc* Cs_3C_{60}). The effective magnetic moment, μ_{eff}, is estimated as follows:

$$\mu_{\mathrm{eff}}=\mu_{\mathrm{B}}\sqrt{8C_{\mathrm{mol}}},$$ **Equation 3.2**

with μ_B representing the Bohr magneton.

Table 3.9: Results of Curie-Weiss fits to $Rb_xCs_{3-x}C_{60}$ ($0.25 \leq x \leq 1$) in the insulating regime.

Nominal x_{Rb}	T range (K)	χ_0 (emu mol^{-1})	C (emu K mol^{-1})	μ_{eff} (μ_B/C_{60}^{3-})	Θ (K)
0.25	170-270	0	0.338(1)	1.645(3)	−95(1)
0.35	150-300	$-0.5(3)\times10^{-4}$	0.39(2)	1.77(5)	−156(11)
0.5	170-280	$-1.9(7)\times10^{-4}$	0.39(5)	1.8(1)	−151(23)
0.75	200-260	2.0×10^{-4}	0.334(3)	1.633(7)	−103(3)
1	240-300	-0.2×10^{-4}	0.348(4)	1.67(1)	−118(5)

At high temperatures, the fits to $\chi(T)$ of $Rb_xCs_{3-x}C_{60}$ ($0.25 \leq x \leq 1$) indicate negative Weiss temperatures (approx. −95 to −160 K) and effective magnetic moments per C_{60}^{3-} (~1.6-1.8 μ_B) comparable to those in *fcc* Cs_3C_{60}, where Θ = −105(2) K and μ_{eff} = 1.614(4) μ_B;[140] this suggests that, at high temperatures, overexpanded

$Rb_xCs_{3-x}C_{60}$ (0.25 ≤ *x* ≤ 1) also assume *S* = ½ localised electron ground states, with strong antiferromagnetic correlations. The theoretical total spin magnetic moment for a single electron with *S* = ½ is ~1.73 μ_B. It follows that C_{60}^{3-} in insulating overexpanded $Rb_xCs_{3-x}C_{60}$ (0.25 ≤ *x* ≤ 1), like *fcc* Cs_3C_{60}, exhibits medium-strength JT coupling; in the absence of JT coupling, the lowest energy state for three electrons in t_{1u} orbitals in a cubic field takes *S* = 3/2.[**76**]

Prior to plotting in Fig. 3.20, the refined χ_0 was subtracted from the susceptibility, so that the plotted susceptibility should best correspond to the Curie-Weiss paramagnetic susceptibility of the *fcc* phase only. The final susceptibility plotted in Fig. 3.20 as a function of temperature, therefore, is [$\chi(5T - 3T) - \chi_{core} - \chi_0$]. The overlap in the high temperature data is striking, underlining the similarity between *fcc* Cs_3C_{60} and *fcc* $Rb_xCs_{3-x}C_{60}$ (0.25 ≤ *x* ≤ 1) in this temperature range.

However, in stark contrast to *fcc* Cs_3C_{60}, the $\chi(T)$ data of $Rb_xCs_{3-x}C_{60}$ (0.25 ≤ *x* ≤ 1) display well-defined cusps on cooling; below a certain temperature, χ decreases with temperature, in contrast to the higher temperature behaviour. Furthermore, the maximum temperature at the cusp, T_{max}, increases with increasing *x* (Table 3.10), and the cusps gradually broaden. The values of T_{max} coincide well with those temperatures at which the collapse in unit cell volume is observed by PXRD, well above the onset of superconductivity.

Table 3.10: The maxima of cusps in the temperature-dependent magnetic susceptibility of overexpanded *fcc*-rich $Rb_xCs_{3-x}C_{60}$ (0.25 ≤ *x* ≤ 1). Precise T_{max} values are defined as the intersection of two linear fits to data directly above and below the approximate maximum point; unit cell volumes at T_{max} are estimated from extrapolation of variable temperature PXRD data (Fig. 3.4).

Nominal Rb_x	T_{max} from magnetic susceptibility (K)	Unit cell volume per C_{60} at T_{max} (Å^3)
0.25	44.2	782.8
0.35	54.7	781.9
0.5	87.8	779.1
0.75	138.3	775.4
1	170.0	770.7

These data suggest that both the susceptibility cusps and the accompanying isosymmetric lattice collapse, with onset temperatures increasing as more Rb is substituted into the *fcc* phase, signify insulator-to-metal transitions, induced through temperature- and substitution-induced lattice contraction effects; the $T_{\max}$ at ambient pressure may be tuned through fine adjustment of the sample stoichiometry.

3.4.4. Susceptibility and density-of-states at the Fermi level in underexpanded $Rb_xCs_{3-x}C_{60}$ (x = 1.5, 2)

In a paramagnetic metal, the Pauli spin susceptibility, χ_P is temperature-independent and proportional to the bare density of states at the Fermi level, $N_{\varepsilon F}$ (*i.e.* in the absence of enhancement through spin fluctuations, neglecting many body effects). The latter quantity can then be estimated from χ_P as follows:

$$\chi_P = 2\mu_B^2 N_{\varepsilon_F}.$$

Equation 3.3

The $\chi(T)$ for two underexpanded $Rb_xCs_{3-x}C_{60}$ compositions (x = 1.5, 2) is presented in Fig. 3.21. The two samples used to collect this data, designated samples II (x = 1.5) and III (x = 2), had *fcc* phase fractions of 93.98(2) % (x = 1.5) and 99.137(2) % (x = 2). The data are already corrected to best subtract χ_{FM} and χ_{core} as detailed in Section 3.4.3; here, therefore, $\chi(T)$ should approximate χ_P well. From previous magnetic susceptibility measurements, the orbital contribution of the conduction electrons to the diamagnetic susceptibility is reportedly quenched in K_3C_{60} and Rb_3C_{60},**[159, 167]** from Landau diamagnetic quenching by molecular rotational disorder; therefore, no χ_{Landau} correction should be required to obtain accurate values of the paramagnetic $\chi(T)$. The exact values of χ_{core} subtracted from the data shown are -3.29×10^{-4} emu mol^{-1} and -3.23×10^{-4} emu mol^{-1}, for x = 1.5 and x = 2 respectively. It is not possible to calculate any χ_0 contribution here as was done for the more expanded compositions, as its temperature-independence does not allow it to be decoupled from the Pauli spin susceptibility.

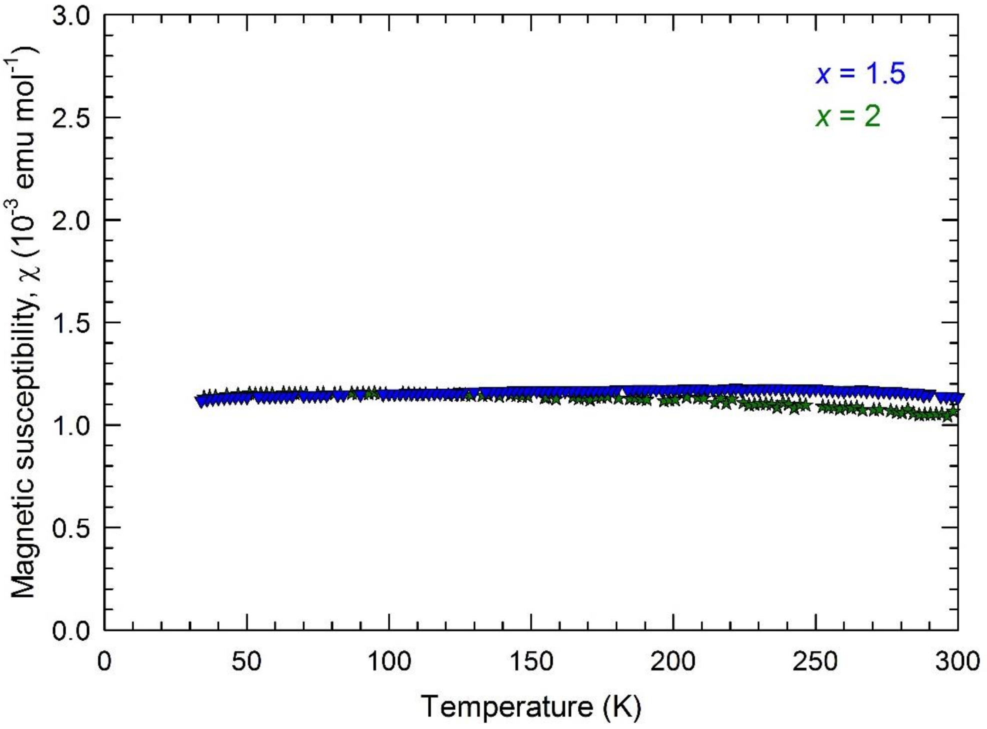

Figure 3.21: Temperature dependence of the magnetic susceptibility, $\chi(T)$, of *fcc*-rich underexpanded $Rb_{1.5}Cs_{1.5}C_{60}$ and Rb_2CsC_{60} (samples II and III, respectively). The scale and range of both axes have been fixed to those, for comparative purposes, from the plot displaying analogous data from overexpanded $Rb_xCs_{3-x}C_{60}$ (Fig. 3.20). However, in these data (x = 1.5, 2), no χ_0 correction could be subtracted.

The trend in χ_P is observed to be broadly temperature-independent in these two materials, which signifies that, in the temperature range investigated, there is a metallic ground state with a Fermi-liquid-like low-energy excitation, consistent with a single temperature-independent Pauli susceptibility term. The broad cusp visible in the $\chi(T)$ of $RbCs_2C_{60}$ is no longer visible for either $Rb_{1.5}Cs_{1.5}C_{60}$ or Rb_2CsC_{60}. A relatively small increase in the Pauli spin susceptibility, χ_p, is, however, observed with decreasing temperature for underexpanded Rb_2CsC_{60}; this is qualitatively consistent with literature magnetic susceptibility data for K_3C_{60} and Rb_3C_{60}.[**167, 169, 170**] This effect was ascribed to the influence of ferro-like magnetic susceptibilities, remaining even after correction by subtraction of values collected at different fields; such ferromagnetic signals would be enhanced at low temperatures.

Another effect resulting in some variation in χ_p with temperature is thermal expansion. The expansivities of the A_3C_{60} phases are relatively large, around twice that of pristine C_{60} at ambient temperature,[**161, 171**] even though the intermolecular potential of undoped C_{60} from compressibility studies is softer; this has been tentatively attributed to highly anharmonic alkali metal-C_{60} interactions.[**161**] Consequently, $N_{\varepsilon F}$, correlated with the unit cell volume, will have a substantial temperature dependence, in contrast to the expected behaviour for a standard Pauli susceptibility. A decrease in $N_{\varepsilon F}$ of 6-8 %, from thermal contraction between ambient temperature and T_c, has been calculated for A_3C_{60} (A = K, Rb).[**161**] As $N_{\varepsilon F}$ is directly related to χ_p, a corresponding decrease in χ_p with temperature would be anticipated, and indeed observed in EPR measurements for A_3C_{60} (A = K, Rb).[**172**] Whilst the effect of the ferro-like magnetic susceptibilities described above was dominant in SQUID magnetisation data, in EPR, the absence of ferro-like behaviour was attributed to strong electron spin-spin correlations of ferro spins, leading to relaxation times too short to be observed in EPR.[**172**]

In order to most accurately determine susceptibility in the metallic regime for these underexpanded compositions, and estimate $N_{\varepsilon F}$, the field dependence of magnetisation has been measured. Susceptibility is extracted in each case through a linear fit, as the gradient of the $M(H)$ data at higher fields, where the ferromagnetic impurity contribution is fully saturated. This also allows the residual magnetisation at zero applied field to be determined, one way of comparing the relative ferromagnetic impurity contribution to susceptibility between different samples. This is illustrated for the Rb_2CsC_{60} sample in Fig. 3.22. These measurements were also repeated four times for each composition, at T = 295 K, to extract χ as the average from individual measurements.

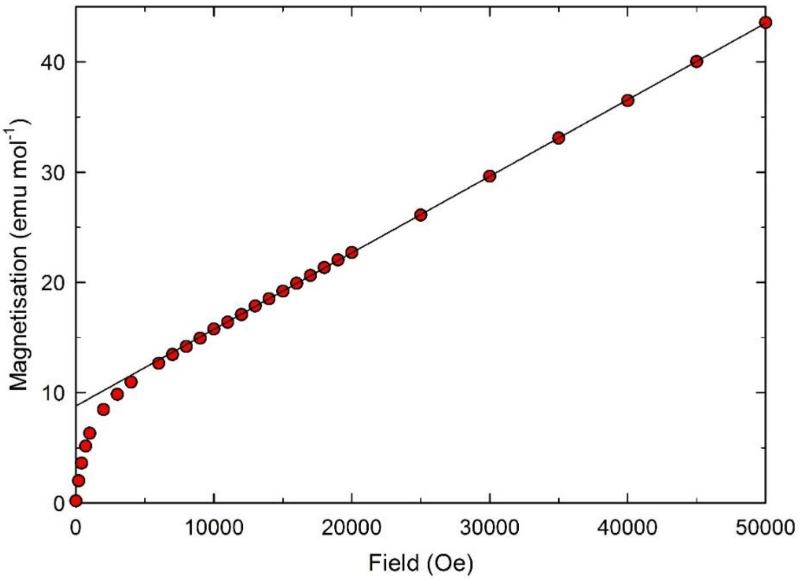

Figure 3.22: The field dependence of magnetisation at 295 K for Rb_2CsC_{60} (57.8 mg, sample III). The straight line is a least-squares fit to the following form: $M = \chi H + M(0\ \mathrm{Oe})$, fitting data between $1\ \mathrm{T} \leq H \leq 5\ \mathrm{T}$. This representative measurement is one of four averaged to best estimate $N_{\varepsilon F}$(295 K); the refined parameters are $\chi = 0.6944(8) \times 10^{-3}$ emu mol^{-1} (prior to correction for χ_{core}) and M(0 Oe) = 8.80(2) emu mol^{-1}.

For Rb_2CsC_{60}, unambiguously metallic throughout the temperature range in Fig. 3.21, the average value of $\chi - \chi_{core}$ (295 K) from four $M(H)$ measurements is 1.02×10^{-3} emu mol^{-1}. Using Equation 3.3, $N_{\varepsilon F}$(295 K) for Rb_2CsC_{60} is ~15.8 states eV^{-1} C_{60}^{-1}. For the more expanded $Rb_{1.5}Cs_{1.5}C_{60}$, the analogous $\chi - \chi_{core}$ (295 K) is 1.00×10^{-3} emu mol^{-1}, yielding a $N_{\varepsilon F}$(295 K) of ~15.4 states eV^{-1} C_{60}^{-1}. However, this composition is not unambiguously metallic at 295 K; upon closer examination of the data shape there may be a weak signature of the MIT, observed clearly in all more expanded compositions, at ~260-280 K. The measured $\chi - \chi_{core}$ at 250 K, more clearly in the metallic regime, is 1.06×10^{-3} emu mol^{-1}, translating to $N_{\varepsilon F}$(250 K) ~ 16.4 states eV^{-1} C_{60}^{-1}. In summary, defined at either temperature, the $N_{\varepsilon F}$ for $Rb_{1.5}Cs_{1.5}C_{60}$ and Rb_2CsC_{60}, is around ~16 states eV^{-1} C_{60}^{-1} and effectively identical in magnitude.

The $N_{\varepsilon F}$ values obtained for $Rb_xCs_{3-x}C_{60}$ (x = 1.5, 2) of ~16 states eV^{-1} C_{60}^{-1} are comparable in magnitude to $N_{\varepsilon F}$ values reported for Rb_3C_{60} at ambient temperature, from magnetic susceptibility measurements (18-20 states eV^{-1} C_{60}^{-1}).[**159, 172**] However, the expected trend based on the more expanded unit cell volume in the present samples would be an increase in $N_{\varepsilon F}$ with respect to Rb_3C_{60}. It is likely, though, that the present samples contain lower levels of ferro-like magnetic susceptibilities than samples in the cited studies, yielding significantly less variation in magnitude of $\chi(T)$; between 75 K and 300 K, χ in the present Rb_2CsC_{60} data varies by 1.1×10^{-4} emu mol^{-1}, compared to ~7.5×10^{-4} emu mol^{-1} in the Rb_3C_{60} data in reference [**172**]. Moreover, the aforementioned $\chi_{core}(C_{60})$ value used for correction, a literature value for pristine C_{60} (-2.43×10^{-4} emu mol^{-1}), is likely to be less negative than the true value for C_{60}^{3-} given that $\chi_{core}(C_{60}^{6-})$ is reportedly ~-5.9×10^{-4} emu mol^{-1}.[**173**] This approximation was made as experimental determination of $\chi_{core}(C_{60}^{3-})$, with these systems being metallic or Curie-Weiss paramagnets, is not trivial; however, resulting values of $N_{\varepsilon F}$ could be underestimated by ~10-15 %.

Theoretical calculations of $N_{\varepsilon F}$ using density functional theory have yielded 8.1 states eV^{-1} C_{60}^{-1} for Rb_3C_{60} and ~10 states eV^{-1} C_{60}^{-1} for fcc Cs_3C_{60},[**87, 174**] although various theoretical techniques have been employed and, more generally, theoretical estimates of $N_{\varepsilon F}$ for A_3C_{60} have typically ranged from ~7–13 states eV^{-1} C_{60}^{-1}.[**22**] Although these are lower than the present $N_{\varepsilon F}$ derived from $\chi(T)$, no correction has so far been made for many-body enhancement effects. A suggested correction to $\chi(T)$ to account for many-body effects is: $\chi_p/\chi_p^0 = [1 - IN_{\varepsilon F}]^{-1}$,[**175**] where I^{-1} = 26 states eV^{-1} C_{60}^{-1}; using this formula with experimental χ_p to estimate χ_p^0 (Pauli susceptibility with no many-body effects), the corrected $N_{\varepsilon F}$(295 K) for Rb_2CsC_{60} becomes 6.2 states eV^{-1} C_{60}^{-1}.

3.4.5. The variation of magnetic susceptibility with unit cell volume

From the magnetic susceptibility data presented, a clear difference in trends in the metallic regime above T_c is observed between the underexpanded and overexpanded members of the $Rb_xCs_{3-x}C_{60}$ series. Whilst the normal state metallic susceptibility is virtually temperature-independent in the less expanded Rb_2CsC_{60} and $Rb_{1.5}Cs_{1.5}C_{60}$, in the overexpanded compositions ($0.25 \leq x \leq 1$), the magnetic susceptibility is clearly observed to increase with increasing T (below the cusp marking the metal-to-insulator transition), with the gradient becoming steeper in more expanded compositions closer to the Mott boundary. We now consider the origins of these effects.

Stoner proposed in 1934 that an attractive contribution, increasing the normal Pauli susceptibility of a metal, should be considered to account for the effect that localised electrons, when near to one another, preferentially align their spin in opposing directions. Quantitatively, this can be expressed as follows:

$$\frac{1}{N_\mathrm{b}} = \frac{1}{N_\chi} + I, \qquad \textbf{Equation 3.4}$$

where I represents the Stoner parameter, N_b corresponds to the 'bare' $N_{\varepsilon F}$ in the absence of interelectron repulsion, and N_χ is $N_{\varepsilon F}$ enhanced by interelectron repulsion. A Stoner enhancement in χ as a function of V has been observed experimentally *e.g.* in conduction-electron-spin susceptibility measurements of underexpanded Na_2CsC_{60}, K_3C_{60} and Rb_3C_{60},[**176**]. Brouet and colleagues reported an increase in $1/T_1T$ with temperature in Rb_3C_{60}, from ^{13}C NMR, too steep to explain through temperature variation of $N_{\varepsilon F}$ alone; they proposed that the relaxation is comprised of both a metallic 'Korringa-like' channel and a molecular channel relating to localised single-triplet excitation.[**177**]

Using the unit cell volume dependences extracted from structural analysis, the unit cell volume dependence of χ for the normal metallic regimes of the whole $Rb_xCs_{3-x}C_{60}$ compositional range under investigation can be derived (Fig. 3.23). The general trend in χ(V) is significant as, whilst some slight experimental scatter is found, the data provide experimental evidence for behaviour predicted by DMFT. Early, general calculations predicted that in the Hubbard model, an anomalously high χ, compared to the free-electron value, should be expected in the strongly-correlated metallic state close to the MIT.[**82**] More recently, Capone *et al.* reported χ as a function of U/W (probed by V in our case) for A_3C_{60}, showing an initial Stoner enhancement at small U/W, then flattening out before a sharp growth close to the Mott transition, from $U/W > 1.1 - 1.3$. They attributed the origin of the susceptibility 'plateau' to a gradual crossover of the maximum spin available at each site, from $S = 3/2$ at small U (Fermi liquid) to $S = ½$ at large U, near the MIT, *i.e.* corresponding to a dynamically JT distorted state at large U.[**76**]

The present data (Fig. 3.23) clearly demonstrate that the magnetic susceptibility is enhanced close to the Mott boundary in *fcc* $Rb_xCs_{3-x}C_{60}$. Such an enhancement, with onset at a unit cell volume in the vicinity of ~760 Å^3, is consistent with the presence of strong electron correlations.

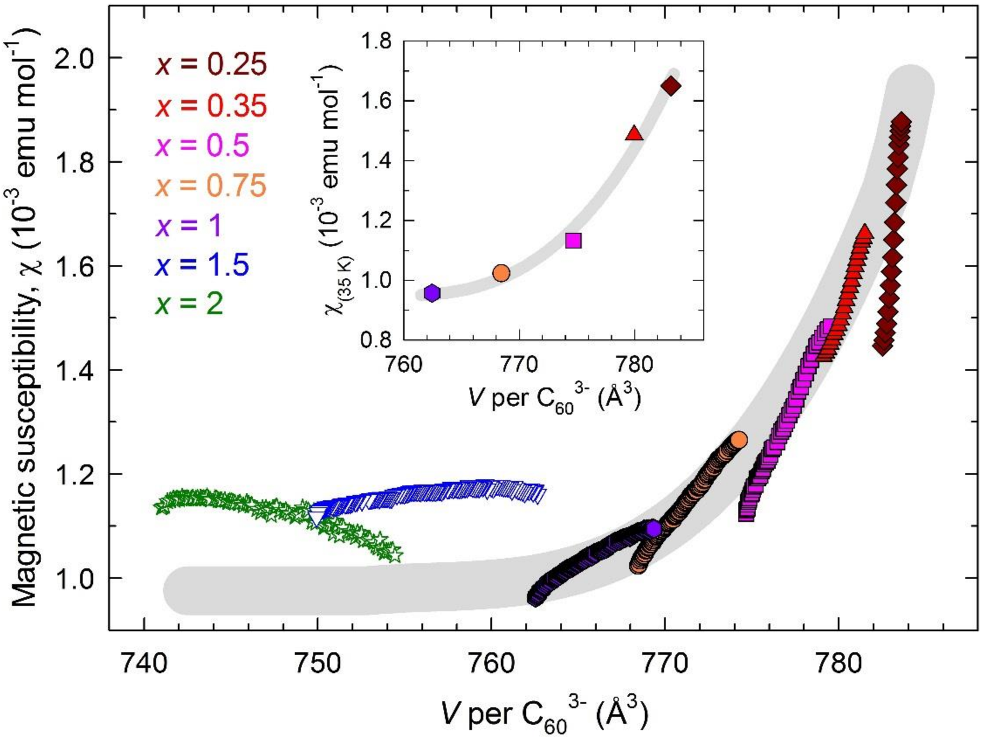

Figure 3.23: The dependence of χ on unit cell volume, V in the normal metallic regime for *fcc*-rich $Rb_xCs_{3-x}C_{60}$ ($0.25 \leq x \leq 2$). Values of χ are those presented in Figs. 3.20 and 3.21; the grey solid line is a guide to the eye. For $x = 1.5$ and 2, the magnitude of χ is likely to be more influenced by impurities, as Curie-Weiss fitting could not be undertaken to estimate χ_0 so no such term was subtracted. The inset shows χ at 35 K (±1 K) as a function of V for the overexpanded compositions ($0.25 \leq x \leq 1$); the solid line is a guide to the eye.

3.4.6. High pressure, low-field ZFC-FC measurements

Magnetisation measurements as a function of temperature have been carried out under applied pressures of up to ~10.5 kbar, to investigate the superconducting response of *fcc*-rich $Rb_xCs_{3-x}C_{60}$ ($0.35 \leq x \leq 2$) to both chemical and external hydrostatic pressure.

Figure 3.24 shows the temperature dependence of magnetisation for *fcc*-rich $Rb_xCs_{3-x}C_{60}$ ($0.35 \leq x \leq 2$), whilst the evolution of superconducting T_c and estimated shielding fraction with pressure for each composition is presented in Figs. 3.25 and 3.26.

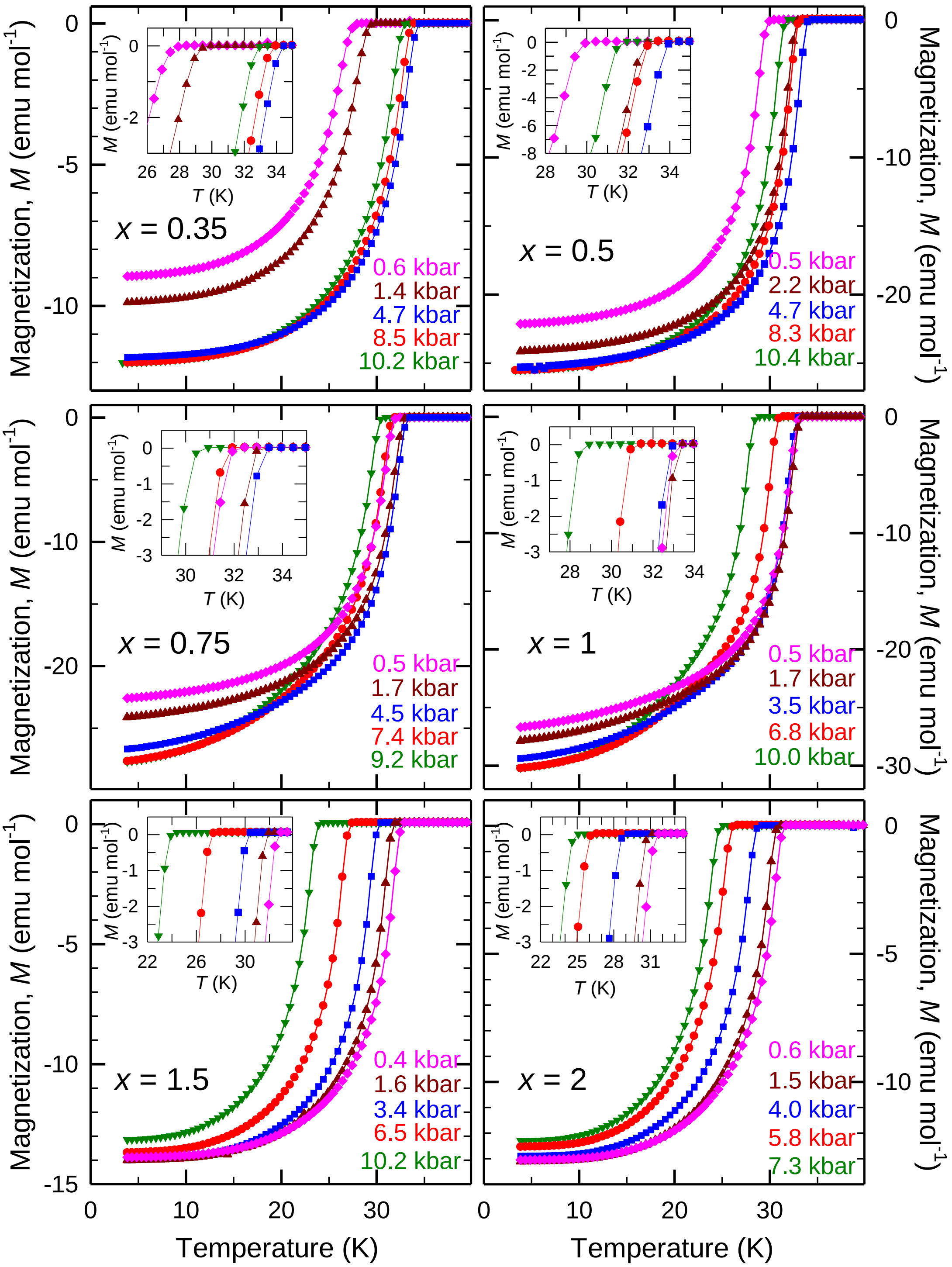

Figure 3.24: Magnetisation, M as a function of temperature (20 Oe, ZFC protocol) for *fcc*-rich $Rb_xCs_{3-x}C_{60}$ ($0.35 \leq x \leq 2$), at selected pressures; for the $x = 1.5$ and 2 compositions, data from sample I are shown in both cases. The insets display expanded regions of the data near T_c.

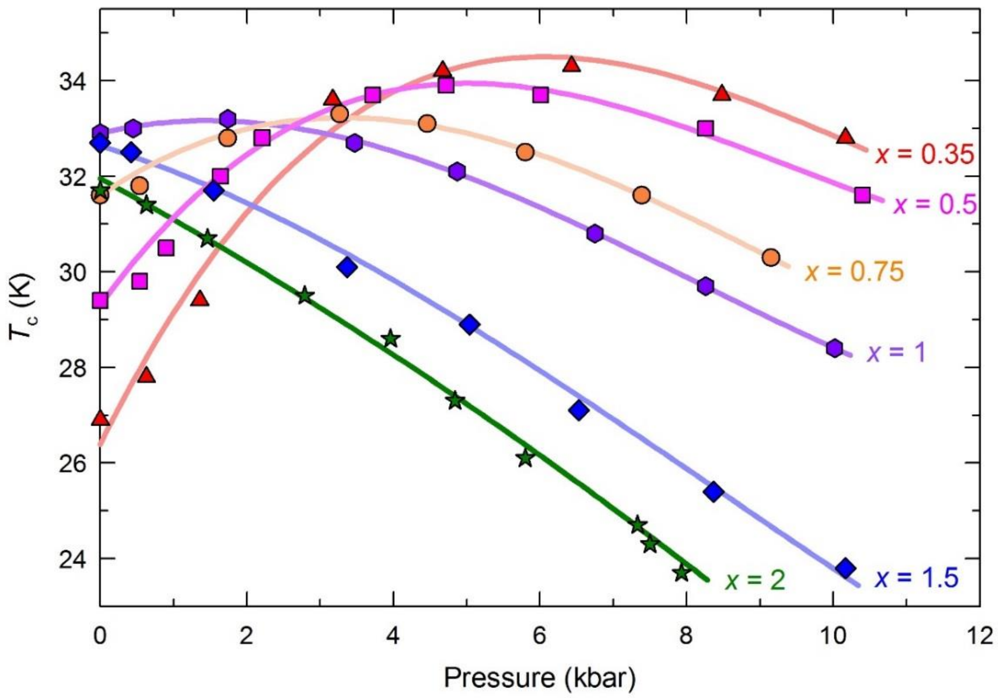

Figure 3.25: The variation of superconducting T_c with pressure for *fcc*-rich $Rb_xCs_{3-x}C_{60}$ ($0.35 \leq x \leq 2$), from magnetisation measurements with applied fields of 20 Oe and under ZFC protocols. The solid lines are guides-to-the-eye. $Rb_{1.5}Cs_{1.5}C_{60}$ and Rb_2CsC_{60} data were collected for samples I in both cases.

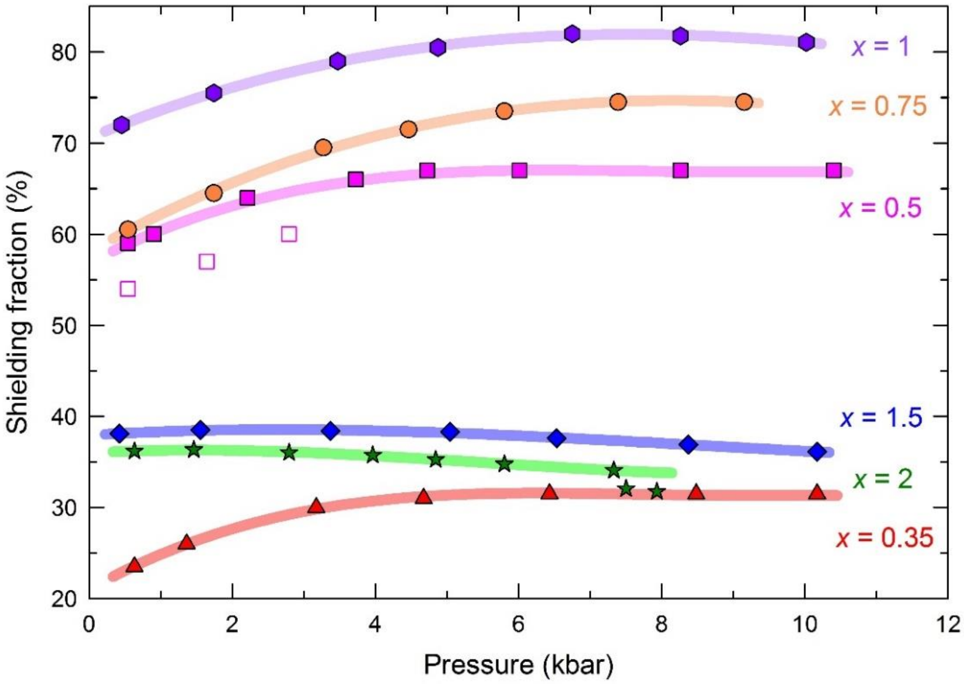

Figure 3.26: The evolution of shielding fraction at 4 K (estimated from ZFC measurements under 20 Oe applied field) for *fcc*-rich $Rb_xCs_{3-x}C_{60}$ ($0.35 \leq x \leq 2$). The solid lines are guides-to-the-eye. $Rb_{1.5}Cs_{1.5}C_{60}$ and Rb_2CsC_{60} data were collected for samples I in both cases. The unfilled squares show results from a second experimental run for $x = 0.5$.

The T_c responds sensitively to applied pressure, with a large positive initial pressure coefficient $(dT_c/dP)_0$ for the most expanded composition $Rb_{0.35}Cs_{2.65}C_{60}$ (+2.2(1) K kbar^{-1}); this gradually decreases as Rb_x increases, approaching zero for $x = 1$ and becomes negative for underexpanded Rb_2CsC_{60} (-0.7(1) K kbar^{-1}). Over the full pressure range, distinct superconductivity $T_c(P)$ domes are observed for all compositions except Rb_2CsC_{60}, which still exhibits a non-linear $T_c(P)$ response at low pressure (in contrast to the large negative linear $T_c(P)$ = -0.97 K kbar^{-1} from conventional underexpanded Rb_3C_{60} [**178**]). The $T_c(P)$ domes are reminiscent of those observed for both *fcc* and A15 Cs_3C_{60}, and consistent with earlier preliminary work investigating the overexpanded ($0 \leq x \leq 0.5$) regime only.[**71, 140**] The pressure at $T_{c(\max)}$, $P_{\max}$, decreases with increasing Rb_x (Fig. 3.25).

For the overexpanded and optimally expanded compositions $Rb_xCs_{3-x}C_{60}$ ($0.35 \leq x \leq 1$), the shielding fraction increases parabolically with pressure as unit cell volume decreases, saturating above ~6 kbar (Fig. 3.26), which may be due to improved intergranular contact as pressure is increased. In contrast, for underexpanded $Rb_{1.5}Cs_{1.5}C_{60}$ and Rb_2CsC_{60}, shielding fractions remain virtually unchanged with pressure; decreases of 2-4 % in shielding fraction are measured, but this is smaller than the estimated experimental uncertainty (exemplified by the ~5 % difference in shielding fraction between the two $x = 0.5$ measurement runs).

Using the low-temperature $V(P)$ compressibility data for the $Rb_xCs_{3-x}C_{60}$ systems described in section 3.3.5 (fits to the Murnaghan EoS have allowed V at arbitrary P to be accurately estimated), in combination with $T_c(P)$ data (Fig. 3.25), the T_c trends as a function of V for $Rb_xCs_{3-x}C_{60}$ ($0.35 \leq x \leq 2$) can now be extracted. These are presented in Fig. 3.27. Low-temperature high-pressure structural data was available for each composition except $Rb_{0.75}Cs_{2.25}C_{60}$, for which the volume compressibility of $RbCs_2C_{60}$ was used to best approximate the $V(P)$ trend.

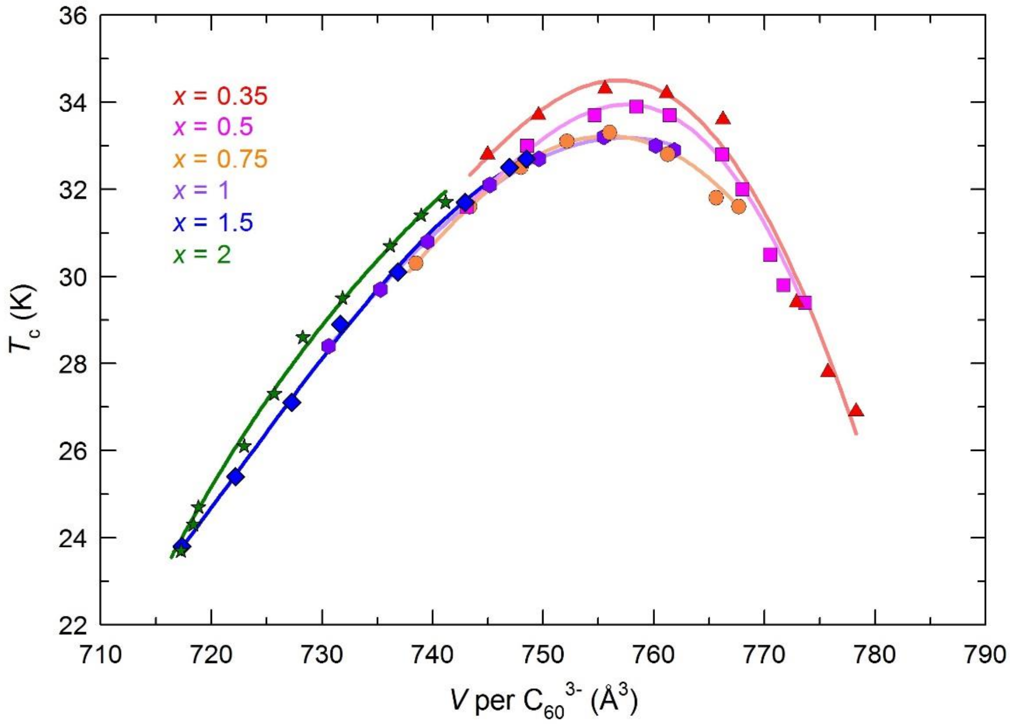

Figure 3.27: Superconducting T_c as a function of unit cell volume at low temperature, V, per C_{60}^{3-}, for *fcc*-rich $Rb_xCs_{3-x}C_{60}$ ($0.35 \leq x \leq 2$). Solid lines are guides-to-the-eye. For $Rb_{1.5}Cs_{1.5}C_{60}$, both magnetic and structural data were collected for sample I, whilst for Rb_2CsC_{60}, magnetic and structural data were collected for samples I and II, respectively.

With structural data collected using He gas as pressure medium and magnetic data collected with Daphne oil pressure medium, there could be a small V offset between the two techniques (in *e.g.* Na_2CsC_{60}, magnetisation data collected with He as pressure medium reportedly has a smaller $T_c(P)$ gradient than when using other pressure media, attributed to He co-intercalation with the alkali cations [**179**]). However, any such effect should be very minor given the low experimental pressures (< 1.1 GPa), and should affect all data sets virtually equally.

Whilst the $T_c(V)$ trends mimic the response of Cs_3C_{60} upon hydrostatic pressure application, and individual domes peak within a narrow volume range ($V_{max} \sim 755\text{-}760$ Å^3), the maximum T_c for each composition is slightly smaller than the $T_{c(max.)}$ of 35 K for *fcc* Cs_3C_{60}. Moreover, $T_{c(max.)}$ decreases marginally with increasing Rb_x, from 34.3 K to 33.2 ($x = 0.35$ and 1, respectively). This effect is tentatively attributed to greater cation disorder in the *fcc* tetrahedral interstitial sites as x_{Rb} increases, yielding a small detrimental effect on superconductivity in overexpanded *fcc* $Rb_xCs_{3-x}C_{60}$. Assuming there are no tetrahedral cation vacancies, in *fcc* Cs_3C_{60}, a given C_{60}^{3-} has a 100%

probability of being surrounded by 8 Cs^+ ions in tetrahedral sites, i.e. a homogeneous distribution; this probability decreases significantly as a greater fraction of Rb^+ is intercalated into the *fcc* lattice, to <1% for $RbCs_2C_{60}$. In one family of cuprate superconductors ($(La_{0.925-f}Nd_fSr_{0.075-g-h}Ca_gBa_h)_2CuO_4$), the superconducting T_c has been shown to decrease linearly with increasing A-site disorder (with fixed doping level), characterised by the variance in distribution of A-site cation radii and ascribed to increasing lattice strains [**180**]. The cation size variance for *fcc* $Rb_xCs_{3-x}C_{60}$ steadily increases with x_{Rb} within the compositional range where the maximum T_c in a superconducting 'dome' can be ascertained in Fig. 3.27, *i.e.* ($0.35 \leq x \leq 1$).

3.4.7. High pressure, high-field ZFC-FC measurements

Upon the application of moderate pressure (1.64 kbar) to $Rb_{0.5}Cs_{2.5}C_{60}$, the T_{max} in $\chi(T)$ shifts to higher temperature and the cusp, well-defined at ambient pressure, becomes flatter (Fig. 3.28). Whilst the broader maximum at 1.64 kbar renders the definition of T_{max} less precise than at 0.54 kbar, the shift with increasing pressure is clearly seen. These changes are analogous to those observed upon 'chemical' pressurisation of $Rb_{0.5}Cs_{2.5}C_{60}$ *via* adjustment of the Cs/Rb ratio to increase the Rb content in the *fcc* unit cell, reducing the interfullerene separation.

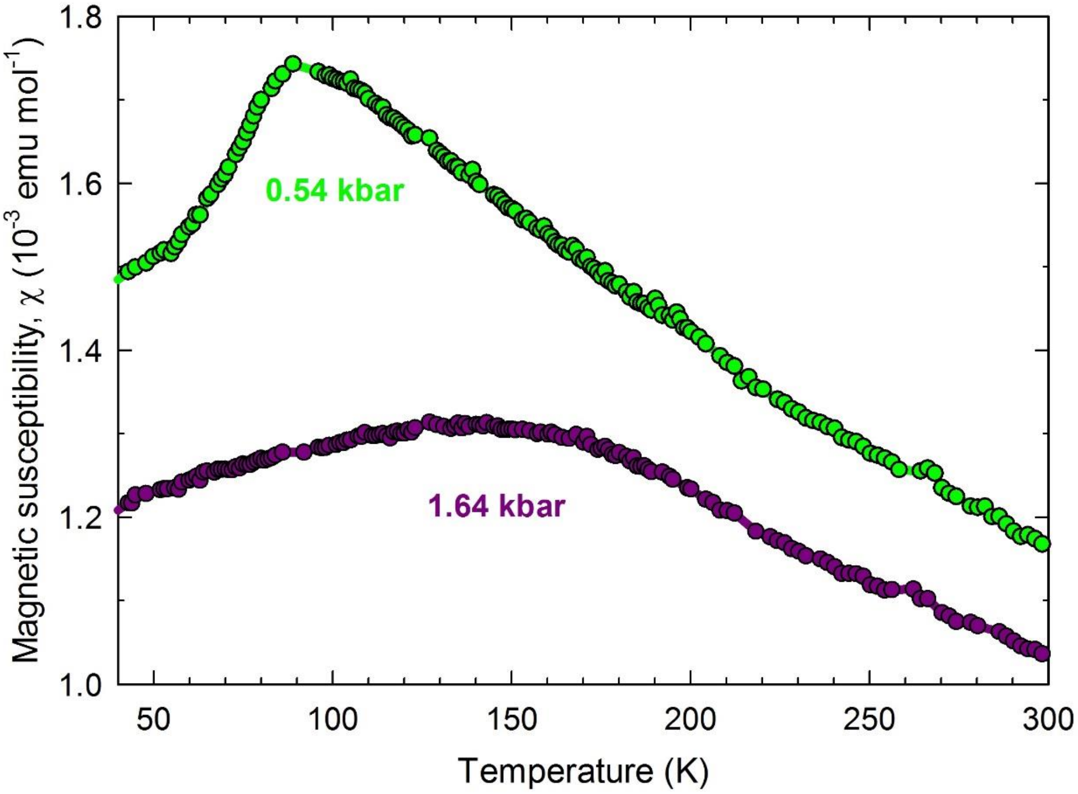

Figure 3.28: The variation of magnetic susceptibility with temperature, under applied pressure, for *fcc*-rich $Rb_{0.5}Cs_{2.5}C_{60}$.

These data are consistent with the results of recent high-pressure NMR studies on *fcc* Cs_3C_{60}, insulating at ambient pressure, where the temperature dependence of $1/T_1T$ revealed the emergence of a maximum upon increasing pressure, becoming flatter ($1/T_1T$ ~ constant) at pressures above ~0.6 GPa indicative of metallic behaviour (Korringa law).[**141, 151**] Further discussion in conjunction with the NMR results is presented later (Section 3.7).

3.4.8. Summary – magnetic properties of the *fcc*-rich $Rb_xCs_{3-x}C_{60}$ series at ambient and at high pressures

Low-field magnetisation measurements have confirmed bulk superconductivity in all the *fcc*-rich $Rb_xCs_{3-x}C_{60}$ ($0.25 \leq x \leq 2$) samples, with T_c initially increasing with Rb content from 25.9 K (shielding fraction 50 %) in overexpanded $Rb_{0.25}Cs_{2.75}C_{60}$ to 32.9 K (85%) for $RbCs_2C_{60}$, then decreasing to 31.8 K (91%) in underexpanded Rb_2CsC_{60}. This chemical pressure effect, with the *fcc* tetrahedral cation distribution controlling the interfullerene spacing, is analogous to the response of the electronic properties of the most expanded *fcc* Cs_3C_{60} upon the application of hydrostatic pressure.[**140**] In contrast to the large negative linear pressure coefficient of T_c in underexpanded K_3C_{60} and Rb_3C_{60}, the $dT_c(dP)$ trends of *fcc* $Rb_xCs_{3-x}C_{60}$ ($0.25 \leq x \leq 1.5$) form distinct superconductivity domes, which combine well to form a single dome in $T_c(V)$ when magnetic results are combined with structural compressibility data. However, $T_{c(max.)}$ decreases with increasing x between Cs_3C_{60} and $RbCs_2C_{60}$, tentatively attributed to increasing tetrahedral interstititial cation disorder.

Magnetic susceptibility measurements have revealed that, whilst overexpanded $Rb_xCs_{3-x}C_{60}$ ($0.25 \leq x \leq 1$) display analogous behaviour to that of insulating *fcc* Cs_3C_{60} at higher temperatures, distinct cusps are observed upon cooling, attributed to insulator-to-metal transitions. However, in contrast, underexpanded compositions with $x = 1.5$ and 2 display $\chi(T)$ behaviour which is virtually temperature-independent, indicative of Pauli metallic behaviour over the experimental temperature range (up to 300 K), with an estimated $N_{\varepsilon F}$ of ~16 states eV^{-1} C_{60}^{-1} in the metallic regime for both compositions. Figure 3.29 presents data from the whole range of compositions, illustrating the differing behaviour.

The transition temperatures from magnetic characterisation, i.e. T_{max} from $\chi(T)$ and superconducting T_c, can now be combined with the T_{MIT} (PXRD) values from structural characterisation (Section 3.3.3) to produce an ambient pressure electronic phase diagram for the *fcc* $Rb_xCs_{3-x}C_{60}$ systems, shown in Fig. 3.30. Here and for later phase diagrams, values of T_{max} from $\chi(T)$ were defined as the intersection point of two linear fits, fitting to ranges of data collected at temperatures directly below and above the approximate maximum. Volumes at each transition temperature were estimated through careful extrapolation between experimental data points from variable-temperature PXRD studies (Fig. 3.4).

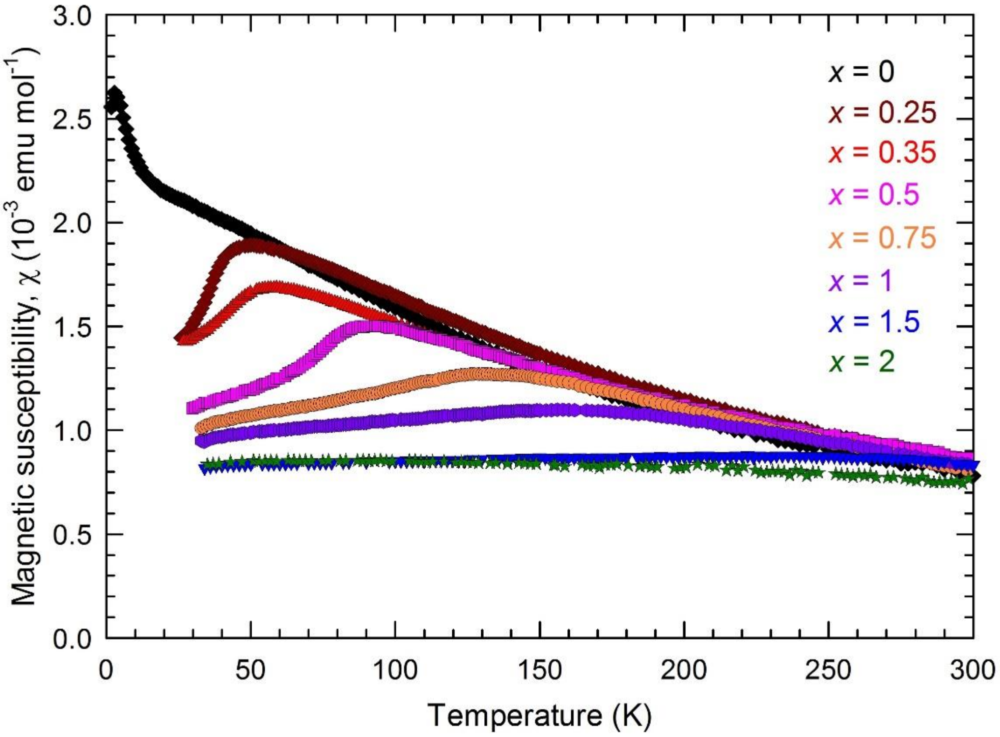

Figure 3.29: Temperature dependence of the magnetic susceptibility, $\chi(T)$, of *fcc*-rich $Rb_xCs_{3-x}C_{60}$ ($0 \leq x \leq 2$), combining data presented in Figs. 3.20 and 3.21; data for $x = 0$ are from ref. [**140**]. Here, an arbitrary factor of 3×10^{-4} emu mol^{-1} has been subtracted from χ for the underexpanded compositions ($x = 1.5$, 2), to aid visual clarity in comparing trends between the underexpanded and overexpanded samples. The true experimental $\chi(T)$ for $x = 1.5$ and 2, both $\sim1\times10^{-3}$ emu mol^{-1} at 295 K from $M(H)$ measurements, is shown in Fig. 3.21.

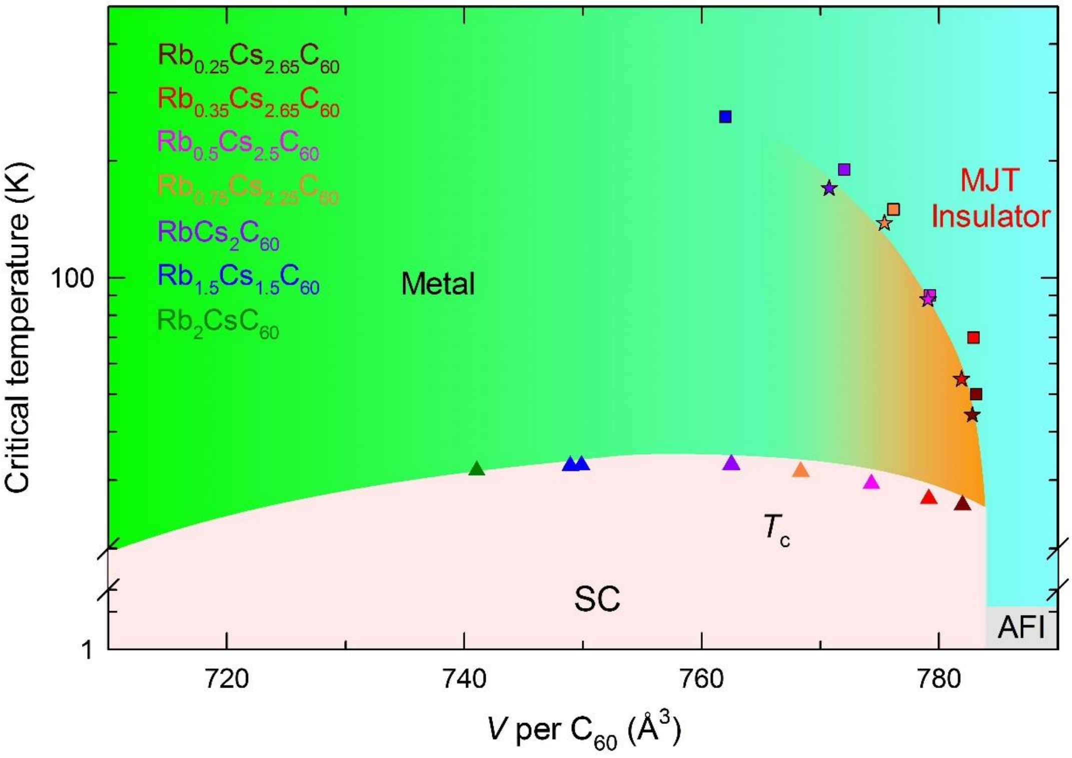

Figure 3.30: Electronic phase diagram for *fcc* $Rb_xCs_{3-x}C_{60}$ ($0.25 \leq x \leq 2$), from data collected at ambient pressure. Triangles, stars and squares represent superconducting (SC) T_c, T_{max} from $\chi(T)$ and T_{MIT}(PXRD), respectively. The antiferromagnetically ordered insulating (AFI) regime in the most expanded *fcc* member, Cs_3C_{60} is also included schematically for clarity, and the SC-metal boundary shown is that determined experimentally for *fcc* Cs_3C_{60}.[**140**] Within the metallic regime, gradient shading from green to orange schematically illustrates the increasingly correlated metallic character approaching the metal-insulator boundary. 'MJT' refers to Mott-Jahn-Teller.

For the single composition $Rb_{0.5}Cs_{2.5}C_{60}$, the present magnetic and structural results show that T_{MIT} can also be tuned by the application of pressure. A phase diagram for $Rb_{0.5}Cs_{2.5}C_{60}$ only, combining $\chi(T)$ data from Figs. 3.20 and 3.28 with V_{MIT} at 295 K from high-pressure structural data (Fig. 3.12), is presented in Fig. 3.31. The $V(T_{max})$ at 1.64 kbar for sample $x = 0.5$ was estimated first through calculating V at 1.64 kbar and 295 K from a fit to $V(P)$ data using the Birch-Murnaghan EoS (Fig. 3.12), then assuming that $V(295\text{ K}, 1\text{ atm}) - V(157\text{ K}, 1\text{ atm}) = V(295\text{ K}, 1.64\text{ kbar}) - V(157\text{ K}, 1.64\text{ kbar})$. Whilst imperfect, this best approximates $V(157\text{ K}, 1.64\text{ kbar})$, as no $V(P)$ experimental data are available at T_{MIT}.

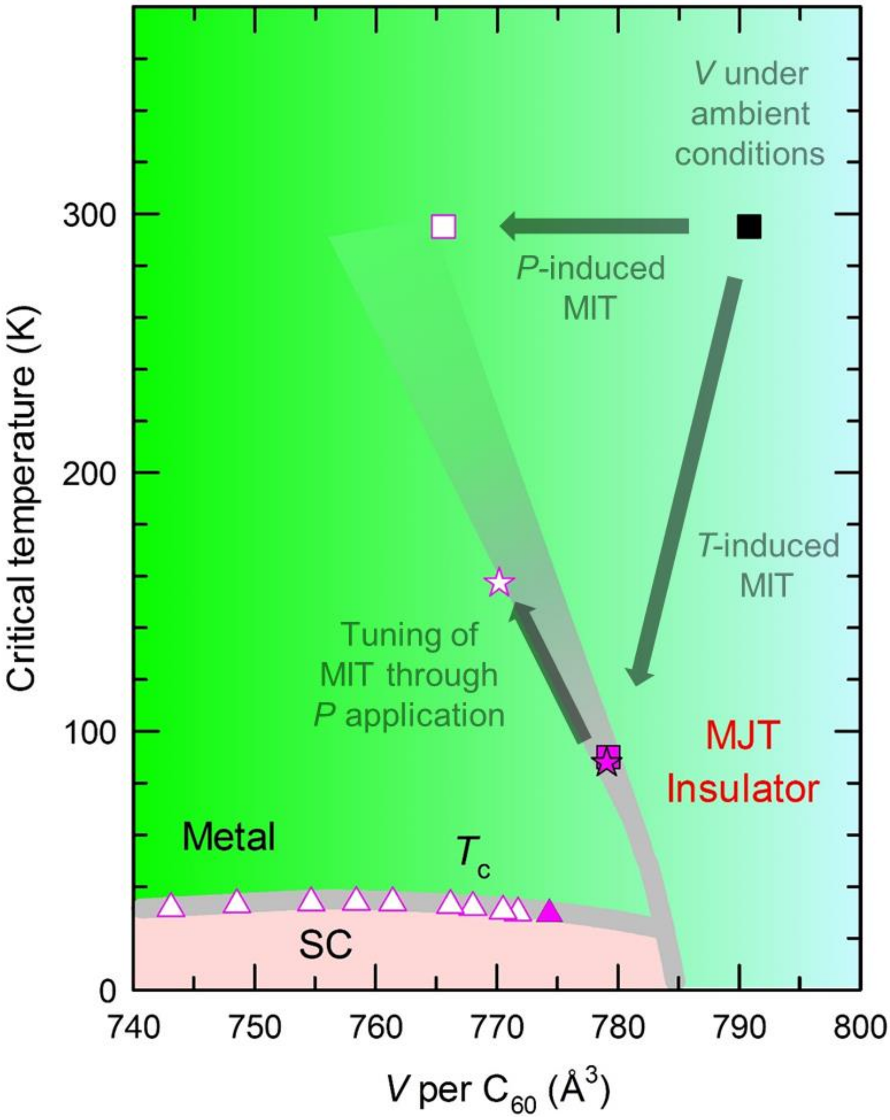

Figure 3.31: Electronic phase diagram for *fcc* $Rb_{0.5}Cs_{2.5}C_{60}$ at ambient and elevated pressures. The MIT from powder X-ray diffraction, MIT from magnetic susceptibility and superconducting T_c values are represented with square, star and triangle symbols, respectively; filled symbols depict ambient pressure measurements, whilst blank symbols show data collected at elevated pressure. The abbreviations ‘SC’ and ‘MJT’ refer to superconducting and Mott-Jahn-Teller, respectively. Solid lines are guides-to-the-eye, with the insulator-metal boundary trajectory, schematically represented with a gradient, also defined by data for other $Rb_xCs_{3-x}C_{60}$ compositions not shown here.

3.5. Raman spectroscopy

3.5.1. Raman spectroscopy measurements under ambient conditions

Raman spectra of the *fcc* C_{60} $A_g(2)$ mode were collected for the *fcc*-rich $Rb_xCs_{3-x}C_{60}$ series ($0 \leq x \leq 2$), and for reference samples of sublimed pristine C_{60} and phase-pure Cs_6C_{60}, as an additional check of sample quality. The experimental setup, sample preparation and data collection were described earlier in Section 2.6.2. For composition $x = 2$, sample II was studied. Prior to fitting, all Raman shifts were calibrated using measurements of toluene, carried out before and after sample data collection. Specifically, an offset of +3.6779 cm^{-1} was applied to all Raman shifts (representing the mean offset needed to bring the positions of the two most intense toluene peaks to their literature values, at 1380 cm^{-1} and 1605 cm^{-1} [**181**]). Over the course of measurements, a small change in Raman shift (~0.875 cm^{-1}) was observed between the 'before' and 'after' toluene spectra. Calibrated data were modelled using least-squares fitting to 4-parameter Lorentzian functions, with the following form:

$$f = y_0 + \frac{a}{1 + \left(\frac{x - x_0}{b}\right)^2} \qquad \textbf{Equation 3.5}$$

Lorentzian fits to the $A_g(2)$ mode of all $Rb_xCs_{3-x}C_{60}$ ($0 \leq x \leq 2$) samples measured are presented in Fig. 3.32. Compositions where $0.5 \leq x \leq 2$ could be modelled well with a single peak, but a second, weaker signal was also observed at higher Raman shift for $Rb_{0.35}Cs_{2.65}C_{60}$ and Cs_3C_{60}, so two-peak fits were carried out for these samples.

The signal positions of the main peak, extracted as x_0 from Equation 3.5, fall in a narrow range from 1448.0-1450.2 cm^{-1} (uncertainties in these values, derived from least-squares fits, are shown in Fig. 3.32). Whilst slight differences between reported experimental signal positions may arise from calibration differences, this range appears consistent with literature values for the A_3C_{60} $A_g(2)$ mode (e.g. 1448 cm^{-1} in Rb_3C_{60} [**182**], ~1448 cm^{-1} for *fcc* Cs_3C_{60} [**140**]). This variation is also minimal compared to e.g. the ~6 cm^{-1} softening expected upon reducing C_{60}^{3-} to C_{60}^{4-} (Section 1.3.8). The small second peak observed for $x = 0$ and 0.35 at ~1461 cm^{-1}, also present in previous measurements of the $x = 0$ sample,[**140**] is attributed to the minority CsC_{60} phase. The $A_g(2)$ mode shifts for Cs_6C_{60} and C_{60}, measured in the same experimental session, are separated by 36.3 cm^{-1}, and separated from C_{60}^{3-} ($x = 0.75$) by 17 cm^{-1} and 19 cm^{-1} respectively (Fig.

3.33, inset), extremely close to the expected ~ 6 cm^{-1} mode softening per A$^+$ in A_xC_{60} (A = alkali metal).

Theoretical and experimental studies report that the amount of phonon mode softening upon variation of the alkali dopant in A_xC_{60} should not be appreciable, being largely determined by the charge transfer per carbon atom;[**182, 183**] here, no systematic trend is observed in the $A_g(2)$ mode frequency as a function of Rb/Cs dopant ratio (or, analogously, unit cell volume, presented in Fig. 3.33).

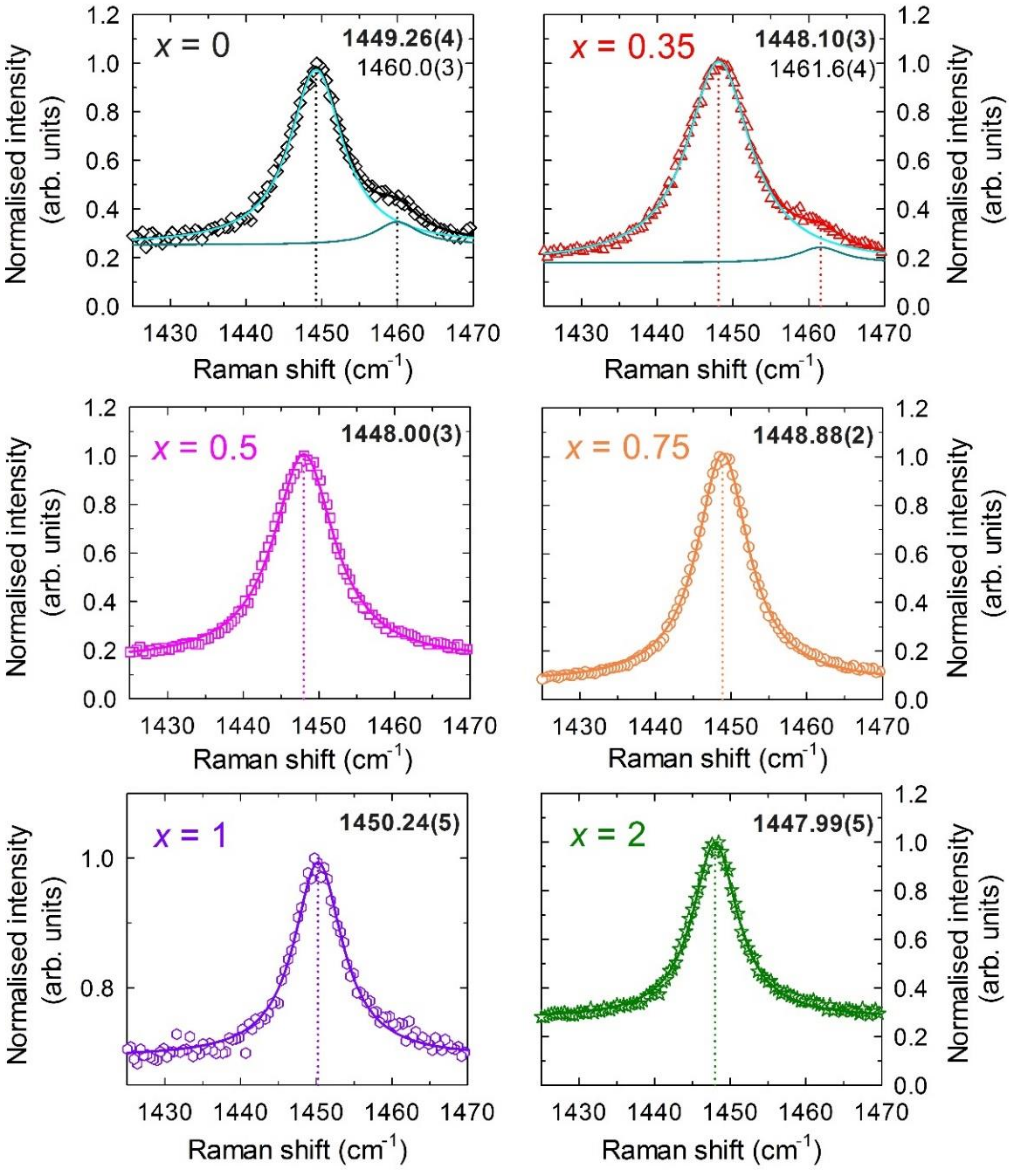

Figure 3.32: Raman spectra of the $A_g(2)$ mode for *fcc*-rich $Rb_xCs_{3-x}C_{60}$ ($0 \leq x \leq 2$). Solid lines display results from 4-parameter one-peak Lorentzian fits. Where two-peak fits were undertaken, individual peak contributions are shown in cyan and teal. Peak position (labelled, in cm^{-1}) are illustrated with dotted lines.

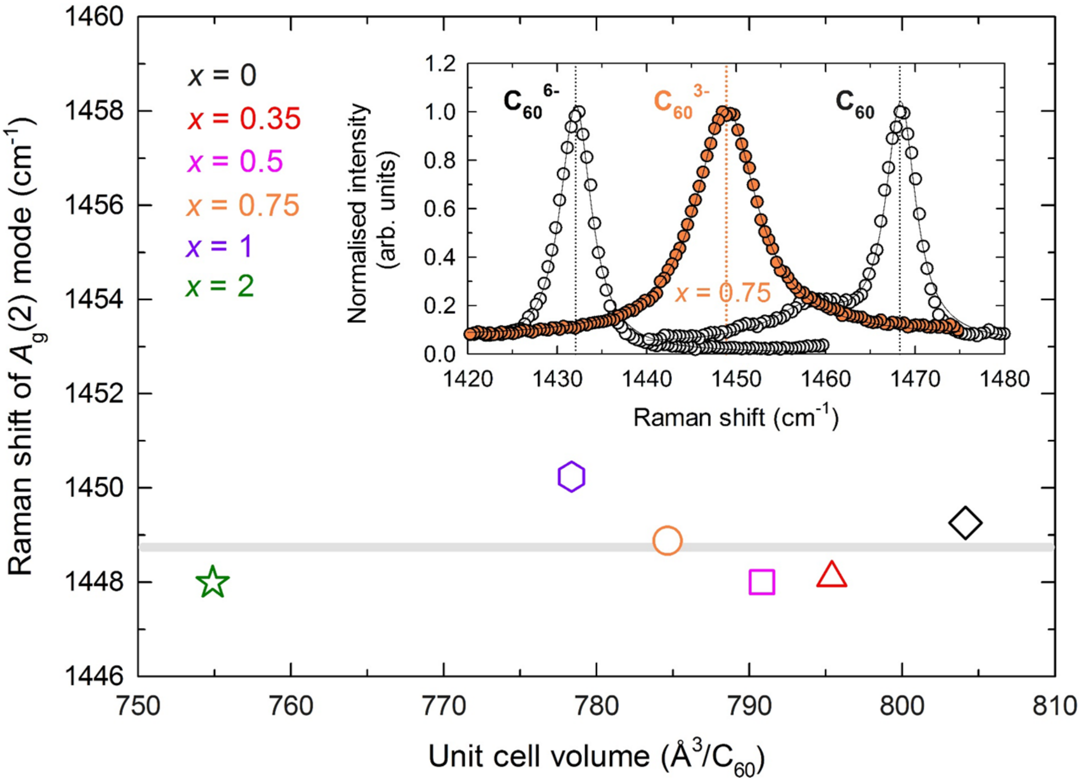

Figure 3.33: The variation in Raman shift of the *fcc* $A_g(2)$ mode for $Rb_xCs_{3-x}C_{60}$ ($0 \leq x \leq 2$), as a function of unit cell volume per C_{60}^{3-}; volumes are derived from Rietveld analysis (Section 3.3.2). The solid grey line marks the mean shift. Inset: spectra showing the $A_g(2)$ modes (left-to-right) for Cs_6C_{60}, $Rb_{0.75}Cs_{2.25}C_{60}$ and C_{60}, dotted lines mark the peak positions and solid-lines show results of peak fits to Lorentzian functions (one peak fit: $Rb_{0.75}Cs_{2.25}C_{60}$, two peak fit: C_{60}, Cs_6C_{60}).

3.5.2. Summary – results of Raman spectroscopy of the *fcc*-rich $Rb_xCs_{3-x}C_{60}$ series under ambient conditions

The tangential $A_g(2)$ mode Raman shift has been studied for a series of *fcc*-rich samples $Rb_xCs_{3-x}C_{60}$ ($0 \leq x \leq 2$). The Raman spectroscopy data presented in Figs. 3.32 and 3.33 demonstrate that fulleride charge state in the *fcc* $Rb_xCs_{3-x}C_{60}$ phases characterised here is indeed C_{60}^{3-}, with complete charge transfer, and provide further evidence that the samples are of high quality with low levels of impurity phases. No evidence is apparent for any systematic trend in the $A_g(2)$ mode shift as Rb/Cs *fcc* phase stoichiometry is varied.

3.6. Investigation of cooling protocols

3.6.1. Introduction and experimental setups

Whilst the 'standard' solid-state synthetic protocol described in Section 3.2.1 was successfully used to synthesise bulk superconducting *fcc*-rich $Rb_xCs_{3-x}C_{60}$ ($0.35 \leq x \leq 2$) materials with good stoichiometric control, this project also aimed to extend the compositional range experimentally accessible through solid-state routes to even smaller Rb_x, *i.e.* more expanded *fcc* phases. Solid-state routes have long been known to increasingly fail with decreasing Rb_x content (approaching Cs_3C_{60}),[**31, 140**] and the compositions with x = 0.35, 0.5 in this study were of only ~80% *fcc* phase purity, as opposed to the virtually *fcc* phase-pure materials achieved where x = 1, 2. In this section, four preliminary experiments aiming to synthesise *fcc*-rich materials with x = 0.2, 0.25 and investigate the effects of varying the cooling rate are described. In each, a large sample, after one initial lower temperature annealing to form a precursor, was split into batches and reannealed. Each batch was then subjected to a different cooling protocol, and all products were characterised by PXRD.

Two initial experiments, employing a chamber furnace for annealing, compared the effects of quenching into a cryogenic bath with removing a sample and allowing it to cool in air. As in the 'standard' protocol (Section 3.2.1), stoichiometric amounts of Rb, Cs and ground sublimed C_{60} were firstly weighed into a tantalum cell (Table 3.11). After 15 mins evacuation with a turbopump (1×10^{-4} mbar), each sample was sealed in a Pyrex ampoule under ~400 mbar He(g). Placed upright in a chamber furnace, each sample was annealed using a stepped protocol up to 300 °C (~26 hrs), described earlier (Section 3.2.1).

After grinding with an agate mortar and pestle, each large sample was divided into two or three portions of approximately equal mass, each of which was pressed into a 7 mm-diameter pellet. Individual pellets were sealed directly inside 12 mm-diameter glass ampoules, after evacuation for 15 minutes (1×10^{-4} mbar) then filling with He(g) (~400 mbar); quartz glass was used for samples intended for rapid cryogenic cooling to minimise the risk of thermal stress breakage, and Pyrex glass for other samples. Sealed samples were placed directly inside a preheated chamber furnace at 430°C.

Quenching samples into two different types of cryogenic bath was trialled: liquid nitrogen (~−196°C) and ice/water-based baths (−3 - 1°C). With high temperatures required to intercalate C_{60} with alkali metals, rapid quenching to either temperature will promptly stop any reaction; the latter setup may provide more rapid cooling as, in the former setup, liquid nitrogen next to the sample will boil so thermal contact between the sample and surrounding cryogenic liquid may be worse.

Two later experiments used a modified procedure, with drop quenching directly from a vertical cylindrical furnace employed to achieve even more rapid cooling. The initial protocol, *i.e.* initial preparation and first annealing, and splitting the sample, was exactly as described above. However, prior to sealing the individual portions, each ampoule was distorted (by melting) near the top for ease of attaching wire to later suspend the ampoules. After sealing, each ampoule was lowered into a preheated vertical cylindrical furnace (set temperature 430 °C, air temperature measured with a thermocouple probe 425 °C), with ends insulated with glass wool, and suspended midway vertically using wire (Fig. 3.34). At the desired quenching time, the lower glass wool was briefly removed, a cryogen flask placed underneath the furnace and wire suspending one sample cut with pliers. A second sample was removed to cool in air, and, with the glass wool replaced, the third sample cooled slowly (~1°C/min) to ambient temperature using the furnace controls. Each sample was opened in the glove box, ground and capillaries prepared for structural characterisation. Details of the four experiments presented here, *e.g.* reagent masses and annealing protocols, are presented in Table 3.11.

Table 3.11: Synthetic details for the four cooling protocol test experiments.

Experiment type	Nominal Rb_x	Mass of Rb (mg)	Mass of Cs (mg)	Mass of C_{60} (mg)	Annealing time at 430 °C (hrs)
Chamber furnace	0.2	3.6	78.4	150.0	189
Chamber furnace	0.25	5.9	101.4	200.0	94
Drop quench 1	0.25	6.1	104.0	205.1	24
Drop quench 2	0.25	6.0	102.1	201.3	26

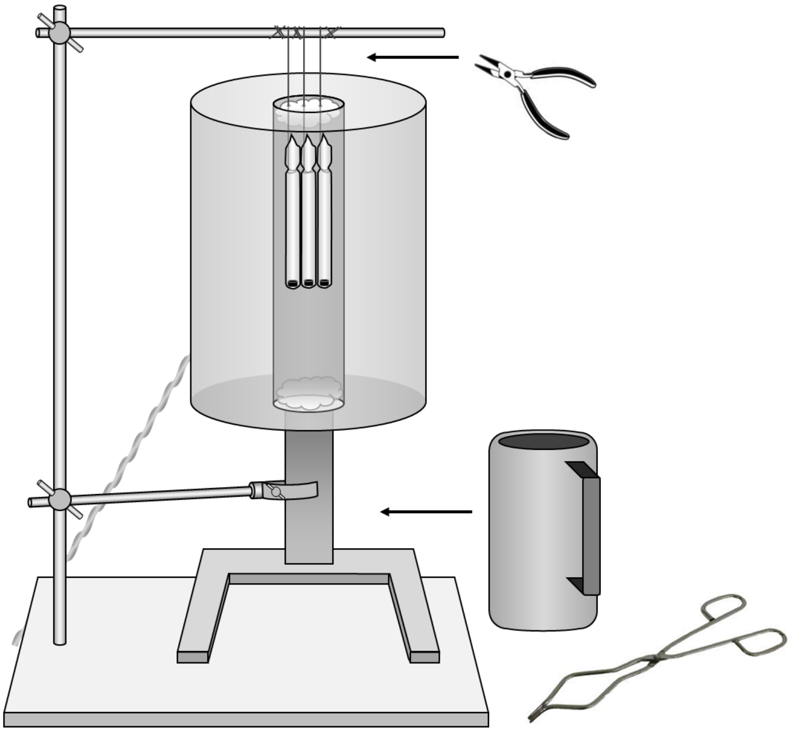

Figure 3.34: Schematic depiction of drop quenching experimental setup. A coolant-containing Dewar was added moments before removing the lower glass wool and severing the wire suspending the sample designated for drop quenching.

3.6.2. Structural characterisation of $Rb_xCs_{3-x}C_{60}$ (x = 0.2, 0.25) cooling protocol test samples

Powder X-ray diffraction data were collected for each sample at ambient temperature, on 2-3 mg ground samples contained in 0.5 mm diameter special glass capillaries (sealed under Ar). Data collection details are summarised in Table 3.12, and Fig. 3.35 presents overplots of all profiles over a selected d-spacing range.

Table 3.12: Overview of powder X-ray diffraction data collection and scan parameters for the four cooling protocol experiments. For data collected with a CuK$_{\alpha}$ X-ray source (λ = 1.5418 Å), both K$_{\alpha1}$ and K$_{\alpha2}$ components were present.

Experiment title	Nominal Rb$_x$	PXRD data source	X-ray wavelength (Å)	2θ scan range (°)	2θ step size (°)	Scan rate (°/min)
Chamber furnace quench	0.2	Bruker d8 lab diffractometer	1.5418	9 - 48	0.04	0.2
Chamber furnace quench	0.25	Bruker d8 lab diffractometer	1.5418	14 - 35	0.04	0.8
Drop quench 1	0.25	Synchrotron (ID31, ESRF)	0.399959	2.5 - 24	0.003	2.0
Drop quench 2	0.25	Bruker d8 lab diffractometer	1.5418	9.5 - 46	0.04	0.4

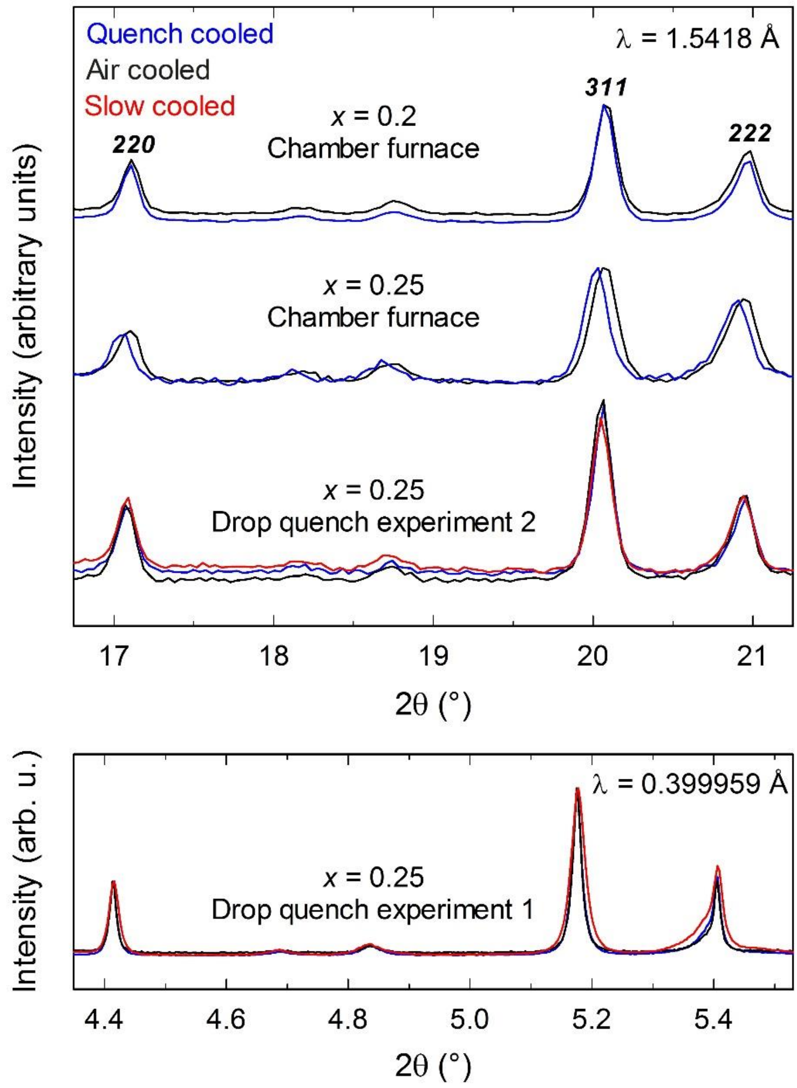

Figure 3.35: Powder X-ray diffraction profiles from all products of the cooling protocol test experiments, collected with a lab diffractometer (upper panel) and with synchrotron X-ray radiation (lower panel), showing a selected d-spacing range only for visual clarity. Intensities are normalised, and Miller indices of *fcc* phase peaks are labelled.

Rietveld analysis was undertaken for each dataset, with a three-phase structural model identical to those described earlier for synchrotron data of $Rb_xCs_{3-x}C_{60}$ ($0.25 \le x \le 2$, Section 3.3.2). Additionally, the relative breadths of *fcc* peaks for each sample were quantified by one-peak fits, as described earlier for two of the extensively characterised samples (Fig. 3.6), to two relatively isolated and intense peaks (*hkl* = 220, 422).

Tables 3.13, 3.14 and 3.15 summarise structural analysis results for products from both ‘chamber furnace quench’ experiments, and from each of the two ‘drop quench’ experiments, respectively. Two representative refinements, for data from the two $Rb_{0.25}Cs_{2.75}C_{60}$ samples subjected to drop quenching, are shown in Fig. 3.36.

It should be noted that these experiments focused on consistency of preparation and setup for the samples subjected to different cooling protocols within each experiment, rather than an overall effort to compare *e.g. fcc* fractions between different experiments; for example, the precise annealing time at 430°C was not fixed over all experiments. Data for all samples in each particular experiment were collected successively with an identical setup (*i.e.* no changes to the diffractometer configuration in between, to minimise zero shift difference between sets).

Table 3.13: Summarised structural analysis results from the two 'chamber furnace quench' experiments, for $Rb_xCs_{3-x}C_{60}$ samples with nominal x = 0.2 and 0.25 (λ = 1.5418 Å). After each was divided into two batches following initial annealing, samples were annealed in a chamber furnace at 430°C (Table 3.11), then each subjected to differing thermal treatment as described in the first column. Reliability indicators $R_{wp}(R_{exp})$, in percent, were as follows; x=0.2 quenched: 1.76(1.18), x=0.2 air cooled: 1.78(1.19), x=0.25 quenched: 2.73(2.06) and x=0.25 air cooled: 3.65(2.48).

Rb_x	Thermal treatment after 430°C annealing	*fcc a* (Å)	*fcc* fraction (%)	*bco* fraction (%)	CsC_{60} fraction (%)	FWHM 220 (°)	FWHM 422 (°)
0.2	Quenched into liquid N_2	14.7044(2)	62.6(3)	37.4(5)	-	0.123(2)	0.173(1)
	Cooled in air	14.7027(2)	59.7(4)	40.3(5)	-	0.130(3)	0.178(2)
0.25	Quenched into ice water (~1°C)	14.6801(7)	48.4(5)	44.7(4)	7(1)	0.157(8)	0.202(5)
	Cooled in air after direct removal	14.6777(5)	47.8(4)	43.3(4)	9(1)	0.168(7)	0.215(3)

Table 3.14: Summarised structural analysis results for three batches of nominal composition $Rb_{0.25}Cs_{2.75}C_{60}$, from 'Drop quench experiment 1' (λ = 0.399959 Å). After division into three batches following initial annealing, samples were suspended in a vertical tube furnace at 430°C (Table 3.11), then each subjected to differing thermal treatment as described in the first column. Reliability indicators R_{wp}(R_{exp}), in percent, were as follows; drop quenched: 7.23(5.61), air cooled: 7.87(7.08) and slow cooled: 6.58(4.09).

Thermal treatment after 430°C annealing	*fcc a* (Å)	*fcc* fraction (%)	*bco* fraction (%)	CsC_{60} fraction (%)	FWHM 220 (°)	FWHM 422 (°)
Drop quenched into ice, water and salt (−3°C)	14.70144(6)	63.7(1)	25.3(2)	11.0(3)	0.0142(2)	0.0210(2)
Cooled in air	14.70159(7)	71.6(1)	23.0(3)	5.4(5)	0.0129(2)	0.0193(2)
Slow cooled at ~1°C/min to 20°C	14.69627(7)	60.2(1)	24.3(1)	15.5(2)	0.0195(2)	0.0323(1)

Table 3.15: Summarised structural analysis results for three batches of nominal composition $Rb_{0.25}Cs_{2.75}C_{60}$, from 'Drop quench experiment 2' (λ = 1.5418 Å). After division into three batches following initial annealing, samples were suspended in a vertical tube furnace at 430°C (Table 3.11), then each subjected to differing thermal treatment as described in the first column. Reliability indicators R_{wp}(R_{exp}), in percent, were as follows; drop quenched: 2.31(1.97), air cooled: 2.12(1.83) and slow cooled: 1.90(1.82).

Thermal treatment after 430°C annealing	*fcc a* (Å)	*fcc* fraction (%)	BCO fraction (%)	CsC_{60} fraction (%)	FWHM 220 (°)	FWHM 422 (°)
Drop quenched into liquid N_2 (~−196 °C)	14.6964(3)	69.5(4)	26.9(6)	4(1)	0.128(5)	0.160(3)
Cooled in air	14.6952(3)	68.0(3)	25.2(4)	6.8(7)	0.139(3)	0.170(2)
Slow cooled at ~1°C/min to 20°C	14.6953(3)	62.5(3)	31.6(5)	5.9(8)	0.127(5)	0.170(2)

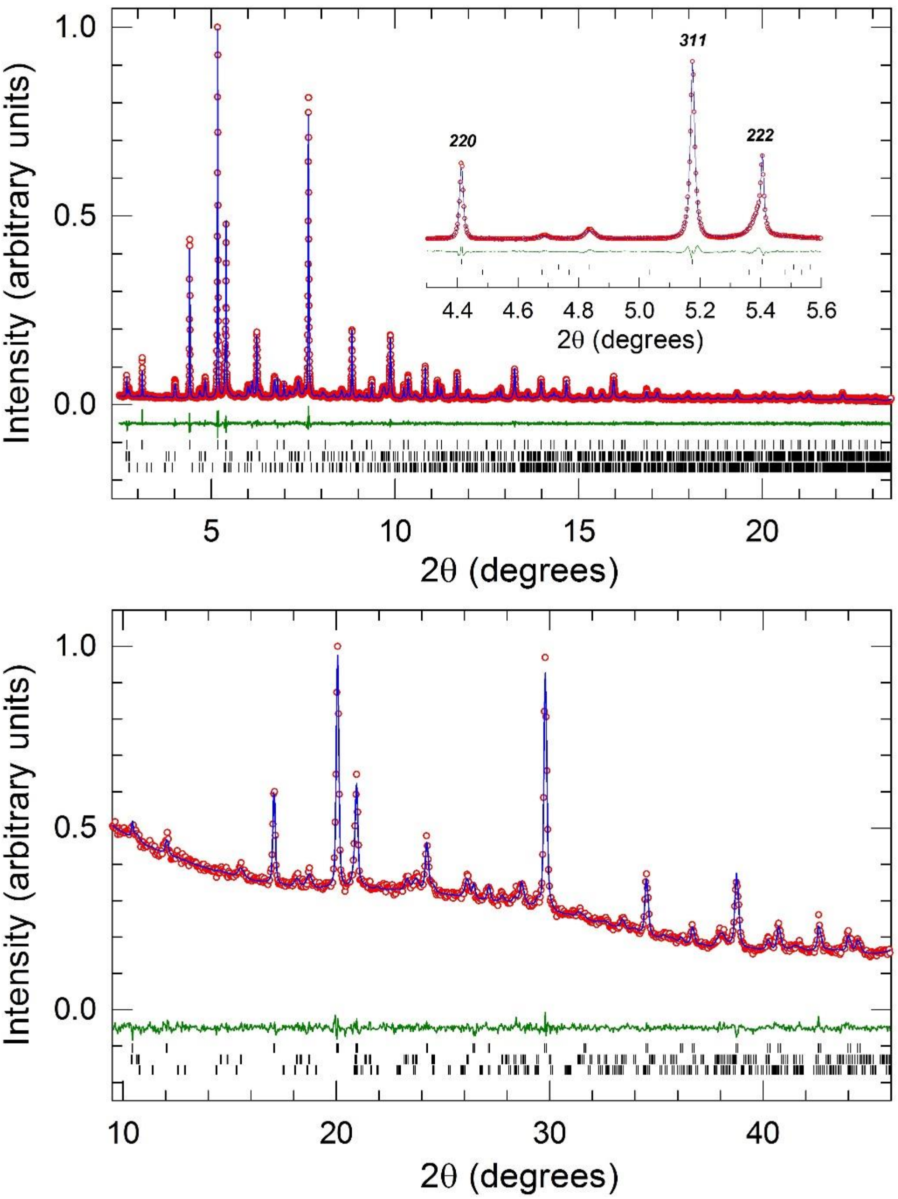

Figure 3.36: Powder X-ray diffraction profiles for *fcc*-rich Rb$_{0.25}$Cs$_{2.75}$C$_{60}$, synthesised with drop quenched rapid cooling protocols. Final observed (o) and calculated (blue line) diffraction profiles for synchrotron PXRD data (upper panel, λ = 0.399959 Å, drop quench experiment 1) and laboratory diffractometer PXRD data (lower panel, λ = 1.5418 Å, drop quench experiment 2). The lower green lines show the difference profiles, and bars mark the reflection positions of the *fcc* (top), *bco* (middle) and CsC$_{60}$ (bottom) phases. The inset shows an expanded view of the upper panel plot, with *fcc* phase reflections labelled.

In both drop quench experiments, the Rb$_{0.25}$Cs$_{2.75}$C$_{60}$ samples subjected to slow cooling had slightly lower *fcc* phase fractions than those cooled more rapidly. For drop quench experiment 1, where synchrotron PXRD data were available hence the analysis results should be most reliable, the *fcc* lattice in the slow-cooled sample was clearly the least expanded, and the *fcc* peaks notably broader than either sample cooled more rapidly.

Any distinction between drop quenched and air cooled samples is more ambiguous. Synchrotron PXRD data indicated that drop quenching into ice, salt and water (−3 °C) did not produce a higher quality *fcc*-rich sample than from cooling in air (the former exhibited a slightly less expanded *fcc* lattice, lower *fcc* fraction and broader *fcc* peaks). However, lab diffractometer data from drop quench experiment 2 suggested that drop quenching into liquid nitrogen produced a sample with slightly higher *fcc* lattice expansion and phase fraction and narrower peaks (on average), than the air cooled sample. Meanwhile, both chamber furnace quench experiments indicate that quench cooled samples had distinctly narrower *fcc* phase peak widths, and slightly higher *fcc* fractions and lattice expansivities than air cooled samples. Overall, no large distinction was seen between using liquid nitrogen and ice/water-based cryogen baths for quenching; more experiments would be required to draw firmer conclusions about their relative effects.

The *fcc* lattice parameters of $Rb_{0.2}Cs_{2.8}C_{60}$ and $Rb_{0.25}Cs_{2.75}C_{60}$ products from the four experiments appeared somewhat low, compared to the trend in *fcc* a with Rb_x established from the 'standard route' $Rb_xCs_{3-x}C_{60}$ ($0.35 \leq x \leq 2$) samples (see e.g. Fig. 3.2). The *fcc* lattice parameters from data collected with the laboratory diffractometer and from the synchrotron range from 14.678 to 14.704 Å and 14.696 to 14.702 Å, respectively; these are all smaller than the ambient temperature lattice parameter for *fcc* $Rb_{0.35}Cs_{2.65}C_{60}$ from synchrotron data (14.70780(9) Å, Table 3.2). From Fig. 3.2, *fcc* lattice parameters of ~14.72-14.73 Å would be expected if the *fcc* phase stoichiometry was close to the nominal stoichiometry. However, precisely comparing small lattice parameter differences between data from the two sources is not necessarily meaningful, owing to calibration/zero point differences.

It was next found that further annealing of the products at 430°C served to further increase their *fcc* phase fractions, in all experiments where this was undertaken (both chamber furnace experiments and drop quench experiment 2). The large number of experimental variables involved render a systematic comparison of these products difficult; one such experiment is now outlined. The x = 0.25 sample with highest *fcc* fraction from drop quench experiment 2, *i.e.* the drop quenched sample (69.5(4) % *fcc*), was subdivided into two ~45 mg pelletised portions. Both were annealed again at 430°C using the same vertical tube furnace setup as for the first quenching; after 52 hrs, one was quenched into ice/water/salt and the other allowed to cool in air, and the products structurally analysed using PXRD. From lab data, their *fcc* lattice parameters (14.6965(1) Å and 14.6967(2) Å) were identical within error to those in the previous stage (Table 3.15), but *fcc* phase fractions had increased to 82.6(1)-82.90(9) %. Significantly, however, Rietveld analysis of synchrotron PXRD data from the latter samples yielded notably higher lattice parameters than the lab data, of 14.71170(5)-14.71345(5) Å, indicating that these $Rb_{0.25}Cs_{2.75}C_{60}$ *fcc* phases are clearly more expanded than the aforementioned $Rb_{0.35}Cs_{2.65}C_{60}$ material. This was confirmed with magnetisation measurements, showing bulk superconductivity (estimated shielding fractions 42-50 %) and T_c, T_{max} ($\chi(T)$) values lower than those for $x = 0.35$, indicative of a more expanded *fcc* lattice. The more expanded sample, *i.e.* that drop quenched twice was characterised extensively, producing the $x = 0.25$ structural and magnetic data reported earlier throughout Sections 3.3 and 3.4.

3.6.3. Summary – effects of varying the cooling protocol on synthesis of *fcc*-rich $Rb_xCs_{3-x}C_{60}$ ($x = 0.2, 0.25$)

Solid-state synthetic routes can, contrary to the previous consensus,[**31, 71**] produce high quality bulk superconducting *fcc*-rich $Rb_xCs_{3-x}C_{60}$ materials where x is as small as 0.25, with excellent stoichiometry control. Two samples of nominal $x = 0.25$, reannealed portions of the drop quenched sample from the second experiment, have been synthesised with ~83% *fcc* phase and estimated shielding fractions of 42-50%; structural and magnetic characterisation confirmed that the interfullerene separations were around the expected value for $x = 0.25$ based on extrapolation of the well established trends from compositions ($0.35 \leq x \leq 2$), reported earlier in this chapter.

It must be noted that precise experimental consistency could unfortunately not be achieved in *e.g.* the preparation conditions for individual samples within each experiment; precise control of all factors was not possible with the available apparatus, *e.g.* the He(g) partial pressure used when sealing each ampoule, exact pellet masses (and therefore surface area, *etc.*), and the pressure applied to form pellets were prone to some variation, which could potentially be improved in future experiments *e.g.* by use of a digital hydraulic press.

The cooling protocol tests indicated that whilst slow cooling is clearly detrimental to sample quality, producing broader diffraction peaks and lower *fcc* phase fractions, any difference between quench cooling and cooling in air is marginal. In three of four cases, the quench-cooled sample had slightly narrower *fcc* peaks, higher *fcc* fraction and larger *fcc* lattice parameter, although in the fourth case, whilst the difference between the two was smallest of all experiments, the air-cooled sample had a larger *fcc* lattice parameter than the quench-cooled. However, increased annealing times at 430°C, interspersed with regrinding and pelletisation for improved sample homogeneity, appear to promote higher *fcc* phase fractions more strongly than cooling more rapidly does. The two most successful syntheses of *fcc*-rich $Rb_{0.25}Cs_{2.75}C_{60}$, described above, combined repeat annealings at 430°C with a drop-quench cooling technique.

3.7. Discussion

The presence of a Mott insulator-to-metal transition is one of the clear manifestations of electron correlation in condensed matter. However, only few materials are available, *i.e.* experimentally accessible, for studying a pure Mott transition without symmetry breaking, one key example being the pressure-induced transition in the κ-(BEDT-TTF)$_2X$ family of materials which are discussed further below [**184**]. Whilst insulator-to-metal transitions upon pressurising are also not unknown in fullerides, such as that reported in orthorhombic (NH_3)K_3C_{60},[**185**] the low symmetry of the crystal field in that case rendered unambiguous distinction between external and internal contributions problematic. The significance of the discovery of an insulator-to-metal transition upon pressurisation in *fcc* Cs_3C_{60}, which retains its cubic structure over all pressures investigated, is thus clear.

Pressure can induce such profound changes in materials such as the conversion of insulators into metals; pressures now accessible in laboratories can produce changes in the free energy of materials which exceed those of the strongest chemical bonds present at ambient pressure, at >10 eV; pressure can thus entirely redistribute electronic densities and alter the nature of chemical bonds.[**109**] Virtually every element is theoretically anticipated to be metallic above a certain pressure.

The $Rb_xCs_{3-x}C_{60}$ systems, however, appear to be unique in undergoing an isostructural transition from insulating, to metallic, and finally becoming superconducting, upon cooling alone (*i.e.* at ambient pressure); this demonstrates the significance of the present results. Whilst most systems exhibiting an insulator-to-metal transition upon changing temperature do so upon warming (*e.g.* RbC_{60} [**186**]), there are some which do demonstrate this behaviour upon cooling. The superconducting fulleride Na_2CsC_{60} reportedly undergoes an insulator-metal transition upon cooling, evidenced through ESR and optical reflectivity measurements;[**187**] however, such behaviour has not been reported in other A_3C_{60} materials until the present study, and in Na_2CsC_{60} the purported transition is coincident with the low temperature simple cubic to high temperature *fcc* structural transition at around 300 K. The hole-doped ($A_{1-x}B_x$)MnO_3-type manganites are a key example of a cooling-induced insulator-to-metal transition in a non-fulleride system (for a representative example, see Ref. [**188**]).

Meanwhile, some organic superconductors, such as several bis(ethylenedithio)tetrathiafulvalene–based *κ*-(BEDT-TTF)$_2X$ materials and

$EtMe_3P[Pd(dmit)_2]_2$ (dmit = 1,3-dithiole-2-thione-4,5-dithiolate), exhibit analogous paramagnetic insulator-metal-superconductor transitions upon cooling, but only under moderate applied pressures.[**90, 189, 190**] Furthermore, these materials possess lower crystallographic symmetry than the highly symmetric *fcc* A_3C_{60} lattice.

The use of hydrostatic pressure and temperature as parameters to control unit cell volume, instead of alloying techniques, allows the fine alteration of experimental conditions, diminishing any effect from impurities which could influence the transition and enabling isobaric and isothermic sweeps.

A cusp in $\chi(T)$, besides characterising an insulator-to-metal transition as found to be the case here, could alternatively be indicative of an antiferromagnetic ordering transition (*e.g.* as observed in A15 Cs_3C_{60} and in $Li_3(NH_3)_6C_{60}$ [**89, 95**]). However, the complementary ^{13}C NMR measurements undertaken by our collaborators on samples of the overexpanded $Rb_xCs_{3-x}C_{60}$ systems provided by us have not found any evidence of ^{13}C NMR line broadening below the MIT, which would be anticipated if the transition were, alternatively, corresponding to the onset of magnetic ordering [**151, 191**]. These results further strengthen the conclusions arising from the characterisation presented in this chapter.

The relaxation of nuclear spins in a metal is typically dominated by their coupling with conduction electrons, resulting in a simple dependence of T_1 (obtained through *e.g.* NMR spectroscopy) on $N_{\varepsilon F}$, termed the Korringa law; $1/T_1T$ is expected to be constant, asssuming negligible variation in $N_{\varepsilon F}$ with temperature.[**192**] In good agreement with the present $\chi(T)$ trends, the evolution of $1/T_1T$ extracted from the ^{13}C NMR measurements for overexpanded $Rb_xCs_{3-x}C_{60}$ has indicated marked deviation from the Korringa law and from expected Fermi liquid behaviour (Fig. 3.37);[**151**] a monotonic increase in $1/T_1T$ with decreasing T is observed, followed by an exponential drop below a maximum (towards a value typical of conventional underexpanded metallic fullerides), finally dropping again below the superconducting T_c and vanishing as T tends towards 0 K.[**151**] In contrast to the ^{13}C NMR results, however, no evidence of an insulator-metal transition in Rb_2CsC_{60}, as evidenced from an anomaly in $V(T)$ behaviour or cusp in $\chi(T)$, is found from the data presented earlier in this chapter. This could relate to the subtlety of the transition in the underexpanded regime, and that ^{13}C NMR is less sensitive to influences *e.g.* from magnetic impurities or minor phases than the magnetic susceptibility is; the maximum in the $1/T_1T$ data for Rb_2CsC_{60}, highlighted with an arrow in Fig. 3.37, was relatively weak and poorly defined.

Deviation from the Korringa law in the temperature dependence of $1/T_1T$ has also been observed in *e.g.* certain of the aforementioned κ-(BEDT-TTF)$_2X$ materials; $1/T_1T$ is significantly enhanced just above the superconducting T_c, signifying that the normal metallic phase is highly correlated, and above a distinct cusp, $1/T_1T$ gradually decreases with increasing T, attributed to magnetic fluctuations.[**90**] This behaviour in these materials is analogous to that observed in the overexpanded $Rb_xCs_{3-x}C_{60}$ systems.

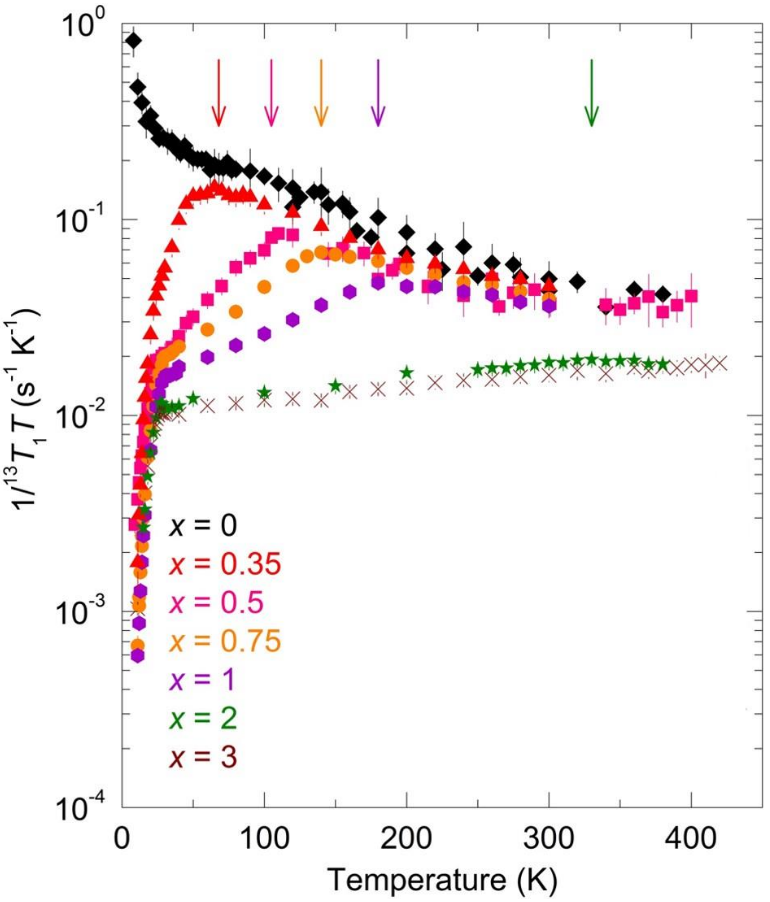

Figure 3.37: Temperature evolution of $1/T_1T$ for *fcc* $Rb_xCs_{3-x}C_{60}$ ($0 \leq x \leq 3$), from ^{13}C NMR measurements (data from Prof. D. Arčon research group, reproduced with permission).[**151, 191**] Arrows on the main plot mark T_{MIT} for each sample, where applicable, defined as follows: 65(5), 110(10), 140(10), 180(5) and 330(5) K, for x = 0.35, 0.5, 0.75, 1 and 2, respectively.

Besides NMR spectroscopy, IR spectroscopic characterisation undertaken by our collaborators on *fcc*-rich $Rb_xCs_{3-x}C_{60}$ samples supplied by us has also yielded novel findings about the electronic properties of this system close to the Mott insulator boundary.[**191**] IR measurements have provided further direct evidence for the nature of the observed transition being Mott insulator-metal, from the step-like appearance of a continuous spectral background upon cooling through the transition caused by free carrier absorption (Fig. 3.38). Upon cooling for compositions $x = 0.75$, 1, 1.5, a gradual change in $T_{1u}(4)$ vibrational mode peak shape is found, evolving from Lorentzian to Fano resonances; the latter is indicative of coupling of localised vibrations to an electronic excitation continuum, *i.e.* conventional metallicity. Meanwhile, the $T_{1u}(4)$ mode splitting in the IR spectra for overexpanded compositions $x = 0.35$ and 0.5, which increases from twofold to fourfold upon cooling,[**191**] indicates the presence of the molecular Jahn-Teller effect, recently established in *fcc* Cs_3C_{60}.[**98**] Magnetic susceptibility measurements presented in this chapter indicated that the normal metallic state (above T_c) of overexpanded $Rb_xCs_{3-x}C_{60}$ ($0.25 \leq x \leq 1$) cannot be described by a simple Pauli susceptibility term and is significantly enhanced approaching the transition because of strong electron correlations; the co-existence of the IR mode splitting, preserved into the metallic state, and the aforementioned absorption background, directly implies the localisation of electrons on C_{60}^{3-} ions for sufficiently long times to be detectable on the IR experimental timescale of 10^{-11} s.[**191**] The Jahn-Teller metallic state in overexpanded $Rb_xCs_{3-x}C_{60}$, distinct from the conventional metallic state observed for Rb_2CsC_{60} and for *e.g.* $Rb_{1.5}Cs_{1.5}C_{60}$ at low temperature, is a key experimental finding from this collaborative work.

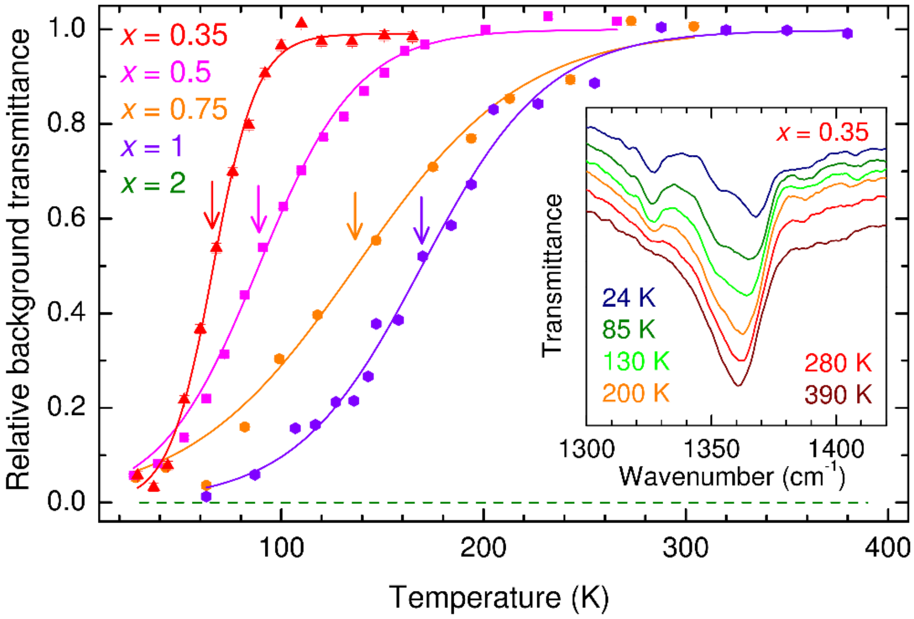

Figure 3.38: Temperature dependence of the normalised IR background transmittance for *fcc* $Rb_xCs_{3-x}C_{60}$ ($0.35 \leq x \leq 1$), defined as average intensity in a featureless spectral region, 750-960 cm^{-1} (data from Prof. K. Kamarás research group, reproduced with permission).[**191**] Arrows indicate the midpoint temperatures of fits to sigmoidal functions (solid lines); Rb_2CsC_{60} (dotted line) has a metallic background over the measured temperature range. Inset: temperature dependence of the $Rb_{0.35}Cs_{2.65}C_{60}$ $T_{1u}(4)$ C_{60}^{3-} vibrational mode IR spectra (shifted vertically for clarity).

One key finding from the data presented here is that no phase separation indicative of a phase co-existence regime is evidenced, *e.g.* from examination of the PXRD profiles (Fig. 3.6). Given that the Mott insulator-metal transition should be of first order, a phase co-existence regime ending in a critical point in the volume-temperature electronic phase diagram would be anticipated; thus, we conclude that for the entire compositional range of *fcc* $Rb_xCs_{3-x}C_{60}$ materials investigated here ($0.25 \le x \le 2$) the insulator-metal transition temperatures are above the critical point temperature, in the supercritical regime. The transition is thus best described as a crossover, consistent with the observed broadening of the crossover over an increasingly wider temperature range as more Rb is substituted into the *fcc* lattice, and the crossover moves further away from the critical point.

Whilst the Mott transition line of the typical Mott insulator κ-(BEDT-TTF)$_2$Cu[N(CN)$_2$]Cl has a positive gradient ($\mathrm{d}T/\mathrm{d}P > 0$) at high temperatures, this becomes negative at low temperatures as AFM ordering appears in the insulating phase.[**193**] In contrast, the presence of spin frustration in κ-(BEDT-TTF)$_2$Cu$_2$(CN)$_2$ has been used to rationalise the positive $\mathrm{d}T/\mathrm{d}P$ of the Mott boundary line to low temperatures;[**189**] this absence of an insulator-metal-insulator re-entrant transition was justified through the Clausius-Clapeyron equation, $dT/dP = \Delta V/\Delta S$. As the metallic unit cell volume was known to be smaller than that of the insulator, ΔS ($= S_{\mathrm{ins}} - S_{\mathrm{metal}}$) must logically be positive, with the authors arguing that this may occur because magnetic ordering is suppressed by the spin frustration (whilst the large spin entropy of a magnetically-ordered paramagnetic Mott insulator should rapidly die away with decreasing temperature, and the sign of ΔS could thus change upon cooling).[**189**]

The lack of evidence found in this study for any change of crystal symmetry at the insulator-metal transition in overexpanded $Rb_xCs_{3-x}C_{60}$, the sole anomaly evident from high resolution synchrotron PXRD data being a distinct volume collapse, is significant. An isostructural phase transition with volume collapse, occuring at a Mott insulator-metal transition, is found in other materials (albeit pressure-induced), *e.g.* MnO, which is another cubic system undergoing a transition from a paramagnetic insulator to paramagnetic metal.[**194**] However, in MnO, increased crystal field splitting upon cooling, competing with the exchange energy, induces a high-spin to low-spin transition, resulting in the observed volume collapse [**195**] (a spin crossover-induced isostructural volume collapse has also been reported in $LaFeO_3$ [**196**]). Pressure-induced isostructural volume collapses have also been ascribed to electronic transitions (*e.g.* a valency transition from $Sm^{2.3+}$ towards Sm^{3+} in $Sm_{2.75}C_{60}$ [**197**], or *f*-electron delocalisation in cubic Ce (γ-α) [**198**]). Neither of these mechanisms, however, can be responsible for the isostructural volume collapse observed in overexpanded *fcc* $Rb_xCs_{3-x}C_{60}$ materials upon reduction of interfulleride spacing; susceptibility measurements (section 3.4.3) indicated the low-spin, $S = ½$ character of these systems under ambient P, T conditions, whilst Rb^+/Cs^+ cannot undergo electronic transitions to yield a Kondo-like volume collapse.

The virial theorem has been used to rationalise the discontinuous variation of unit cell volume with hole doping level in the $LaTiO_{3-\delta}$ perovskites, which accompanies a first-order isosymmetric transition from localised, or strongly correlated to itinerant electronic behaviour as δ is increased[**199, 200**]. The equilibrium Ti-O bond length is smaller in the itinerant-electron phase (from the virial theorem, a transition from localised to itinerant behaviour entails a decrease in mean kinetic energy of the electronic system, which must be balanced by a decreased magnitude of mean electron potential energy; the *d*-like electrons in a TiO_3 array subject to this change occupy antibonding states).[**200**]

This investigation also sought to compare the effects of applying hydrostatic pressure, to those of chemical pressure, on the metal-insulator transition; $Rb_{0.5}Cs_{2.5}C_{60}$ was selected for high-pressure structural and magnetic characterisation at $T > T_c$. Earlier NMR investigations of both Cs_3C_{60} superconducting polymorphs found a large variation in the Mott transition pressure with temperature, with the transition boundary tending towards a liquid-gas-like critical point, typically found at high temperature in Mott transitions.[**141**] In the $Rb_xCs_{3-x}C_{60}$ analogues, applying chemical pressure (through increasing the Rb/Cs ratio) induces analogous effects to that induced through hydrostatic pressure in Cs_3C_{60}; the insulator-metal transition in overexpanded $x = 0.25$, 0.35 etc is relatively sharp, whilst the transition becomes more gradual, extending over a larger temperature range as the Rb content is increased, eventually smearing out such that there is no longer a detectable cusp in $\chi(T)$ nor is any anomaly detectable in the expansivity ($x = 2$).

Electron paramagnetic resonance (EPR) measurements indicated that relaxation times of conduction electrons in underexpanded A_3C_{60} are highly influenced by the alkali metals used.[**167**] This study has shown that the key effects on the structural and electronic properties from varying the alkali metal stoichiometry in *fcc* $Rb_xCs_{3-x}C_{60}$ arise solely from the variation in unit cell volume, controlled in turn by stoichiometry (*e.g.* Raman measurements have provided no evidence for variation in charge transfer across the compositional series, and $T_{c(max.)}$ occurs at a unit cell volume of ~755 $Å^3/C_{60}$, irrespective of composition). However, the increasing disorder predicted with increasing x_{Rb} was experimentally found to suppress $T_{c(max.)}$.

In the κ-$(ET)_2X$ systems, χ_{spin} at ambient temperature and pressure of the Mott insulator κ-$Cu[N(CN)_2]Cl$ is close to those of several metallic members, interpreted in terms of there being no significant anomaly in the uniform (q = 0) spin fluctuation through the Mott transition, where a perceptible change occurs in the charge degrees of freedom.[**184**]

In Na_2CsC_{60}, deviation from the Korringa law (observed in ^{13}C NMR), i.e. strong deviation from the linear T dependence expected for a simple metal, was attributed to enhanced stability of dynamic Jahn-Teller-distorted C_{60}^{2-} and C_{60}^{4-} species, with the authors arguing that this should be applicable for other A_3C_{60} materials, including Rb_3C_{60}. Although these systems are known to be metallic, the extracted characteristic fluctuation times for the electronic spins were typically $\sim 10^{-14}$ s, comparable to the hopping rate and thus compatible with metallic character.[**201**]

3.8. Conclusions

Previous studies had demonstrated that overexpanded *fcc* $Rb_xCs_{3-x}C_{60}$ phases could be synthesised by solution chemistry, superconducting at ambient pressure in contrast to the most expanded member Cs_3C_{60} subsequently synthesised [**140**], and that the superconducting T_c may decrease with unit cell volume above a certain critical value.[**31, 71**] This behaviour contrasts starkly with the well-established trend in the lesser expanded *fcc* A_3C_{60} systems and, along with other evidence, demonstrated that superconductivity in the highly-expanded *fcc* system cannot be described with a simple BCS-type model. However, issues with sample quality were present and limited characterisation was undertaken *e.g.* of the normal state properties above T_c. The first successful synthesis of *fcc* Cs_3C_{60}, insulating at ambient pressure, served to highlight that the evolution of the normal state properties between metallicity in *e.g.* K_3C_{60} and insulating Cs_3C_{60} had not yet been experimentally probed.

In this study, for the first time, solid-state synthesis has successfully been employed to obtain *fcc*-rich $Rb_xCs_{3-x}C_{60}$ materials, with x systematically varied between 2 and 0.25. All samples exhibited bulk superconductivity (in contrast to *e.g.* a previous work [**71**]), with good stoichiometry control, and with Raman spectroscopy confirming the C_{60}^{3-} reduction state of the majority phase. Extensive structural and magnetic characterisation of the series has been undertaken, at both ambient and elevated pressures, leading to several novel observations. Firstly, combining high-pressure structural and magnetization data to parameterise the variation in T_c with unit cell volume, a universal superconductivity 'dome' could be established. Significantly, in overexpanded $Rb_xCs_{3-x}C_{60}$ ($0.25 \leq x \leq 1$), an isostructural insulator-to-metal transition can be induced through cooling alone at ambient pressure, evidenced through a distinctive unit cell volume collapse and by a cusp in the magnetic susceptibility (together with complementary evidence from other techniques such as solid-state NMR spectroscopy, undertaken on materials provided by me through collaboration with other researchers [**151**]). The transition onset temperature may be tuned through application of both chemical pressure via adjusting the Rb^+/Cs^+ dopant ratio, or hydrostatic pressure, which has allowed us to clearly establish a new Mott insulator-metal boundary on the *fcc* A_3C_{60} electronic phase diagram.

Whilst above the transition the paramagnetic insulating state appears extremely similar to that of Cs_3C_{60} in character ($S = ½$, negative Weiss temperatures of similar magnitude), below the transition the magnetic susceptibility of the magnetic state indicates it is significantly different in character to that of e.g. K_3C_{60} (Pauli paramagnetic behaviour); the present results show that magnetic susceptibility as a function of volume is strongly enhanced approaching the Mott insulator transition boundary, underlining the significance of strong electron correlations in these materials. As Rb_x increases, the onset temperature increases and the transition becomes increasingly smeared out and broader, until it can no longer be defined in Rb_2CsC_{60} in the characterisation presented in this thesis. Evidence is also presented for an insulator-metal transition induced in $Rb_{0.5}Cs_{2.5}C_{60}$ at ambient temperature, through applying hydrostatic pressure, as indicated through a volume collapse (with the onset being consistent with the transition boundary established through ambient pressure investigations). These results may lead to more in-depth experimental and theoretical studies of the nature of the insulator-metal transition, providing a rare example of such a transition in a highly symmetric system (which is not further complicated by *e.g.* crystallographic symmetry change at the transition) which is easily experimentally accessible at ambient pressure, potentially paving the way for *e.g.* even higher resolution structural investigation.

Chapter 4- The A15-structured A_3C_{60} (A = Cs, Ba) systems

4.1 Introduction

4.1.1 Structural properties of A15 A_3C_{60} (A = alkali, alkaline earth metal)

The A15 structure type (A_3B) comprises three non-intersecting orthogonal A chains, bisecting the faces of a cube; the linearity of these chains is known to be favourable for high T_c in A15 intermetallic systems.[**202**] Three fulleride systems, of A_3C_{60} stoichiometry, are known to adopt this structure type (to date): A = Cs, Ba and Sr. A15 A_3C_{60} can be considered an ordered defect structure of A_6C_{60}, where one of two tetrahedral interstitial sites are occupied by cations, instead of both in the latter structure.

Prior to any experimental observation of the A15 structure in alkali-metal fullerides, its existence was predicted to be most probable for A = Cs, due to the good size match and the anticipated relative destabilising of the *fcc* structure by the size mismatch between Cs and its tetrahedral voids.[**38**] The tetrahedral sites in a bcc sphere packing, which have distorted tetrahedral symmetry, are 31% larger than the tetrahedral sites in the *fcc* sphere packing.[**63**] In contrast to the *fcc* A_3C_{60} compositional series (A = K, Rb, Cs or a combination), the A15 structure in alkali-metal fullerides has indeed to date only been reported experimentally for A = Cs;[**49**] an attempt to partially substitute Rb^+ into the lattice proved challenging,[**71**] with the latter study concluding that the A15 phase is resilient to cationic substitution of Cs^+ by Rb^+.

Two different C_{60} orientations are possible in the $Pm\overline{3}n$ A15 A_3C_{60} structure (the twofold axis of the body-centre molecule is rotated by 90° with respect to the molecule at the origin).[**63**] Therefore two inequivalent tetrahedral sites are potentially available for cation doping; one which faces only pentagons on the neighbouring C_{60} molecules, and one facing only hexagons (Fig. 4.1). Prior to the synthesis and structural characterisation of A15 Cs_3C_{60}, a theoretical study of the energetics and structural stability of Cs_3C_{60} reported that a 'hexagonally-coordinated' A15 Cs_3C_{60} phase should be lower in energy than a 'pentagonally-coordinated' equivalent (at the optimised lattice constant of the study, 11.67 Å).[**54**] However, the pentagonally-coordinated phase was found to be softer than the hexagonally-coordinated phase, and at lower volume (*i.e.* higher pressure), a crossover between the energy-volume trajectories of the two phases was found, such that below a certain packing density, the pentagonally-coordinated phase should be lowest in energy. Experimentally, however, only hexagonally-coordinated A15 Cs_3C_{60} has hitherto been reported, at both ambient and under moderate applied pressures.[**49, 140**]

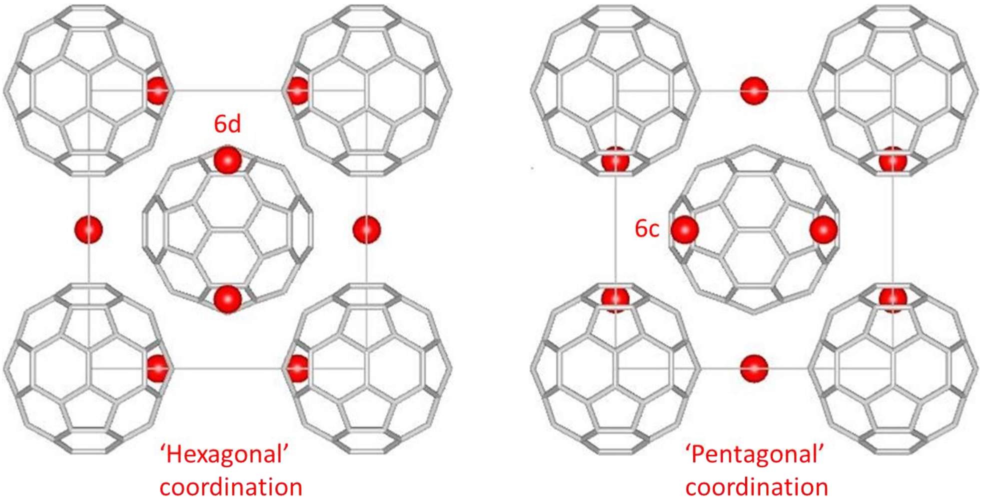

Figure 4.1: The two possible structures of A15 A_3C_{60}, where the A^{n+} cation is surrounded by hexagonal faces (left) and by pentagonal faces (right). With the C_{60} orientation depicted, these correspond to full occupation of the Wyckoff sites 6*d* and 6*c*, respectively, by A^{n+}.

The A15 structure has also been identified in the alkaline earth metal fullerides, namely Ba_3C_{60} and Sr_3C_{60}.[**63, 64**] In contrast to A15 Cs_3C_{60}, however, occupation of the pentagonally-coordinated site in Ba_3C_{60} is reportedly strongly favoured over occupation of the hexagonally-coordinated site (from Rietveld analysis of laboratory X-ray diffraction data); electron deficiency of the five-membered rings, together with the divalent nature of the Ba^{2+} dopant cations, purportedly plays a significant part in determining the coordination geometry.[**63**] The close correspondence between the computed tetrahedral interstitial site radius, at 1.32 Å, and that of Ba^{2+}, of 1.33 Å, suggested that divalent barium cations in Ba_3C_{60} are virtually completely ionised; this was later confirmed by photoelectron spectroscopy.[**203**]

Kortan and coworkers predicted a varying orientation dependence of C_{60} dopant interaction with charge state, whereby the C_{60}^{3-} cation energy is lower for the hexagonal coordination. Whilst the *fcc* structure has a perfectly orientated hexagonal interstitial site, and is indeed observed experimentally for A_3C_{60} (A = K, Rb, Cs or a combination), the preferential hexagonal cation coordination found in A15 Cs_3C_{60} [**49**] is also consistent with this. No *fcc* Ba_3C_{60} phase has been experimentally reported. As a rule, the occupation of octahedral interstices by donor atoms in Ba_xC_{60} fullerides is avoided, as a consequence of a less efficient covalent Ba-C interaction compared to the case where Ba is tetrahedrally coordinated.[**204**]

Like Cs_3C_{60}, Sr_3C_{60} reportedly exists in two cubic forms: *bcc* A15 and *fcc*.[**64**] A15 Sr_3C_{60} is, in contrast to Ba_3C_{60} and Cs_3C_{60}, orientationally disordered, with space group $Pm\overline{3}$; this has precluded clear determination of cation interstitial locations from structural investigation reported thus far.[**64, 205**] As the Cs and Ba analogues only were studied in this experimental work, further discussion will focus on these two systems.

4.1.2 Electronic and magnetic properties of A15 A_3C_{60} (A = Cs, Ba)

The A15 crystal structure has long attracted attention in the field of superconductivity, since superconductivity in A_3B intermetallic compounds with A15 structure was discovered in 1953, with T_cs of up to 23.2 K (Nb_3Ge)[**206**]. Superconductivity in an A15-structured fulleride has been confirmed in one material only, with the discovery of bulk superconductivity under applied pressure in A15 Cs_3C_{60} in 2008.[**49**] Uniquely in fullerides, Cs_3C_{60} has two superconducting polymorphs; *fcc* Cs_3C_{60}, isostructural to the well-established A_3C_{60} series (A = K, Rb, Cs or a combination), also shows pressure-induced superconductivity (as discussed in Chapter 3).[**140**] Superconductivity in A15 Cs_3C_{60} emerges from an antiferromagnetic insulating state upon the application of hydrostatic pressure, with T_c initially increasing with pressure up to ~0.7 GPa, and reaching a maximum T_c = 38 K.[**89**] The superconducting gap magnitude was recently found to be significantly larger ($2\Delta/k_BT_c > 5$) than the BCS value established for underexpanded *fcc* A_3C_{60}, and increases with increasing unit cell volume approaching the Mott insulator boundary.[**207**]

A15 Cs_3C_{60} has an ambient pressure insulating ground state with an effective magnetic moment of ~1.3-1.6 μ_B per C_{60}^{3-} in the paramagnetic regime,[**208, 209**] which orders antiferromagnetically below T_N = 46-47 K with a reduced staggered moment of 0.6-0.9 μ_B/C_{60}^{3-} (somewhat reduced below 1 μ_B/C_{60}^{3-}),[**89, 141, 208**] consistent with a low-spin $S = ½$ electronic state. Above T_N, the paramagnetic susceptibility adheres to the Curie-Weiss law with negative Θ (−68 K [**89**]), indicative of antiferromagnetic exchange interactions.[**89, 209**]

A magnetic structure for A15 Cs_3C_{60} with a magnetic wave vector **q** = (0.5, 0.5, 0.5) has been tentatively proposed from ^{133}Cs NMR spectroscopy,[**208**] implying doubling of the nuclear unit cell along all three directions, indicating that interfulleride exchange coupling between both first and second nearest C_{60}^{3-} neighbours is significant. This so-called 'AF2' ordering, illustrated schematically in Fig. 4.2, was described earlier theoretically for a bcc S = ½ Heisenberg antiferromagnet [**210**]. However, a small spin canting between the two magnetic sublattices, resulting in weak ferromagnetism, has also been proposed from the small positive spontaneous magnetic moment observed in the ordered state (rationalised by either ferromagnetic exchange from an antiferrodistortive contribution to dynamical coupling of Jahn-Teller distortion axes, or by Dzyaloshinskii-Moriya coupling from the lack of an inversion centre on the direct exchange pathway between adjacent fulleride ions).[**89**] Zero-field μ^+SR experiments have demonstrated the long-range nature of the antiferromagnetic ordering.[**89**] Upon moderate pressurisation, T_N increases up to 49.5 K (0.36 GPa), with exchange coupling enhanced by reduced interfulleride distances; above 0.26 GPa superconductivity and antiferromagnetism coexist, with antiferromagnetism suppressed above 0.42 GPa (consistent with a first-order insulator-superconductor transition).[**89**]

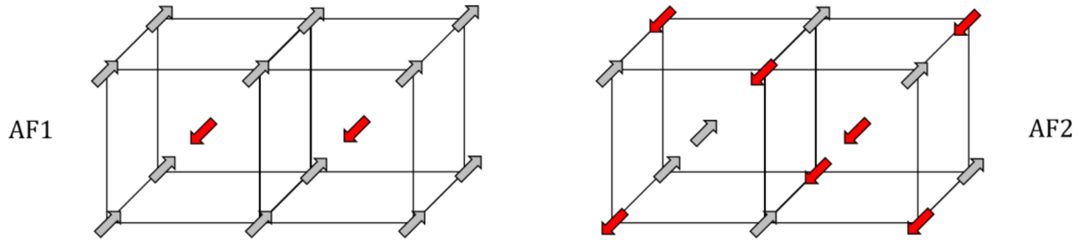

Figure 4.2: Two collinear magnetic ordering arrangements as discussed for a body-centred-cubic S = ½ Heisenberg antiferromagnet, with the spin direction arbitrarily shown (adapted from ref. [**210**]); simulations to an experimental ^{133}Cs NMR spectrum for A15 Cs_3C_{60} at 14 K indicated that the AF2 structure is most probable.[**208**]

Recently, the presence of the dynamic Jahn-Teller (JT) effect was confirmed using infrared spectroscopy in the A15 Cs_3C_{60} insulating ground state;[**98**] it was also recently detected in *fcc* $Rb_xCs_{3-x}C_{60}$ (x = 0, 0.5) using magic-angle-spinning (MAS) NMR and IR spectroscopy.[**98, 151**]

In contrast to the Cs analogue, A15 Ba_3C_{60} has a filled t_{1u} band and is an insulator with a band gap of at least ~0.35 eV;[**203, 211**] this behaviour differs from that of Ba_4C_{60} and

Ba_6C_{60}, which are known to be superconducting and metallic, respectively,[**18, 173**] though the latter phase was originally incorrectly proposed to be superconducting.[**212**] Whilst bcc Ba_6C_{60} also has a filled HOMO band (t_{1g}), its metallicity, in contrast to the insulating alkali-metal A_6C_{60} analogues, has been attributed to hybridisation effects between Ba d orbitals and C_{60} pπ levels.[**213**]

4.1.3 Purpose of present study

Superconductivity in A15 Cs_3C_{60} emerges under applied pressure, from an antiferromagnetic insulating state through a first-order transition, with T_c first increasing with pressure up to a maximum of 38 K and decreasing at pressures above ~7 kbar (which cannot be explained by conventional theory used to desribe superconductivity in the underexpanded A_3C_{60} systems). Significantly, this transition was classified as purely of electronic origin, with no structural changes observed under pressure in the cubic lattice besides the smooth contraction expected upon pressurisation.[**49**] The appearance of superconductivity and the dome-shaped T_c *vs.* pressure behaviour were thus attributed solely to the effects of volume contraction, leading to the conclusion that the transition to the superconducting state is purely electronic in nature.

Given the symmetry breaking associated with magnetic order, if any anomalous structural changes as a function of temperature or pressure were clearly demonstrated in A15 Cs_3C_{60}, besides the expected effects of lattice expansion or contraction, it would be of fundamental importance in interpreting and understanding the electronic and magnetic behaviour of this material. For instance, studies of the alkali-metal *fcc* A_3C_{60} superconductors have demonstrated that lattice expansions and symmetry changes caused by ammonia intercalation (even when, in some systems, such changes are relatively small in magnitude) dramatically suppress superconducting and metallic behaviour, yielding antiferromagnetic and insulating states.[**21, 95**] The t_{1u} molecular orbital (MO) triple degeneracy resulting from the cubic lattice symmetry is thought to be critical for retaining metallicity and allowing superconductivity to emerge in the alkali-metal fullerides. In face-centred-orthorhombic $(NH_3)A_3C_{60}$ and $(CH_3NH_2)K_3C_{60}$, AFM ordering at low temperatures is a consequence of C_{60} orientational order and the removal of t_{1u} MO degeneracy through reduction of crystal symmetry; the (U/W) ratio then exceeds the critical value for the metal-to-insulator transition.

We now consider the antiferromagnetic ordering transition found in A15 Cs_3C_{60} on cooling and its possible implications on the material's structure. In the general case, the Curie principle necessitates that crystal symmetry must be a subgroup of each physical quantity, e.g. magnetic order; magnetic ordering transitions are thus often accompanied by small lattice distortions, producing anomalies in elastic properties. Spontaneous magnetostriction, which increases on cooling, can lower the crystal symmetry below the magnetic ordering onset. The onset of antiferromagnetic order in A15 Cs_3C_{60} should theoretically be accompanied by the breaking of both spin rotational and orbital rotational symmetry, *i.e.* orbital ordering should ensue below T_N.[**76**]

However, existing high-resolution ambient-temperature and low-temperature high-pressure synchrotron PXRD studies have hitherto provided no indication of deviation from cubic symmetry at low temperatures in A15 Cs_3C_{60}.[**49, 89**] Neither did a single dataset high-resolution PXRD dataset collected at 10 K at ambient pressure.[**89**] A study of PXRD datasets collected at nominal temperatures of ambient temperature and 12 K found no significant structural differences between the two datasets;[**71**] however, cryostat calibration error was suspected, and comparison of the '12 K' lattice parameter with new results reported in the current study reveals that the low temperature data was likely to have been collected at ~60 K, above the T_N. Yet no systematic or reliable study of structural variation with temperature has been reported until now; such an investigation is now presented for the first time in this thesis. The close relation of magnetic and crystallographic properties renders knowledge of the crystal symmetry and lattice parameters at different temperatures essential for understanding the properties of A15 Cs_3C_{60}.

Due to the time scale, it would only be possible to detect a JT distortion in fulleride anions through diffraction techniques if some static component were present; if the JT effect were purely dynamical, quantum tunnelling and/or thermal hopping of C_{60} between equivalent distorted energy 'valleys' would be expected to re-establish, on average, the original icosahedral molecular symmetry. Whilst contrary to the present experimental consensus, the hypothetical presence of a static component in the JT distortion could actually be anticipated from theory, through surmising that orbital ordering should occur below T_N, to resolve the spin and orbital degeneracy.[**76**] Such a static JT distortion would lower the crystallographic symmetry from the time-averaged cubic structure, which would be highly significant development in understanding the properties of these materials if proven experimentally. Evidence for the static JT effect has recently been reported in insulating *fcc* Cs_3C_{60} at low temperatures.[**214**] However, in the recent IR study, no evidence was found for a static component of orbital ordering in A15 Cs_3C_{60} down to 28 K, leading to the conclusion that if such a component is present, it must be small in magnitude.[**98**]

Although a high resolution PXRD study has indicated that no structural transformations occur in *fcc* Cs_3C_{60} upon pressurising to 12 GPa,[**140**] the structural evolution of A15 Cs_3C_{60} with pressure has been investigated only up to ~2.5 GPa;[**49, 89**] the structural (and electronic) response of the system to higher applied pressures has remained unestablished. Intriguingly, the disappearance of a phase indexed with A15 structure in multiphase $Cs_{3+\alpha}C_{60}$ at high pressures (between 30-40 kbar) has been reported by Fujiki and coworkers;[**58**] however, no explanation was proposed for this observation. Palstra *et al.* had also reported diminishing intensity of XRD peaks attributed to an A15-structured phase with pressure in Cs_xC_{60}, tentatively ascribing the changes to a structural transition to a body-centred-cubic or body-centred-tetragonal phase.[**56**] In this chapter, the structural properties of A15 Cs_3C_{60} under hydrostatic pressure are investigated, at both low and ambient temperature, extending the studies to higher pressures than those previously reported and using a much higher quality sample (*e.g.* high A15 phase content and crystallinity) than those employed in references [**58**] and [**56**].

Meanwhile, no *in situ* high pressure structural studies have been reported for A15 Ba_3C_{60} as a bulk phase to date, so its structural properties at high pressure remain unknown. However, two high pressure structural studies of Ba_4C_{60}, where the compressibility of Ba_3C_{60} as a minority phase present in the samples was also reported, both indicated the existence of a potential compressibility anomaly in Ba_3C_{60}, with onset ~2 GPa (Fig. 4.3).[**165, 215**]

At the time, this was not investigated further. Despite the limitations in these studies (the low Ba_3C_{60} phase fraction led to relatively large errors in volumes, and no detailed analysis of the phase was possible), upon a phase pure and highly crystalline sample of Ba_3C_{60} recently becoming available, this observation was deemed to merit further investigation. A recent study of the structural properties of Ba_3C_{60} under ambient conditions, of samples recovered after pressurisation up to 15 GPa, reported that Ba_3C_{60} amorphises upon pressurisation, though not significantly after application of only 5 GPa.[**216**] However, data were only collected for samples recovered after depressurisation, *i.e.* no structural analysis was undertaken at elevated pressures. In this chapter, the first detailed structural investigation (to our knowledge) of bulk A15 Ba_3C_{60}

under applied pressure is described and the origin of the anomalous compressibility feature is elucidated. Amorphisation was not observed upon pressurisation up to 11 GPa.

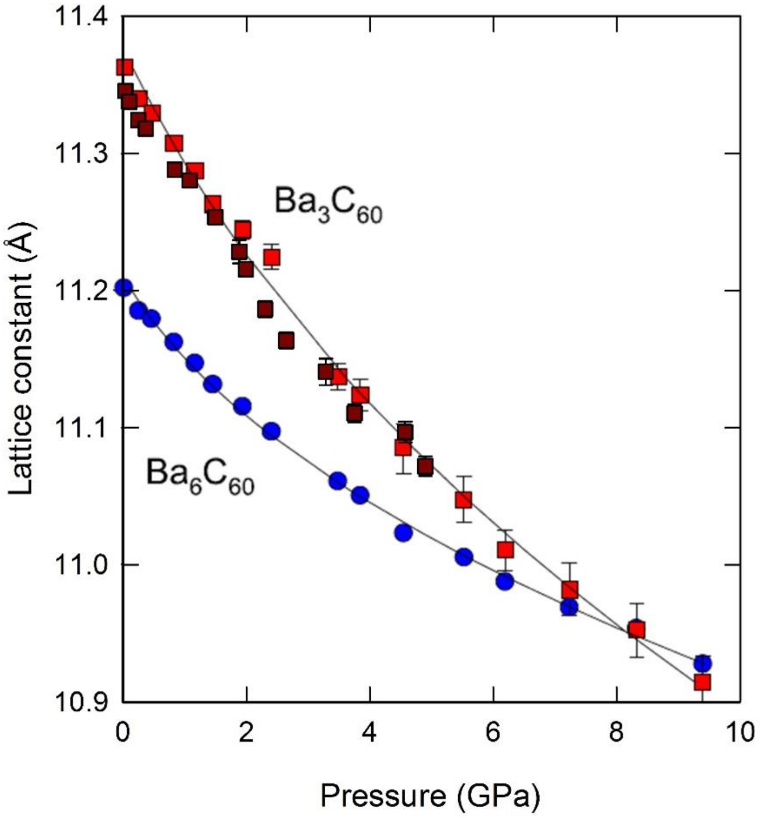

Figure 4.3: Variation of the lattice constants of Ba_3C_{60} and Ba_6C_{60} with pressure, at ambient temperature, from existing synchrotron PXRD studies.[**165, 215**] Solid lines represent fits using the second-order Murnaghan EoS to data for Ba_3C_{60} (red squares) and Ba_6C_{60} (blue circles), from reference [**215**]; K_0 and K_0' are 118(18) GPa, 18(4) for Ba_3C_{60}, and 142(28) GPa, 49(13) for Ba_6C_{60}.

A recent theoretical study, also worth noting, reported that whilst A15 Ba_3C_{60} has a far lower cohesive energy than hypothetical *fcc* Ba_3C_{60} under ambient conditions, a 'crossover' where the cohesive energy of the *fcc* structure should become lower is predicted upon reduction of unit cell volume to ~670 Å/C_{60} and lower;[**217**] from Fig. 4.3, at ambient temperature this unit cell volume would be anticipated upon application of ~6 GPa pressure.

4.2 Experimental Methods

4.2.1 Preparation of A_3C_{60} (A = Cs, Ba) samples

One sample each of A15-rich Cs_3C_{60} and A15 Ba_3C_{60} were used in this study, prepared by Manolis Tzirakis and Dominic Myers respectively at Durham University in our laboratory. All reactions were carried out under inert atmosphere, analogously to the procedure described in Section 3.2, and the synthetic procedures are summarised as follows: Phase-pure A15 Ba_3C_{60} was obtained by annealing a stoichiometric mixture of pelletised Ba_6C_{60} and sublimed C_{60} (MER Corp., 99.9%+), contained in a tantalum reaction cell sealed under ~450 mbar He(g), at 600 °C for 8 hours, followed by drop quenching into ice (annealing repeated twice more with intermediate grindings). Phase-pure Ba_6C_{60} was first synthesised by annealing a pelletised mixture of Ba (SLS, 99%+) and C_{60} in a stoichiometric ratio, sealed in the same manner, at 720-740 °C for ~50 hours, with two intermediate grindings.

A15-rich Cs_3C_{60} was synthesised using an initial low-temperature solvent route (CH_3NH_2), followed by annealings at 100 °C (9 hours) and 180 °C (48 hours); the detailed synthetic technique and initial characterisation of this sample has been described elsewhere.[**71**]

4.3 Synchrotron X-ray diffraction studies of A15 A_3C_{60} (A = Cs, Ba)

4.3.1 Experimental procedures

High-resolution X-ray powder diffraction data were collected for A15-rich Cs_3C_{60} and A15 Ba_3C_{60} on beamline ID31, ESRF. Ground samples of 2-3 mg were sealed in 0.5 mm-diameter special glass capillaries, under inert He(g) atmosphere (~500 mbar) for low-temperature measurements (Cs_3C_{60}) or under Ar(g) atmosphere for measurement under ambient conditions (Ba_3C_{60}). X-ray wavelengths of 0.399838(3) Å and 0.399959(4) Å were employed, calibrated with a Si standard, for Cs_3C_{60} and Ba_3C_{60} respectively.

For Cs_3C_{60} only, the capillary was mounted inside a liquid-helium cooled cryostat; data were collected at fifteen temperatures between 4 K and 250 K, with six scans collected at 4 K (3 × -5 - 30°, and 3 × 15 - 30° in 2θ) and two scans collected at other temperatures (-5 - 30° in 2θ). Good temperature stability was ascertained, with maximum fluctuation at a particular temperature of ±0.4 K (at 22 K), but significantly less fluctuation measured at most temperatures. For Ba_3C_{60}, three scans were collected at ambient temperature (2 × -5 - 30° and 1 × -5 - 10°). The final profiles used for refinement were obtained by summing all individual scans, over an 2θ angular range of 3.9° to 25.0° for Cs_3C_{60} (*d*-spacing, 0.92 to 5.9 Å) and 2.5° to 19.2° for Ba_3C_{60} (*d*-spacing, 9.2 to 1.2 Å). Data were binned using step sizes of 0.005° and 0.003° for Cs_3C_{60} and Ba_3C_{60}, respectively, values selected appropriately for the respective sample peak breadths.

The A15-rich Cs_3C_{60} sample above was also measured at elevated pressures, in four separate experimental loadings of different portions from the same sample on beamline BL10XU, SPring-8 (once at ambient temperature and once at 7 K, λ = 0.41317 Å) and beamline ID27, ESRF (once at ambient temperature and once at 20 K, λ = 0.3738 Å). For each experiment, ~1 mg of powder sample were loaded into an MDAC (with diamond culet diameters of 500 μm, stainless steel gasket thicknesses of 60-70 μm and gasket hole diameters of 200-250 μm). Initial He gas pressures in the MDAC after He gas loading were 0.5 GPa and 0.22 GPa (BL10XU, RT and 7 K) and 0.074 and 0.13 GPa (ID27, RT and 20 K). Finally, Ba_3C_{60} was also measured at ambient temperature under elevated pressures on BL10XU, with an X-ray wavelength of 0.41621(4) Å. Around 1 mg of powder sample was loaded into a MDAC with diamond culet diameter of 500 μm, within a gasket of thickness 100 μm, and with hole diameter 200 μm. The initial He gas pressure in the MDAC was 0.30 GPa.

4.3.2 Ba_3C_{60} – Synchrotron XRD under ambient conditions

The ambient temperature high-resolution PXRD data collected for Ba_3C_{60} were analysed with the Rietveld technique, in order to ascertain the sample quality and derive a good starting model for structural analysis as a function of pressure. Literature atomic coordinates and unit cell parameters were used as a starting model.[**63**]

Firstly, a series of test refinements focusing on the location of Ba^{2+} in the C_{60} lattice were undertaken, to confirm whether the previously report of Ba^{2+} being located in the 6*c* sites would be the most appropriate model (both the available sample and PXRD data quality being significantly higher than those in the investigation of Kortan *et al*., who used laboratory diffractometer PXRD data). All attempts to place Ba^{2+} solely in the 6*d* interstitial site (with site occupancy alternatively fixed at 1 or allowed to freely refine) led to divergence – no stable refinement could be achieved. Where the total Ba^{2+} occupancy was fixed at 1 but allowed to refine distributed over the 6*c* and 6*d* sites in a single-phase refinement (otherwise the refinement parameters were identical to the final, 6*c* only, refinement described below), the final refined occupancies of the 6*c* and 6*d* sites were 0.994(1) and 0.006(1), respectively (χ^2 = 3.845, R_{wp} = 4.91, R_{F^2} = 3.34). In a different approach, a two-phase refinement with 100% 6*c* and 100% 6*d* Ba^{2+} occupation respectively (fixed at 1 in both cases), was also undertaken, again otherwise in an identical manner to the final 6*c*-only refinement described below. Phase fractions refined to 98.43(3)% 6*c*-occupied A15 phase and 1.57(8)% 6*d*-occupied phase (χ^2 = 3.688, R_{wp} = 4.82, R_{F^2} = 3.32). Given that occupation of the two different tetrahedral sites manifests in relatively small peak intensity changes in PXRD data, it can be concluded that a structural model solely with 6*c* occupation is indeed appropriate.

In the final Rietveld fit to the Ba_3C_{60} data, described in the remainder of this section, the Ba^{2+} was therefore modelled as solely occupying the 6*c*, 'pentagonally-coordinated' site. The fractional occupancy of the Ba^{2+} cation was allowed to freely refine, converging at 0.975(2). A pseudo-Voigt profile function was used (continuous wavelength profile function 3 in GSAS). The L_{xy} parameters modelling anisotropic broadening were allowed to freely refine. Appropriate corrections were made for absorption ($\mu r \sim 0.11$, where μ is the linear absorption constant and r the specimen radius), and to account for the effects of anomalous scattering. A shifted Chebyschev polynomial function was used to model the background (GSAS background function 1), with 12 terms.

The carbon thermal displacement parameters were modelled as isotropic and constrained to refine to equal values, given the high molecular symmetry and weak X-ray scattering power of carbon; the Ba^{2+} thermal displacement was modelled as anisotropic and refined freely. From a starting model of the Ba_3C_{60} fractional coordinates reported by Kortan *et al.*,[**63**] the carbon fractional coordinates were allowed to refine, with a C-C bond distance restraint of 1.43 ± 0.01 Å (weight = 50). Other parameters allowed to vary in the course of the refinement included the scale factor, zero shift, and several profile parameters to model isotropic Gaussian and Lorentzian strain and crystallite broadening ('*GU*', '*GV*', '*GW*', '*LX*' and '*LY*'). Low angle asymmetry arising from axial divergence was modelled with fixed profile parameters S/L = 0.001 and H/L = 0.0005, found empirically to provide an excellent fit to the peak shape. These latter values were also used for all subsequent analysis described in this chapter. The final Rietveld fit to the ambient temperature Ba_3C_{60} PXRD data is shown in Fig. 4.4; parameters from the fit are tabulated in Table 4.1 and Table 4.2.

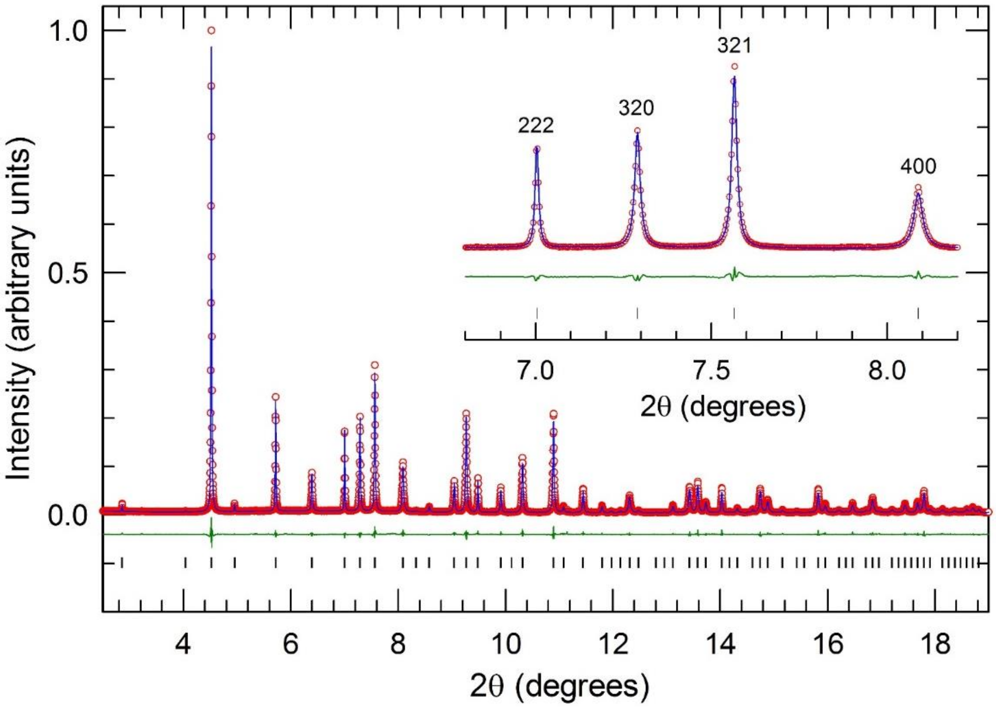

Figure 4.4: Observed (open red circles) and calculated (blue line) fit for the ambient temperature X-ray powder diffraction pattern for A15 Ba_3C_{60} (λ = 0.39959 Å). The bars represent the positions of the Bragg reflections; the green line corresponds to the difference plot (obs-calc).

An excellent fit to the XRRD data could be achieved, with $\chi^2 = 3.887$, $R_{\mathrm{wp}} = 4.93$ % and $R_{\mathrm{F}^2} = 3.56$ %. Figure 4.5 illustrates a view along the *b* axis of the refined crystal structure.

The unit cell volume of A15 Ba_3C_{60} under ambient conditions, of 1461.599(8) Å^3, is significantly smaller than that of A15 Cs_3C_{60}, of 1634.59(4) Å^3. This contraction partly arises from tighter crystal packing in Ba_3C_{60}, with the ionic radius of Ba^{2+}, of 1.34 Å, smaller than that of Cs^+, of 1.67 Å, and from the stronger electrostatic interactions between the Ba^{2+} ions and the C_{60}^{6-} anions.

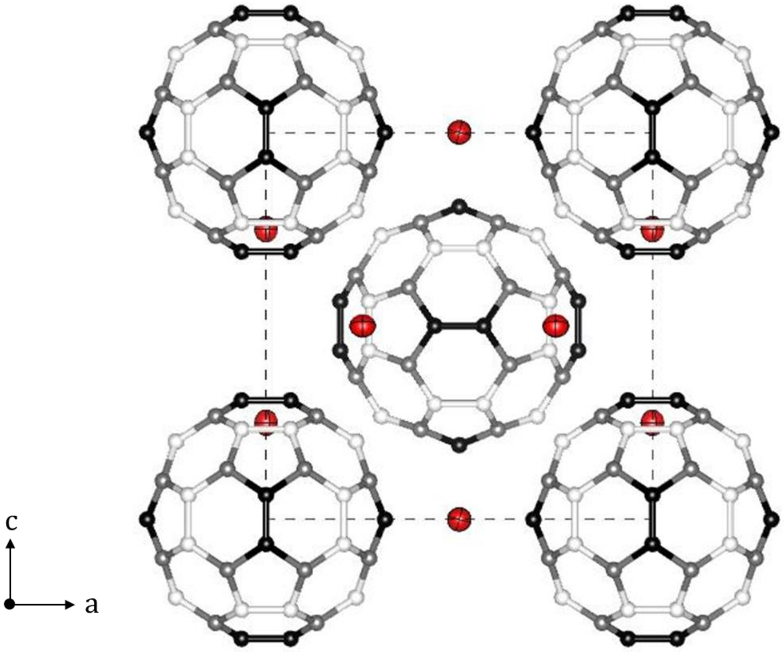

Figure 4.5: Projection view along the *b* unit cell axis of the A15 Ba_3C_{60} crystal structure at ambient temperature and pressure, from Rietveld analysis (created using the software VESTA [**218**]). The three inequivalent carbon atoms are represented with black, grey and white spheres. The Ba^{2+} cations (red), which are all equivalent, are illustrated as displacement ellipsoids.

The anisotropic thermal displacement parameters for Ba^{2+} refined to $U_{11} = 0.0124(7)$ Å^2, U_{12} and $U_{13} = 0.0104(4)$ Å^2, indicating a slight directional preference for Ba^{2+} thermal motion along the orthogonal chain direction. The C-C bond distances ranged from 1.431(2) – 1.444(2) Å. The average C-C bond length is 1.439(2) Å, slightly smaller than the average C-C bond length of 1.466 Å reported by Kortan *et al.* for A15 Ba_3C_{60},[**63**] but consistent with average C-C bond distances of 1.438(5) Å and 1.439(5) Å reported for the structurally related Ba_4C_{60}, from a neutron diffraction study at 295 K.[**165**] The present experimental C-C bond lengths are also remarkably consistent with average C-C bond lengths from neutron diffraction data for another formally C_{60}^{6-}

species, K_6C_{60}, of 1.433(4) Å and 1.443(1) Å.[**219**] Interatomic distances between Ba^{2+} and the three inequivalent carbon atoms were 3.040(3) Å, 3.181(2) Å and 3.470(2) Å.

Table 4.1: Derived structural parameters from Rietveld analysis of PXRD data for single phase A15 Ba_3C_{60}, collected at ambient temperature.

	x/a	y/b	z/c	N	B_{iso} or B_{ij} (Å^2)
Ba^{2+}	0.25	0	0.5	0.975(2)	B_{11}: 0.98(5) B_{22}: 0.82(3) B_{33}: 0.82(3)
C(1)	0	0.3079(3)	0.0632(1)	1	B_{iso}: 0.47(7)
C(2)	0.1305(2)	0.0999(2)	0.2670(2)	1	B_{iso}: 0.47(7)
C(3)	0.0630(1)	0.2013(2)	0.2330(2)	1	B_{iso}: 0.47(7)

Table 4.2: Summary results of the Rietveld analysis of X-ray powder diffraction data collected at ambient temperature for A15 Ba_3C_{60}.

R_{wp} (%)	R_{exp} (%)	χ^2	R_{F^2} (%)	λ (Å)	A15 a (Å)	A15 V (Å^3)
4.93	2.50	3.887	3.56	0.399959(4)	11.34861(2)	1461.599(8)

These results demonstrated that the A15 Ba_3C_{60} sample employed in this study was of high quality, being comprised of 100% A15 phase and highly crystalline. Furthermore, the Ba-C coordination geometry reported in earlier work,[**63**] *i.e.* that Ba solely occupies the tetrahedral site which is surrounded by pentagonal C_{60} faces, was confirmed. A high-pressure structural investigation of this sample at ambient temperature is reported later in this chapter (Section 4.3.7).

4.3.3 Cs_3C_{60} (A15-rich) – Synchrotron XRD as a function of temperature

We now turn to the structural analysis of A15 Cs_3C_{60} as a function of temperature. Firstly, Rietveld analysis of the highest-statistics data set collected at 4 K was undertaken, employing the cubic A15 Cs_3C_{60} structural coordinates previously reported [**49**] to model the majority phase. Additional weak peaks were also observable in the profile, which could be accounted for by the presence of co-existing minority *fcc* Cs_3C_{60} and bco Cs_4C_{60} phases. Literature C_{60} coordinates determined from high-statistics PXRD data for these three phases were employed, then rescaled to the refined lattice constants (*fcc* phase: ref. [**140**], A15 and bco phases: ref. [**49**]).

A pseudo-Voigt profile function which incorporates the Finger-Cox-Jephcoat approach to axial divergence (profile type 3 in GSAS) was used. Corrections were made for absorption ($\mu r \sim 0.09$) and for the effects of anomalous scattering. The fractional occupancy of the Cs^+ cation in the A15 phase was allowed to freely refine, converging at 0.916(4). The background was again modelled with a shifted Chebyschev polynomial function (20 terms). A15 C_{60} thermal displacement parameters were modelled as isotropic and constrained to refine to equal values. Overall, the following parameters were refined: lattice metrics for the three phases, isotropic thermal displacement parameters (A15 all sites, *fcc* octahedral and tetrahedral interstitial sites), A15 Cs fractional occupancy, background, phase fractions, and A15 phase Gaussian and Lorentzian isotropic peak broadening parameters (*GU*, *GV*, *GW*, *LX*, *LY*), plus *LY* alone for the *fcc* phase; anisotropic broadening parameters L_{11}-L_{23} were also allowed to refine away from zero but fixed in the final cycles. The final fit and analysis parameters are presented in Table 4.3, Table 4.4 and Fig. 4.6.

Whilst the literature A15 Cs_3C_{60} model where Cs solely occupies the 'hexagonally coordinated' (6*d*) sites provides a good fit to the 4 K data, a test was undertaken whereby starting from the final 4 K refinement, a Cs^+ cation was also placed in the 'pentagonally coordinated' (6*c*) site with starting fractional occupancy of 0.084 (such that the overall stoichiometry of the phase would be Cs_3C_{60}). The fractional occupancy of Cs^+ in both the 6*d* and 6*c* sites was then allowed to freely refine along with the other parameters (the U_{iso} of the 6*d* and 6*c* sites was constrained to adopt the same value). This resulted in a Cs^+ fractional occupancy in the 6*d* site of 0.924(4), and 0.014(1) in the 6*c* site ($\chi^2 = 1.839$; $R_{wp} = 2.80$, $R_{F^2} = 3.28$). It could thus be concluded that there is negligible Cs^+ occupation of the 6*c* site, in agreement with earlier work;[**49**] remaining analyses of these data therefore assumed 6*d* site occupancy only.

Next, the analysis of each of the datasets between 4 and 250 K was undertaken sequentially using the same basic approach. However, for the remaining temperatures, the fractions of the co-existing phases and the A15 Cs fractional occupancy were fixed to the refined values from the analysis of the highest-statistics 4 K dataset. The Lorentzian contribution to peak width arising from isotropic microstrains (modelled by 'LY' within GSAS) was allowed to vary with temperature; all other profile parameters were fixed to those determined from the highest-statistics 4 K data set. The zero point for each refinement was fixed to 0.20208 centidegrees (the mean value derived from a preliminary set of refinements undertaken in the same manner but where zero was allowed to refine). The C_{60} radii were fixed over all temperatures by rescaling the coordinates of each phase to the refined lattice metrics at each temperature. Details of the analysis and the Rietveld fit for the highest temperature dataset, 250 K, are also shown in Table 4.3, Table 4.4 and Fig. 4.6.

Table 4.3: Summary results from the initial analysis of Rietveld analysis of X-ray powder diffraction data collected at 4 K and at 250 K for A15-rich Cs_3C_{60} (cubic A15 structural model used to model the majority phase; changes in peak broadening with temperature modelled as isotropic in nature, using GSAS CW profile 3).

Cs_3C_{60}	250 K	4 K
R_{wp} (%)	3.54	2.84
R_{exp} (%)	2.92	2.07
χ^2	1.474	1.887
R_{F^2} (%)	5.92	3.44
A15 Cs_3C_{60} (%)	73.2	73.2(2)
fcc Cs_3C_{60} (%)	24.1	24.1(2)
bco Cs_4C_{60} (%)	2.69	2.69(8)
A15 *a* (Å)	11.7656(1)	11.71513(8)
A15 *V* (Å^3)	1628.71(4)	1607.84(3)
fcc a (Å)	14.766(1)	14.696(1)
fcc V (Å^3)	3219(1)	3174.2(9)
bco a (Å)	11.848(4)	11.818(3)
bco b (Å)	12.180(4)	12.121(3)
bco c (Å)	11.452(3)	11.424(3)
bco V (Å^3)	1652.6(6)	1636.3(5)

Table 4.4: Derived structural parameters from Rietveld analysis of PXRD data for the majority A15 phase of A15-rich Cs_3C_{60}, collected at 4 K and at 250 K, from initial analysis (cubic A15 structural model used for majority phase, and changes in peak broadening with temperature modelled as isotropic in nature, using GSAS CW profile 3).

4 K	x/a	y/b	z/c	N	B_{iso} (Å^2)
Cs^+	0.25	0.5	0	0.916(4)	0.33(2)
C(1)	0	0.2982	0.0613	1	1.08(8)
C(2)	0.1216	0.1002	0.2561	1	1.08(8)
C(3)	0.0624	0.2013	0.2220	1	1.08(8)

250 K	x/a	y/b	z/c	N	B_{iso} (Å^2)
Cs^+	0.25	0.5	0	0.916	2.38(3)
C(1)	0	0.2969	0.0610	1	2.2(1)
C(2)	0.1211	0.0997	0.2550	1	2.2(1)
C(3)	0.0621	0.2004	0.2210	1	2.2(1)

The evolution of unit cell volume with temperature is shown in Fig. 4.7. The thermal expansivity between 4 K and 250 K appears to vary smoothly with temperature, with no evidence of any low temperature anomaly, *i.e.* diffraction peaks continuously shift to higher angles upon cooling. The $V(T)$ data were parameterised using the model described by Sayetat *et al.*[**129**] outlined in Section 2.4.5, yielding an estimated V (0 K) of 1607.89(7) Å^3 and an estimated Debye temperature θ_D of 84(4) K. This is in reasonable agreement with θ_D = 54 K recently estimated from specific heat measurements for A15 Cs_3C_{60},[**220**] although notably smaller than the θ_D = 218 K obtained for *fcc* Cs_3C_{60} using the same experimental technique (Table 3.4).

However, upon examining the changes in profile shape with temperature, an anomalous feature became clearly evident; whilst some gradual increase in LY may be seen on cooling down from 250 K to T_N, a distinct change in LY with onset temperature around $T_N \sim 46$ K can be observed. Below this temperature, the magnitude of LY doubles (Fig. 4.8).

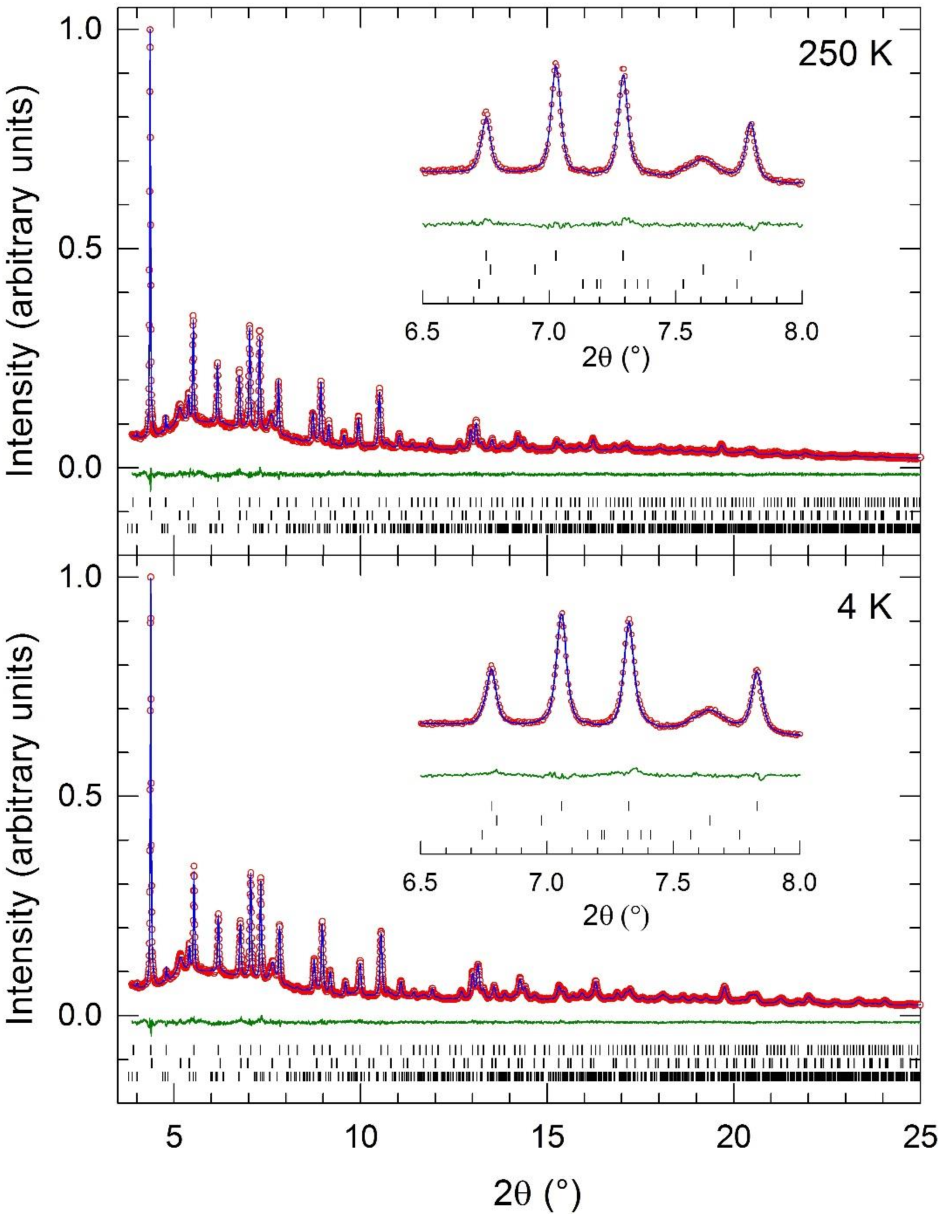

Figure 4.6: Observed (open red circles) and calculated (blue line) X-ray powder diffraction profiles for A15-rich Cs_3C_{60}, collected at 250 K (upper) and 4 K (lower) (λ = 0.39984 Å). The bars represent the positions of the Bragg reflections of the A15, *fcc* and *bco* phases (from top to bottom); the green line corresponds to the difference plot (obs-calc). The insets show expanded regions of the profiles. The Rietveld fits are from the initial analysis of these data (cubic A15 structural model used for majority phase, and changes in peak broadening with temperature modelled as isotropic in nature, using GSAS CW profile 3).

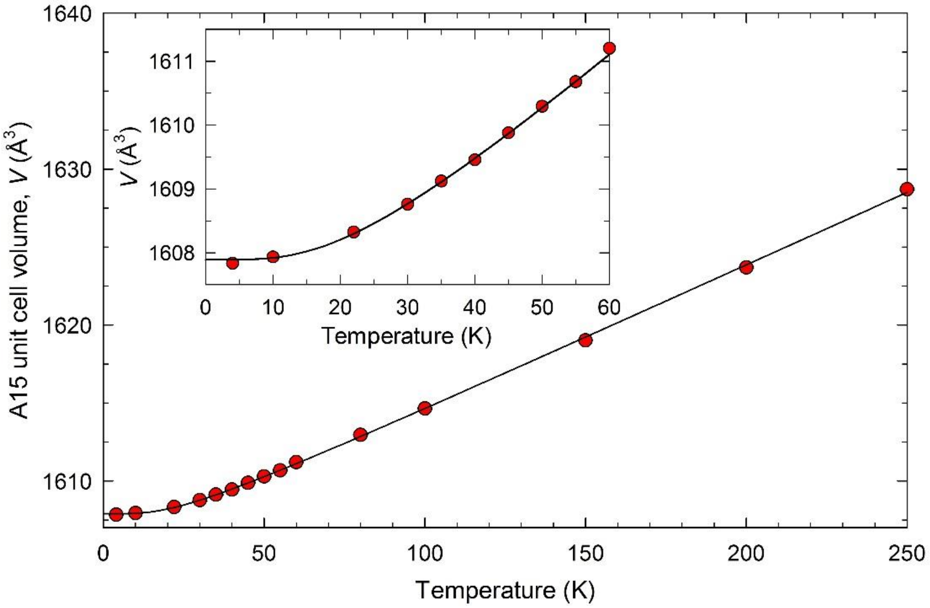

Figure 4.7: The thermal expansivity $V(T)$ of A15 Cs_3C_{60}, from initial Rietveld analysis (the A15 phase was modelled with space group $\boldsymbol{Pm\overline{3}n}$; changes in peak broadening were modelled as isotropic). The solid line shows a least-squares fit to $V = V_0 + I_v T\varphi(\theta_D/T)$; φ is comprised of two polynomial functions of T (see Section 2.4.5 and ref. [**129**]) and V_0 = 1607.89(7) Å^3, I_v = 0.0937(7) Å^{3}K^{-1} and θ_D = 84(4) K. Inset: the expanded low-temperature region.

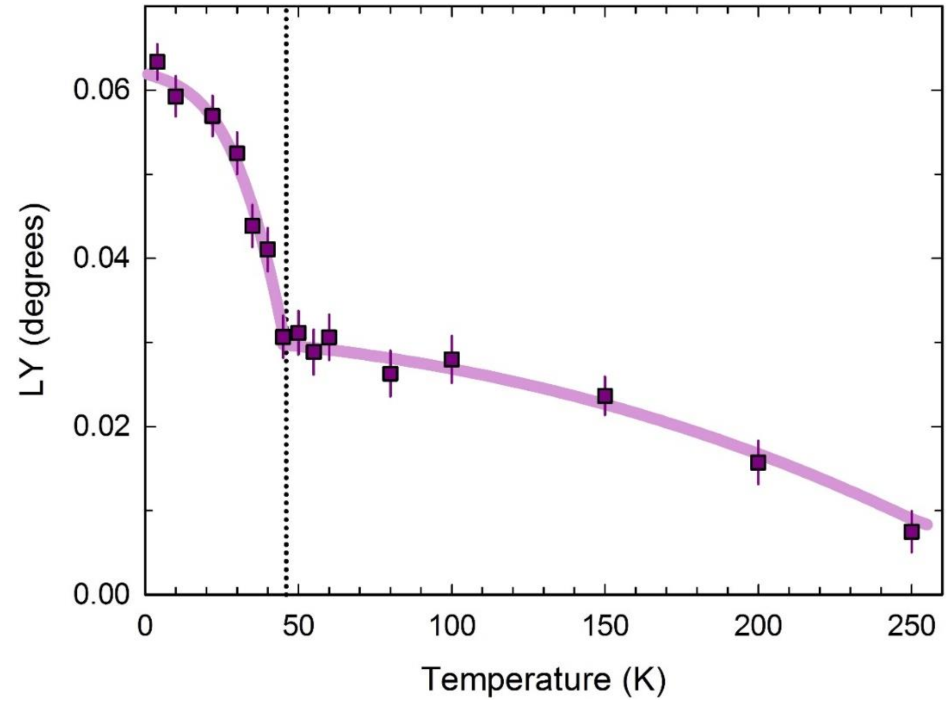

Figure 4.8: Variation of the Lorentzian isotropic strain broadening parameter, LY with temperature as derived from Rietveld analysis of synchrotron PXRD data of Cs_3C_{60}, with a cubic A15 model used to model the majority phase and no other profile function parameters allowed to vary with temperature. The solid line is a guide to the eye; errors are statistical arising from Rietveld analysis, and the dotted vertical line marks the ambient pressure T_N (46 K).

Upon closer examination of the data, it became evident that this well-defined increase in broadening with onset around T_N is dependent on reflection class, *i.e.* that the isotropic peak broadening model employed for the first series of refinements is not particularly appropriate to describe these profile changes. Fits to individual peaks using the Winplotr application (FullProf suite) revealed that, whilst the width of the A15 *400* peak remains essentially constant over the full temperature range investigated (4–250 K), those of *e.g.* the *320* and *222* peaks showed distinctive broadening below ~45-50 K (Fig. 3.6).

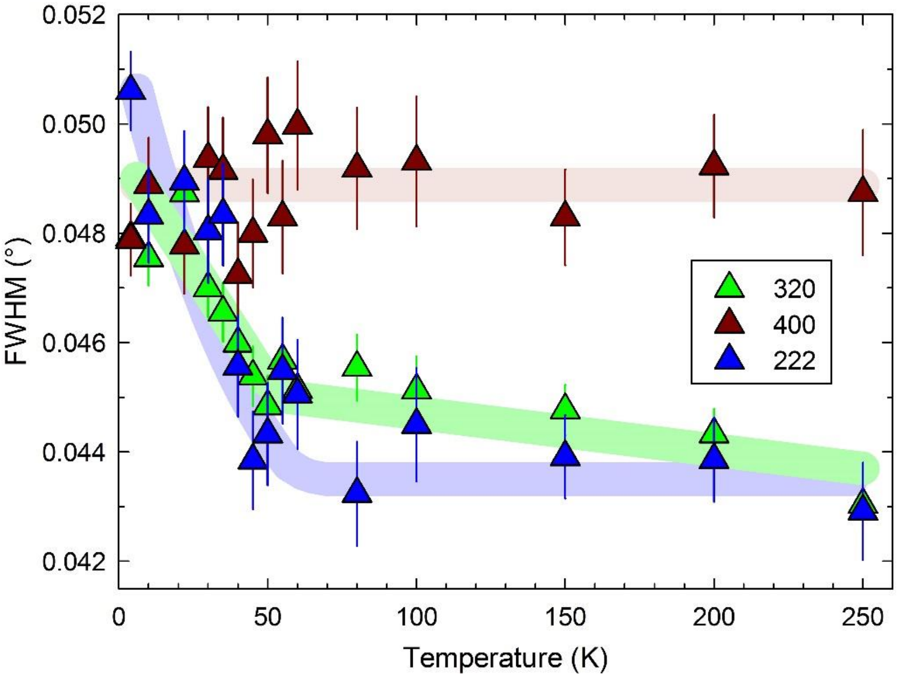

Figure 4.9: Evolution of full-width-at-half-maximum (FWHM) with temperature for three representative A15 phase peaks (Miller indices *222*, *320* and *400*). Values of FWHM were extracted through least-squares fitting of a pseudo-Voigt peak shape model to individual peaks with statistical errors shown with bars; solid lines are guides to the eye. For each peak, for consistency, the Gaussian-Lorentzian mixing parameter eta was refined for the 250 K fit then fixed to this value over all temperatures; additionally, the 2θ ranges fitted were fixed in size over all temperatures. For the *400* reflection, one *fcc* peak with slightly overlapping tail was fitted simultaneously at each temperature.

Further confirmation that this broadening has a well-defined dependence on reflection class, and does not vary smoothly with 2θ, was next obtained through reanalysis of the 4 K to 250 K data sets using a profile function which incorporates the Stephens' model of anisotropic microstrain broadening into the Rietveld fits;[**221**] this has been directly implemented in GSAS for continuous wavelength profile function 4. In this model, the variance in $1/d^2$, where d is the spacing between lattice planes, can be described as follows: $\sigma^2(M_{hkl}) = \sum_{HKL} S_{HKL} h^H k^K l^L$. However, in the implementation of this model in GSAS, the S_{HKL} values which are output have been scaled (see the appendix of ref. [**221**] for details), and the microstrain broadening can be obtained from these values as follows:

$$\Gamma_S^2 = \sum_{HKL} S_{HKL} h^H k^K l^L, \qquad \textbf{Equation 4.1}$$

where up to fifteen terms S_{HKL}, depending on lattice type, are defined for H + K + L = 4; Γ_S^2 represents the microstrain broadening. Hereafter, quoted values of S_{HKL} are those extracted from GSAS (using continuous wavelength profile function 4).

To model strain broadening in a cubic system, only two independent S_{hkl} parameters are required, S_{400} and S_{220}; strain components are restricted in terms of 1st and 2nd-order terms permitted by lattice symmetry. A third parameter, the mixing coefficient η, describes the relative contribution to Gaussian and Lorentzian broadening (η = 0 and η = 1 correspond to microstrain contributing purely to Gaussian and purely to Lorentzian broadening, respectively).

With the knowledge that well-defined anisotropic peak broadening is found at low temperatures, for this second set of refinements using the Stephens model to describe the A15 phase peak shape, the highest temperature dataset (250 K) was used as the starting point (rather than the highest statistics data collected at 4 K); however, profile type 3 was retained for the minority *fcc* and bco phases for simplicity. For this dataset, A15 isotropic profile broadening parameters GU, GV, GW, LX and anisotropic S_{400}, S_{220} (and *fcc* phase Lorentzian strain broadening, LY), phase fractions, background coefficients, lattice metrics for each phase, isotropic thermal displacement parameters for the A15 phase and the tetrahedral/octahedral *fcc* phase sites, and the A15 phase Cs fractional occupancy were refined. Then, consecutive refinements were undertaken down to the 4 K dataset, with A15 isotropic profile terms, phase fractions and Cs fractional occupancy fixed to the final refined values from the 250 K dataset. Besides this change in approach, the refinements were undertaken in an identical manner to the first set described above (*i.e.* background function, absorption correction, anomalous scattering corrections, constraint on A15 carbon thermal displacement parameters, *etc.*). Anisotropic microstrain broadening was modelled as Lorentzian in character only (η was fixed at 1), in a bid to reduce the complexity of the model, and because earlier testing of the series with profile type 3 allowing both Lorentzian and Gaussian isotropic broadening terms to vary with temperature indicated negligible change in the latter in comparison with the former.

With all other profile shape parameters fixed, allowing S_{400} and S_{220} to vary with temperature revealed a distinct change in S_{220} below ~60 K, in contrast to the behaviour of S_{400} (Fig. 4.10). This represents a more powerful confirmation of anisotropic peak broadening with onset slightly above T_N than fits to individual peaks, which may be affected to a greater extent by phase overlap or noise than this 'averaged' result over all A15 reflections.

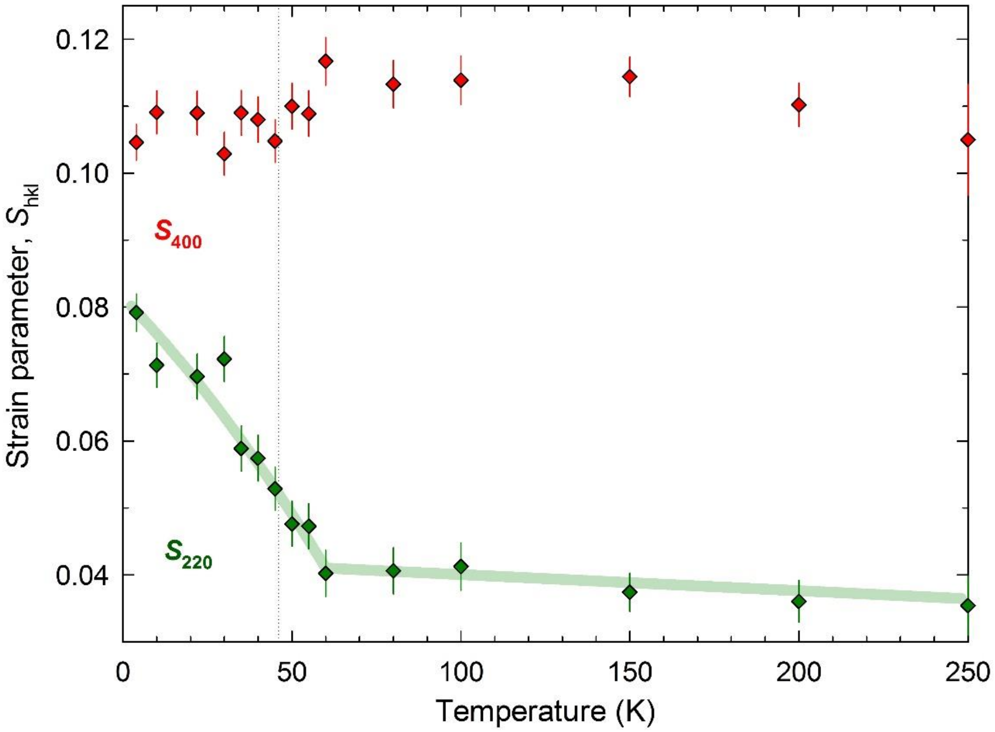

Figure 4.10: Variation in microstrain broadening coefficients, S_{hkl}, with temperature in the cubic $\boldsymbol{Pm\overline{3}n}$ model of A15 Cs_3C_{60}, extracted from Rietveld analysis. Solid lines represent guides-to-the-eye, whilst the vertical dotted line indicates T_N, at 46 K (ambient pressure)[**89**].

Using S_{hkl} values, the microstrain broadening for a particular set of Miller indices hkl may then be extracted. Microstrain broadening Γ_S^2, for a given reflection in a cubic lattice is expressed as follows:

$$\Gamma_S^2 = S_{400}(h^4 + k^4 + l^4) + 3S_{220}(h^2k^2 + h^2l^2 + k^2l^2) \qquad \textbf{Equation 4.2}$$

The microstrain broadening for three representative peaks of classes $h00$, hhh and $hk0$ is plotted as a function of temperature in Fig. 4.11.

The extracted trends in microstrain broadening indicate that peaks arising from reflections of class $h00$ show no evidence of additional broadening at low temperatures, whilst other classes exhibit well-defined peak broadening developing at or just above T_N

(at ~45-60K), with the largest increase found for peaks originating from reflections of class *hhh*.

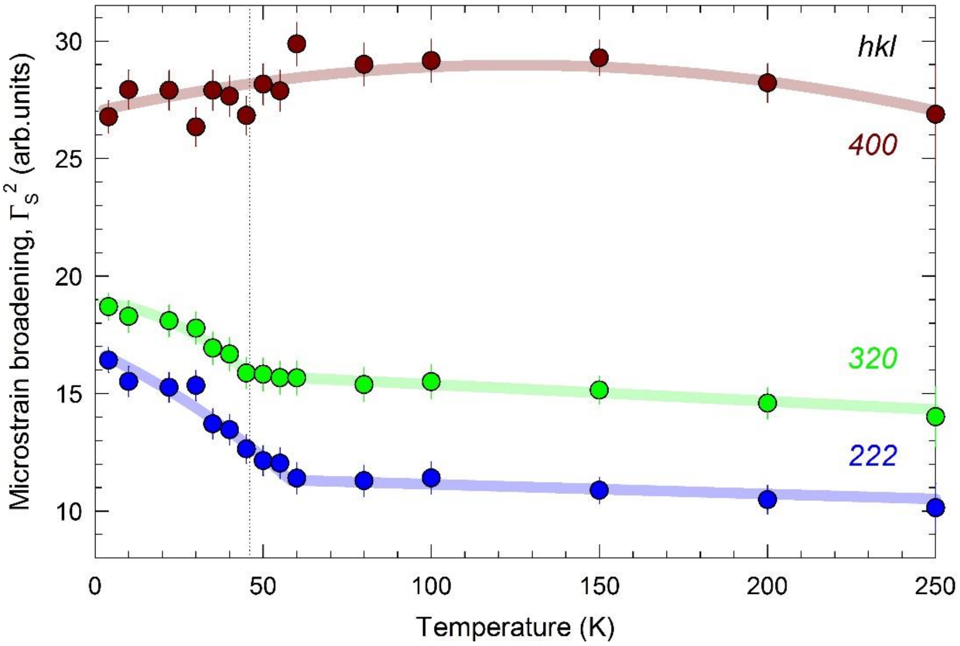

Figure 4.11: Microstrain broadening as a function of temperature in the cubic $\boldsymbol{Pm\overline{3}n}$ model of A15 Cs_3C_{60}, for the *400*, *222* and *320* reflections. Solid lines represent guides-to-the-eye, whilst the vertical dotted line indicates T_N for this system at 46K (ambient pressure).

For a comparison of fit quality, an additional series of refinements were carried out using the same model as described above for all temperatures but here keeping S_{400} and S_{220} (and thus all profile coefficients) fixed to the final refined values from the 250 K refinement. For the 4 K (highest statistics) data set, where anisotropic profile broadening (*i.e.* S_{hkl}) terms were allowed to vary (Fig. 4.12, upper panel), reliability indices of R_{wp} = 2.88% and R_{F^2} = 2.79% resulted (R_{exp} = 2.07%); when they were fixed to the 250 K values (Fig. 4.12, lower panel), these indices were notably higher (R_{wp} = 3.14%, R_{F^2} = 3.25%).

Such a lattice strain could potentially be purely uncorrelated local strain, or there could be long-range correlation with the effect of a lowering in symmetry. If long-range cubic lattice symmetry were to be maintained at all temperatures, these anisotropic profile broadening trends would necessitate the appearance of spontaneous trigonal strain – oriented principally along the unit cell body diagonal – below ~45-60K. Such behaviour could reflect the emergence of local structural inhomogeneities preceding or accompanying some structural transformation at T_N, undetectable by Bragg peak splitting even with the high resolution of the present measurements.

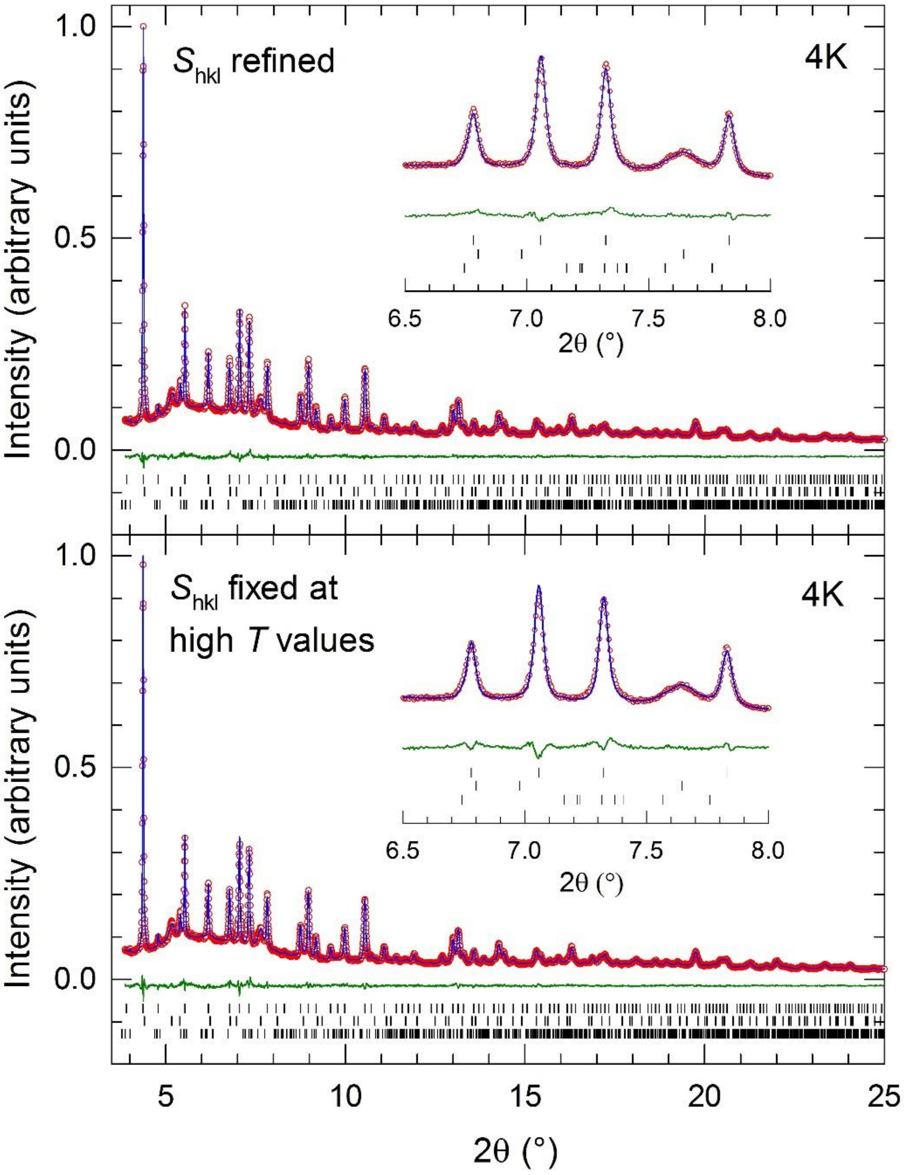

Figure 4.12: Final observed (circles) and calculated (blue solid line) synchrotron X-ray powder diffraction profiles for the Cs_3C_{60}-rich sample at 4 K (λ = 0.39984 Å); the majority phase is modelled as cubic A15, with S_{hkl} terms allowed to vary (upper panel), or fixed to values from analysis of data collected at 250 K (lower panel). All other profile parameters were fixed to values from the latter (250 K) analysis. Solid green lines show the difference profiles; bars mark reflection positions of the A15 (top), *fcc* (middle) and bco (bottom) phases. Insets show expanded regions of the respective larger panels.

This possibility would necessitate the onset of a subtle crystal symmetry reduction at approximately $T \leq T_N$. Qualitatively, sizeable microstrain broadening of the cubic *hhh* reflections may originate from a miniscule compression or elongation of the cubic unit cell along its body diagonal, effectively leading to a rhombohedral structure below T_N. Consistent with this assumption is the lack of any observable broadening associated with the cubic $h00$ Bragg peaks which should remain unsplit in rhombohedral symmetry (conversely, a symmetry reduction from cubic to orthorhombic (or tetragonal) would render *hhh* reflections unsplit).

Therefore, a final series of Rietveld refinements was performed with the majority 'A15' phase modelled using a lower symmetry, rhombohedral space group; hereafter, this model will be termed 'A15-R'. As a starting point, the literature ambient temperature $Pm\bar{3}n$ A15 unit cell coordinates [**49**] were firstly rescaled to the 4K lattice metrics (*i.e.* coordinates as used in the earlier refinements of the 4K dataset with cubic A15 models), but were then transformed into $R\bar{3}c$ symmetry using the online tool ISODISTORT [**222**]. ISODISTORT explores physical distortions of structural phase transitions induced by irreducible representations, providing a graphical user interface for investigation of possible distortion symmetries of a higher-symmetry parent structure.

The $R\bar{3}c$ space group, used here in rhombohedral setting, was selected to use for the model as the only rhombohedral maximal (*translationengleiche*) subgroup of the cubic A15 A_3C_{60} space group, $Pm\bar{3}n$. It is important to state that this analysis cannot definitively exclude *e.g.* the possibility that the true space group is a lower-symmetry, non-maximal rhombohedral subgroup of $Pm\bar{3}n$ (*e.g.* $R3c$, $R\bar{3}$, $R32$ or $R3$). Rather, it was deemed that accurate distinction between these possibilities (involving refinement of the carbon fractional coordinates) would not be possible with the available data quality, small distortion magnitude and the weak X-ray scattering of carbon. The main purpose of this analysis series was to test the viability of a rhombohedral space group to model the low-temperature behaviour and to track the evolution of lattice metrics (*e.g.* the rhombohedral angle) with temperature. Furthermore, within ISODISTORT it may be verified that for a hypothetical strain distortion mode (*i.e.* unit cell parameter changes) applied to a parent structure $Pm\bar{3}n$ A15 Cs_3C_{60}, $R\bar{3}c$ is the only possible rhombohedral space group for a distorted structure.

With $R\bar{3}c$ input as the space group for the distorted structure and strain distortion mode selected as a search criterion, only one, one-dimensional, order parameter direction (and thus one set of symmetry-transformed atomic coordinates) are possible, with the symbol P3 in Stokes and Hatch notation.[**223**] This distorted structure ('isotropy subgroup') has a 1×1×1 superstructure relative to the parent cell, with the supercell origin at (0, 0, 0). The rhombohedral unit cell is the same size relative to the cubic parent, and the isotropy subgroup index *i* is 4, *i.e.* the cubic $Pm\overline{3}n$ parent structure has 4 symmetry elements for each symmetry element in the distorted structure. ISODISTORT generates a cif file for this distorted structure which can then be imported into GSAS. For each dataset collected at a different temperature in this study, $R\overline{3}c$ atomic coordinates were generated using ISODISTORT from the cubic coordinates (rescaled to the refined lattice metrics at each particular temperature) and used to model the majority phase, A15-R.

The $R\overline{3}c$ space group necessitates the displacement of the Cs^+ ions, which now reside at the $6e$ (0.25, x, $-x$+0.5) sites (local symmetry $C2$) away from the [100] faces (in the cubic structure, Cs^+ occupies the $6d$ site (0.25, 0.5, 0)). The ten resulting carbon coordinates generated from the three in $Pm\overline{3}n$ symmetry were fixed, whilst the position of Cs^+ was allowed to refine. Refinement of carbon fractional coordinates was not possible due to high correlations between them. Resulting C-C bond lengths in the rhombohedral model are 1.41-1.46 Å. Closest contact C_{60}-C_{60} distances are 3.642 Å along the body diagonal direction, and 3.648 Å in all other directions (4 K refinement). Isotropic thermal displacement parameters for the ten C atoms were constrained to be identical. Earlier, unrestrained refinement of the Cs fractional occupancy in the cubic A15 model at 250 K (second analysis series, where S_{hkl} were used to model anisotropic profile broadening) had led to an A15 phase stoichiometry of $Cs_{2.76(2)}C_{60}$, a value then fixed over all temperatures for the rhombohedral refinements series. Phase fractions were also fixed to refined values from the aforementioned 250 K cubic refinement.

The four symmetry-allowed S_{hkl} terms (S_{400}, S_{220}, S_{310} and S_{211}) were refined at the lowest temperature (4 K), finally refining to the following values: S_{400} = 0.099(3), S_{220} = 0.075(4), S_{310} = 0.000(5) and S_{211} = −0.067(6). Isotropic broadening terms GU, GV, GW and LX were fixed to values from the 250 K cubic model refinement. For the remaining data collected at higher temperatures, all profile parameters were fixed to these values because of significant correlation of profile broadening with rhombohedral cell metrics due to the small magnitude of distortion (*i.e.* to see whether solely a rhombohedral distortion could model the changes in anisotropic broadening well). The final refinement of the 4 K data employing the A15-R model and tabulated parameters are presented in Fig. 4.13, and Table 4.5.

Stable excellent quality refinement of the 4 K diffraction profile was quickly achieved with a refined rhombohedral angle, α only minutely larger than 90° (α = 90.072(5)°) and with the strain along the body diagonal now considerably relieved. The increase in α above 90° implies a small compression of the cubic unit cell along the body diagonal, accompanied by the displacement of the Cs^+ ions away from their original site on the unit cell face by ~0.0038(4) Å. Such a small lattice distortion is reminiscent of the behaviour of other metrically cubic systems which order antiferromagnetically; for instance, NiO undergoes a cubic-to-rhombohedral structural transition at T_N with α ~ 90.075° at 6 K,[**224**] very similar in magnitude to the present case.

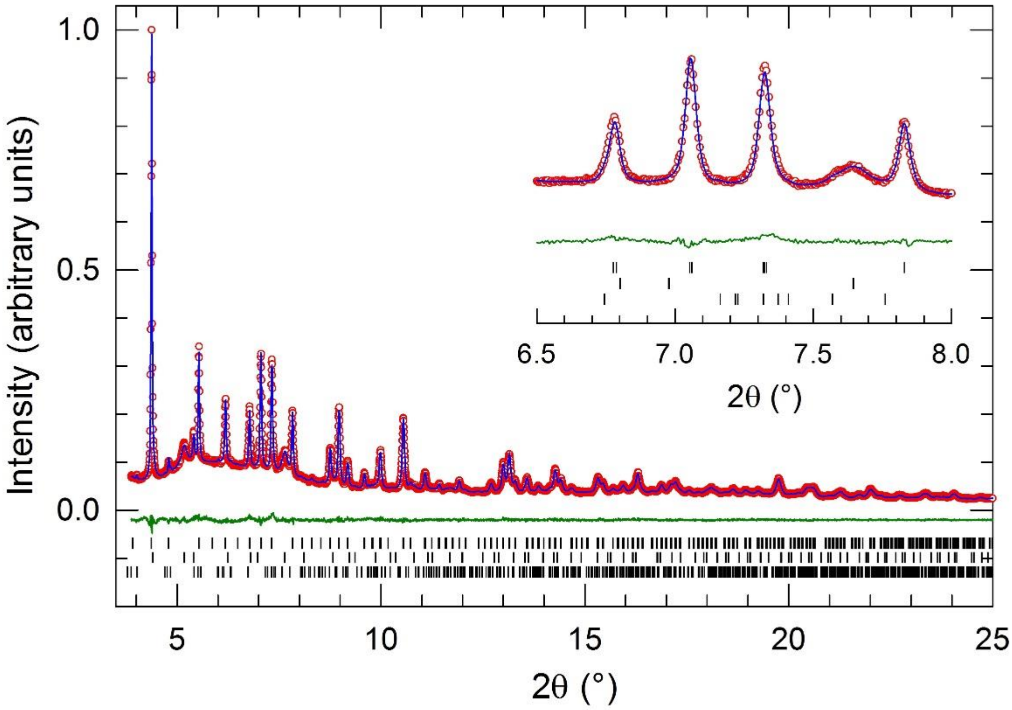

Figure 4.13: Final observed (circles) and calculated (blue solid line) synchrotron X-ray powder diffraction profiles for the 4 K dataset, from Rietveld analysis where the main phase is modelled with a rhombohedrally-distorted unit cell (A15-R). The green solid line shows the difference profile; bars mark the reflection positions of A15-R (top), *fcc* (middle) and *bco* (bottom) phases. The inset displays an expanded view of the profiles.

No discernable anomalies were present in the temperature variation of thermal displacement parameters, which were modelled as isotropic. As in the A15 cubic structure, in the A15-R model there is no centre-of-inversion between nearest-neighbour C_{60} molecules, so previously proposed explanations for the weak ferromagnetic component observed in the magnetisation at low fields remain valid.[**89**]

The series of refinements with the A15-R model were extended to above 45 K as a test to establish the temperature limit where the model breaks down. Above 100 K, the A15-R model broke down completely and the refinements could not converge. Between 50 K and 100 K, the rhombohedral model can be used to achieve stable refinements, but in this temperature region there is no statistical difference in the fit quality between the cubic A15 (S_{hkl} refined) and A15-R models, and the refined unit cell angle was very small, showing little change with temperature (~90.02°) in stark contrast to the clear evolution seen below T_{N}, and with much larger error bars than for $T < T_{\mathrm{N}}$ (~±0.01° *vs.* ~±0.005°).

Table 4.5: Refined parameters for the majority, rhombohedrally distorted A15-R (space group $\boldsymbol{R\bar{3}c}$) phase in the A15-rich Cs_3C_{60} sample obtained from Rietveld refinement of synchrotron X-ray powder diffraction data at 4 K. Estimated errors in the last digits are given in parentheses.

	x/a	*y/b*	*z/c*	Position	*N*	B_{iso} (Å^2)
Cs	0.25	0.5027(3)	−0.0027(3)	6e	0.921	0.28(2)
C(1)	0	0.2982	0.0613	12f	1	1.06(6)
C(2)	0.1216	0.1002	0.2561	12f	1	1.06(6)
C(3)	0.0624	0.2013	0.2220	12f	1	1.06(6)
C(4)	0	0.2982	−0.0613	12f	1	1.06(6)
C(5)	0.1216	0.8998	0.7439	12f	1	1.06(6)
C(6)	0.8784	0.1002	0.7439	12f	1	1.06(6)
C(7)	0.8784	0.8998	0.2561	12f	1	1.06(6)
C(8)	0.0624	0.7987	0.7780	12f	1	1.06(6)
C(9)	−0.0624	0.2013	0.7780	12f	1	1.06(6)
C(10)	−0.0624	0.7987	0.2220	12f	1	1.06(6)

The evolution of A15-R unit cell angle α and Cs *x* coordinate with temperature is displayed in Fig. 4.14. The metrics for a cubic phase are displayed at $T > T_{\mathrm{N}}$ to represent the breakdown of the A15-R model in this temperature range. The temperature evolution of unit cell angle in the A15-R model bears a striking resemblance to that of the magnetisation; the onset temperature of structural distortion coincides remarkably well with the onset of antiferromagnetic ordering.

The changes in anisotropic broadening as a function of temperature in A15 Cs_3C_{60} can thus be modelled well by either maintaining the cubic A15 $Pm\bar{3}n$ structure but with significantly increased trigonal strain, or by a small lattice distortion to rhombohedral symmetry (space group $R\bar{3}c$) at low temperature. A definitive distinction between the development of uncorrelated strain around the AFM ordering onset and long-range strain correlation to lower the lattice symmetry from cubic to rhombohedral is not possible with the available PXRD data alone, given the small magnitude of distortion; however, the rhombohedral model is stable, and below 45 K the deviation away from cubic unit cell angle and Cs x coordinate is at least 3σ. The thermal expansivity in the A15-R model at low temperatures is consistent with that in the cubic A15 model at higher temperatures, with $V(T)$ of the two regions connecting smoothly (Fig. 4.15).

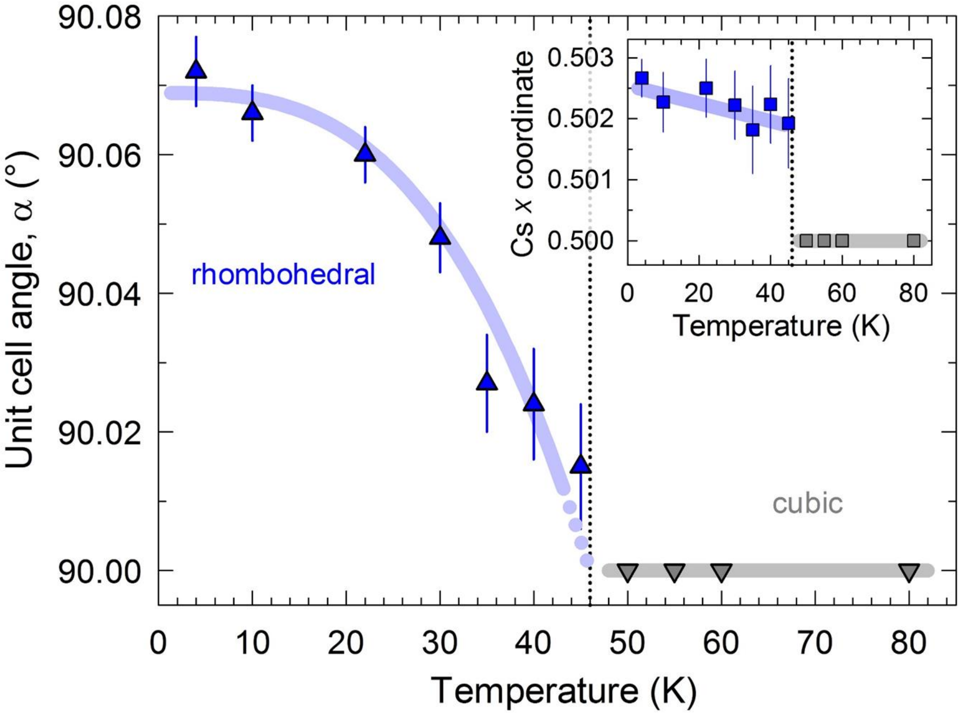

Figure 4.14: Evolution of the unit cell angle with temperature in the A15-R ($\boldsymbol{R\overline{3}c}$) model. Inset: the variation of Cs x coordinate with temperature. Solid lines are guides to the eye; errors are statistical from Rietveld analysis. The dotted lines mark T_N at ambient pressure, 46 K.

As discussed above, alternative symmetry-lowering distortion possibilities to tetragonal or orthorhombic crystal symmetry were deemed highly improbable as they would necessitate that the *hhh* reflections do not split (or broaden) in contradiction with the experimental observations. However, for completeness, structural models with tetragonal and orthorhombic symmetry with space groups $P4_2/mmc$ and $Pmmm$, respectively (both also *translationengleiche* subgroups of $Pm\overline{3}n$), were tested against the 4 K diffraction profile. Coordinates were generated by symmetry transformation as described for the A15-R model above; all three Rietveld refinements were carried out consistently, with lattice metrics, isotropic thermal parameters (carbon for ‘A15’ phase, constrained equal, and Cs for ‘A15’ and *fcc* phases), ‘A15’ Cs coordinates when not on special sites, S_{hkl} parameters (‘A15’ phase) and isotropic Lorentzian strain broadening (*fcc* phase) refined in the final cycles. This totalled 17, 18 and 24 variables in the final cycles for the rhombohedral, tetragonal and orthorhombic models, respectively. Rietveld refinements with the tetragonal and orthorhombic space groups led to worse agreement factors despite having more refined variables and were therefore discarded (

Table 4.6).

In summary, the structure of the A15 phase was investigated between 4 K and 250 K by PXRD. Increasing anisotropic profile broadening is found to develop upon cooling below the T_N, found to be modelled well by a small rhombohedral distortion. Further discussion of these results is presented later in Section 4.4.

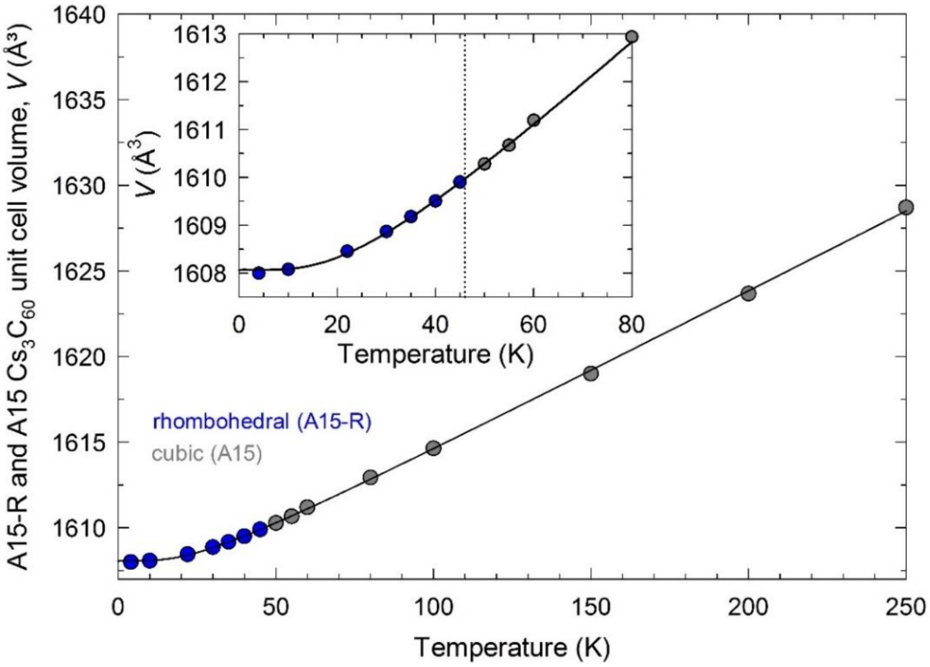

Figure 4.15: Temperature evolution of the unit cell volume, V, of Cs_3C_{60}, for both A15 cubic and A15-R rhombohedral models. The black solid line shows a fit to the data with a Debye-Grüneisen model,[**129**] corresponding to a distribution of phonon frequencies with estimated Debye temperature, θ_D = 92(4) K. Statistical error in V from Rietveld analysis is smaller in magnitude than the data point size. Inset: expanded region of the $V(T)$ data and fit at low temperature; the dotted line indicates T_N at ambient pressure, 46 K.

Table 4.6: Summary of reliability indices for different models tested for the A15 majority phase (for the 4K PXRD dataset). The number of refined variables excludes the background coefficients (20 in each case) which were not refined in the final cycles.

Space group	χ^2	R_{wp} (%)	R_{F^2} (%)	Number of refined variables
$R\bar{3}c$	1.886	2.84	2.36	17
$P4_2/mmc$	1.912	2.85	2.33	18
$Pmmm$	1.903	2.85	2.43	24
$Pm\bar{3}n$	1.940	2.88	2.79	13

4.3.4 Cs_3C_{60} (A15-rich) – Synchrotron XRD at high pressure and ambient temperature

Having examined the structural evolution of A15 Cs_3C_{60} as a function of temperature, its evolution with pressure will now be discussed, as followed by synchrotron PXRD, starting with pressurisation at ambient temperature. Two separate ambient temperature experiments were undertaken (see section 4.3.1 for experimental procedures), and firstly data collected at BL10XU, SPring-8, will be presented.

Initial visual examination of the pressure evolution of the profiles indicated that the crystalline cubic A15 phase was stable up to the highest pressure studied, 15.0 GPa, albeit with some pressure-induced peak broadening and diminishment in intensity relative to the background (Fig. 4.16). However, some irregularity is seen in the trend of peak shift with pressure: the profile collected at 7.3 GPa appears slightly shifted to lower angle relative to that collected at 5.7 GPa, which could indicate a slight lattice expansion upon pressurisation between these two pressures. Upon further pressure application to 15.0 GPa, there is relatively little peak shift with pressure. Rietveld analysis of each data set was undertaken to analyse the structural evolution with pressure in detail.

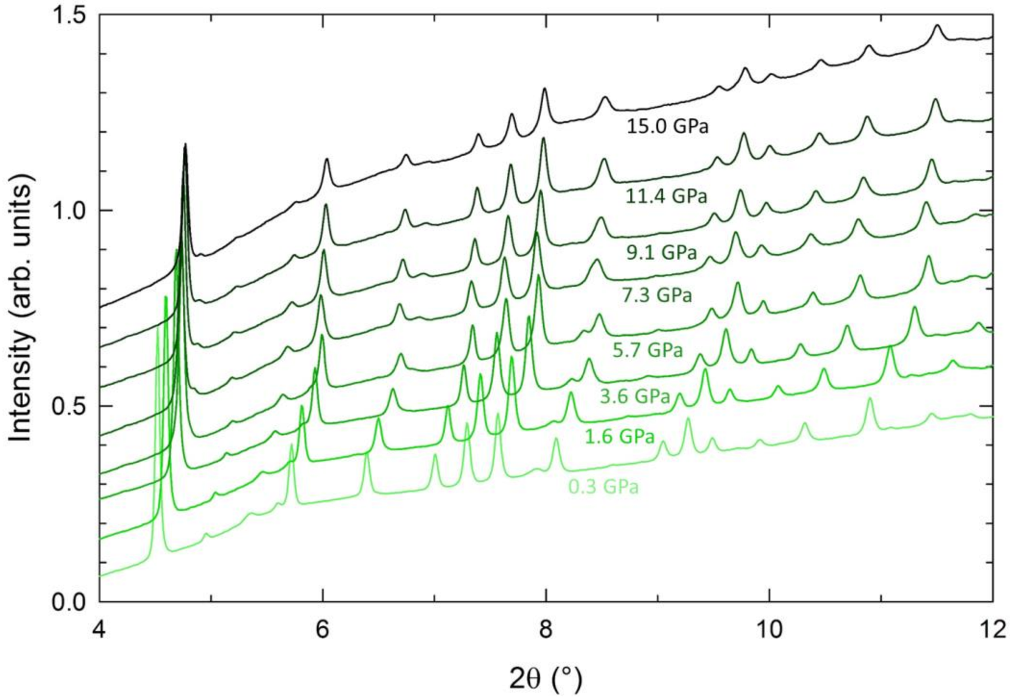

Figure 4.16: Evolution of A15-rich Cs_3C_{60} PXRD profiles as a function of pressure between 0.3 and 15.0 GPa, at ambient temperature (from BL10XU, λ = 0.41317 Å); data from selected representative pressures only are displayed for visual clarity. Profiles are intensity-normalised and shifted vertically for visual clarity.

The same general strategy was used for Rietveld analysis of these data sets and also for those of the other three experiments, described as follows: the Cs^+ fractional occupancy of the A15 phase was fixed to 0.92 as determined from high resolution ambient temperature data (Section 4.3.3). For each experiment, the zero point was fixed in these final series of refinements to a mean value derived from earlier iterations of each series of refinements where zero was allowed to refine, a best approximation given the correlation between lattice metrics and zero point and *e.g.* the relatively limited 2θ range sampled in these high-pressure experiments (BL10XU at RT = 0.0012849°, BL10XU at 8K = 0.0030538°, ID27 at RT = −0.0005006° and ID27 at 20K = −0.0010407°). The same literature coordinates for the three phases (A15, *fcc* and *bco*) were used as for the ambient pressure data (section 4.3.3) and rescaled with the lattice metrics at each pressure to retain fixed C_{60} radii and bond lengths with pressure. Chebyschev polynomial background functions were used (16-22 terms, refined at each pressure). No absorption corrections were applied as this would have been inappropriate for the experimental geometry. Phase fractions and lattice metrics were refined at each pressure. Typically, the U_{iso} values for all phases were defined at the lowest pressure (and allowed to refine for the Cs^+ sites) and then fixed to these values over the pressure series, and profile terms again defined at the lowest pressure and only A15 phase GU, GW and LY and *fcc* phase LY

refined to model pressure-induced broadening changes, though this strategy was altered slightly between experiments depending on the relative phase fractions and data quality.

Returning to the experiment conducted at ambient temperature at BL10XU, the A15 Cs_3C_{60} unit cell volume with pressure (Fig. 4.17) appears to show a smooth compression up to ~5.7 GPa, but above this pressure a distinct deviation is seen: the volume actually appears to increase with pressure up to 7.0 GPa. It then decreases very gradually up to ~10.6 GPa, then shows negligible variation upon further pressurisation. To examine the effects of any measurement errors, the pressure response of the lattice metrics of the minor *fcc* Cs_3C_{60} phase was also examined (Fig. 4.17): whilst the high-pressure structure and compressibility behaviour of A15 Cs_3C_{60} is hitherto unknown, *fcc* Cs_3C_{60} reportedly contracts smoothly to at least 12 GPa (from low temperature measurements,[**140**] though ambient- and low- temperature measurements of overexpanded *fcc* $Rb_xCs_{3-x}C_{60}$ showed analogous behaviour, see Section 3.3). Fig. 4.17 shows that the anomalous high-pressure *P*-*V* trend is seen here in both Cs_3C_{60} polymorphs. It is therefore concluded that data above 8.4 GPa, above which anomalous deviation appears in the *fcc* data, are highly likely to suffer from significant measurement irregularities (strongly non-hydrostatic conditions at high pressure being the most likely explanation, or incorrect pressure definition) and thus these data are not discussed further.

However, between ~5.7-8.4 GPa, the *fcc* phase does not appear to exhibit anomalous behaviour, and the anomaly in the A15 phase data could genuinely result from intrinsic behaviour of the phase. Little else, though, could be determined from this series of refinements to elucidate the cause of this behaviour. The variation in tetrahedral interstitial site-carbon distances with pressure will be examined later in conjunction with the trend observed in A15 Ba_3C_{60} (Fig. 4.41). The A15 phase fraction remained relatively constant between 79-82% upon pressurisation up to 5.2 GPa, above which this decreased gradually to 70% at 8.4 GPa, whilst the relative *fcc* and *bco* fractions increased correspondingly. At high pressures approaching 8.4 GPa, some slight intensity mismatches were observed relative to the low pressure data, but no clear evidence of phase transition was evident (see Fig. 4.22, inset of upper panel), and no obvious anomalies were observed in the refined profile function terms over the pressure range either. Several extremely weak and broad contributions which could not be indexed by the A15 phase began to appear in the profiles above ~5 GPa, discussed further below.

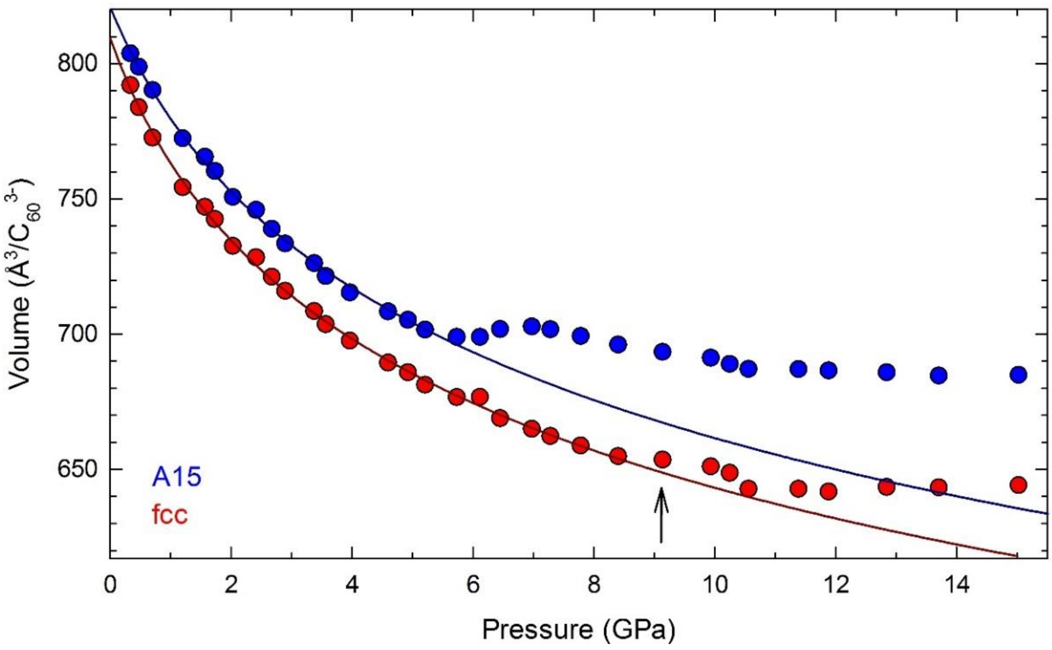

Figure 4.17: The variation in unit cell volume (per C_{60}^{3-}) with pressure for both cubic Cs_3C_{60} polymorphs in the A15-rich sample, at ambient temperature (BL10XU). Statistical uncertainty in volume from Rietveld analysis is smaller than the data point size. Solid lines show results from Murnaghan EoS fits, highlighting the onset of compressibility anomalies (*fcc*, dark red: 0.3-8.4 GPa data fitted, V_0 = 809(2) Å^3, K_0 = 12.9(7) GPa and K' = 9.1(3); A15, dark blue: 0.3-5.7 GPa data fitted, V_0 = 821(2) Å^3, K_0 = 15(1) GPa and K' = 8.9(6)). The arrow indicates the onset (lowest pressure) of visual deviation, *i.e.* 9.1 GPa, from the *fcc* compressibility trend established below this pressure.

A separate specimen of the same sample was also measured at ambient temperature at beamline ID27. However, this specimen contained a far higher proportion of *fcc* phase (54% at 0.1 GPa, with 43% *fcc* phase) and therefore significant peak overlap was evident in the profiles. Nevertheless, Rietveld refinements enabled the compressibility of the minority A15 phase to be extracted and qualitative conclusions about its behaviour can be drawn.

The evolution with pressure of the specimen measured at ID27 is depicted in Fig. 4.18. In stark contrast to the BL10XU data, above ~4-4.5 GPa the A15 peaks start to diminish in intensity (Fig. 4.19), and by 6.4 GPa they were no longer visible, which continued on further pressurisation to 14.5 GPa. Rietveld refinements were discontinued above 6.4 GPa as the A15 phase was no longer visible and some broad, unindexable contributions appeared (see below). The relative fractions of *fcc* and *bco* phases in the sample increased with pressure but their absolute peak intensities appeared to vary little with pressure, *i.e.* the A15 phase was not converting to either phase upon pressurisation. Furthermore, up to ~6 GPa, the A15 compressibility behaviour extracted from the two experiments is very similar (Fig. 4.20). It is interesting that the compressibility anomaly or suppression of the A15 peaks appeared at approximately the same pressure (~4.5-5.5 GPa) in the two experiments. At pressures above ~4.5 GPa, some weak, relatively broad contributions began to appear in the profiles, which do not correspond to *fcc*, A15 or *bco* phases and unfortunately could not be indexed (Fig. 4.21).

Upon depressurisation from 14.5 GPa, below ~4 GPa, A15 peaks began to reappear and increase in intensity with decreasing pressure. Pressure was decreased to 1.7 GPa, then the DAC was fully depressurised to ambient pressure and a final profile was measured approximately 4 minutes after the 1.7 GPa measurement, where the A15 peaks appear to have fully recovered in intensity (Fig. 4.21). This recovery further evidences that the A15 phase is not converting to *fcc* or *bco* phase upon pressurisation, as these are stable at ambient pressure and irreversible pressure-induced A15 peak suppression would thus be expected. Representative refinements at low and at high pressure from both ID27 and BL10XU experiments are depicted in Fig. 4.22.

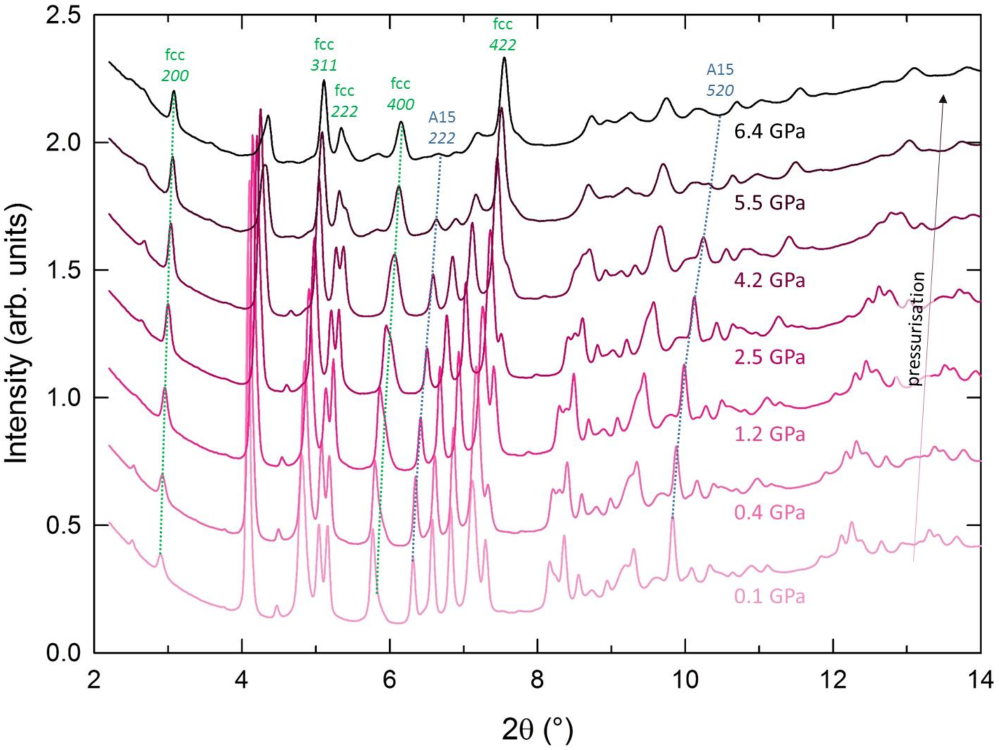

Figure 4.18: Evolution of Cs_3C_{60} PXRD profiles upon pressurisation between 0.1 and 6.4 GPa, at ambient temperature (from ID27, λ = 0.3738 Å); data from selected representative pressures only are displayed for visual clarity. Profiles are intensity-normalised to the background at 3.5°, and shifted vertically for visual clarity; some representative A15 and *fcc* phase peaks are labelled with dotted lines.

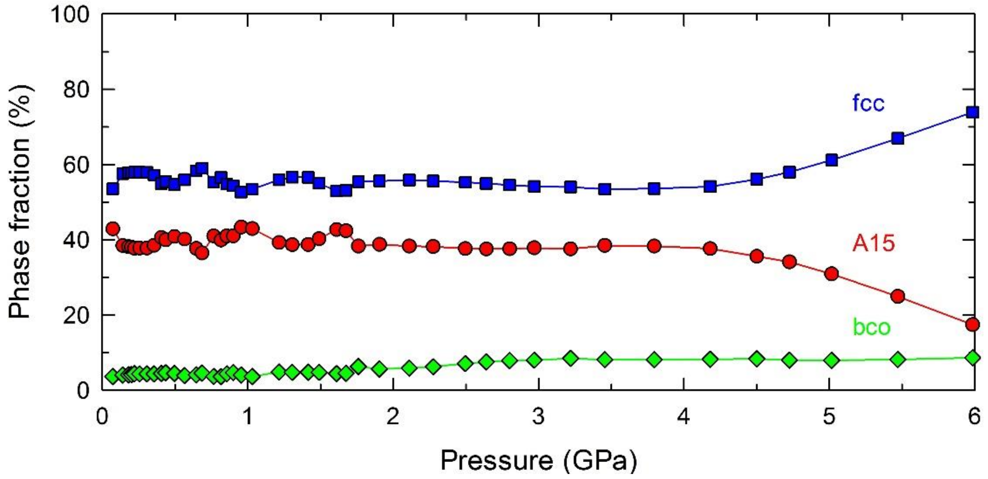

Figure 4.19: Variation of phase fractions with pressure, for the Cs_3C_{60} specimen measured at ambient temperature at ID27.

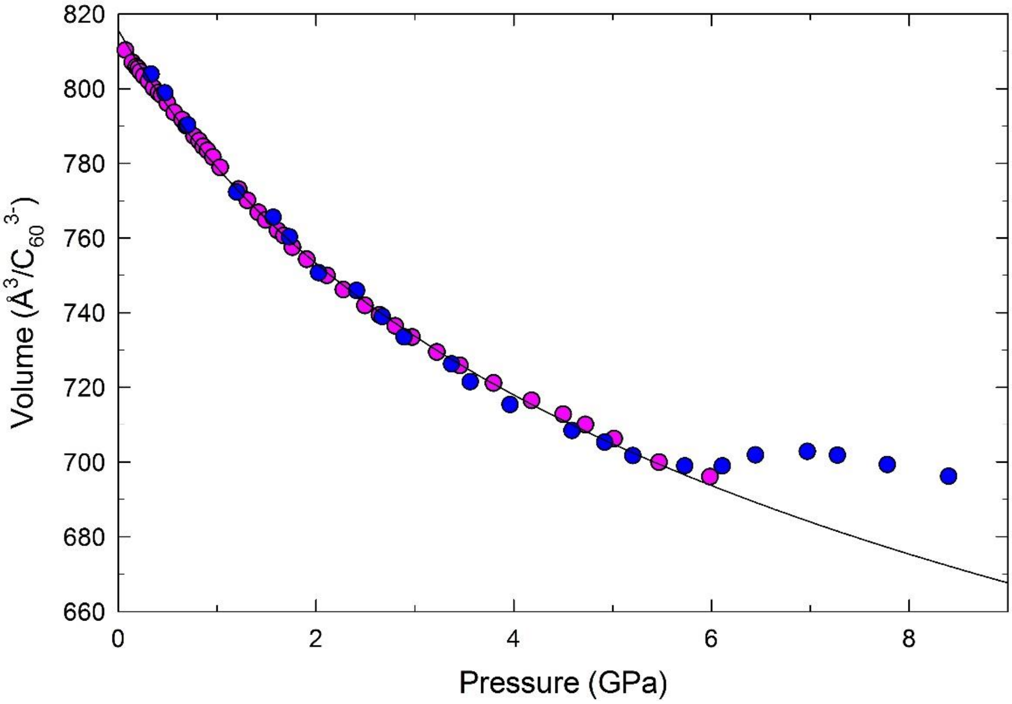

Figure 4.20: Evolution of the A15 Cs_3C_{60} unit cell volume with pressure at ambient temperature, from ID27 (pink) and BL10XU (blue) data. Statistical uncertainties in volume are smaller than the data points. The solid line shows the trend as modelled with a Murnaghan EoS fit to all data from both experiments between 0.1 and 6.0 GPa (V_0 = 815.5(6) Å^3, K_0 = 17.9(5) GPa and K' = 8.1(3)).

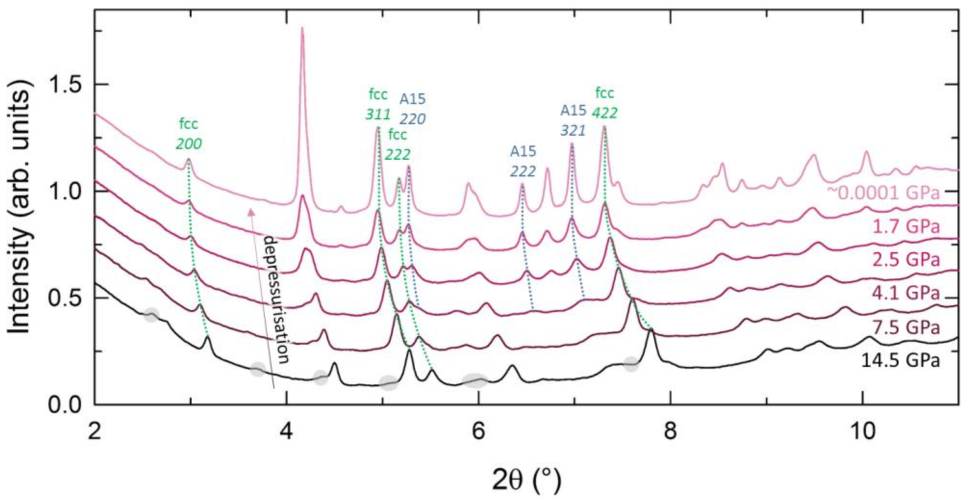

Figure 4.21: Evolution of Cs_3C_{60} PXRD profiles upon depressurisation between 14.5 and 0.0001 GPa, at ambient temperature (ID27, λ = 0.3738 Å); data from selected representative pressures only are displayed for visual clarity. Profiles are intensity-normalised to the background at 3.5°, and shifted vertically for visual clarity; some representative A15 and *fcc* phase peaks are labelled with dotted lines. Some broad contributions which appeared upon pressurisation (grey highlight), suppressed upon depressurisation, could not be indexed.

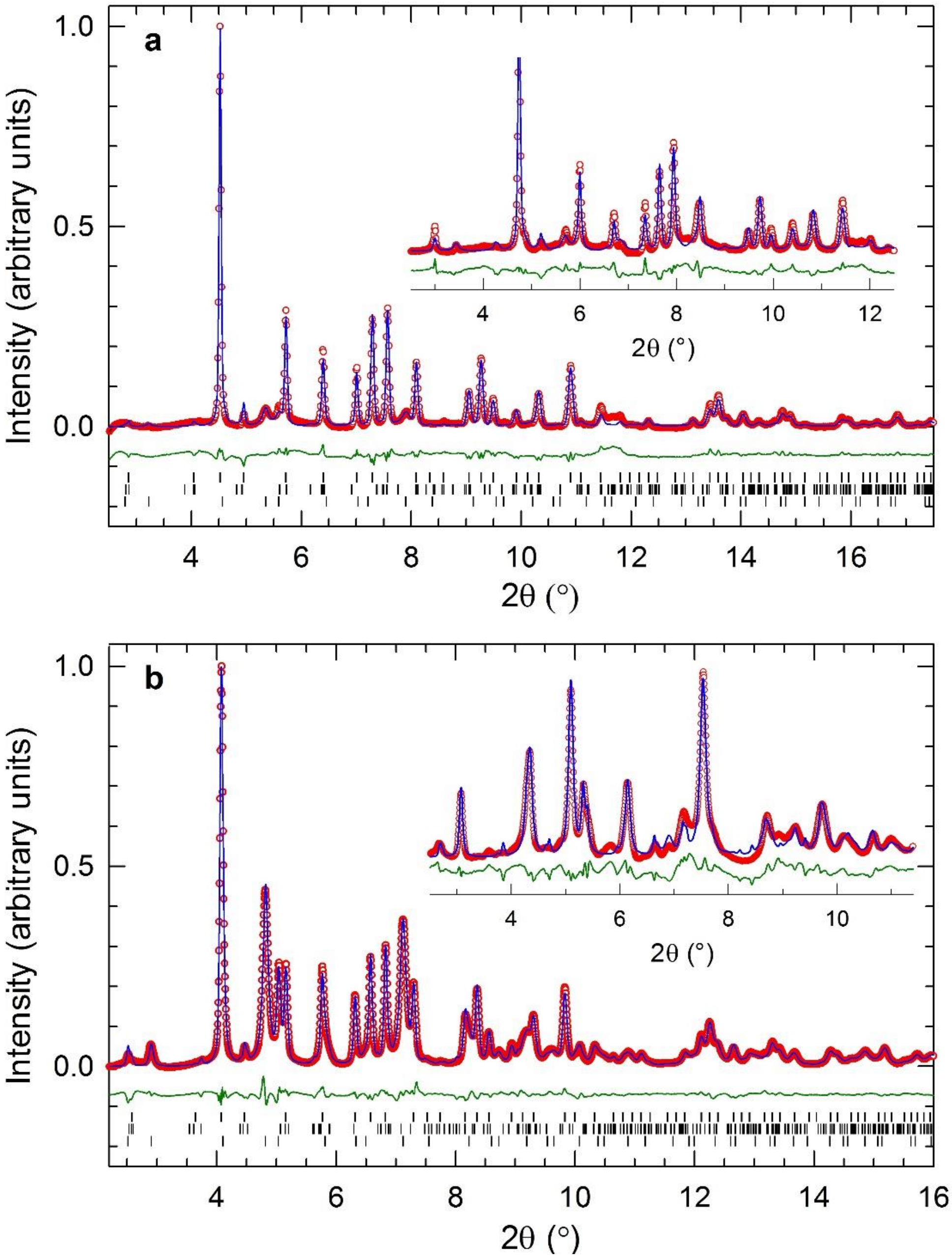

Figure 4.22: Observed (open red circles) and calculated (blue line) X-ray powder diffraction profiles for the A15-rich Cs_3C_{60} sample, collected at ambient temperature at (a) BL10XU (λ = 0.41317 Å, main panel and inset data collected at 0.3 GPa and 8.4 GPa, respectively) and at (b) ID27 (λ = 0.3738 Å, main panel and inset data collected at 0.1 GPa and 6.0 GPa, respectively). Bars represent the positions of the Bragg reflections (for, from top to bottom, the A15, *bco* and *fcc* phases); the green lines correspond to the difference plots (obs-calc). R_{wp} and χ^2 were, respectively, 0.50% and 1.443 (0.3 GPa BL10XU), 0.48% and 1.371 (8.4 GPa BL10XU), 0.63% and 0.2130 (0.1 GPa ID27) and 0.80% and 0.2386 (6.0 GPa ID27). The refined background contributions have been subtracted for visual clarity. A broad contribution from the gasket at ~11.5° in (a) was not excluded from the fits.

4.3.5 Cs_3C_{60} (A15-rich) – Synchrotron XRD at high pressure and low temperature

We now examine the structural evolution of the A15-rich sample upon pressurisation at low temperatures, at 8 K and 20 K (*i.e.* which should correspond to the antiferromagnetic regime at ambient pressure and the superconducting regime at elevated pressures of ~0.3-2.6 GPa).

At 8 K at BL10XU, the A15 peaks were also gradually suppressed on pressurisation (no longer visible above ~5 GPa), but recovered upon depressurisation, as in the ambient temperature ID27 experiment (Fig. 4.23).

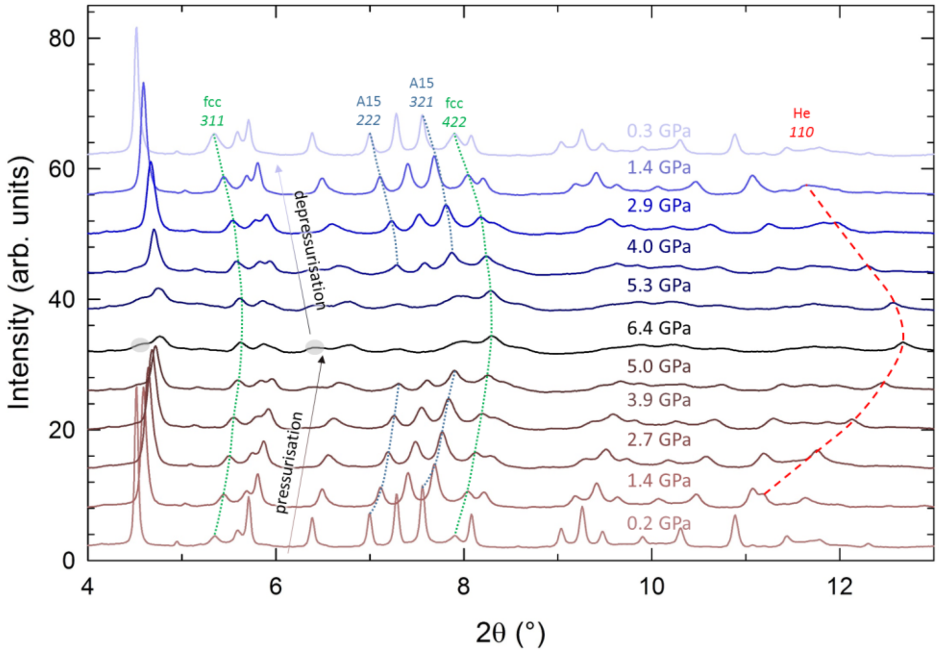

Figure 4.23: Evolution of A15-rich Cs_3C_{60} PXRD profiles as a function of pressure between 0.2 and 6.4 GPa, at 8 K, upon pressurisation and subsequent depressurisation (from BL10XU, λ = 0.41317 Å); data from selected representative pressures only are displayed for visual clarity, with the refined background intensity contributions subtracted for display, and profiles are shifted vertically. Selected representative A15 and *fcc* phase peaks are labelled with dotted lines (and a peak arising from solid He with a dashed line); broad unindexable contributions appearing at high pressure are highlighted in grey.

For the other low temperature experiment (20 K) at ID27, the prominent background contributions deriving from the cryostat were not possible to model with a background function in Rietveld refinement, and relatively overlapped with sample peaks. Therefore, background datasets were collected at regular intervals (every ~0.2 GPa at low pressures and every ~1-2 GPa at higher pressures) where a part of the DAC was irradiated where no sample was present, and for each sample profile, the background data profile collected closest in pressure was subtracted. These profiles were used for Rietveld analysis, where a background function with refinable terms was also employed as throughout this work. The evolution of the profiles with pressure (Fig. 4.24), analogously to the BL10XU 8 K (and ID27 RT) experiments, shows the gradual suppression of the A15 peaks at ~6.5 GPa, and their eventual recovery upon depressurisation. At high pressure, the profiles indicate that the sample was poorly crystalline, but as with the three aforementioned experiments, some broad contributions appeared, which disappeared again upon depressurisation, and due to their complexity could not be indexed or definitively identified. These contributions appear at approximately the same positions in each of the datasets; at ~6 GPa they are visible in multiple experiments at approximate d-spacings 2.33, 2.85, 3.32, 3.45, 3.67, 3.70, 4.35, 4.77, 5.25, 5.85, 5.95, 8.25 and 8.50 Å (others may be present but not detectable because of peak overlap).

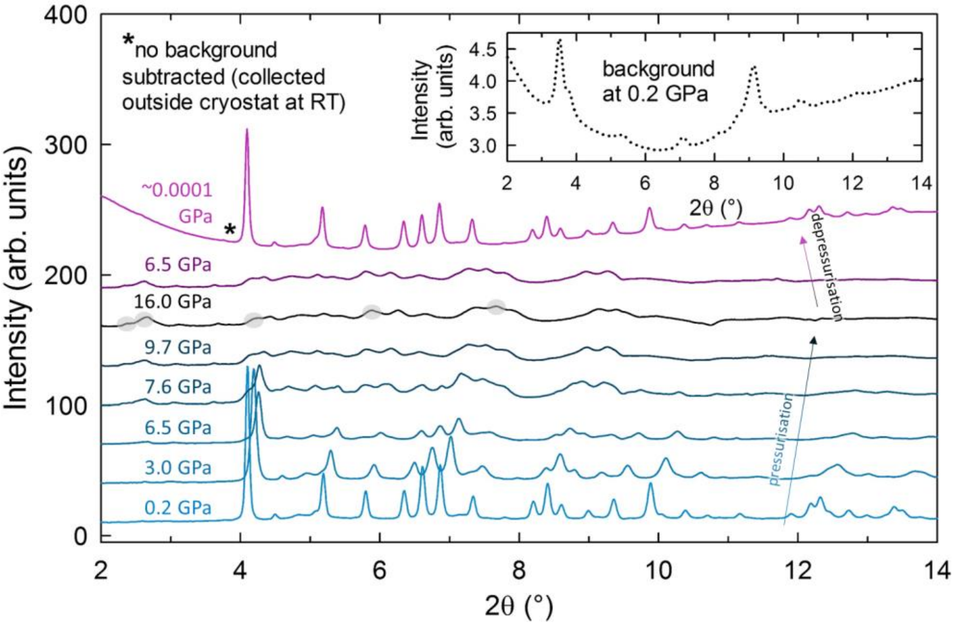

Figure 4.24: Evolution of A15-rich Cs_3C_{60} PXRD profiles with pressure between 0.2 and 16.0 GPa, at 20 K, upon pressurisation and subsequent depressurisation (from ID27, λ = 0.3738 Å); data from selected representative pressures only are shown. A profile collected under ambient conditions after depressurisation, outside the cryostat, is also included (marked as *). Background profiles (a representative one is shown in the inset) were subtracted from the sample profiles, prior to refinement, in an attempt to remove the large cryostat contributions (inset). Profiles are intensity-normalised to the background at 3.4° and shifted vertically. Several broad unindexable contributions appearing at high pressure are highlighted in grey.

Sequential Rietveld analysis was undertaken for data from each experiment in the same manner as for the ambient temperature data, up to 6.4-6.5 GPa where the A15 phase was relatively suppressed. A fourth phase, solid He, was included in the BL10XU series of refinements. Representative refinements at low and at high pressures are shown in Fig. 4.25 for the two experiments.

We now seek to draw some comparisons between the observed low temperature and ambient temperature behaviour. The trends in unit cell volume as a function of pressure for all four data sets collected for the A15 sample on pressurisation, at ambient and at low temperatures, are displayed in Fig. 4.26. Examining the compressibility trends for all data, certain observations are evident. Three of the four experiments showed a smooth compression with pressure up to ~6-6.5 GPa with K_0 values from Murnaghan fits of ~15-18 GPa, comparable to ~14 GPa reported for the *fcc* polymorph at 15 K [**140**], whilst ~33 GPa was reported for the structurally related Cs_6C_{60}. [**225, 226**] However, at 20 K at ID27, above ~0.4 GPa the sample abruptly became far less compressible. A Murnaghan fit to the data between 0.4 and 6.5 GPa yielded a K_0 value of 38.1(4) GPa, similar in magnitude to *e.g.* K_0 values of ~40 GPa reported for the 1D polymers KC_{60} and CsC_{60}.[**165, 227**]

Upon further increase in pressure, A15-phase peak suppression was seen in 3 out of 4 experiments, though fully reversible upon depressurisation. In the remaining experiment at BL10XU at ambient temperature, whilst crystalline A15 phase peaks appeared to be preserved above 8 GPa, the $V(P)$ trend above ~6.5 GPa is anomalous, appearing to correspond to a transformation to a less compressible phase. Speculatively, from the $V(P)$ trends in the two data sets, this latter transformation could be analogous to that which appeared to occur at a much lower pressure in the ID27 20 K data. However, besides the compressibility changes there are no clear indications from the profiles from those two experiments of any phase transition or structural changes which could give rise to this behaviour. For each experiment, specimens from the same sample were used with extremely similar experimental setups, including initial He pressures *etc.*; it unfortunately remains unclear as to why the four experiments (particularly between each pair of experiments carried out at similar temperatures) yielded such different results, *e.g.* peak suppression at ~6 GPa *vs.* no peak suppression at ambient temperatures, and transition to a markedly less compressible phase at ~0.4 GPa *vs.* no anomalous behaviour in the compressibility at low temperatures.

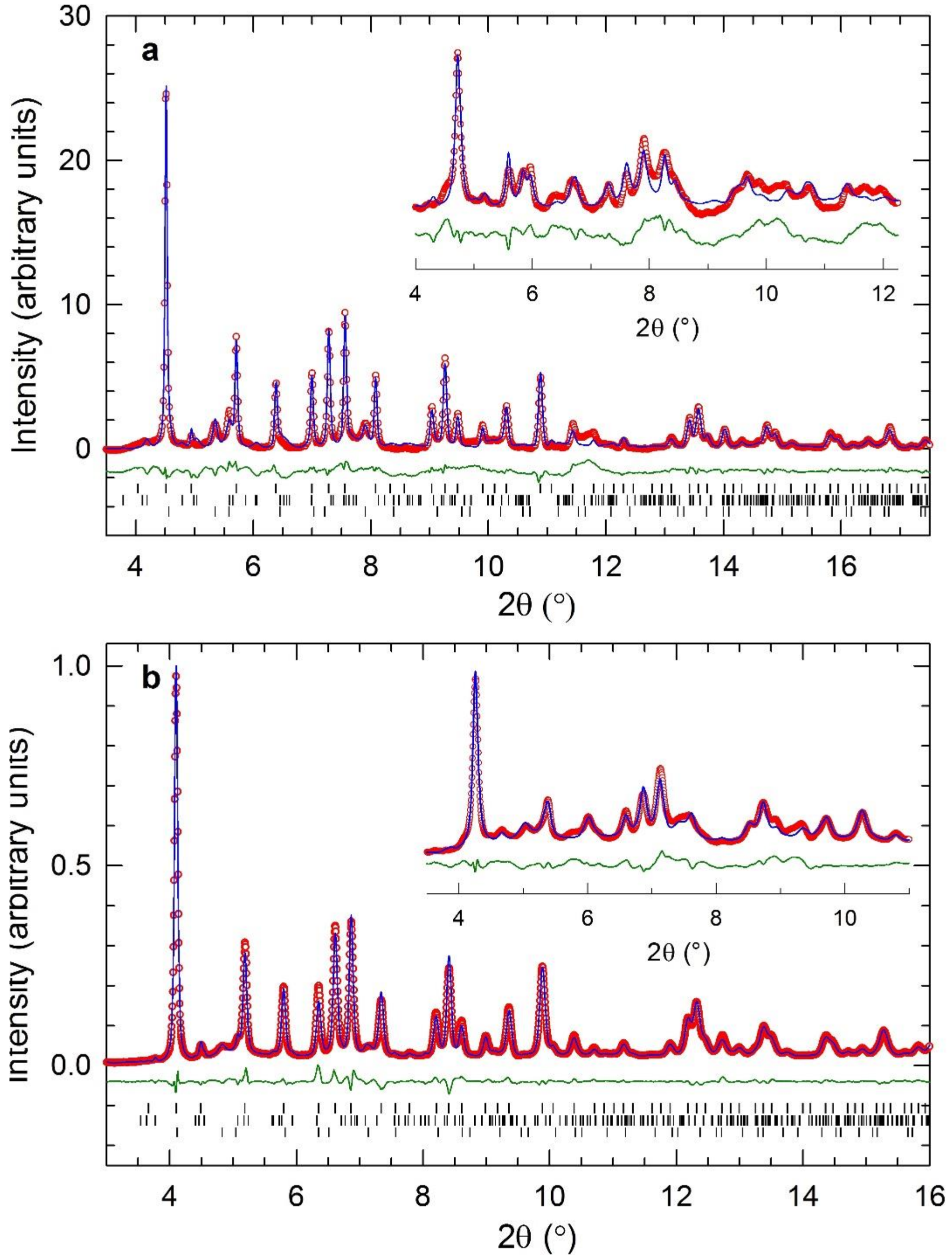

Figure 4.25: Observed (open red circles) and calculated (blue line) X-ray powder diffraction profiles for the A15-rich Cs_3C_{60} sample, collected at 8 K at BL10XU ((a), λ = 0.41317 Å, main panel and inset data collected at 0.2 GPa and 5.4 GPa, respectively) and at 20 K at ID27 ((b), λ = 0.3738 Å, main panel and inset data collected at 0.2 GPa and 6.5 GPa, respectively). Bars represent the positions of the Bragg reflections; the green lines correspond to the difference plots (obs−calc). R_{wp} and χ^2 were, respectively, 0.39% and 0.7996 (0.2 GPa BL10XU), 0.44% and 1.008 (5.4 GPa BL10XU), 6.32% and 1.091 (0.2 GPa ID27) and 8.69% and 2.561 (6.5 GPa ID27). The refined background contributions have been subtracted for visual clarity. A broad contribution from the gasket at ∼11.5° in (a) was not excluded from the fits.

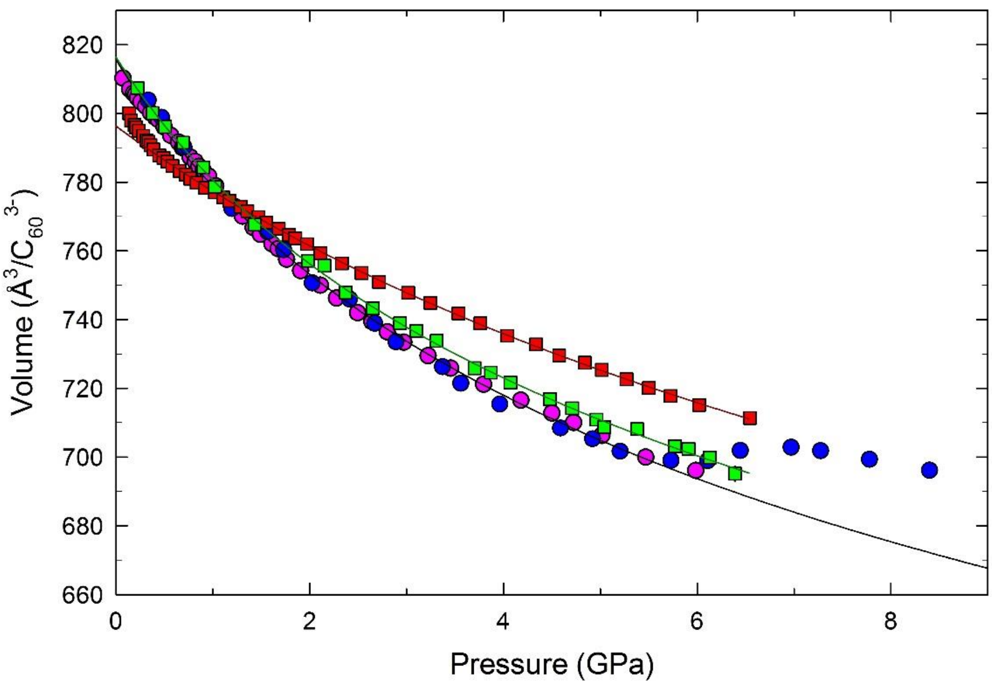

Figure 4.26: Evolution of the A15 Cs_3C_{60} unit cell volume with pressure at low temperature, from ID27 (red squares) and BL10XU (green squares); data collected at ambient temperature (purple and blue circles) and the Murnaghan fit from Fig. 4.20 are included for comparison. Statistical uncertainties in volume are smaller than the data points. Solid lines show results from Murnaghan EoS fits (ID27, dark red: 0.4-6.5 GPa data fitted, V_0 = 796.3(2) Å^3, K_0 = 38.1(4) GPa and K' = 6.9(2); BL10XU, dark green: 0.2-6.4 GPa data fitted, V_0 = 816(1) Å^3, K_0 = 18.1(7) GPa and K' = 9.0(3)).

In summary, in this section some preliminary results on the behaviour of A15 Cs_3C_{60} under pressurisation, both at low and at ambient temperatures, have been presented. Whilst many questions remain unanswered, *e.g.* as to the precise identity of the low crystallinity phase which is stable at high pressures only, and why individual experiments exhibited such different behaviour, various potentially relevant factors and hypotheses are discussed later in conjunction with the results in Section 4.4.

4.3.6 A15 Ba_3C_{60} – Synchrotron XRD at high pressures and at ambient temperature

Synchrotron PXRD data for the phase-pure A15 Ba_3C_{60} sample earlier characterised under ambient conditions (section 4.3.2) were also collected upon applying hydrostatic pressure, at 33 discrete pressures up to a maximum of 11.50 GPa, as described in Section 4.3.1. The evolution of the Ba_3C_{60} PXRD profiles with pressure is illustrated in Fig. 4.27.

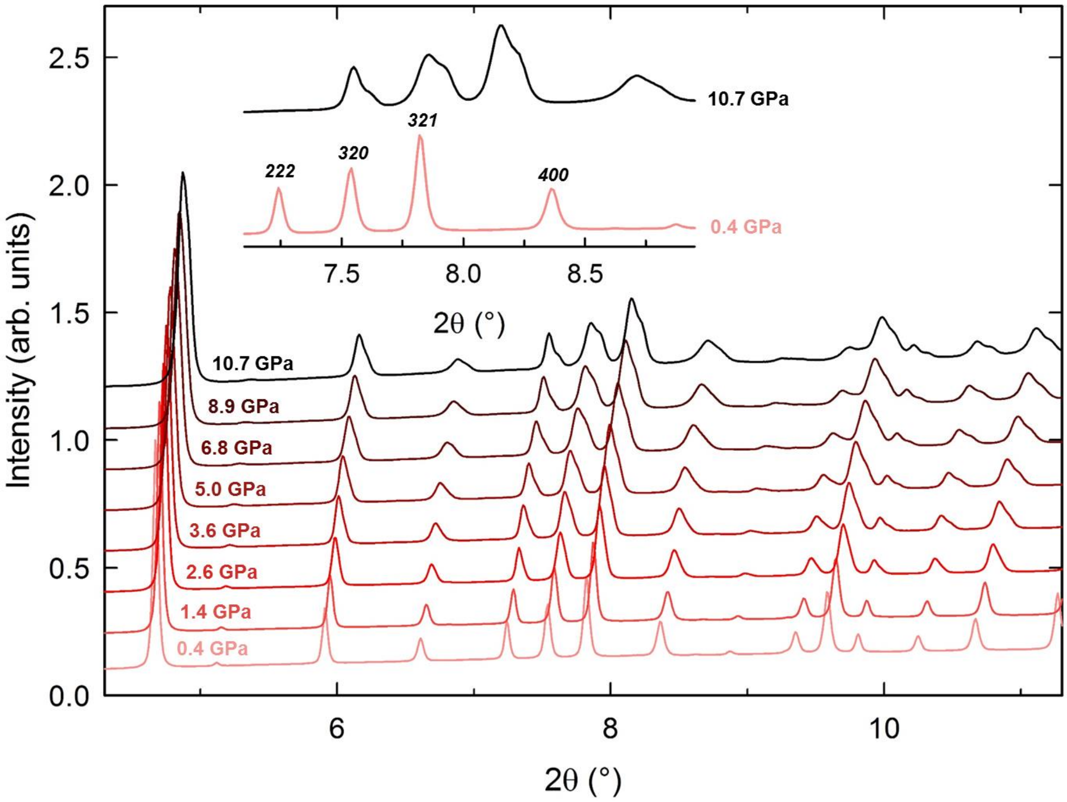

Figure 4.27: The evolution of Ba_3C_{60} PXRD profiles as a function of pressure between 0.4 and 10.7 GPa, at ambient temperature (λ = 0. 41261 Å); data from selected representative pressures only are displayed for visual clarity. Profiles are normalised in intensity to that of the highest peak and vertically shifted for visual clarity. Inset: an expanded region of profiles collected at 0.4 and 10.7 GPa, with Miller indices of reflections in the low-pressure A15 cubic structure labelled.

From visual inspection of the profiles evolution with pressure, whilst the cubic A15 structure is retained initially at pressures below ~2 GPa, above this pressure a distinct peak anisotropy emerges which evolves into well-defined peak splitting as pressure is further increased. Hitherto, no transitions to another crystalline phase have been reported in Ba_3C_{60} as a function of pressure.

Firstly, structural analysis was undertaken for the low-pressure region using a conventional A15 cubic structural model in single-phase Rietveld refinements. An initial refinement was undertaken to derive the best structural model to the lowest-pressure data set, 0.31 GPa; this refinement approach, described below, was then extended sequentially to data sets collected upon increasing pressure.

The refined fractional C_{60} coordinates derived in section 4.3.2 for the Ba_3C_{60} sample under ambient conditions were employed for the high pressure refinements, rescaled at each pressure to the refined cubic lattice parameter, thus C-C distances were fixed to those derived at ambient pressure (as negligible molecular deformation is expected upon moderate pressurisation, and the data are intrinsically of lower quality than those collected at ambient pressure). In the analysis of the 0.31 GPa data set, lattice metrics, isotropic thermal displacement U_{iso} for Ba^{2+}, background (20-term Chebyschev polynomial), scale factor, isotropic Lorentzian and Gaussian profile broadening parameters GU, GV, GW, LX and LY (using GSAS profile function type 3), and anisotropic profile broadening terms L_{xy} were allowed to refine, although L_{xy} and background terms were unchecked in the final cycles because of high correlations. For higher pressures, U_{iso} for Ba^{2+} and GU, GV, GW and LX were fixed to the final values deriving from the 0.31 GPa refinement. A fixed zero point value of 0.04518 centidegrees was used for all refinements, extracted as the mean refined zero point from a preliminary analysis of the series of datasets, where zero was allowed to vary.

The Rietveld refinement results and details of the structural model employed for the lowest pressure dataset, 0.31 GPa are presented in Fig. 4.28 and

Table 4.7. The refinement strategy described above provided an excellent fit to the 0.31 GPa data.

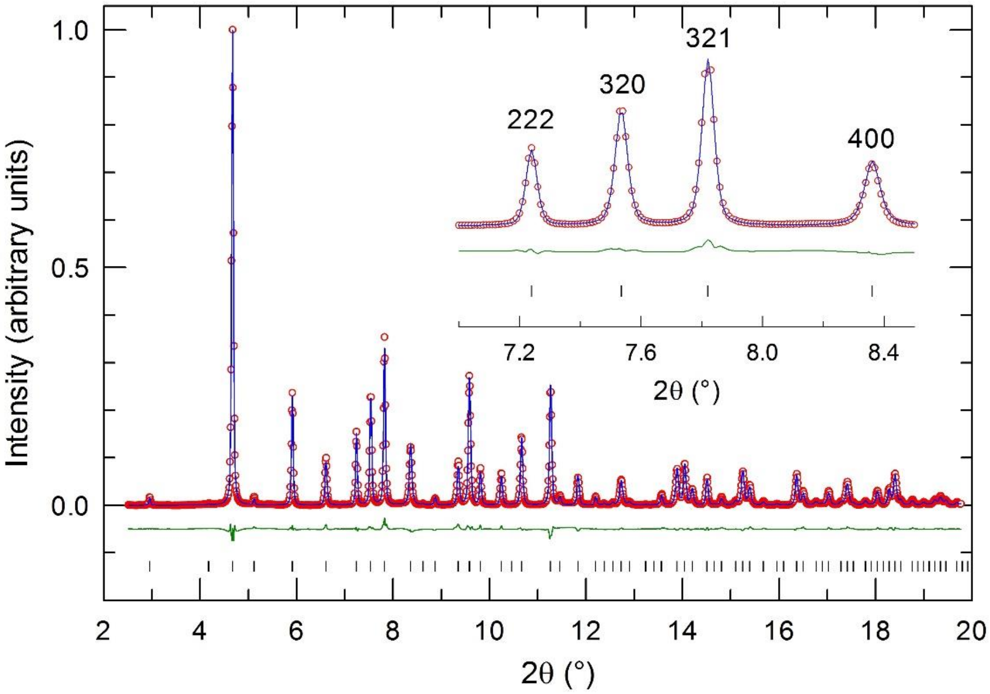

Figure 4.28: Observed (open red circles) and calculated (blue line) X-ray powder diffraction profiles for A15 Ba_3C_{60}, collected at 0.31 GPa and at ambient temperature (λ = 0.41261 Å). Bars represent the positions of the Bragg reflections; the green line corresponds to the difference plot (obs-calc). The refined background contribution has been subtracted for visual clarity. The inset shows an expanded region, with Miller indices labelled.

For data sets collected at pressures up to and including 2.17 GPa, the reliability indices χ^2 and R_{wp} ranged between ~1.2-1.8 and ~0.9-1.2%, respectively. However, when analysis was extended to higher pressures, χ^2 and R_{wp} began to markedly increase with pressure, *e.g.* χ^2 increased from 2.752 to 7.376 between 2.33 and 2.72 GPa, whilst R_{wp} increased from 1.41% to 2.30% over the same pressure range. A consequence of the developing peak anistropy marking the onset of the peak splitting, this indicated that a single-phase cubic A15 structural model can no longer provide a satisfactory description for Ba_3C_{60} at pressures above ~2.17 GPa, and this analysis was not extended further above 2.72 GPa. Results from this series of refinements, between 0.31 and 2.72 GPa, are presented later in the chapter together with results from analysis of the higher pressure data (see Fig. 4.32 onwards); the latter will now be discussed.

Table 4.7: Refined structural parameters for the Rietveld fit of the A15 Ba_3C_{60} model ($\boldsymbol{Pm\bar{3}n}$) to synchrotron X-ray powder diffraction data collected at 0.31 GPa and at ambient temperature. Estimated errors in the last digits are given in parentheses (R_{wp} = 0.90%, R_F^2 = 4.07%, χ^2 = 1.158).

	x/a	y/b	z/c	Position	N	B_{iso} (Å^2)
Ba^{2+}	0.25	0	0.5	6c	1	1.25(3)
C(1)	0	0.3087	0.0634	24k	1	0.45
C(2)	0.1308	0.1001	0.2676	48l	1	0.45
C(3)	0.0632	0.2018	0.2336	48l	1	0.45

Next, the origin of the peak splitting at moderate pressures was considered, aiming to derive a structural model which could provide a satisfactory description for Ba_3C_{60} above ~2.17 GPa. In assigning a lattice system and space group to the high-pressure phase, it is clearly evident from the peak shapes that all peaks are split, with respect to the low-pressure cubic phase, meaning that a symmetry-lowering transition to an orthorhombic, tetragonal or rhombohedral structure is not a feasible cause for the splitting.

One possibility considered was phase separation into two cubic phases at high pressure, *i.e.* retention of the low-pressure A15 'pentagonally coordinated' phase and a new cubic phase appearing (with a smaller lattice volume than the majority A15 phase, as peak intensity appears on the high angle shoulder of the majority A15 phase peaks). However, this was determined to be unfeasible: if a secondary phase were emerging, this would also need to be A15 and cubic based on it appearing to have the same systematic absences as the majority A15 phase. The only other type of A15 phase is the 'hexagonally coordinated' structure (found in A15 Cs_3C_{60} under ambient conditions), but simulations of the diffraction patterns of pentagonal and hexagonal coordination in the A15 structure show that of the distinctive three peaks observed between ~7 and 8° 2θ, only the *320* peak visibly differs in intensity, whilst the intensity of the *222* and *321* peaks appear identical for the two coordination types. This does not match the observed relative intensities of the new peaks appearing at high-pressure in the patterns here (besides, simulations of the related A15 Cs_3C_{60} indicated that hexagonal coordination is energetically disfavoured over pentagonal coordination at high pressures [**54**]). The splitting was therefore determined to be more likely to result from a symmetry-lowering transition of the low-pressure cubic A15 phase.

The high-pressure structure was indeed found to be best indexed by a monoclinic phase, through a relatively small distortion of the low-pressure cubic symmetry. Hereafter, this monoclinic phase will be referred to as 'A15-M'. Upon close examination, systematic absences then revealed that the high-pressure structure is most consistent with space groups *C2/c*, *Cc*, *C2*, *Cm* or *C2/m* (no peak intensity is observed at the 2θ positions for Miller indices *hkl* where $h + k \neq 2$n). Further distinction between these five groups from examination of these high-pressure PXRD data alone was deemed unreliable, with peak intensity for reflections *h*0*l* being very weak and significant overlap between peaks (for the two former groups, an additional selection rule is that for reflections *h*0*l*, $l = 2$n). *C2/c*, *Cc* and *C2* are subgroups (albeit not maximal) of the low-pressure cubic $Pm\bar{3}n$ structure, and could theoretically result from a series of symmetry-lowering steps through *translationengleiche* subgroups. However, if a hypothetical strain distortion (*i.e.* unit cell parameter changes) which would lower the symmetry of $Pm\bar{3}n$ to monoclinic is considered, ISODISTORT shows that the only feasible distortion mode has as its space-group symmetry *C2/c*. Therefore, a space group of *C2/c* has been used for Rietveld analysis of the high-pressure structure. A setting $C\,1\,2/c\,1$ has been employed, with *b* as the unique axis. Only one order parameter direction (and thus one possible set of symmetry-transformed atomic coordinates) is possible for a symmetry reduction of A15 $Pm\bar{3}n$ to *C2/c* with strain distortive modes; the resulting supercell has basis vectors [(1,0,1)(1,0,−1)(0,1,0)] and an origin (0,0,0.5) in parent lattice units, the primitive unit cell of the subgroup is the same size as the parent lattice and $i = 12$ (the order parameter direction is C2 in Stokes and Hatch notation, *i.e.* two-dimensional [**223**]).

Fig. 4.29 schematically depicts the relationship between the A15 and A15-M unit cells. The unit cell volume size in the A15-M model is twice that of the conventional A15 structure, with the former structure containing four molecules per unit cell to the latter's two.

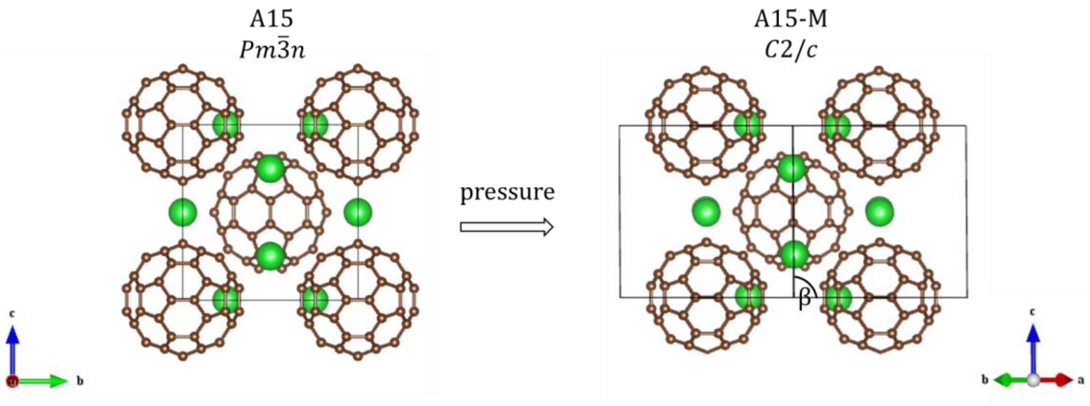

Figure 4.29: Schematic depiction of the relationship between the A15 and A15-M structural models for Ba_3C_{60} (generated using VESTA).

Transformation of the C_{60} fractional unit cell coordinates from $Pm\bar{3}n$ to $C2/c$ symmetry generates thirty unique carbon atoms in the monoclinic structure, from the initial three in the cubic structure. Given the large number of inequivalent atoms in the cell at high pressures, the relatively slight nature of the distortion and the fact that only high-pressure powder diffraction data are currently available for the monoclinic phase, the following strategy was undertaken to best model the monoclinic C_{60} coordinates for Rietveld analysis.

Realistic cubic $Pm\bar{3}n$ fractional coordinates were generated for each of the experimental pressures (*i.e.* a hypothetical model assuming no structural distortion/symmetry reduction), then each set of coordinates were transformed into $C2/c$ using ISODISTORT. The $Pm\bar{3}n$ C_{60} fractional coordinates were generated as follows: having first been determined at ambient pressure through structural refinement of high-resolution PXRD data, the cubic C_{60} coordinates were rescaled (in order to fix bond lengths, angles etc) to the refined latice metrics for each individual experimental pressure. For pressures above the onset of peak splitting, a series of initial refinements where the splitting was crudely modelled using two cubic $Pm\bar{3}n$ phases was first undertaken, to extract a best approximation to the cubic lattice parameter at every experimental pressure in the hypothetical case of no pressure-induced symmetry-lowering transition, to in turn generate reasonable monoclinic atomic coordinates and lattice metrics for use in the Rietveld analysis.

Upon generation of best $C2/c$ monoclinic atomic coordinates at each of the experimental pressures, purely from transformation of the cubic fractional coordinates derived by refinement under ambient conditions (section 4.3.2), the C_{60} fractional coordinates were fixed for the refinements and not refined, although the unit cell metrics were allowed to refine. Although this model is imperfect as this causes a very slight change to the C_{60} cage dimensions, the small magnitude of distortion here meant that this model provided an excellent fit to the diffraction data, with no visible distortion to the cage. C-C bond lengths at ambient pressure in the cubic model ranged from 1.43–1.44 Å; at the highest pressure, 11.5 GPa, where the maximum distortion away from the cubic structure is found, the thirty C-C bond lengths ranged from 1.42–1.45 Å.

In cubic $Pm\bar{3}n$ Ba_3C_{60}, Ba^{2+} occupies a special site, $6c$, at (0.25, 0, 0.5), whilst in the monoclinic $C2/c$ model, Ba^{2+} is situated in sites $8f$ (x, y, z) and $4e$ (0, y, 0.25); upon symmetry reduction of the A15 structure from $Pm\bar{3}n$ symmetry these are (0.125, 0.125, 0) and (0, 0.5, 0.25), respectively. The Ba^{2+} fractional coordinates were allowed to refine at each pressure in the monoclinic regime to study changes in Ba-C coordination and interatomic distances as a function of pressure and to provide a more realistic model.

In order to analyse the pressure dependence of the high-pressure lower symmetry structure using this A15-M model, firstly a single-phase Rietveld refinement was undertaken for the highest pressure dataset (*i.e.* where the distortion away from cubic symmetry appears to be greatest), collected at 11.50 GPa (Fig. 4.30,

Table 4.8). Lattice metrics, fractional coordinates and isotropic thermal displacement U_{iso} for Ba^{2+}, background (20-term Chebyschev polynomial), scale factor, isotropic Lorentzian strain broadening (LY), anisotropic profile broadening terms L_{xy} and spherical harmonic preferential orientation coefficients (order = 4) were allowed to refine, although L_{xy} and background terms were as previously unchecked in the final cycles. Other profile terms and carbon U_{iso} values were fixed equal to those values used for the cubic A15 low-pressure Ba_3C_{60} model, and not refined.

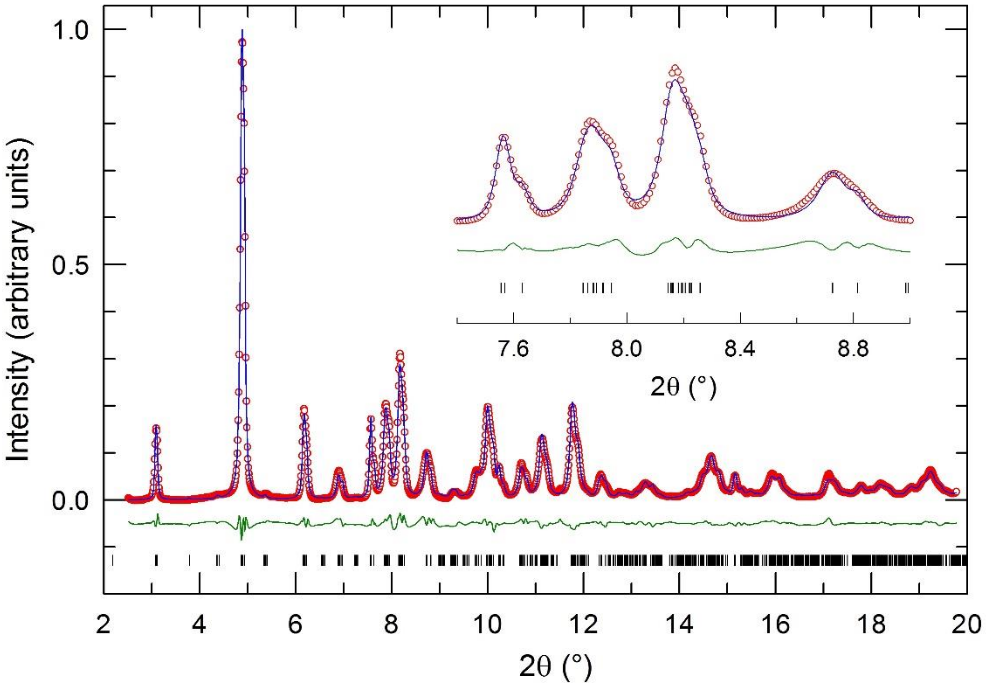

Figure 4.30: Observed (open red circles) and calculated (blue line) X-ray powder diffraction profiles for 'A15-M' Ba_3C_{60}, collected at 11.50 GPa and at ambient temperature (λ = 0.41261 Å). The bars represent the positions of the Bragg reflections; the green line corresponds to the difference plot (obs-calc). The refined background contribution has been subtracted for visual clarity. The inset shows an expanded region of the profiles and the difference plot.

Table 4.8: Refined structural parameters for the Rietveld fit of the high-pressure monoclinic A15-M (space group $C2/c$) Ba_3C_{60} model to synchrotron PXRD data collected at 11.50 GPa and at ambient temperature. Estimated errors in the last digits are given in parentheses (R_{wp} = 1.09%, R_{F}^2 = 2.80%, χ^2 = 1.695).

	x/a	*y/b*	*z/c*	Position	*N*	B_{iso} (Å^2)
Ba^{2+}(1)	0.1210(6)	0.1215(5)	0.0059(5)	8f	1	0.30(8)
Ba^{2+}(2)	0	0.5068(8)	0.25	4e	1	3.0(3)
C(1)	0.7831	0.2169	0.3222	8f	1	0.45
C(2)	0.7169	0.2831	0.3222	8f	1	0.45
C(3)	0.9111	0.4111	0.0662	8f	1	0.45
C(4)	0.9111	0.4111	0.9338	8f	1	0.45
C(5)	0.9442	0.1220	0	8f	1	0.45
C(6)	0.6220	0.4442	0	8f	1	0.45
C(7)	−0.0421	0.1786	0.1045	8f	1	0.45
C(8)	0.6786	0.4579	0.8955	8f	1	0.45
C(9)	0.5421	0.3214	0.1045	8f	1	0.45
C(10)	0.8214	0.0421	0.8955	8f	1	0.45
C(11)	0.8705	0.2340	0.2794	8f	1	0.45
C(12)	0.7340	0.3705	0.7207	8f	1	0.45
C(13)	0.6295	0.2660	0.2794	8f	1	0.45
C(14)	0.7660	0.1295	0.7207	8f	1	0.45
C(15)	0.9419	0.3374	0.1365	8f	1	0.45
C(16)	0.8374	0.4419	0.8635	8f	1	0.45
C(17)	0.5581	0.1626	0.1365	8f	1	0.45
C(18)	0.6626	0.0581	0.8635	8f	1	0.45
C(19)	0.9049	0.1611	0.2106	8f	1	0.45
C(20)	0.6611	0.4049	0.7894	8f	1	0.45
C(21)	0.5951	0.3389	0.2106	8f	1	0.45
C(22)	0.8389	0.0951	0.7894	8f	1	0.45
C(23)	0.8883	0.3223	0.2439	8f	1	0.45
C(24)	0.8223	0.3883	0.7562	8f	1	0.45
C(25)	0.6117	0.1777	0.2439	8f	1	0.45
C(26)	0.6777	0.1117	0.7562	8f	1	0.45
C(27)	−0.0228	0.2666	0.0660	8f	1	0.45
C(28)	0.7666	0.4772	0.9340	8f	1	0.45
C(29)	0.5228	0.2334	0.0660	8f	1	0.45
C(30)	0.7334	0.0228	0.9340	8f	1	0.45

This A15-M model provided an excellent fit to the 11.50 GPa diffraction data (R_{wp} = 1.10%, R_{F^2} = 2.60%, χ^2 = 1.700), yielding monoclinic lattice constants of a = 15.304(2) Å, b = 15.379(2) Å, c = 10.739(1) Å and β = 90.60(1)° and a unit cell volume of 2527.6(3) Å^3.

The analysis approach described above was then extended sequentially to each data set, upon decreasing pressure, with the aforementioned parameters allowed to vary (excepting Ba^{2+} U_{iso} values, which were fixed to those values determined for the highest pressure data set). As for the low-pressure A15 refinements, a fixed zero point value of 0.04518 centidegrees was used for all refinements. Stable refinements were successfully achieved upon decreasing pressure to 2.34 GPa (see Fig. 4.31 for a representative Rietveld fit to data collected at 3.09 GPa); when an attempt to extend the analysis down to 2.17 GPa (the next data set) was made, a stable converged refinement could not be achieved. The preferred orientation correction required was small in magnitude, with the texture index varying between 1.04-1.09 over the whole series.

Whilst both series of single-phase Rietveld analyses (using the A15 and A15-M models) used to model the $\mathrm{Ba_3C_{60}}$ structure were extended over the intermediate pressure range 2.34-2.72 GPa, the A15-M Rietveld fits in this pressure regime have significantly lower χ^2 and R_{wp} values than the equivalent A15 fits (at 2.34 GPa, these values were 1.673 and 1.09% respectively for A15-M and 2.752 and 1.41% for A15; meanwhile, at 2.72 GPa, χ^2 and R_{wp} were only 1.750 and 1.12% for A15-M but were 7.376 and 2.30% for A15). Attempts to determine whether there is any coexistence regime within this small range of pressures, with two-phase Rietveld analysis with A15-M and A15 to estimate the relative phase fractions, did not produce stable refinements, which could be due to the very subtle nature of the transition in this pressure range (manifesting as slight anisotropic broadening only).

Therefore in summary, on the basis of the available data, the system is best described by the cubic A15 model up to 2.17 GPa, and by the monoclinic A15-M model between 2.33 and 11.50 GPa, and data extracted from these refinements will now be presented.

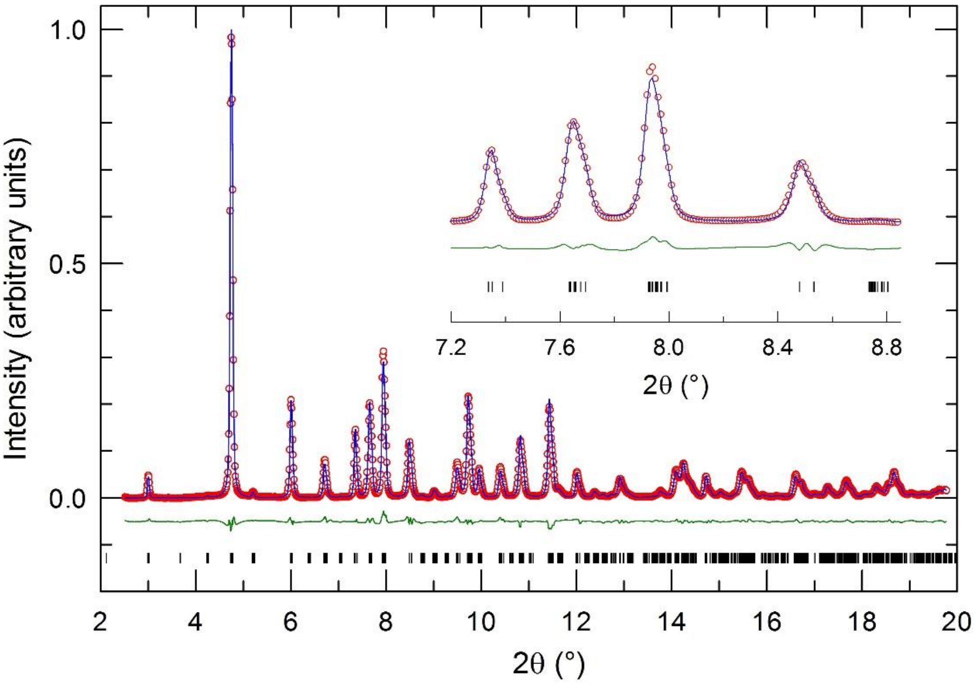

Figure 4.31: Observed (open red circles) and calculated (blue line) X-ray powder diffraction profiles for 'A15-M' Ba_3C_{60}, collected at 3.09 GPa and at ambient temperature (λ = 0.41261 Å). The bars represent the positions of the Bragg reflections; the green line corresponds to the difference plot (obs−calc). The refined background contribution has been subtracted for visual clarity. The inset shows an expanded region of the profiles and the difference plot.

The overall evolution of unit cell volume per fulleride ion with pressure for both the A15-M and A15 phases (Fig. 4.32) is relatively continuous over the full pressure range, with no sudden changes in volume evident at the transition. The variation of lattice parameters with pressure for the two phases is shown in Fig. 4.33. Upon symmetry reduction of the A15 $Pm\bar{3}n$ structural model to A15-M ($C2/c$), but hypothetically assuming no structural distortion, the A15-M c parameter is equal to A15 a (and equivalently b and c), whilst A15-M a and b are equal to one another and to $\sqrt{2} \times$ A15-M c. The lattice parameter trends are more easily visualised if A15-M a and b are divided by $\sqrt{2}$ (Fig. 4.34). At the initial emergence of the A15-M phase, A15-M a and b are very similar to one another but their values gradually diverge with increasing pressure. Meanwhile, A15-M c, initially very close to A15 a at the same pressure, deviates with increasing pressure to slightly lower values than would be anticipated from extrapolation of the A15 lower pressure data (hypothetically, assuming no transition).

The unique unit cell angle, β, in the A15-M structure initially increases rapidly with pressure (Fig. 4.35), from 90.182(4)° at 2.33 GPa to 90.346(6)° at 2.58 GPa, evolving away from the 90° expected in the cubic A15 parent structure, then increasing more gradually as pressure is increased further, eventually reaching 90.59(1)° at 11.50 GPa. The mean nearest-neighbour interfulleride distance undergoes a relatively smooth evolution with pressure (Fig. 4.36).

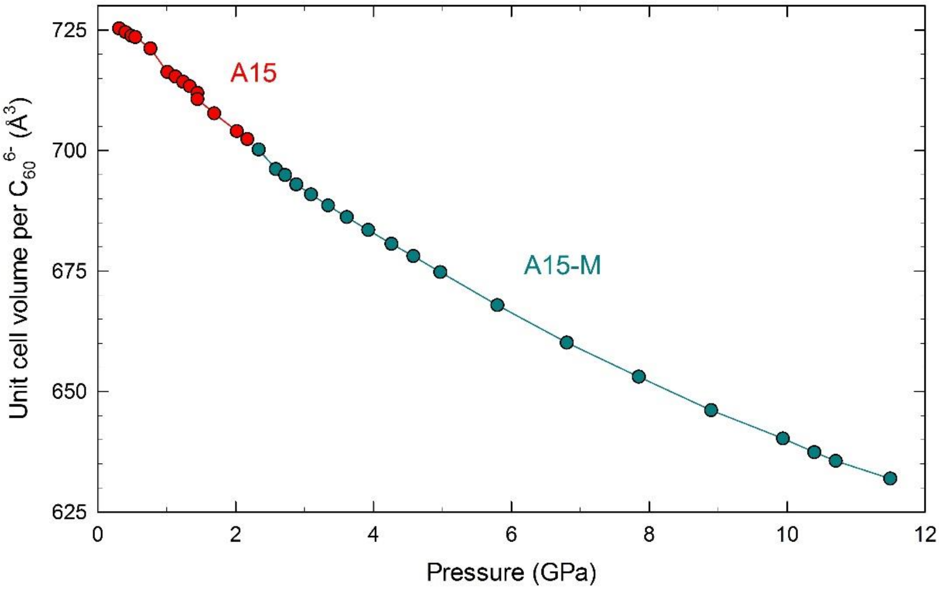

Figure 4.32: Evolution of volume per fulleride ion with pressure for Ba_3C_{60} over the full pressure range investigated, for the A15 (red) and A15-M (cyan) structural models. Statistical errors in the volume from Rietveld fitting are smaller in magnitude than the symbol sizes.

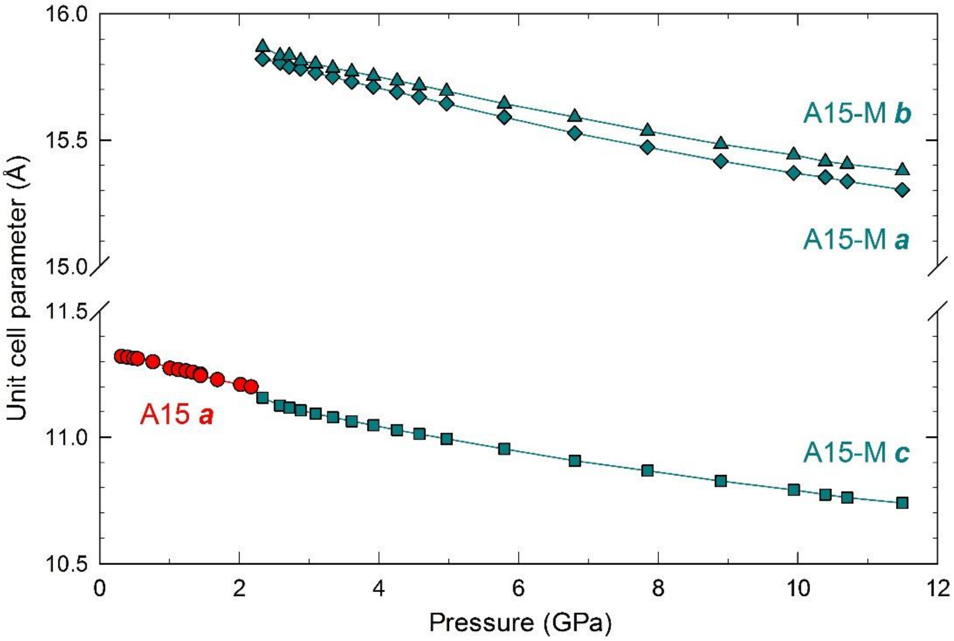

Figure 4.33: Evolution of lattice parameters *a*, *b* and *c* with pressure for Ba_3C_{60} for the A15 (red) and A15-M (cyan) structural models. Statistical errors in lattice parameters from Rietveld fitting are smaller in magnitude than the symbol sizes.

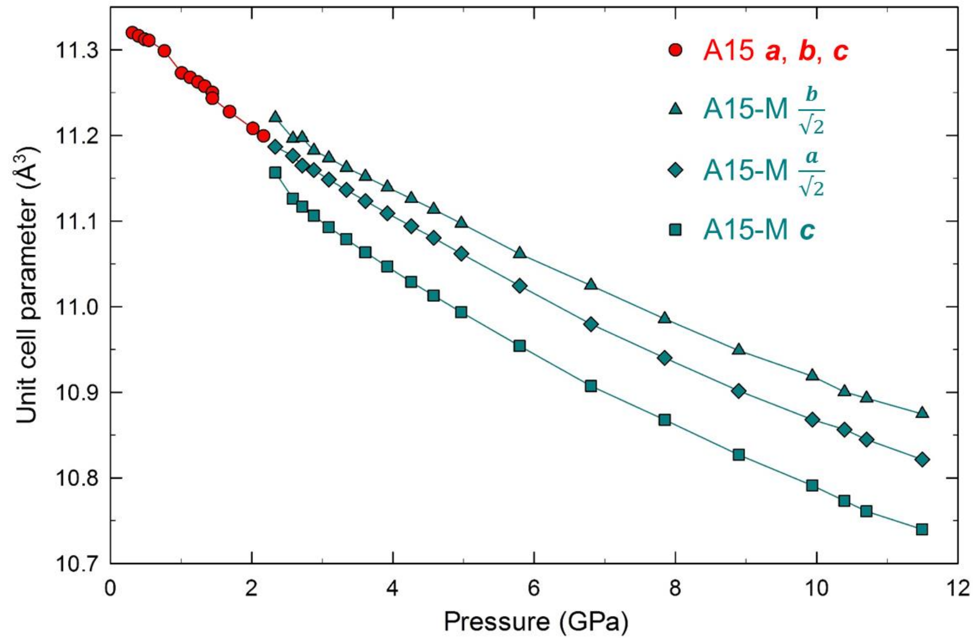

Figure 4.34: Evolution of lattice parameters *a*, *b* and *c* with pressure for Ba_3C_{60} for the A15 (red) and A15-M (cyan) structural models; A15-M *b* and *a* have been divided by √2 for visual clarity. Statistical errors in lattice parameters from Rietveld fitting are smaller in magnitude than the symbol sizes.

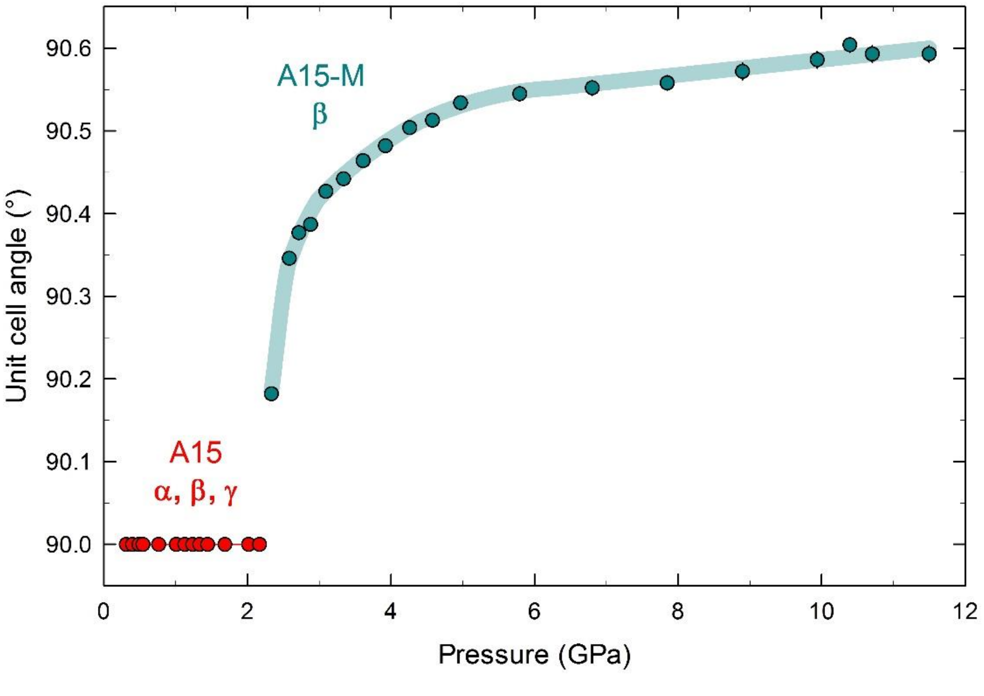

Figure 4.35: Evolution of the A15-M unit cell angle β with pressure (cyan circles); the cyan solid line is a guide-to-the-eye, and black vertical lines indicate statistical errors in β from Rietveld analysis. The unit cell angle of A15 (red circles) is also shown for completeness.

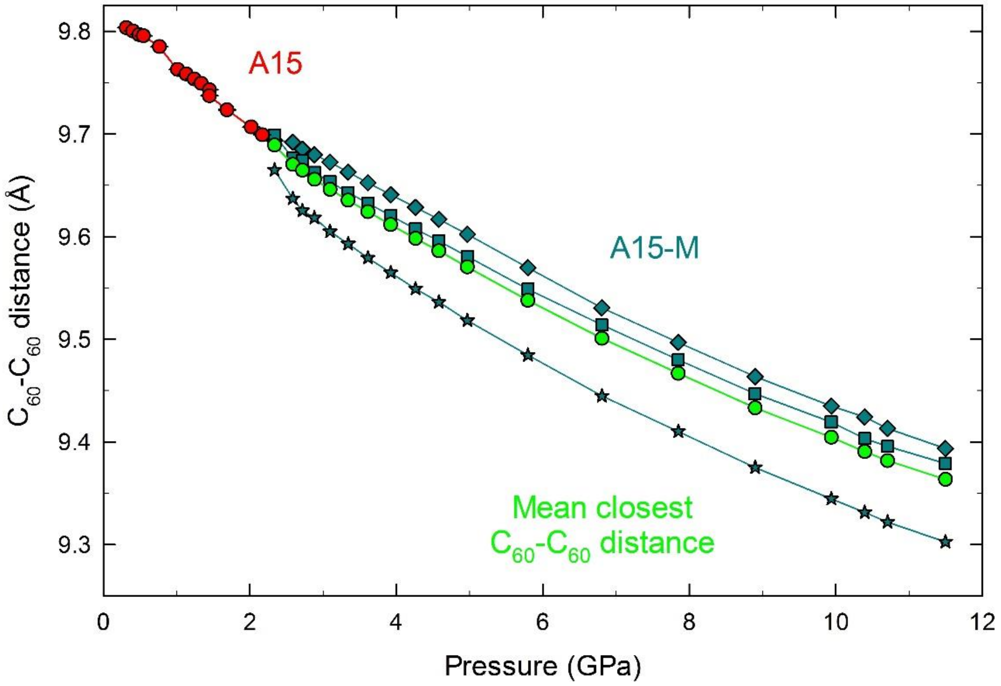

Figure 4.36: Evolution of the shortest unique interfulleride distances in the A15 (red symbols) and A15-M (cyan) structures, and the mean shortest interfulleride distance in the A15-M structure (green), with pressure; distances are defined between the centres of neighbouring molecules.

The evolution of fractional coordinates for the two inequivalent Ba^{2+} ions with pressure (Fig. 4.37) show some scatter, but both *y* coordinates in particular show gradually increasing deviation away from their 'ideal' positions (*i.e.* assuming an undistorted cubic structure) with increasing pressure.

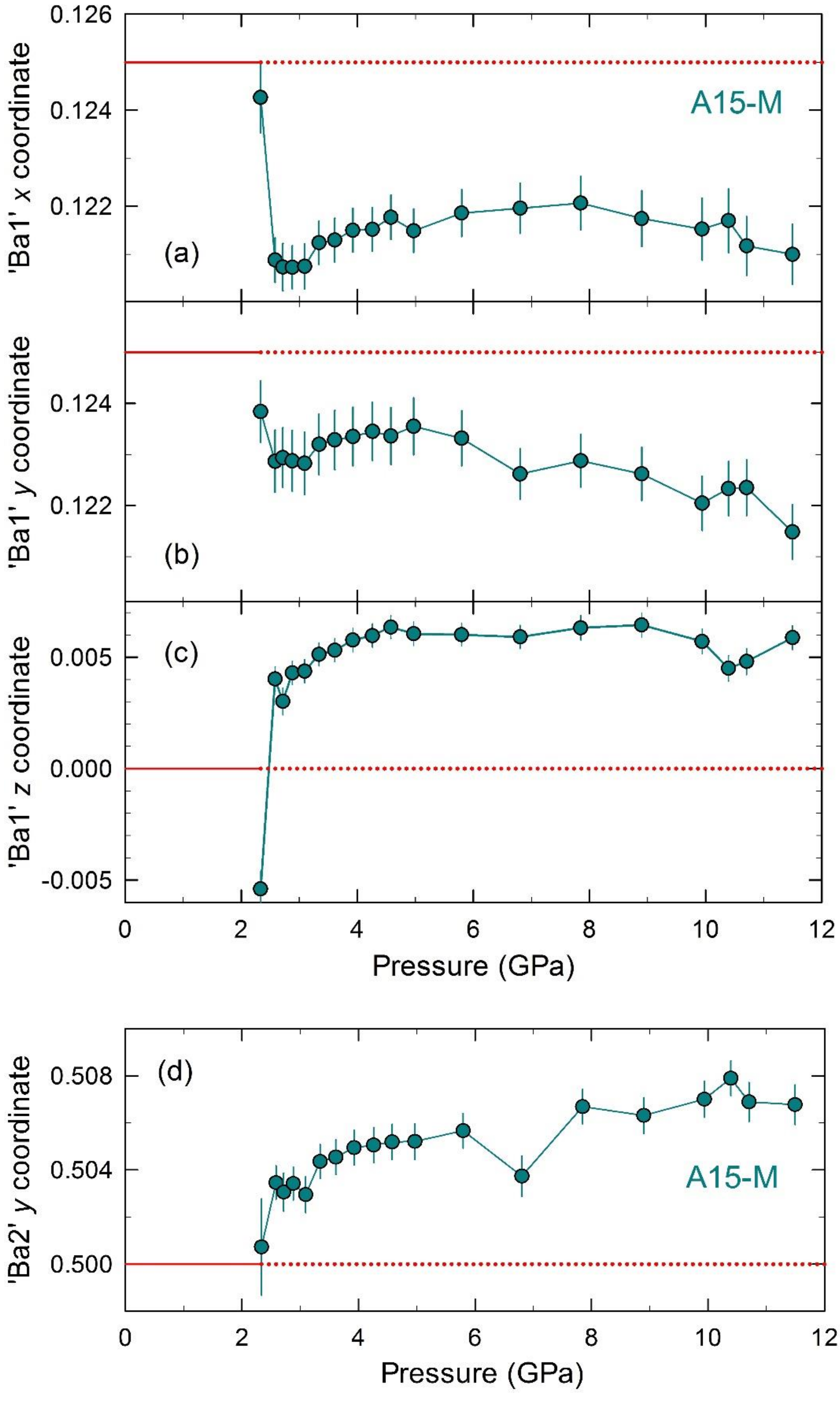

Figure 4.37: Evolution of fractional coordinates of the two inequivalent Ba^{2+} ions in the A15-M structure with pressure (those on general sites, *i.e.* the *x*, *y* and *z* coordinates of 'Ba1', in panels (a), (b) and (c) respectively, and the *y* coordinate of 'Ba2' in panel (d)). Errors arising from Rietveld analysis are shown with vertical cyan lines; red horizontal lines, for reference, show the hypothetical values if no distortion away from a cubic structure were to occur.

The evolution of volume with pressure extracted for the A15 and A15-M phases, together with that extracted from the ambient pressure data (Section 4.3.2), were analysed with least-squares-fitting to the Murnaghan equation-of-state, to characterise the compressibility properties of Ba_3C_{60} (Fig. 4.38).

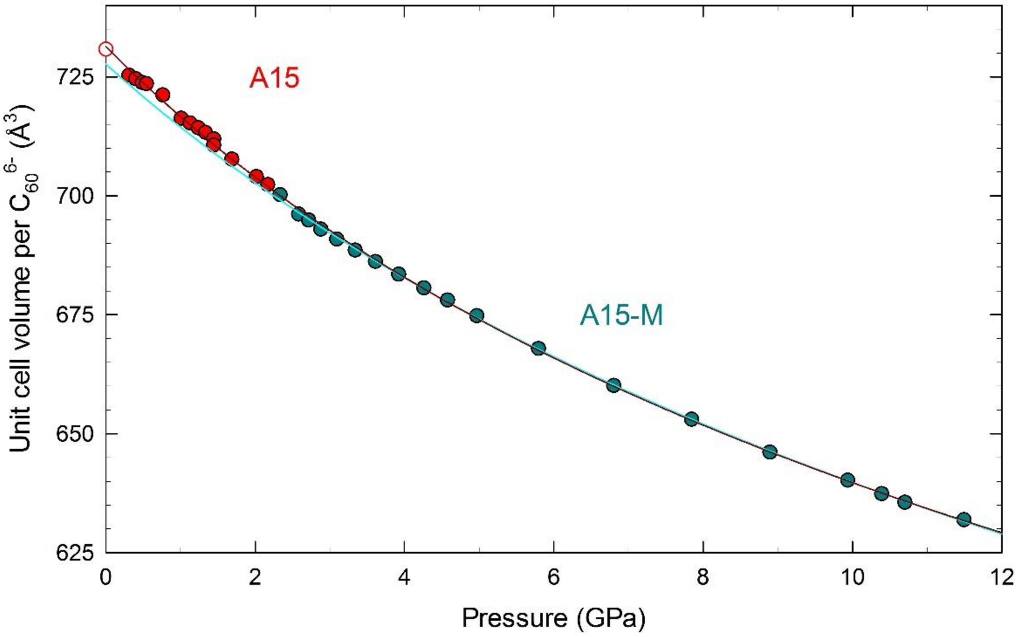

Figure 4.38: The evolution of unit cell volume per C_{60}^{3-} with pressure for the A15 (red) and A15-M (cyan) phases, including the ambient pressure volume (hollow red circle, see Section 4.3.2); Murnaghan equation-of-state fits (solid lines) are shown to all data (dark red; V_0 = 731.4(3) Å^3, K_0 = 45.7(8) GPa and K' = 6.8(2)) and to the A15-M data only (light blue; V_0 = 728(1) Å^3, K_0 = 52(2) GPa and K' = 6.0(3)).

The Murnaghan equation-of-state provides a reasonably good fit to the combined data from A15 and A15-M phases, yielding K_0 = 45.7(8) GPa, in excellent agreement with the K_0 = 45(4) GPa reported for Ba_3C_{60} in the aforementioned high-pressure PXRD study where it was present as a minority phase in bulk Ba_4C_{60} (resulting in large errors in the EoS parameters obtained).[**165**] However, a fit to the A15-M data only (Fig. 4.38, K_0 = 52(2) GPa) suggests that the A15-M phase is slightly less compressible than the A15 phase. The alkaline-earth fulleride solids are indeed known to be significantly less compressible than pristine C_{60}, where K_0 = 18(2) GPa,[**228**] with Ba_6C_{60} [**165**] found to be less compressible still (K_0 = 62(2) GPa).

Interestingly, upon undergoing the transition from A15 to A15-M, the average Ba…C distance in Ba_3C_{60} initially shows a marked increase relative to the A15 structure (Fig. 4.39) although the average Ba^{2+}…C distance continues to decrease with pressurisation, eventually becoming even smaller than the sum of the Ba^{2+} and C van der

Waals radii at above ~8.5 GPa. The former observation may relate to why the A15-M structure appears to become more energetically favourable than A15 above a certain pressure. Individual tetrahedral interstitial site - carbon distances are discussed in the next section in conjunction with the trends observed in A15 Cs_3C_{60} (Fig. 4.41).

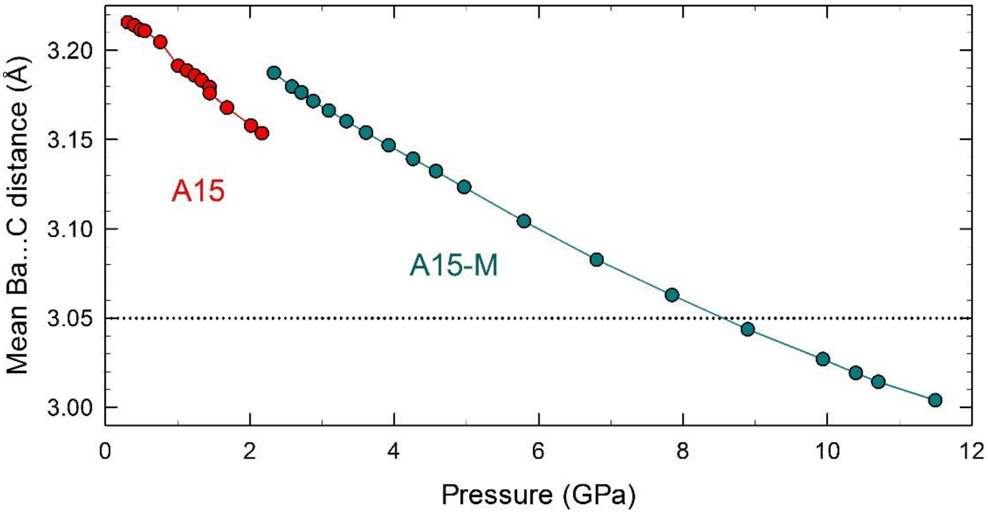

Figure 4.39: Variation of the mean Ba^{2+}...C distance in the A15 and A15-M structures with pressure. The dotted line indicates a separation equal to the sum of the Ba^{2+} and C van der Waals radii, for reference.

4.4 Discussion

Firstly, the ambient pressure structural evolution of A15 Cs_3C_{60} will be further discussed and placed in a wider context. In a given PXRD profile of *e.g. fcc* A_3C_{60}, the diffraction peak widths do not vary smoothly with 2θ, a well-known effect which has been attributed to strain anisotropy and a difference in rigidity of the structure along different directions[**155**]. However, such marked anisotropy in the peak broadening with temperature as has been observed in A15 Cs_3C_{60} in the present study, a discontinuity with approximate onset at T_N, is strongly indicative of the occurrence of a structural transition.

In general, the A15 structure type is known to be prone to low-temperature instabilities. Several A_3B A15 intermetallic superconductors, *e.g.* V_3Si and Nb_3Sn, undergo structural distortions from cubic to tetragonal structures upon cooling; these can be sufficiently small in magnitude that they are evidenced solely as slightly asymmetric broadening in PXRD, rather than visually resolved peak splitting. Even at temperatures well above the structural transformation, significant anisotropy in the cubic phase thermal strain has been detected, along with other so-called 'precursor phenomena'.[**229**]

The evolution of unit cell angle α in the A15-R and A15 Cs_3C_{60} phases as a function of temperature closely mirrors the shape of the field-cooled magnetisation (Fig. 4.40). Looking at other systems, a structural distortion, termed magnetic exchange striction, is known to occur at or slightly below T_N in several transition metal oxides, to achieve a higher magnetic exchange interaction energy.[**230**] Several of these undergo cubic-to-rhombohedral distortions, *e.g.* the Mott insulator MnO is subject to a structural transition upon cooling through T_N. Upon pressurisation, further transformations to a cubic paramagnetic phase, followed by a cubic diamagnetic phase, are observed.[**194**] In the frustrated antiferromagnet α-$NaMnO_2$, the ground state degeneracy was found to be lifted by magneto-elastic coupling, demonstrated by anisotropic broadening of Bragg peaks above T_N, followed by a structural transition from a monoclinic to a triclinic cell below T_N.[**231**] The antiferromagnet NiO, cubic above T_N (523K), undergoes a rhombohedral distortion below T_N where it contracts in the [111] direction perpendicular to planes of ordered Ni^{2+} ions. However, this distortion is extremely small and only detectable through reflection splitting in high resolution NPD. Subtle distortions, with magnitudes small such that they manifest in PXRD as anisotropic peak broadening rather than visibly resolved peak splitting, are thus not unprecedented in cubic materials which undergo antiferromagnetic ordering; yet these should be distinguished from the molecular system discussed here, in which this effect is considered to reflect orbital ordering accompanying the magnetic order below T_N.

As previously mentioned, a magnetic cell with ordering vector **q** = (0.5, 0.5, 0.5) for A15 Cs_3C_{60} below T_N has been proposed,[**208**] implying doubling of the nuclear unit cell along all three directions. This study has found that a rhombohedral unit cell model provides a good model for the structure below T_N, with the observed anisotropic peak broadening, and α > 90° implying a small compression along the unit cell diagonal. The present structural data may thus imply the onset, around T_N, of increased lattice strain or a contraction in a direction perpendicular to the ordered planes.

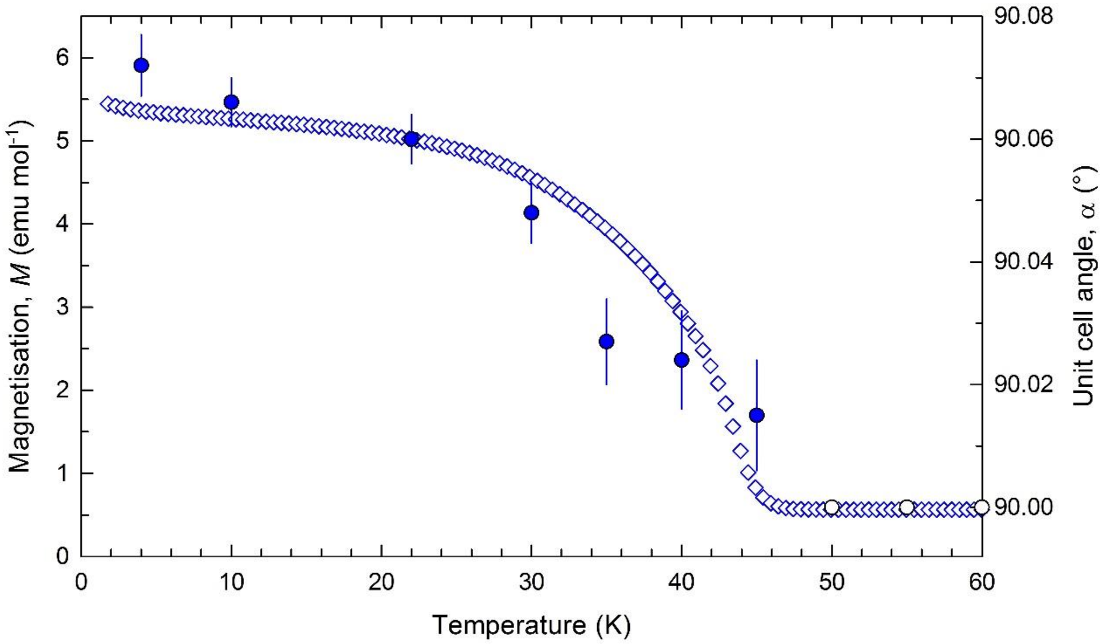

Figure 4.40: The evolution of unit cell angle with temperature from Rietveld analysis with the A15-R and A15 Cs_3C_{60} structural models (blue and blank circles, respectively) and the variation of magnetisation with temperature for 'A15' Cs_3C_{60} (blank diamonds, field-cooled under 100 Oe; data are adapted from ref. [**89**]).

Some theory is now briefly recalled. The most symmetric model for a bimodal-type C_{60}^{3-} JT distortion is the point group D_{2h}, with the three C_2 twofold axes forming principal axes.[**98**] However, in fullerides, besides the JT effect, a separate potential molecular symmetry-lowering effect arises from the crystal field, determined by the counter-anion arrangement and which can induce a static distortion; if the crystal symmetry is lower than cubic, the t_{1u} orbital degeneracy can be lifted, with resultant splitting determined by the largest common subgroup of the icosahedral group and the crystal space group. In a trigonal, hexagonal or rhombohedral lattice system, with the axis of molecular distortion along a threefold axis, a D_{3d} point group results and crystal field splitting would cause twofold t_{1u} level splitting; in a tetragonal or orthorhombic system, threefold splitting should occur (with a molecular distortion axis along a twofold axis, and point group D_{2h}).[**232**]

However, theory predicts that for C_{60}^{n-} (n = 3), a JT distortion should be bimodal with the t_{1u} orbitals split threefold, and that it should be unimodal for n = 1, 2, 4, or 5, with the three t_{1u} levels split such that two remain degenerate, because of the axial symmetry.[**233, 234**] Nevertheless, these calculations were performed for non-magnetic structures, so the effects of AFM ordering in A15 Cs_3C_{60} must also be considered. The Jahn-Teller effect, competing with the crystal field, can produce numerous virtually equivalent distortions along symmetry-related axes in different directions.

A symmetry reduction from cubic $Pm\overline{3}n$ to rhombohedral $R\overline{3}c$ corresponds to point group symmetry reduction from T_h to S_6 at the C_{60} site. In this scenario, the triple degeneracy of the T_{1u} states would lift, with them spliting as follows: $\psi_x + \psi_y \rightarrow E_u$ and $\psi_z \rightarrow A_u$. We stress here that a lifting of the T_{1u} degeneracy in the antiferromagnetic regime does not necessitate any distortion away from cubic A15 in the superconducting regime at elevated pressure. The latter is highly improbable, given that superconductivity has not been confirmed in any t_{1u} fulleride superconductor distorted away from cubic symmetry. As magnetic ordering becomes suppressed in this system upon pressurisation, the orbital ordering and rhombohedral structural distortion (away from cubic symmetry) should also be suppressed. However, direct experimental confirmation of this could not be obtained from the high pressure PXRD data presented in this thesis (owing to factors such as the small magnitude of distortion and intrinsic data limitations such as pressure-induced peak broadening).

Whilst robust evidence for the occurrence of a structural phase transition upon cooling in A15 Cs_3C_{60} has been provided, it should be mentioned that limited A15-phase reflections of class $h00$ were both sufficiently isolated and of sufficient intensity for accurate fitting, exacerbated by the $h00$ (h = odd) reflections being systematically absent in the A15 structure. Whilst this is unavoidable with the presently available PXRD data, this could potentially be partially alleviated if neutron powder diffraction data were available.

We now turn to the structural evolution of A15 Cs_3C_{60} upon the application of pressure, attempting to place the experimental results into context by drawing comparisons to behaviour in related systems and also outlining some factors which could account for the differing behaviour shown in individual experimental runs (these are, however, hypothetical, in that definitively ascertaining the origin of the differences in behaviour could not be achieved). Firstly, it should be noted that systems with competing *fcc* and *bcc* phases are known to posess intrinsic disorder,[**64**] and that it is impossible to achieve identical conditions between repeat experiments (*e.g.* the loading and initial pressure of He pressure medium, temporal aspects, masses loaded in the DACs *etc.*, and given that the experiments were carried out at different beamlines).

Reversible peak suppression at high pressures is not actually unprecedented *e.g.* in bcc-structured alkali fullerides: intriguingly, in the structurally related bcc fulleride Rb_6C_{60}, a reversible high-pressure phase transition to a hexagonal phase has been reported, accompanied by significant broadening with the new phase appearing significantly suppressed.[**225, 235**] The hexagonal phase was speculated to feature 2D C_{60} polymerisation in the (001) plane direction, and further evidence for a phase transition was provided by complementary Raman spectroscopy measurements, but full structural determination was not achieved. Attempts to fit the specific hexagonal unit cell proposed by Poloni *et al.* to the broad contributions observed at high pressure (those not attributed to *fcc* or *bco* phases) were unsuccessful, but it is not improbable that the high-pressure structure of A15 Cs_3C_{60} is related to the polymeric one proposed for Rb_6C_{60}. If the high pressure 'A15' Cs_3C_{60} phase were polymeric, theoretical calculations of the stability of $(C_{60}{}^{3-})_p$ polyanions have indicated that the energetically preferred bonding pattern should be single intermolecular bonds[**236**] (as has been experimentally found in e.g. Na_2RbC_{60}).[**237**]

Another feature of the Rb_6C_{60} study was that diffraction peaks for the high pressure tentative hexagonal phase were significantly more broadened when the material was compressed at ambient temperature than at 600K, attributed to less structural strain and better crystallisation at the higher temperature.[**225, 235**] We know, for instance, in the experiment undertaken at 8K in the present study, solidified He peaks could be seen in the PXRD profiles upon pressure application: in such an environment, the pressure encountered by the sample is unlikely to be hydrostatic. It is worth noting that the only experiment where sharp A15 peaks were preserved above ~6 GPa was undertaken at ambient temperature, although this does not explain why they were suppressed in the second ambient temperature experiment.

In the present work, no attempt was made to track changes in molecular geometry with pressure (owing to limitations of the high-pressure data quality, multiphasic nature of samples, the weak X-ray scattering power of carbon, *etc.*). However, interestingly, an X-ray difraction and and X-ray absorption study of Cs_6C_{60} reported pressure-induced modification of the molecular shape (elongation along the three orthogonal axes pointing towards the bcc phases), manifesting in minor relative intensity changes in the PXRD patterns;[**226**] for instance, the *321* peak substantially increased in intensity relative to the *222* peak. No high-pressure fractional coordinates were, however, proposed. Whilst this has not been experimentally confirmed in this study, such an effect may account for the increasing intensity mismatch with pressure observed between the observed and calculated profiles in each experiment.

In evaluating potential causes of the differing compressibility behaviour observed in A15 Cs_3C_{60} at low temperature and at ambient temperature, possible effects arising from the He gas pressure medium should not be discounted. Use of gaseous media can enable pressure conditions at the sample to remain hydrostatic to high pressures, avoiding high shear stresses, yet intercalation effects have been reported which alter the properties of fullerene-based materials.[**238**] He intercalation into fullerides such as Rb_3C_{60}, K_3C_{60} and Na_2CsC_{60} has been evidenced by smaller changes in $T_c(P)$ when He is used as pressure medium than when other media are employed.[**179**] In pristine C_{60}, where the use of He as pressure medium is known to lower the material's compressibility with respect to non-penetrating pressure media,[**239**] temperature is known to significantly affect He intercalation rates. At ambient temperature, He purportedly diffuses in and out of C_{60} interstitial sites within minutes (although a second study has reported a diffusion timescale, measurable through a gradual increase in C_{60} lattice parameter through He uptake, of weeks under 1 atm of He), but below 180 K, a He diffusion rate too slow to detect over a period of days, even at a He pressure of 0.5 GPa, has been reported.[**240-242**]. However, He intercalation effects would be expected to be more prominent in a weak 'van-der-Waals' molecular solid (C_{60}) than in an 'ionic' A_3C_{60} crystal structure, and the relative effects of temperature on He intercalation in A_3C_{60} systems do not appear to have been studied. The choice of pressure medium for compressing A15 Cs_3C_{60} may affect the peak suppression pressure: in the tentative report of pressure-induced A15 phase suppression from Fujiki *et al.*,[**58**] where mineral oil was used as the pressure medium, the suppression pressure at ~3 GPa was significantly lower than the ~6 GPa observed in the present study where He was employed as pressure medum.

Finally, we briefly return to the structural behaviour of A15 Ba_3C_{60} upon hydrostatic pressure application, to compare with that of the structural analogue A15 Cs_3C_{60}. The onset pressure of the symmetry-lowering phase transition at ambient temperature in

Ba_3C_{60}, *i.e.* ~2 GPa, is notably lower than the ~6 GPa at which (reversible) suppression of diffraction peaks is typically observed in A15 Cs_3C_{60}. The evolution of tetrahedral interstitial site – carbon distances with pressure for the cubic A15 Ba_3C_{60} and Cs_3C_{60} (BL10XU) structures is shown in Fig. 4.41. In both structures, one M^{n+}…C distance is shorter than the sum of the carbon van der Waal's radius and cation ionic radius over virtually the entire pressure range, but it appears that the two cubic A15 structures could become unstable when a second M^{n+}…C interatomic distance approaches this threshold, giving rise to a markedly anomalous compressibility or PXRD peak suppression (Cs_3C_{60}) or transition to a lower-symmetry crystalline phase (Ba_3C_{60}), although this apparent similarity between the Ba_3C_{60} and Cs_3C_{60} behaviour could admittedly be coincidental.

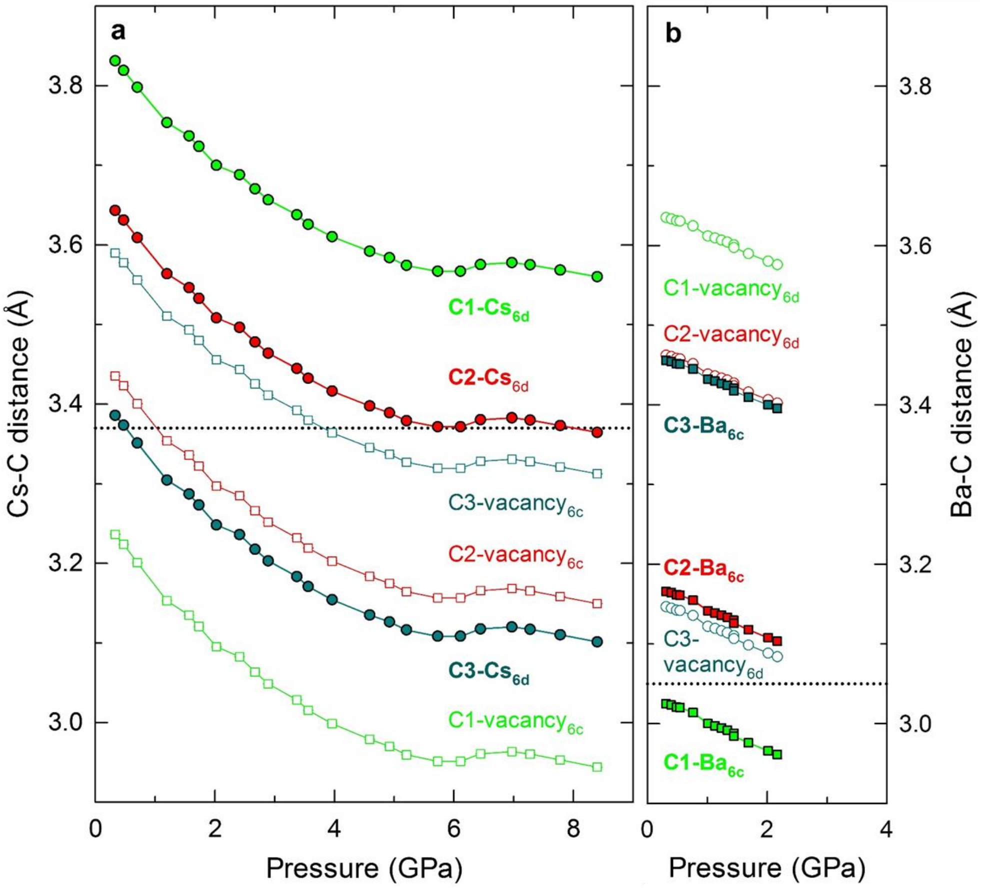

Figure 4.41: Evolution of tetrahedral interstitial site – carbon distances with pressure, at ambient temperature, for A15 Cs_3C_{60} (**a**, data from BL10XU) and A15 Ba_3C_{60} (**b**). Solid (hollow) symbols represent occupied (vacant) tetrahedral sites, with the two inequivalent 6*d* (circles) and 6*c* tetrahedral sites (squares) indicated with subscripts, and the three inequivalent carbons differentiated with green, red and cyan symbols. Data are shown over the full range of pressures for which reliable measurements of pressure are available in (**a**), and up to the point of the symmetry-lowering transition (**b**). Dotted horizontal lines represent the sum of the carbon van der Waal's radius and the ionic radius of the respective cation type (Cs^+ or Ba^{2+}), for reference.

4.5 Conclusions

The investigations presented in this chapter, a series of PXRD experiments under non-ambient conditions, were undertaken to elucidate the structural properties of A15 Cs_3C_{60} and Ba_3C_{60} *in situ* as a function of temperature and under applied hydrostatic pressure. The structural evolution of A15 Cs_3C_{60} as a function of temperature, investigated in detail for the first time, has been shown to exhibit a discontinuity below T_N, as anticipated by theory (though no such experimental evidence has been provided until now [**89**]). A subtle increase in anisotropic peak broadening was reported in this chapter, with approximate onset at T_N and increasing as temperature decreased. A rhombohedral structural model, termed 'A15-R', provided a good fit to the low temperature data, with α evolving away from 90° with decreasing temperature to 90.072(5)° at 4 K.

We also sought to clarify the structural behaviour of A15 Cs_3C_{60} upon pressurisation, at ambient and low temperatures. Whilst further investigations are necessary here, some preliminary conclusions were drawn. A poorly-crystalline low-symmetry phase emerged at above ~5 GPa. A15 peaks were preserved up to ~6 GPa, and above this pressure either peak suppression (reversible upon depressurisation) or an apparent transformation to a less compressible phase ensued, with compressibility akin to fulleride polymers; one of the two low temperature experiments also showed apparent transformation to this phase at pressures as low as ~0.4 GPa. However, besides the compressibility anomalies, no clear evidence of structural transition was found in the latter two experiments. Moreover, the lack of reproducibility between experiments remains to be definitively explained.

Finally, pressurisation of highly crystalline phase-pure A15 Ba_3C_{60} resulted in a hitherto unreported symmetry-lowering phase transition at ~2.1 GPa. The high-pressure phase remained crystalline up to at least 11 GPa; it could be well described by a monoclinic structural model termed 'A15-M', with β smoothly evolving away from 90° with increasing pressure and reaching 90.59(1)° at 11.5 GPa. In the next and final chapter (Chapter 5), several proposals will be outlined as to how the investigations described in this chapter, and those from the previous chapter about the *fcc* $Rb_xCs_{3-x}C_{60}$ systems, could be extended in future studies.

Chapter 5 - Summary, conclusions and future directions

5.1 Results of work described in this thesis

One key aim of this work was to gain further understanding about the structural, magnetic and electronic properties of the A_3C_{60} family of *fcc*-structured superconductors in the key regime of the electronic phase diagram between that of the well-explored conventional BCS-type superconductivity (underexpanded A_3C_{60}) and Mott-Jahn-Teller insulating behaviour (highly-expanded Cs_3C_{60}), hitherto not studied in any detail. This regime had only been accessed before by physical pressurization of the Cs_3C_{60} end member. To this end, a series of *fcc*-rich bulk superconducting $Rb_xCs_{3-x}C_{60}$ compositions ($0.25 \leq x \leq 2$) have been synthesized by a solid-state route, with excellent stoichiometry control. Their structural and magnetic properties were investigated with high-resolution synchrotron PXRD techniques and magnetisation measurements, described in Chapter 3. Success in optimising the synthetic conditions yielded, for instance, a sample $Rb_{0.25}Cs_{2.75}C_{60}$ (refined $x = 0.22$) of ~83% *fcc* phase and ~50% shielding fraction lying the closest on the metallic/superconducting side of the Mott insulator-metal boundary; synthesis of such high-quality overexpanded A_3C_{60} materials *via* solid-state synthesis was previously thought impossible. Crucially, this synthetic advance has provided access to the Mott insulating, underexpanded metallic and intermediate regions of the phase diagram at ambient pressure, permitting the deployment of a wide variety of experimental techniques which are not feasible at elevated pressures; these are described in detail in our forthcoming work.[**191**] Combining the results from high-pressure magnetisation and high-pressure PXRD studies has allowed us to extract the T_c dependence on C_{60} packing density in *fcc* $Rb_xCs_{3-x}C_{60}$, revealing a universal superconductivity dome (albeit with a slight decrease in the maximum T_c with increasing x). The *fcc* crystal structures were preserved upon cooling to 5-10 K, and upon pressurisation to at least 11 GPa.

Significantly, in this work we have found, for the first time, that, in contrast to the smooth contraction to low temperatures of Cs_3C_{60} and underexpanded A_3C_{60} (*e.g.* A = K, Rb) analogues, the overexpanded compositions such as *fcc* $Rb_{0.5}Cs_{2.5}C_{60}$ undergo an anomalous isostructural volume collapse upon cooling. This occurs well above the superconductity onset, at an onset temperature tunable by 'chemical' pressurisation (*i.e.* by adjusting the Rb:Cs cation ratio). At the same time, complementary measurements of magnetic susceptibility have revealed distinct cusps, with maxima at temperatures closely matching with those at which the lattice volume collapses were observed; this behaviour is significantly different to that of the virtually temperature-independent (Pauli) magnetic susceptibility of the underexpanded compositions. Both characterisation methods have shown that the transition becomes more smeared out over a wider temperature range with increasing *x*, as the transition temperature shifts to higher temperatures.

At ambient temperature, overexpanded $Rb_xCs_{3-x}C_{60}$ display paramagnetic insulating behaviour with negative Weiss temperatures and indicative of low spin S = ½ state, like Cs_3C_{60};[**89**] however, below the cusps, the magnetic susceptibility is strongly temperature-dependent. We attribute this to an unconventional paramagnetic metallic state and the susceptibility maxima and volume collapse as signatures of metal-Mott insulator transitions (MIT). The magnetic susceptibility is found to increase sharply approaching the Mott transition as a function of volume when plotted together for all compositions, as predicted by dynamical mean-field theory (close to the Mott transition at large U, S=1/2 is predicated and Fermi-liquid behaviour should be lost, with each molecule effectively in a dynamically Jahn-Teller distorted state).[**76**] No evidence of symmetry-lowering upon cooling has been found (and NMR measurements undertaken by our collaborators on these materials have found analogous cusps and confirmed that these do not arise from magnetic ordering [**151**]). High pressure magnetic susceptibility and PXRD experiments presented here for $Rb_{0.5}Cs_{2.5}C_{60}$ have also indicated that the MIT crossover temperature can be tuned by application of physical, as well as chemical pressurisation, and that the transition can be induced solely by pressuriation at ambient temperature. The Mott boundary line from experiments has a negative $\mathrm{d}T/\mathrm{d}V$ (corresponding to a positive $\mathrm{d}T/\mathrm{d}P$), consistent with the Clausius-Clapeyron equation $\mathrm{d}T/\mathrm{d}P = \Delta V/\Delta S$ – spin entropy in the paramagnetic Mott insulating state is expected to be higher than that in the metal ($\Delta S > 0$) and the observed ΔV is also positive.

These results provide significant new insight into the A_3C_{60} electronic phase diagram, which in turn has similar features to those of other unconventional high temperature superconductors, *e.g.* a superconductivity dome in proximity to a Mott insulating state. Key findings from our forthcoming investigation of these materials, undertaken in conjunction with other research groups, are as follows [**191**]: we define the strongly correlated metallic state in highly overexpanded $Rb_xCs_{3-x}C_{60}$ (e.g. x = 0.35, 0.5), between T_c and the Mott crossover temperature, as a Jahn-Teller metal where localised Jahn-Teller active and itinerant electrons coexist; the molecular distortion persists into the superconducting regime. The Jahn-Teller metallic state gradually gives rise to a Fermi liquid with a less prominent molecular electronic signature as x is increased. Unconventional superconductivity is found in these overexpanded *fcc* systems, with the superconducting gap increasing with decreasing x, to values far higher than predicted for the BCS weak-coupling limit, and the trend in specific heat jump at T_c also deviates markedly for $x<3$ from that expected in the BCS weak-coupling limit.[**191**]

Few materials are experimentally accessible for studying a pure Mott transition without symmetry breaking. The high-symmetry nature of *fcc* A_3C_{60} renders this system particularly amenable to theoretical modelling, and hydrostatic pressure and temperature control of bandwidth, as employed here, also avoid potential effects from impurities which may ensue from doping control of bandwidth (as applied in other high-temperature superconductors *e.g.* cuprates) – here, a state akin to underdoped cuprates can be accessed, and isobaric and isothermal sweeps undertaken. Moreover, to our knowledge, the overexpanded $Rb_xCs_{3-x}C_{60}$ materials appear to be unique in undergoing isostructural transitions from Mott insulating, to metallic then to superconducting states at ambient pressure. These factors could motivate further experimental and theoretical studies by other techniques to gain further understanding of the transition and the behaviour in the strongly correlated metallic regime.

The other main focus of this work has been on elucidation of the structural properties of the A15-structured fullerides Cs_3C_{60} and Ba_3C_{60} under non-ambient conditions of temperature and pressure, employing high-resolution synchrotron PXRD (Chapter 4). The first systematic study of the structural evolution of A15 Cs_3C_{60} with temperature is reported, and both materials were also studied as a function of pressure. Whilst theory predicts that the low-temperature antiferromagnetic ordering should be accompanied by orbital ordering to resolve the spin and orbital degeneracy,[**76**] and thus the JT distortion below T_N should have a static component, no anomalous structural changes or symmetry lowering around T_N have been evidenced until now [**89, 98**]: we report that increasing anisotropic PXRD peak broadening develops upon cooling below T_N (~46 K). This could be modelled well in Rietveld refinements by a small rhombohedral distortion (α = 90.072(5)° at 4 K) using the space group $R\bar{3}c$, a maximal subgroup of $Pm\bar{3}n$; the low-temperature model is termed 'A15-R'. The temperature evolution of α below T_N tracks the magnetic ordering parameter, *e.g.* the temperature evolution of FC magnetisation. This striking observation has obvious implications *e.g.* for future theoretical studies and also on the high pressure properties; superconductivity is known to emerge in A15 Cs_3C_{60} under applied hydrostatic pressure, yet it was thought that the superconducting phase must need be cubic, to retain the triple t_{1u} LUMO degeneracy. Interestingly though, our forthcoming work on *fcc* $Rb_xCs_{3-x}C_{60}$ has shown that whilst the overexpanded superconductors emerging from the Jahn-Teller metallic regime close to the Mott boundary have cubic crystallographic symmetry on average, they contain locally distorted C_{60} units which co-exist with metallicity.[**191**]

The PXRD experiments at elevated pressures reported in Chapter 4 for this material (including at $T < T_N$) did not permit this question to be successfully resolved, given the small magnitude of the anisotropic broadening and the lower resolution, profile broadening, more restricted 2θ range and potentially increased strain from pressure anistropy *etc.* inherent in this type of experiment. Previous studies only reported the structural properties at pressures up to 2.5 GPa[**89**], and the present work has extended the investigated range up to ~15 GPa: above ~5.5 GPa, reversible suppression of the A15 peaks is observed in the profiles (or in one ambient temperature experiment, peaks were preserved up to ~15 GPa but the sample became abruptly less compressible above ~6 GPa, with compressibility akin to certain fulleride polymer phases). Moreover, some weak, relatively broad peaks, stable at high pressure only (disappearing again upon depressurisation) were observed in each experiment at both ambient and low temperatures, emerging at approximately the same *d*-spacing values, but indexing and identification of this hitherto unreported phase(s) has not yet been successful.

Finally, the structural properties of A15 Ba_3C_{60} have been investigated under applied pressure up to ~11 GPa, at ambient temperature, representing to our knowledge the first detailed high-pressure study of this material *in situ*. We report that this material undergoes a previously unknown symmetry-lowering transition at ~2.1 GPa, above which the structure is best described by a monoclinic model (labelled 'A15-M'). Clear visual splitting is seen in the diffraction profiles at high pressure, and β evolves gradually with pressure, reaching ~90.6° at ~11 GPa.

5.2 Future directions

To further progress with this work, we first consider the *fcc* $Rb_xCs_{3-x}C_{60}$ materials. From a synthetic perspective, further repeats of specialized quenching experiments would be required to draw firmer conclusions, which could not be undertaken in this study because of time limitations, as these produced very promising results for the synthesis of *fcc*-rich bulk superconducting samples of highly expanded compositions with low *x*, *i.e.* $x = 0.25$. Ideally, if the equipment were available, certain changes could be made to the protocol to improve the reproducibility (such as using a hydraulic press rather than a hand press for pelletisation in the glove box, to apply uniform pressure to all pellets). Additionally, further variations to the experimental conditions could be systematically tested, *e.g.* investigating the effects of annealing at and quenching from different tempereratures, to further optimise the synthetic route aiming towards phase-pure samples of overexpanded *fcc* $Rb_xCs_{3-x}C_{60}$ ($x < 1$). Overall, an important future synthetic target is to approach the Mott boundary still closer by synthesizing high-quality *fcc*-rich *fcc* $Rb_xCs_{3-x}C_{60}$ materials where $x < 0.25$, either by solid state or solution routes. At some limit of small *x*, we would anticipate that analogous structural and magnetic characterisation to that presented in this thesis may reveal evidence of phase co-existence at the Mott boundary, being below the critical point (which could allow the location of the latter in the electronic phase diagram to be more precisely defined).

Besides the well-defined volume contraction, no further anomalous structural changes (*e.g.* changes in peak shapes or intensities) were observed at the insulator-metal transition, in the structural PXRD investigations of *fcc* $Rb_xCs_{3-x}C_{60}$ with temperature reported in this thesis. This implies that the insulator-metal transitions in the compositions investigated in this work were in the supercritical regime (and thus best considered as a crossover), as the Mott transition is of 1st order and co-existence is expected. However the structural characterisation results from this work do not represent definitive evidence that such changes do not occur. As mentioned earlier, carbon has a weak X-ray scattering power and the data quality were such that refinement of the C atom fractional coordinates, for instance, as a function of temperature was not undertaken. Whilst the ambient pressure data was of high resolution, naturally some compromises in the data collection statistics had to be made to study the widest range of compositions possible in the available time. To elucidate whether any changes in *e.g.* electron distribution or any subtle structural changes occur at the metal-insulator transition in overexpanded $Rb_xCs_{3-x}C_{60}$, studies by complementary techniques, such as combined X-ray and neutron powder diffraction (NPD) analysis and maximum entropy method analysis, are thus of interest. As Rb occupies the tetrahedral *fcc* site only in $Rb_xCs_{3-x}C_{60}$ ($0.25 \leq x \leq 1$), X-ray absorption fine structure (EXAFS) measurements at the Rb edge could be employed to obtain fine detail about any structural changes at the tetrahedral site at the MIT, *e.g.* any changes in relative nearest-neighbour distances. Pair distribution function (PDF) analysis as a function of temperature could also be undertaken to characterise the local structural changes at the MIT, with high-statistics PXRD data collection extended to high Q.

Further high-pressure structural studies of *fcc* $Rb_xCs_{3-x}C_{60}$ at room temperature, focusing on the low pressure region, could help elucidate the nature of the MIT and establish how the character of the pressure-induced MIT compares to that induced through cooling. NPD would be the most suitable technique considering the aforementioned factors, and investigation of highly overexpanded compositions ($x < 0.5$) would permit sufficient data to be collected both below and above the transition (P_c) to optimally define its properties, and complement the results reported here for $x = 0.5$.

Aside from powder diffraction studies, more accurate measurements of the lower critical field, H_{c1} of the $Rb_xCs_{3-x}C_{60}$ would reveal with more certainty how this important quantity varies approaching the Mott boundary. A different method than the one presented here could be attempted (trying to define the field at which a deviation from linearity in $M(H)$ is first observed), *e.g.* a trapped magnetisation method,[**243**] developed from the fact that trapped magnetic flux can only be built up in a sample when the field has been increased above H_{c1}. More generally, with large masses of high-quality overexpanded *fcc* $Rb_xCs_{3-x}C_{60}$ samples available for the first time, certain experiments of interest which are now feasible include searching for the presence of a Hebel-Slichter coherence peak through longitudinal-field (LF) μSR. This increase in the temperature dependence of the inverse spin-lattice relaxation rate, $1/T_1$ just below T_c is an important proof of BCS-type superconductivity, and has been observed in LF μSR measurements of Rb_3C_{60} [**75**](though never in NMR experiments, including recently for *fcc* Cs_3C_{60} [**142**]). Such experiments could shed further light on the nature of the superconductivity in overexpanded $Rb_xCs_{3-x}C_{60}$. Though NMR investigations of this type may be undertaken with much smaller samples, significantly higher magnetic fields are required, and high fields are known to suppress the Hebel-Slichter peak.

Moving to the A15-structured materials, for A15 Cs_3C_{60}, undertaking a NPD experiment as a function of temperature could give a clearer indication of any structural changes occuring on AFM ordering, and could also potentially provide further confirmation as to whether the magnetic structure proposed from NMR experiments is correct,[**208**] as NPD can detect long range magnetic ordering. The proposed rhombohedral model used for analysis of the A15 Cs_3C_{60} low-temperature structure could be further developed in future work using output from ISODISTORT, which can be used to generate details of distorted structures as a list of distortion-mode amplitudes instead of conventional *xyz* atomic coordinates, and importing these mode definitions into TOPAS Academic for Rietveld analysis (which can directly refine structural distortion-mode amplitudes).[**244**] Using such a strategy for Rietveld refinement of the A15-R phase would greatly reduce the degrees of freedom necessitated to refine the positions of the 10 inequivalent carbon atoms, and may thus even enable this to be carried out with the presently available data (which was not possible in the analysis presented in this thesis), potentially significantly improving the accuracy of the rhombohedral structural model.

EXAFS experiments and analysis could be employed to directly follow how <M-C> distances in A15 Cs_3C_{60} vary upon pressurisation, and any potential C_{60} molecular distortion, as experimentally established at high pressures in structurally-related bcc Cs_6C_{60} and Rb_6C_{60}, could be detected.[**245**] Other techniques such as high-pressure Raman spectroscopy and *ab initio* DFT calculations (as applied in studies of the latter materials [**245**]) could provide complementary information, *e.g.* about discontinuities in the frequencies of intramolecular vibrations and the mechanism taking place upon compression. Identification of the high-pressure low-crystallinity phase which forms upon pressurisation of A15 Cs_3C_{60}, unstable at lower pressures, has not been possible from these PXRD data alone. A high pressure PXRD experiment undertaken at slightly higher temperature (*e.g.* 50-80 °C), could result in a high pressure phase forming with higher crystallinity, due to reduction of strain *etc.*, and thus render it easier to characterise.

For Ba_3C_{60}, high pressure Raman, high pressure SQUID magnetometry and potentially low temperature high-pressure PXRD experiments could further clarify the nature of the high pressure phase and investigate its magnetic, electronic and optical properties. To access the transition pressure when undertaking magnetisation measurements, a DAC custom-designed for the MPMS, such as the EasyLab Mcell Ultra, could be employed (the maximum internal pressure is ~150 kbar, compared to the ~12 kbar achievable with the clamp cell Mcell 10 used in this work). In contrast to A15 Cs_3C_{60}, it is not yet known whether the pressure-induced symmetry lowering is reversible upon pressure release; depressurisation was not possible here as one diamond in the DAC broke at the highest pressure. According to a recent study,[**216**] the crystalline Ba_3C_{60} structure was preserved upon depressurisation after applying 5 GPa of pressure, which tentatively indicates that formation of the A15-M phase should be reversible, but an amorphous phase was found upon depressurisation after 15 GPa was applied. This could be clarified by repeating the synchrotron X-ray diffraction experiment and measuring upon depressurisation too.

Finally, no experimental investigations of either A15 or *fcc* polymorphs of the related material Sr_3C_{60} as a function of pressure have been reported; in light of the pressure-induced phase transformations reported here in the other two known A15 A_3C_{60} systems (A = Ba, Cs), this may now present an interesting comparison. One might predict that Sr^{2+}, with its smaller ionic radius, may undergo an analogous phase transition to the Ba analogue but at lower pressure. Moreover, to our knowledge mixed A15 phases $Sr_xBa_{3-x}C_{60}$ have not been reported, though as mentioned, an attempt to synthesize A15 $Rb_xCs_{3-x}C_{60}$ was deemed unsuccessful; the discrepancy between the ionic radii of Sr^{2+} and Ba^{2+} is similar to that between Rb^+ and Cs^+. Nevertheless, these could be an interesting synthetic target, *e.g.* to investigate how the characteristics of the symmetry-lowering transition vary as the cation ratio is tuned. Whilst the A15 Ba_3C_{60} and Sr_3C_{60} systems are insulating under ambient conditions, a recent study on the former found semi-metallic conductivity following high-pressure and high-temperature treatment, with electrical properties comparable to superconducting B-doped diamond.[**216**] Moreover, the silicon clathrate superconductor Ba_8Si_{46}, prepared under high-pressure and high-temperature conditions, is isotypic with Ba_3C_{60}, also crystallising in the space group $Pm\bar{3}n$.[**246**] Further investigation of the A15 carbon analogues at high pressure may thus reveal interesting electronic properties, and comparison with the latter systems could be helpful in the development of new functional materials.

References

1. H.W. Kroto, J.R. Heath, S.C. O'Brien, R.F. Curl, and R.E. Smalley, *Nature*, 1985. **318**(6042): p. 162-163.
2. W. Krätschmer, L.D. Lamb, K. Fostiropoulos, and D.R. Huffman, *Nature*, 1990. **347**(6291): p. 354-358.
3. W.I.F. David, R.M. Ibberson, J.C. Matthewman, K. Prassides, T.J.S. Dennis, J.P. Hare, H.W. Kroto, R. Taylor, and D.R.M. Walton, *Nature*, 1991. **353**(6340): p. 147-149.
4. R. Moret, S. Ravy, and J.M. Godard, *Journal De Physique I*, 1992. **2**(9): p. 1699-1704.
5. W.I.F. David, R.M. Ibberson, T.J.S. Dennis, J.P. Hare, and K. Prassides, *Europhysics Letters*, 1992. **18**(3): p. 219-225.
6. W.I.F. David, R.M. Ibberson, T.J.S. Dennis, J.P. Hare, and K. Prassides, *Europhysics Letters*, 1992. **18**(8): p. 735-736.
7. A. Hirsch and M. Brettreich, *Fullerenes: Chemistry and Reactions*. 2006: Wiley-VCH.
8. S. Saito and A. Oshiyama, *Physical Review Letters*, 1991. **66**(20): p. 2637-2640.
9. M.J. Rosseinsky, *Chemistry of Materials*, 1998. **10**(10): p. 2665-2685.
10. A.F. Hebard, M.J. Rosseinsky, R.C. Haddon, D.W. Murphy, S.H. Glarum, T.T.M. Palstra, A.P. Ramirez, and A.R. Kortan, *Nature*, 1991. **350**(6319): p. 600-601.
11. M.J. Rosseinsky, D.W. Murphy, R.M. Fleming, R. Tycko, A.P. Ramirez, T. Siegrist, G. Dabbagh, and S.E. Barrett, *Nature*, 1992. **356**(6368): p. 416-418.
12. K. Tanigaki, I. Hirosawa, T.W. Ebbesen, J. Mizuki, Y. Shimakawa, Y. Kubo, J.S. Tsai, and S. Kuroshima, *Nature*, 1992. **356**(6368): p. 419-421.
13. M. Kosaka, K. Tanigaki, K. Prassides, S. Margadonna, A. Lappas, C.M. Brown, and A.N. Fitch, *Physical Review B*, 1999. **59**(10): p. R6628-R6630.
14. O. Zhou, R.M. Fleming, D.W. Murphy, M.J. Rosseinsky, A.P. Ramirez, R.B. Vandover, and R.C. Haddon, *Nature*, 1993. **362**(6419): p. 433-435.
15. T. Yildirim, L. Barbedette, J.E. Fischer, C.L. Lin, J. Robert, P. Petit, and T.T.M. Palstra, *Physical Review Letters*, 1996. **77**(1): p. 167-170.
16. A.R. Kortan, N. Kopylov, S. Glarum, E.M. Gyorgy, A.P. Ramirez, R.M. Fleming, F.A. Thiel, and R.C. Haddon, *Nature*, 1992. **355**(6360): p. 529-532.
17. M. Baenitz, M. Heinze, K. Lüders, H. Werner, R. Schlögl, M. Weiden, G. Sparn, and F. Steglich, *Solid State Communications*, 1995. **96**(8): p. 539-544.
18. C.M. Brown, S. Taga, B. Gogia, K. Kordatos, S. Margadonna, K. Prassides, Y. Iwasa, K. Tanigaki, A.N. Fitch, and P. Pattison, *Physical Review Letters*, 1999. **83**(11): p. 2258-2261.
19. Y. Iwasa, H. Hayashi, T. Furudate, and T. Mitani, *Physical Review B*, 1996. **54**(21): p. 14960-14962.
20. Y. Iwasa, M. Kawaguchi, H. Iwasaki, T. Mitani, N. Wada, and T. Hasegawa, *Physical Review B*, 1998. **57**(21): p. 13395-13398.
21. Y. Iwasa and T. Takenobu, *Journal of Physics-Condensed Matter*, 2003. **15**(13): p. R495-R519.
22. M.S. Dresselhaus, G. Dresselhaus, and P.C. Eklund, *Science of Fullerenes and Carbon Nanotubes*. 1996: Academic Press.
23. G.K. Wertheim and D.N.E. Buchanan, *Solid State Communications*, 1993. **88**(2): p. 97-100.
24. J.P. McCauley, Q. Zhu, N. Coustel, O. Zhou, G. Vaughan, S.H.J. Idziak, J.E. Fischer, S.W. Tozer, D.M. Groski, N. Bykovetz, C.L. Lin, A.R. McGhie, B.H. Allen, W.J. Romanow, A.M. Denenstein, and A.B. Smith, *Journal of the American Chemical Society*, 1991. **113**(22): p. 8537-8538.

25. H.H. Wang, A.M. Kini, B.M. Savall, K.D. Carlson, J.M. Williams, M.W. Lathrop, K.R. Lykke, D.H. Parker, P. Wurz, M.J. Pellin, D.M. Gruen, U. Welp, W.K. Kwok, S. Fleshler, G.W. Crabtree, J.E. Schirber, and D.L. Overmyer, *Inorganic Chemistry*, 1991. **30**(15): p. 2962-2963.
26. H.H. Wang, A.M. Kini, B.M. Savall, K.D. Carlson, J.M. Williams, K.R. Lykke, P. Wurz, D.H. Parker, M.J. Pellin, D.M. Gruen, U. Welp, W.K. Kwok, S. Fleshler, and G.W. Crabtree, *Inorganic Chemistry*, 1991. **30**(14): p. 2838-2839.
27. D.R. Buffinger, R.P. Ziebarth, V.A. Stenger, C. Recchia, and C.H. Pennington, *Journal of the American Chemical Society*, 1993. **115**(20): p. 9267-9270.
28. S. Cooke, S. Glenis, X. Chen, C.L. Lin, and M.M. Labes, *Journal of Materials Chemistry*, 1996. **6**(1): p. 1-3.
29. X.H. Liu, W.C. Wan, S.M. Owens, and W.E. Broderick, *Journal of the American Chemical Society*, 1994. **116**(12): p. 5489-5490.
30. X. Chen, Y. Maniwa, C.A. Kuper, S. Glenis, C.L. Lin, and M.M. Labes, *Chemistry of Materials*, 1997. **9**(12): p. 3049-3051.
31. P. Dahlke, M.S. Denning, P.F. Henry, and M.J. Rosseinsky, *Journal of the American Chemical Society*, 2000. **122**(49): p. 12352-12361.
32. R.D. Boss, J.S. Briggs, E.W. Jacobs, T.E. Jones, and P.A. Mosier-Boss, *Physica C-Superconductivity and Its Applications*, 1995. **243**(1-2): p. 29-34.
33. R.E. Douthwaite, M.L.H. Green, and M.J. Rosseinsky, *Chemistry of Materials*, 1996. **8**(2): p. 394-400.
34. N.S. Sidorov and A.V. Palnichenko, *Physics of the Solid State*, 2010. **52**(1): p. 212-215.
35. F. Bensebaa, B. Xiang, and L. Kevan, *Journal of Physical Chemistry*, 1992. **96**(15): p. 6118-6120.
36. L. Cristofolini, M. Riccò, and R. De Renzi, *Physical Review B*, 1999. **59**(13): p. 8343-8346.
37. C.C. Chen, S.P. Kelty, and C.M. Lieber, *Science*, 1991. **253**(5022): p. 886-888.
38. D.W. Murphy, M.J. Rosseinsky, R.M. Fleming, R. Tycko, A.P. Ramirez, R.C. Haddon, T. Siegrist, G. Dabbagh, J.C. Tully, and R.E. Walstedt, *Journal of Physics and Chemistry of Solids*, 1992. **53**(11): p. 1321-1332.
39. Y. Chabre, D. Djurado, M. Armand, W.R. Romanow, N. Coustel, J.P. McCauley, J.E. Fischer, and A.B. Smith, *Journal of the American Chemical Society*, 1992. **114**(2): p. 764-766.
40. R.C. Haddon, A.F. Hebard, M.J. Rosseinsky, D.W. Murphy, S.J. Duclos, K.B. Lyons, B. Miller, J.M. Rosamilia, R.M. Fleming, A.R. Kortan, S.H. Glarum, A.V. Makhija, A.J. Muller, R.H. Eick, S.M. Zahurak, R. Tycko, G. Dabbagh, and F.A. Thiel, *Nature*, 1991. **350**(6316): p. 320-322.
41. G.P. Kochanski, A.F. Hebard, R.C. Haddon, and A.T. Fiory, *Science*, 1992. **255**(5041): p. 184-186.
42. K. Holczer, O. Klein, S.M. Huang, R.B. Kaner, K.J. Fu, R.L. Whetten, and F. Diederich, *Science*, 1991. **252**(5009): p. 1154-1157.
43. P.W. Stephens, L. Mihaly, P.L. Lee, R.L. Whetten, S.M. Huang, R. Kaner, F. Diederich, and K. Holczer, *Nature*, 1991. **351**(6328): p. 632-634.
44. M.J. Rosseinsky, A.P. Ramirez, S.H. Glarum, D.W. Murphy, R.C. Haddon, A.F. Hebard, T.T.M. Palstra, A.R. Kortan, S.M. Zahurak, and A.V. Makhija, *Physical Review Letters*, 1991. **66**(21): p. 2830-2832.
45. K. Tanigaki, T.W. Ebbesen, S. Saito, J. Mizuki, J.S. Tsai, Y. Kubo, and S. Kuroshima, *Nature*, 1991. **352**(6332): p. 222-223.
46. R.M. Fleming, A.P. Ramirez, M.J. Rosseinsky, D.W. Murphy, R.C. Haddon, S.M. Zahurak, and A.V. Makhija, *Nature*, 1991. **352**(6338): p. 787-788.
47. S. Teslic, T. Egami, and J.E. Fischer, *Physical Review B*, 1995. **51**(9): p. 5973-5976.
48. K. Prassides, C. Christides, I.M. Thomas, J. Mizuki, K. Tanigaki, I. Hirosawa, and T.W. Ebbesen, *Science*, 1994. **263**(5149): p. 950-954.

49. A.Y. Ganin, Y. Takabayashi, Y.Z. Khimyak, S. Margadonna, A. Tamai, M.J. Rosseinsky, and K. Prassides, *Nature Materials*, 2008. **7**(5): p. 367-371.
50. A.Y. Ganin, Y. Takabayashi, P. Jeglič, D. Arčon, A. Potočnik, P.J. Baker, Y. Ohishi, M.T. McDonald, M.D. Tzirakis, A. McLennan, G.R. Darling, M. Takata, M.J. Rosseinsky, and K. Prassides, *Nature*, 2010. **466**(7303): p. 221-U93.
51. V. Buntar, M. Riccò, L. Cristofolini, H.W. Weber, and F. Bolzoni, *Physical Review B*, 1995. **52**(6): p. 4432-4437.
52. M. Tokumoto, Y. Tanaka, N. Kinoshita, T. Kinoshita, S. Ishibashi, and H. Ihara, *Journal of Physics and Chemistry of Solids*, 1993. **54**(12): p. 1667-1673.
53. R. Movshovich, J.D. Thompson, C.C. Chen, and C.M. Lieber, *Physical Review B*, 1994. **49**(5): p. 3619-3621.
54. S. Saito, K. Umemoto, S.G. Louie, and M.L. Cohen, *Solid State Communications*, 2004. **130**(5): p. 335-339.
55. S.P. Kelty, C.C. Chen, and C.M. Lieber, *Nature*, 1991. **352**(6332): p. 223-225.
56. T.T.M. Palstra, O. Zhou, Y. Iwasa, P.E. Sulewski, R.M. Fleming, and B.R. Zegarski, *Solid State Communications*, 1995. **93**(4): p. 327-330.
57. A. Messaoudi, J. Conard, R. Setton, and F. Beguin, *Chemical Physics Letters*, 1993. **202**(6): p. 506-508.
58. S. Fujiki, Y. Kubozono, M. Kobayashi, T. Kambe, Y. Rikiishi, S. Kashino, K. Ishii, H. Suematsu, and A. Fujiwara, *Physical Review B*, 2002. **65**(23).
59. A.G. McLennan, A.Y. Ganin, Y. Takabayashi, R.H. Colman, R.H. Zadik, M.J. Rosseinsky, and K. Prassides, *Faraday Discussions*, 2014. **173**: p. 95-103.
60. S. Heguri and M. Kobayashi, *Solid State Communications*, 2010. **150**(31-32): p. 1489-1492.
61. D. Pontiroli, M. Aramini, M. Gaboardi, M. Mazzani, A. Gorreri, M. Riccò, I. Margiolaki, and D. Sheptyakov, *Carbon*, 2013. **51**: p. 143-147.
62. D. Quintavalle, F. Borondics, G. Klupp, A. Baserga, F. Simon, A. Jánossy, K. Kamarás, and S. Pekker, *Physical Review B*, 2008. **77**(15).
63. A.R. Kortan, N. Kopylov, R.M. Fleming, O. Zhou, F.A. Thiel, R.C. Haddon, and K.M. Rabe, *Physical Review B*, 1993. **47**(19): p. 13070-13073.
64. A.R. Kortan, N. Kopylov, E. Özdas, A.P. Ramirez, R.M. Fleming, and R.C. Haddon, *Chemical Physics Letters*, 1994. **223**(5-6): p. 501-505.
65. O. Gunnarsson, *Reviews of Modern Physics*, 1997. **69**(2): p. 575-606.
66. C.M. Varma, J. Zaanen, and K. Raghavachari, *Science*, 1991. **254**(5034): p. 989-992.
67. C. Christides, D.A. Neumann, K. Prassides, J.R.D. Copley, J.J. Rush, M.J. Rosseinsky, D.W. Murphy, and R.C. Haddon, *Physical Review B*, 1992. **46**(18): p. 12088-12091.
68. K. Prassides, J. Tomkinson, C. Christides, M.J. Rosseinsky, D.W. Murphy, and R.C. Haddon, *Nature*, 1991. **354**(6353): p. 462-463.
69. J. Diederichs, A.K. Gangopadhyay, and J.S. Schilling, *Physical Review B*, 1996. **54**(14): p. R9662-R9665.
70. M.H. Whangbo, J.M. Williams, A.J. Schultz, T.J. Emge, and M.A. Beno, *Journal of the American Chemical Society*, 1987. **109**(1): p. 90-94.
71. M.T. McDonald, *Structural and electronic properties of fulleride superconductors*, in *Department of Chemistry*. 2010, Durham University.
72. M.Z. Huang, Y.N. Xu, and W.Y. Ching, *Physical Review B*, 1992. **46**(10): p. 6572-6577.
73. D.L. Novikov, V.A. Gubanov, and A.J. Freeman, *Physica C*, 1992. **191**(3-4): p. 399-408.
74. G. Sparn, F. Laube, A. Link, F. Steglich, M. Baenitz, K. Lüders, H. Werner, and R. Schlögl, *Journal of Low Temperature Physics*, 1996. **105**(5-6): p. 1703-1708.
75. R.F. Kiefl, W.A. Macfarlane, K.H. Chow, S. Dunsiger, T.L. Duty, T.M.S. Johnston, J.W. Schneider, J. Sonier, L. Brard, R.M. Strongin, J.E. Fischer, and A.B. Smith, *Physical Review Letters*, 1993. **70**(25): p. 3987-3990.

76. M. Capone, M. Fabrizio, C. Castellani, and E. Tosatti, *Reviews of Modern Physics*, 2009. **81**(2): p. 943-958.
77. G. Baskaran and E. Tosatti, *Current Science*, 1991. **61**(1): p. 33-39.
78. S. Chakravarty and S. Kivelson, *Europhysics Letters*, 1991. **16**(8): p. 751-756.
79. S. Chakravarty, M.P. Gelfand, and S. Kivelson, *Science*, 1991. **254**(5034): p. 970-974.
80. O. Gunnarsson, *Alkali-Doped Fullerides: Narrow-Band Solids with Unusual Properties*. 2004: World Scientific Publishing
81. R.W. Lof, M.A. van Veenendaal, B. Koopmans, H.T. Jonkman, and G.A. Sawatzky, *Physical Review Letters*, 1992. **68**(26): p. 3924-3927.
82. A. Georges, G. Kotliar, W. Krauth, and M.J. Rozenberg, *Reviews of Modern Physics*, 1996. **68**(1): p. 13-125.
83. M. Zacharias, L. Bartosch, and M. Garst, *Physical Review Letters*, 2012. **109**(17).
84. N.F. Mott, *Metal-Insulator Transitions*. 2nd ed. 1990, London: Taylor & Francis.
85. N. Manini and E. Tosatti, *Jahn-Teller and Coulomb correlations in fullerene ions and compounds: From isolated ions to metal, insulator and superconductor phases of alkali fulleride solids*. 2010: Lambert.
86. O. Gunnarsson, E. Koch, and R.M. Martin, *Physical Review B*, 1996. **54**(16): p. 11026-11029.
87. G.R. Darling, A.Y. Ganin, M.J. Rosseinsky, Y. Takabayashi, and K. Prassides, *Physical Review Letters*, 2008. **101**(13).
88. X.Y. Zhang, M.J. Rozenberg, and G. Kotliar, *Physical Review Letters*, 1993. **70**(11): p. 1666-1669.
89. Y. Takabayashi, A.Y. Ganin, P. Jeglič, D. Arčon, T. Takano, Y. Iwasa, Y. Ohishi, M. Takata, N. Takeshita, K. Prassides, and M.J. Rosseinsky, *Science*, 2009. **323**(5921): p. 1585-1590.
90. K. Kanoda, *Hyperfine Interactions*, 1997. **104**(1-4): p. 235-249.
91. B. Batlogg and C. Varma, *Physics World*, 2000. **13**(2): p. 33-37.
92. E. Tosatti, *Science*, 2009. **323**(5921): p. 1570-1571.
93. Y. Iwasa, *Nature*, 2010. **466**(7303): p. 191-192.
94. V. Brouet, H. Alloul, S. Gàràj, and L. Forrò, *NMR studies of insulating, metallic, and superconducting fullerides: Importance of correlations and Jahn-Teller distortions*, in *Fullerene-Based Materials: Structures and Properties*, K. Prassides, Editor. 2004, Springer. p. 165-199.
95. P. Durand, G.R. Darling, Y. Dubitsky, A. Zaopo, and M.J. Rosseinsky, *Nature Materials*, 2003. **2**(9): p. 605-610.
96. A.Y. Ganin, Y. Takabayashi, M. Pregelj, A. Zorko, D. Arčon, M.J. Rosseinsky, and K. Prassides, *Chemistry of Materials*, 2007. **19**(13): p. 3177-3182.
97. H. Tou, Y. Maniwa, Y. Iwasa, H. Shimoda, and T. Mitani, *Physical Review B*, 2000. **62**(2): p. R775-R778.
98. G. Klupp, P. Matus, K. Kamarás, A.Y. Ganin, A. McLennan, M.J. Rosseinsky, Y. Takabayashi, M.T. McDonald, and K. Prassides, *Nature Communications*, 2012. **3**.
99. J. Winter and H. Kuzmany, *Solid State Communications*, 1992. **84**(10): p. 935-938.
100. K.A. Wang, Y. Wang, P. Zhou, J.M. Holden, S.L. Ren, G.T. Hager, H.F. Ni, P.C. Eklund, G. Dresselhaus, and M.S. Dresselhaus, *Physical Review B*, 1992. **45**(4): p. 1955-1958.
101. P. Zhou, K.A. Wang, A.M. Rao, P.C. Eklund, G. Dresselhaus, and M.S. Dresselhaus, *Physical Review B*, 1992. **45**(18): p. 10838-10840.
102. J.K. Cockcroft and A.N. Fitch, *Experimental Setups*, in *Powder Diffraction: Theory and Practice*. 2008, RSC.
103. C. Kittel, *Introduction to Solid State Physics*. 8th ed. 2005: Wiley.
104. R.C. Reynolds, *Principles of Powder Diffraction*, in *Modern Powder Diffraction*, D.L. Bish and J.E. Post, Editors. 1989.

105. R.E. Dinnebier and S.J.L. Billinge, *Principles of Powder Diffraction*, in *Powder Diffraction: Theory and Practice*. 2008, RSC.
106. C. Giacovazzo, H.L. Monaco, G. Artioli, D. Viterbo, M. Milanesio, G. Ferraris, G. Gilli, P. Gilli, G. Zanotti, and M. Catti, *Fundamentals of Crystallography*. 2011: Oxford University Press.
107. C. Hammond, *The basics of crystallography and diffraction*. 2009: IUCr.
108. L.B. McCusker, R.B. Von Dreele, D.E. Cox, D. Louër, and P. Scardi, *Journal of Applied Crystallography*, 1999. **32**: p. 36-50.
109. F.J. Manjón and D. Errandonea, *Physica Status Solidi B-Basic Solid State Physics*, 2009. **246**(1): p. 9-31.
110. P. Norby and U. Schwarz, *Powder Diffraction under Non-Ambient Conditions*. Powder Diffraction: Theory and Practice. 2008: RSC.
111. H.K. Mao, J. Xu, and P.M. Bell, *Journal of Geophysical Research-Solid Earth and Planets*, 1986. **91**(B5): p. 4673-4676.
112. *Introduction to the ESRF for journalists*. 2013, ESRF.
113. J.P. Wright, G.B.M. Vaughan, and A.N. Fitch, *Merging data from a multi-detector continuous scanning powder diffraction system*. 2003, IUCr Computing Commision Newsletter. p. 92.
114. M. Mezouar, W.A. Crichton, S. Bauchau, F. Thurel, H. Witsch, F. Torrecillas, G. Blattmann, P. Marion, Y. Dabin, J. Chavanne, O. Hignette, C. Morawe, and C. Borel, *Journal of Synchrotron Radiation*, 2005. **12**: p. 659-664.
115. A.P. Hammersley, S.O. Svensson, M. Hanfland, A.N. Fitch, and D. Häusermann, *High Pressure Research*, 1996. **14**(4-6): p. 235-248.
116. Y. Ohishi, N. Hirao, N. Sata, K. Hirose, and M. Takata, *High Pressure Research*, 2008. **28**(3): p. 163-173.
117. H. Fujihisa, *Review of High Pressure Science and Technology*, 2005. **15**: p. 29-35.
118. M. Wunschel, *X-ray Powder Diffraction Studies at non-Ambient Conditions on the Compounds* $In_xNb_3Te_4$ *(x = 0, 0.54) and* $Si[C(CH_3)_3]n\,[Si(CH_3)_3]4\text{-}n$ *(n = 0, 1, 2)*. 2003, Universität Bayreuth.
119. H.M. Rietveld, *Journal of Applied Crystallography*, 1969. **2**: p. 65.
120. R.A. Young, *Introduction to the Rietveld Method*, in *The Rietveld Method*, R.A. Young, Editor. 1995, Oxford University Press, USA.
121. B.H. Toby, *Powder Diffraction*, 2006. **21**(1): p. 67-70.
122. A. Le Bail, H. Duroy, and J.L. Fourquet, *Materials Research Bulletin*, 1988. **23**(3): p. 447-452.
123. A.C. Larson and R.B. Von Dreele, *General Structure Analysis System (GSAS)*. 2000, Los Alamos National Laboratory Report LAUR 86-748.
124. B.H. Toby, *Journal of Applied Crystallography*, 2001. **34**: p. 210-213.
125. R.M. Hazen, R.T. Downs, and C.T. Prewitt, *Principles of Comparative Crystal Chemistry*, in *High-Temperature and High-Pressure Crystal Chemistry*, R.M. Hazen and R.T. Downs, Editors. 2000, Mineralogical Society of America. p. 1-33.
126. R.J. Angel, *High-Temperature and High-Pressure Crystal Chemistry*, 2000. **41**: p. 35-59.
127. F.D. Murnaghan, *Proceedings of the National Academy of Sciences of the United States of America*, 1944. **30**: p. 244-247.
128. F. Birch, *Physical Review*, 1947. **71**(11): p. 809-824.
129. F. Sayetat, P. Fertey, and M. Kessler, *Journal of Applied Crystallography*, 1998. **31**: p. 121-127.
130. Y. Fei, *Thermal Expansion*, in *Mineral Physics & Crystallography: A Handbook of Physical Constants*, T.J. Ahrens, Editor. 1995, American Geophysical Union.
131. M. McElfresh, *Fundamentals of Magnetism and Magnetic Measurements featuring Quantum Design's Magnetic Property Measurement System*, in *Quantum Design*, P. University, Editor. 1994, Quantum Design.

132. B.D. Cullity and C.D. Graham, *Magnetic properties of superconductors*, in *Introduction to Magnetic Materials, Second Edition.* 2008, the Institute of Electrical and Electronics Engineers, Inc.
133. W.L. McMillan, *Physical Review*, 1968. **167**(2): p. 331-&.
134. H. Alloul, *Eurasia-Pacific Summer School and Conference on Correlated Electrons*, 2012. **23**.
135. G. Kotliar and D. Vollhardt, *Physics Today*, 2004. **57**(3): p. 53-59.
136. *Magnetic Property Measurement System MPMS XL, Hardware Reference Manual*. 1996, Quantum Design, : San Diego, CA.
137. R. Kleiner, D. Koelle, F. Ludwig, and J. Clarke, *Proceedings of the IEEE*, 2004. **92**(10): p. 1534-1548.
138. *easyLab Mcell 10 User Guide*. 2006, easyLab Technologies Limited.
139. T.F. Smith, C.W. Chu, and M.B. Maple, *Cryogenics*, 1969. **9**(1).
140. A.Y. Ganin, Y. Takabayashi, P. Jeglič, D. Arčon, A. Potočnik, P.J. Baker, Y. Ohishi, M.T. McDonald, M.D. Tzirakis, A. McLennan, G.R. Darling, M. Takata, M.J. Rosseinsky, and K. Prassides, *Nature*, 2010. **466**(7303).
141. Y. Ihara, H. Alloul, P. Wzietek, D. Pontiroli, M. Mazzani, and M. Riccò, *Europhysics Letters*, 2011. **94**(3).
142. A. Potočnik, A. Krajnc, P. Jeglič, Y. Takabayashi, A.Y. Ganin, K. Prassides, M.J. Rosseinsky, and D. Arčon, *Scientific Reports*, 2014. **4**: p. 5.
143. G.W. Stinton and J.S.O. Evans, *Journal of Applied Crystallography*, 2007. **40**: p. 87-95.
144. L.W. Finger, D.E. Cox, and A.P. Jephcoat, *Journal of Applied Crystallography*, 1994. **27**: p. 892-900.
145. J. Laugier and B. Bochu, *LMGP-Suite Suite of Programs for the interpretation of X-ray Experiments*. 1999, ENSP/Laboratoire des Matériaux et du Génie Physique.
146. O. Zhou and D.E. Cox, *Journal of Physics and Chemistry of Solids*, 1992. **53**(11): p. 1373-1390.
147. P. Dahlke, P.F. Henry, and M.J. Rosseinsky, *Journal of Materials Chemistry*, 1998. **8**(7): p. 1571-1576.
148. A. Lappas, M. Kosaka, K. Tanigaki, and K. Prassides, *Journal of the American Chemical Society*, 1995. **117**(28): p. 7560-7561.
149. S. Rouzière, S. Margadonna, K. Prassides, and A.N. Fitch, *Europhysics Letters*, 2000. **51**(3): p. 314-319.
150. G.M. Bendele, P.W. Stephens, and J.E. Fischer, *Europhysics Letters*, 1998. **41**(5): p. 553-558.
151. A. Potočnik, *Magnetic Resonance of Molecular Superconductors Bordering the Antiferromagnetic Mott-Insulating State*, in *Department of Physics*. 2013, University of Ljubljana.
152. Y. Maniwa, K. Mizoguchi, K. Kume, K. Tanigaki, T.W. Ebbesen, S. Saito, J. Mizuki, J.S. Tsai, and Y. Kubo, *Solid State Communications*, 1992. **82**(10): p. 783-785.
153. I. Hirosawa, K. Tanigaki, J. Mizuki, T.W. Ebbesen, Y. Shimakawa, Y. Kubo, and S. Kuroshima, *Solid State Communications*, 1992. **82**(12): p. 979-982.
154. S. Saito, S.G. Louie, and M.L. Cohen, *Solid State Communications*, 2007. **142**(4): p. 186-189.
155. J.E. Fischer, G. Bendele, R. Dinnebier, P.W. Stephens, C.L. Lin, N. Bykovetz, and Q. Zhu, *Journal of Physics and Chemistry of Solids*, 1995. **56**(10): p. 1445-1457.
156. I. Hirosawa, J. Mizuki, K. Tanigaki, and H. Kimura, *Solid State Communications*, 1994. **89**(1): p. 55-58.
157. G. Nowitzke, G. Wortmann, H. Werner, and R. Schlögl, *Physical Review B*, 1996. **54**(18): p. 13230-13241.
158. Y. Yoshida, Y. Kubozono, H. Maeda, Y. Nishihata, S. Kashino, and T. Ishii, *Solid State Communications*, 1996. **100**(3): p. 153-156.

159. A.P. Ramirez, M.J. Rosseinsky, D.W. Murphy, and R.C. Haddon, *Physical Review Letters*, 1992. **69**(11): p. 1687-1690.
160. Y. Kasahara, Y. Takeuchi, T. Itou, R.H. Zadik, Y. Takabayashi, A.Y. Ganin, D. Arčon, M.J. Rosseinsky, K. Prassides, and Y. Iwasa, *Physical Review B*, 2014. **90**: p. 014413.
161. G.J. Burkhart and C. Meingast, *Physical Review B*, 1996. **54**(10): p. R6865-R6868.
162. R.M. Hazen, R.T. Downs, and C.T. Prewitt, *High-Temperature and High-Pressure Crystal Chemistry*, 2000. **41**: p. 1-33.
163. A.A. Sabouri-Dodaran, M. Marangolo, C. Bellin, F. Mauri, G. Fiquet, G. Loupias, M. Mezouar, W. Crichton, C. Hérold, F. Rachdi, and S. Rabii, *Physical Review B*, 2004. **70**(17).
164. H.A. Ludwig, W.H. Fietz, F.W. Hornung, K. Grube, B. Renker, and G.J. Burkhart, *Physica C*, 1994. **234**(1-2): p. 45-48.
165. I. Margiolaki, *D. Phil. thesis*. 2003, University of Sussex.
166. V. Buntar and H.W. Weber, *Superconductor Science & Technology*, 1996. **9**(8): p. 599-615.
167. K. Tanigaki, M. Kosaka, T. Manako, Y. Kubo, I. Hirosawa, K. Uchida, and K. Prassides, *Chemical Physics Letters*, 1995. **240**(5-6): p. 627-632.
168. G.A. Bain and J.F. Berry, *Journal of Chemical Education*, 2008. **85**(4): p. 532-536.
169. W.H. Wong, M.E. Hanson, W.G. Clark, G. Grüner, J.D. Thompson, R.L. Whetten, S.M. Huang, R.B. Kaner, F. Diederich, P. Petit, J.J. André, and K. Holczer, *Europhysics Letters*, 1992. **18**(1): p. 79-84.
170. A. Jánossy, O. Chauvet, S. Pekker, J.R. Cooper, and L. Forró, *Physical Review Letters*, 1993. **71**(7): p. 1091-1094.
171. F. Gugenberger, R. Heid, C. Meingast, P. Adelmann, M. Braun, H. Wühl, M. Haluska, and H. Kuzmany, *Physical Review Letters*, 1992. **69**(26): p. 3774-3777.
172. K. Tanigaki and K. Prassides, *Journal of Materials Chemistry*, 1995. **5**(10): p. 1515-1527.
173. B. Gogia, K. Kordatos, H. Suematsu, K. Tanigaki, and K. Prassides, *Physical Review B*, 1998. **58**(3): p. 1077-1079.
174. V.P. Antropov, I. Mazin, O.K. Andersen, A.I. Liechtenstein, and O. Jepsen, *Physical Review B*, 1993. **47**(18): p. 12373-12376.
175. S. Satpathy, V.P. Antropov, O.K. Andersen, O. Jepsen, O. Gunnarsson, and A.I. Liechtenstein, *Physical Review B*, 1992. **46**(3): p. 1773-1793.
176. J. Robert, P. Petit, T. Yildirim, and J.E. Fischer, *Physical Review B*, 1998. **57**(2): p. 1226-1230.
177. V. Brouet, H. Alloul, S. Garaj, and L. Forró, *Physical Review B*, 2002. **66**(15): p. 9.
178. G. Sparn, J.D. Thompson, R.L. Whetten, S.M. Huang, R.B. Kaner, F. Diederich, G. Grüner, and K. Holczer, *Physical Review Letters*, 1992. **68**(8): p. 1228-1231.
179. J.E. Schirber, W.R. Bayless, M.J. Rosseinsky, O. Zhou, R.M. Fleming, D. Murphy, and J.E. Fischer, *Science and Technology of Fullerene Materials*, 1995. **359**: p. 289-294.
180. J.P. Attfield, A.L. Kharlanov, and J.A. McAllister, *Nature*, 1998. **394**(6689): p. 157-159.
181. J. Kapitán, L. Hecht, and P. Bouř, *Physical Chemistry Chemical Physics*, 2008. **10**(7): p. 1003-1008.
182. P. Zhou, K.A. Wang, P.C. Eklund, G. Dresselhaus, and M.S. Dresselhaus, *Physical Review B*, 1993. **48**(11): p. 8412-8417.
183. R.A. Jishi and M.S. Dresselhaus, *Physical Review B*, 1992. **45**(12): p. 6914-6918.
184. K. Kanoda, *Journal of the Physical Society of Japan*, 2006. **75**(5).
185. O. Zhou, T.T.M. Palstra, Y. Iwasa, R.M. Fleming, A.F. Hebard, P.E. Sulewski, D.W. Murphy, and B.R. Zegarski, *Physical Review B*, 1995. **52**(1): p. 483-489.
186. O. Chauvet, G. Oszlànyi, L. Forro, P.W. Stephens, M. Tegze, G. Faigel, and A. Jànossy, *Physical Review Letters*, 1994. **72**(17): p. 2721-2724.

187. N. Čegar, F. Simon, S. Garaj, L. Forró, B. Ruzicka, L. Degiorgi, V. Brouet, and L. Mihály, *arXiv:cond-mat/0002447v1*, 2000.
188. N.A. Babushkina, L.M. Belova, O.Y. Gorbenko, A.R. Kaul, A.A. Bosak, V.I. Ozhogin, and K.I. Kugel, *Nature*, 1998. **391**(6663): p. 159-161.
189. Y. Kurosaki, Y. Shimizu, K. Miyagawa, K. Kanoda, and G. Saito, *Physical Review Letters*, 2005. **95**(17): p. 177001.
190. Y. Shimizu, H. Akimoto, H. Tsujii, A. Tajima, and R. Kato, *Physical Review Letters*, 2007. **99**(25).
191. R.H. Zadik, Y. Takabayashi, G. Klupp, R.H. Colman, A.Y. Ganin, A. Potočnik, P. Jeglič, D. Arčon, P. Matus, K. Kamarás, Y. Kasahara, Y. Iwasa, A.N. Fitch, Y. Ohishi, G. Garbarino, K. Kato, M.J. Rosseinsky, and K. Prassides, *Science Advances*, 2015. **in press**.
192. C.P. Slichter, *Principles of Magnetic Resonance*. 1989, Berlin: Springer-Verlag.
193. S. Lefebvre, P. Wzietek, S. Brown, C. Bourbonnais, D. Jérome, C. Mézière, M. Fourmigué, and P. Batail, *Physical Review Letters*, 2000. **85**(25): p. 5420-5423.
194. C.S. Yoo, B. Maddox, J.H.P. Klepeis, V. Iota, W. Evans, A. McMahan, M.Y. Hu, P. Chow, M. Somayazulu, D. Häusermann, R.T. Scalettar, and W.E. Pickett, *Physical Review Letters*, 2005. **94**(11).
195. J. Kunes, A.V. Lukoyanov, V.I. Anisimov, R.T. Scalettar, and W.E. Pickett, *Nature Materials*, 2008. **7**(3): p. 198-202.
196. S. Javaid, M. Javed Akhtar, I. Ahmad, M. Younas, S.H. Shah, and I. Ahmad, *Journal of Applied Physics*, 2013. **114**: p. 243712.
197. J. Arvanitidis, K. Papagelis, S. Margadonna, and K. Prassides, *Dalton Transactions*, 2004: p. 3144-3146.
198. A.W. Lawson and T.Y. Tang, *Physical Review*, 1949. **76**: p. 301-302.
199. J.B. Goodenough, *Localized to Itinerant Electronic Transition in Perovskite Oxides*, 2001. **98**: p. 1-16.
200. H.D. Zhou and J.B. Goodenough, *Physical Review B*, 2005. **71**(16): p. 6.
201. V. Brouet, H. Alloul, S. Gàràj, and L. Forrò, *NMR Studies of Insulating, Metallic, and Superconducting Fullerides: Importance of Correlations and Jahn-Teller Distortions*, in *Fullerene-Based Materials Structures and Properties*, K. Prassides, Editor. 2004, Springer.
202. J. Muller, *Reports on Progress in Physics*, 1980. **43**(5): p. 641-687.
203. M. Knupfer, F. Stepniak, and J.H. Weaver, *Physical Review B*, 1994. **49**(11): p. 7620-7624.
204. M.C. Böhm, J. Schulte, J. Schütt, T. Schedel-Niedrig, H. Werner, and R. Schlögl, *International Journal of Quantum Chemistry*, 1997. **65**(4): p. 333-373.
205. K. Brigatti, *D. Phil. thesis*. 2004, University of Sussex.
206. L.R. Testardi, J.H. Wernick, and W.A. Royer, *Solid State Communications*, 1974. **15**(1): p. 1-4.
207. P. Wzietek, T. Mito, H. Alloul, D. Pontiroli, M. Aramini, and M. Ricco, *Physical Review Letters*, 2014. **112**(6): p. 5.
208. P. Jeglič, D. Arčon, A. Potočnik, A.Y. Ganin, Y. Takabayashi, M.J. Rosseinsky, and K. Prassides, *Physical Review B*, 2009. **80**(19).
209. Y. Ihara, H. Alloul, P. Wzietek, D. Pontiroli, M. Mazzani, and M. Ricco, *Physical Review Letters*, 2010. **104**(25): p. 4.
210. J. Oitmaa and W.H. Zheng, *Physical Review B*, 2004. **69**(6): p. 5.
211. A. Rezzouk, D. Dafir, Y. Errammach, and F. Rachdi, *Comptes Rendus Physique*, 2003. **4**(6): p. 715-720.
212. A.R. Kortan, N. Kopylov, S. Glarum, E.M. Gyorgy, A.P. Ramirez, R.M. Fleming, O. Zhou, F.A. Thiel, P.L. Trevor, and R.C. Haddon, *Nature*, 1992. **360**(6404): p. 566-568.
213. S. Saito and A. Oshiyama, *Physical Review Letters*, 1993. **71**(1): p. 121-124.

214. A. Potocnik, A.Y. Ganin, Y. Takabayashi, M.T. McDonald, I. Heinmaa, P. Jeglic, R. Stern, M.J. Rosseinsky, K. Prassides, and D. Arcon, *Chemical Science*, 2014. **5**(8): p. 3008-3017.
215. C.M. Brown, *D. Phil. thesis*. 1998, University of Sussex.
216. M. Tanaka, S. Zhang, T. Onimaru, T. Takabatake, K. Inumaru, and S. Yamanaka, *Carbon*, 2014. **73**: p. 125-131.
217. K. Seema and R. Kumar, *Physica Scripta*, 2011. **83**(2).
218. K. Momma and F. Izumi, *Journal of Applied Crystallography*, 2011. **44**: p. 1272-1276.
219. K.M. Allen, W.I.F. David, J.M. Fox, R.M. Ibberson, and M.J. Rosseinsky, *Chemistry of Materials*, 1995. **7**(4): p. 764-770.
220. Y. Kasahara, K. Takeuchi, T. Itou, R.H. Zadik, Y. Takabayashi, A.Y. Ganin, D. Arčon, M.J. Rosseinsky, K. Prassides, and Y. Iwasa, *Physical Review B*, 2014. **90**: p. 014413.
221. P.W. Stephens, *Journal of Applied Crystallography*, 1999. **32**: p. 281-289.
222. B.J. Campbell, H.T. Stokes, D.E. Tanner, and D.M. Hatch, *Journal of Applied Crystallography*, 2006. **39**: p. 607-614.
223. H.T. Stokes and D.M. Hatch, *Isotropy subgroups of the 230 crystallographic space groups*. 1987, Singapore: World Scientific.
224. L.C. Bartel and B. Morosin, *Physical Review B*, 1971. **3**(3): p. 1039.
225. R. Poloni, *Heavy alkali metal-intercalated fullerenes under high pressure and high temperature conditions: Rb_6C_{60} and Cs_6C_{60}*. 2007, Université Claude Bernard - Lyon 1.
226. R. Poloni, M.V. Fernandez-Serra, S. Le Floch, S. De Panfilis, P. Toulemonde, D. Machon, W. Crichton, S. Pascarelli, and A. San-Miguel, *Physical Review B*, 2008. **77**(3).
227. K. Khazeni, J. Hone, N.G. Chopra, A. Zettl, J. Nguyen, and R. Jeanloz, *Applied Physics a-Materials Science & Processing*, 1997. **64**(3): p. 263-269.
228. S.J. Duclos, K. Brister, R.C. Haddon, A.R. Kortan, and F.A. Thiel, *Nature*, 1991. **351**(6325): p. 380-382.
229. T.R. Finlayson and T.F. Smith, *Phase Transitions*, 1999. **69**(3): p. 409-424.
230. S. Greenwald and J.S. Smart, *Nature*, 1950. **166**(4221): p. 523-524.
231. M. Giot, L.C. Chapon, J. Androulakis, M.A. Green, P.G. Radaelli, and A. Lappas, *Physical Review Letters*, 2007. **99**(24).
232. G. Klupp and K. Kamarás, *Dalton Transactions*, 2014. **43**: p. 7366.
233. A. Auerbach, N. Manini, and E. Tosatti, *Physical Review B*, 1994. **49**(18): p. 12998-13007.
234. C.C. Chancey and M.C.M. O'Brien, *The Jahn-Teller effect in C_{60} and other icosahedral complexes*. 1997, Chichester: Princeton University Press.
235. R. Poloni, G. Aquilanti, P. Toulemonde, S. Pascarelli, S. Le Floch, D. Machon, D. Martinez-Blanco, G. Morard, and A. San-Miguel, *Physical Review B*, 2008. **77**(20).
236. S. Pekker, G. Oszlányi, and G. Faigel, *Chemical Physics Letters*, 1998. **282**(5-6): p. 435-441.
237. G.M. Bendele, P.W. Stephens, K. Prassides, K. Vavekis, K. Kordatos, and K. Tanigaki, *Physical Review Letters*, 1998. **80**(4): p. 736-739.
238. B. Sundqvist, *Low Temperature Physics*, 2003. **29**(5): p. 440-444.
239. G.A. Samara, L.V. Hansen, R.A. Assink, B. Morosin, J.E. Schirber, and D. Loy, *Physical Review B*, 1993. **47**(8): p. 4756-4764.
240. J.E. Schirber, G.H. Kwei, J.D. Jorgensen, R.L. Hitterman, and B. Morosin, *Physical Review B*, 1995. **51**(17): p. 12014-12017.
241. L. Pintschovius, O. Blaschko, G. Krexner, and N. Pyka, *Physical Review B*, 1999. **59**(16): p. 11020-11026.
242. Y.E. Stetsenko, I.V. Legchenkova, K.A. Yagotintsev, A.I. Prokhvatilov, and M.A. Strzhemechnyi, *Low Temperature Physics*, 2003. **29**(5): p. 445-448.

243. V. Buntar, F.M. Sauerzopf, and H.W. Weber, *Physical Review B*, 1996. **54**(14): p. R9651-R9654.
244. B.J. Campbell, J.S.O. Evans, F. Perselli, and H.T. Stokes, *IUCr Computing Commission Newsletter* 2007. **No. 8**: p. 81-95.
245. R. Poloni, *Heavy alkali metal-intercalated fullerenes under high pressure and high temperature conditions: Rb_6C_{60} and Cs_6C_{60}*. 2007, University Claude Bernard - Lyon 1.
246. S. Yamanaka, E. Enishi, H. Fukuoka, and M. Yasukawa, *Inorganic Chemistry*, 2000. **39**(1): p. 56-58.

Appendix

Synchrotron X-ray powder diffraction data were collected for several compositions of *fcc*-rich $Rb_xCs_{3-x}C_{60}$ ($0.25 \leq x \leq 2$) under variable temperature and pressure conditions, as described in detail in Chapter 3. Due to space limitations, only representative data are included in Chapter 3 (*i.e.* data for selected compositions), and thus further data for the remaining compositions are presented in this Appendix.

Ambient-pressure synchrotron X-ray powder diffraction of *fcc*-rich $Rb_xCs_{3-x}C_{60}$ ($0.25 \leq x \leq 2$)

For Rietveld fits to PXRD data collected at 300 K and at 10 K for the sample with nominal Rb content $x = 0.25$, the observed, calculated and difference profiles and the derived structural parameters for the majority *fcc* phase are presented in Fig. A1 and Table A1, respectively. Equivalent data for $x = 0.35$ are displayed in Fig. A2 and Table A2, and those for $x = 0.75$ in Fig. A3 and Table A3. Analogous data for compositions with $x = 0.5$ and $x = 1$ were provided in Chapter 3. For the $x = 1.5$ and $x = 2$ compositions, where multiple samples were used in the study, ambient temperature data for each of the samples is presented in Fig. A4 and Table A4, and Fig. A5 and Table A5, respectively.

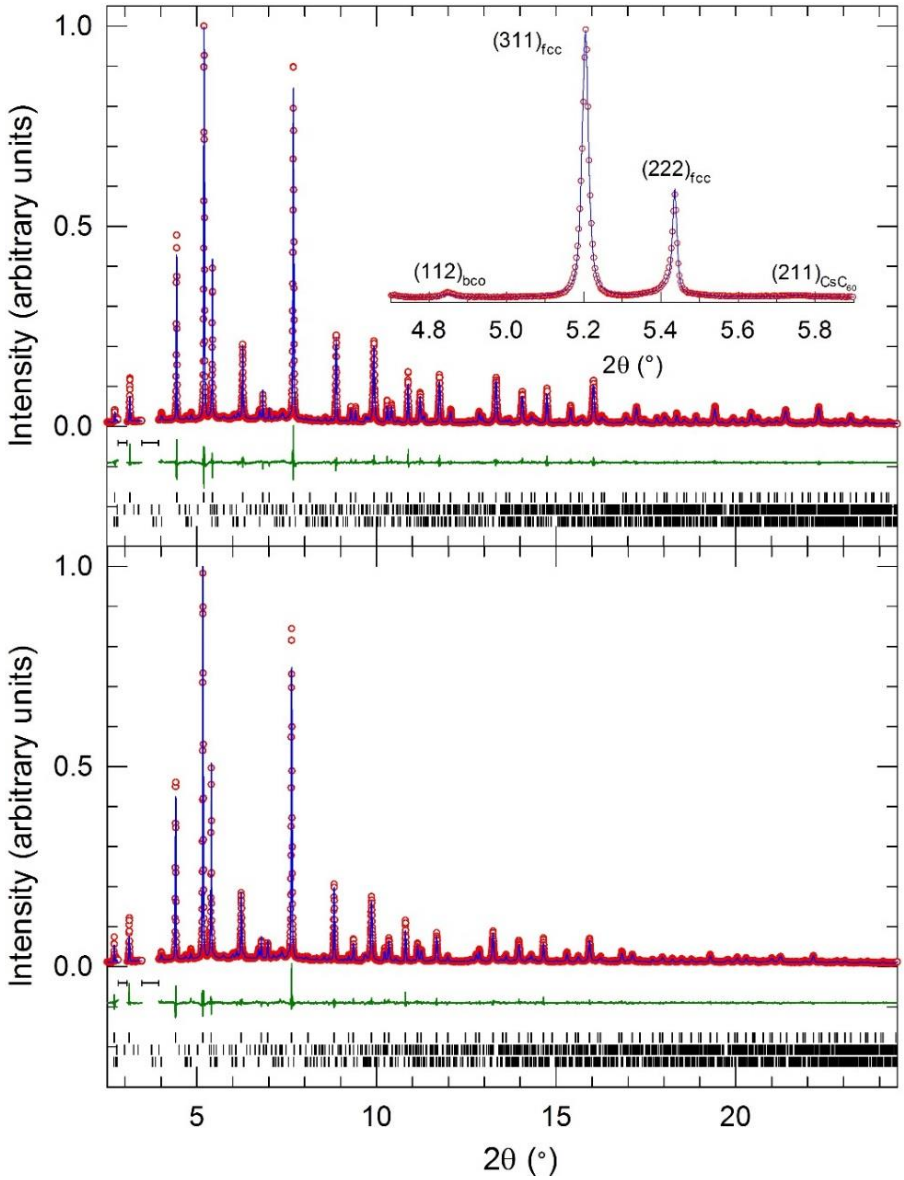

Figure A1: Rietveld fits to synchrotron PXRD data collected for *fcc*-rich $Rb_{0.25}Cs_{2.75}C_{60}$ at 10 K (upper panel) and 300 K (lower panel) (λ = 0.39984 Å). Red circles, blue lines and green lines represent the observed, calculated and difference profiles. Bars mark the reflection positions, from top-to-bottom, of co-existing *fcc*, CsC_{60} and Cs_4C_{60} ('body-centred orthorhombic') phases. Inset: expanded region of the fit to the data collected at 10 K, with reflections labelled. Two broad peaks arising from the cryostat were visible at low angles (< 4°), and these regions were excluded from the fitting.

Table A1: Refined *fcc* phase structural parameters for $Rb_{0.25}Cs_{2.75}C_{60}$, from Rietveld analysis of synchrotron PXRD data collected at 10 K and at 300 K (*fcc* phase fraction = 83.28(5)%, see Table 3.3). The fractional cation occupancies, N of the tetrahedral interstitial site were fixed to values refined from the 10 K (highest statistics) data, as described in Chapter 3; values in parentheses are statistical errors from the least-squares fitting. As detailed in Chapter 3, C_{60} radii and C-C bond distances were fixed, with fractional coordinates rescaled to the refined lattice metrics; C-C bond distances were fixed to 1.42 Å, using literature C_{60} coordinates originally determined for Rb_3C_{60},[1] an approach adopted as the resulting fits were of excellent quality (and for reasons of consistency, as available data quality and crystallographic phase fractions, *i.e.* extent of multiphasic character and thus PXRD peak overlap, varied across the series).

T = 10 K	x/a	y/b	z/c	N	B_{iso} (Å^2)
Rb	0.25	0.25	0.25	0.108(7)	0.34(2)
Cs(1)	0.25	0.25	0.25	0.892(7)	0.34(2)
Cs(2)	0.5	0.5	0.5	1.0	1.55(3)
C(1)	0	0.04866	0.23599	0.5	0.15(5)
C(2)	0.20598	0.07866	0.09712	0.5	0.15(5)
C(3)	0.17578	0.15716	0.04866	0.5	0.15(5)

T = 300 K	x/a	y/b	z/c	N	B_{iso} (Å^2)
Rb	0.25	0.25	0.25	0.108	1.74(2)
Cs(1)	0.25	0.25	0.25	0.892	1.74(2)
Cs(2)	0.5	0.5	0.5	1.0	9.92(8)
C(1)	0	0.04833	0.23438	0.5	1.08(7)
C(2)	0.20458	0.07812	0.09646	0.5	1.08(7)
C(3)	0.17458	0.15609	0.04833	0.5	1.08(7)

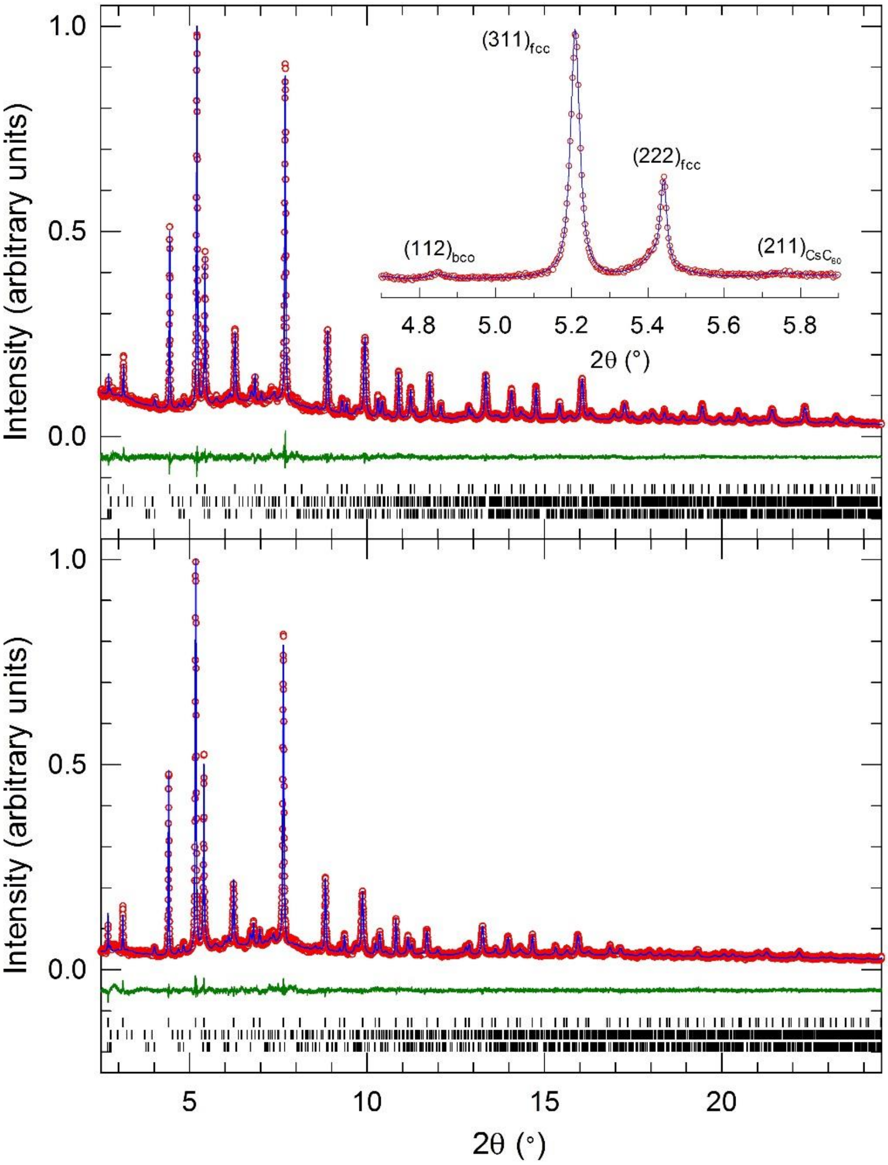

Figure A2: Rietveld fits to synchrotron PXRD data collected for *fcc*-rich $Rb_{0.35}Cs_{2.65}C_{60}$ at 10 K (upper panel) and 300 K (lower panel) (λ = 0.40006 Å). Red circles, blue lines and green lines represent the observed, calculated and difference profiles. Bars mark the reflection positions, from top-to-bottom, of co-existing *fcc*, CsC_{60} and Cs_4C_{60} ('body-centred orthorhombic') phases. Inset: expanded region of the fit to the data collected at 10 K, with reflections labelled.

Table A2: Refined *fcc* phase structural parameters for $Rb_{0.35}Cs_{2.65}C_{60}$, from Rietveld analysis of synchrotron PXRD data collected at 10 K and at 300 K (*fcc* phase fraction = 76.48(7)%, see Table 3.3). The fractional cation occupancies, N of the tetrahedral interstitial site were fixed to values refined from the 10 K (highest statistics) data, as described in Chapter 3; values in parentheses are statistical errors from the least-squares fitting.

T = 10 K	x/a	y/b	z/c	N	B_{iso} (Å^2)
Rb	0.25	0.25	0.25	0.163(8)	0.22(2)
Cs(1)	0.25	0.25	0.25	0.837(8)	0.22(2)
Cs(2)	0.5	0.5	0.5	1.0	1.18(3)
C(1)	0	0.04871	0.23620	0.5	0.03(5)
C(2)	0.20617	0.07873	0.09721	0.5	0.03(5)
C(3)	0.17594	0.15730	0.04871	0.5	0.03(5)

T = 300 K	x/a	y/b	z/c	N	B_{iso} (Å^2)
Rb	0.25	0.25	0.25	0.163	1.93(3)
Cs(1)	0.25	0.25	0.25	0.837	1.93(3)
Cs(2)	0.5	0.5	0.5	1.0	10.0(1)
C(1)	0	0.04836	0.23450	0.5	0.93(9)
C(2)	0.20468	0.07816	0.09650	0.5	0.93(9)
C(3)	0.17467	0.15617	0.04836	0.5	0.93(9)

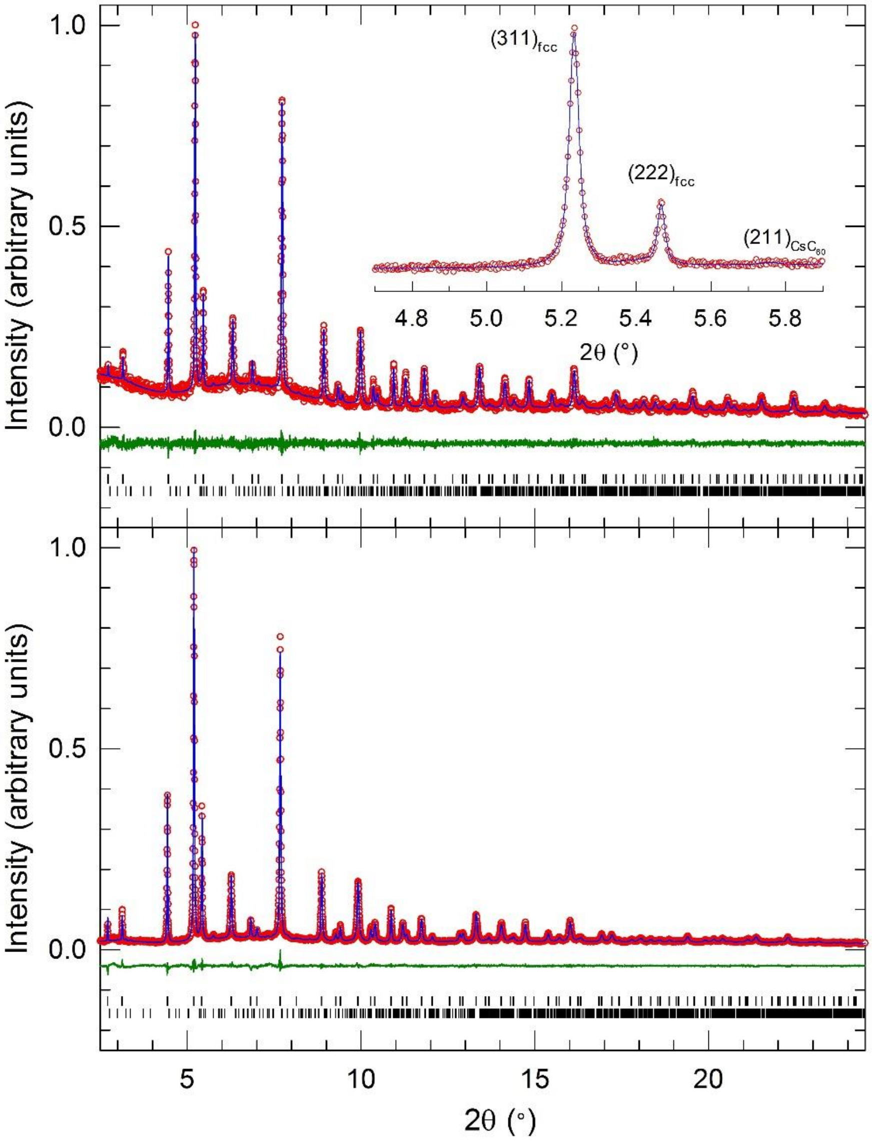

Figure A3: Rietveld fits to synchrotron PXRD data collected for *fcc*-rich $Rb_{0.75}Cs_{2.25}C_{60}$ at 10 K (upper panel) and 300 K (lower panel) (λ = 0.40006 Å). Red circles, blue lines and green lines represent the observed, calculated and difference profiles. Bars mark the reflection positions, from top-to-bottom, of co-existing *fcc* and CsC_{60} phases. Inset: expanded region of the fit to the data collected at 10 K, with reflections labelled. An experimental issue rendered the signal-to-noise ratio of the 10 K data worse than that of the 300 K data (partial movement of the powder sample out of the X-ray beam due to spinning).

Table A3: Refined *fcc* phase structural parameters for $Rb_{0.75}Cs_{2.25}C_{60}$, from Rietveld analysis of synchrotron PXRD data collected at 10 K and at 300 K (*fcc* phase fraction = 94.30(1)%, see Table 3.3). The fractional cation occupancies, N of the tetrahedral interstitial site were fixed to values refined from the 300 K data, which had significantly better signal-to-noise than the 10 K data (due to partial movement of the powder sample out of the X-ray beam upon cooling). Due to this experimental issue in collection of the 10 K data, the data were such that the thermal displacement parameters of the C atoms and the tetrahedral interstital site could not refine to physically meaningful values, so were fixed to values of appropriate magnitude (based on analysis of higher quality low-temperature data available for the other compositions). Values in parentheses are statistical errors from the least-squares fitting.

T = 10 K	x/a	y/b	z/c	N	B_{iso} (Å^2)
Rb	0.25	0.25	0.25	0.367	0.32
Cs(1)	0.25	0.25	0.25	0.633	0.32
Cs(2)	0.5	0.5	0.5	1.0	0.08(4)
C(1)	0	0.04893	0.23729	0.5	0.20
C(2)	0.20712	0.07909	0.09765	0.5	0.20
C(3)	0.17675	0.15803	0.04893	0.5	0.20

T = 300 K	x/a	y/b	z/c	N	B_{iso} (Å^2)
Rb	0.25	0.25	0.25	0.367(5)	1.56(2)
Cs(1)	0.25	0.25	0.25	0.633(5)	1.56(2)
Cs(2)	0.5	0.5	0.5	1.0	8.39(6)
C(1)	0	0.04858	0.23556	0.5	0.87(5)
C(2)	0.20561	0.07852	0.09694	0.5	0.87(5)
C(3)	0.17546	0.15688	0.04858	0.5	0.87(5)

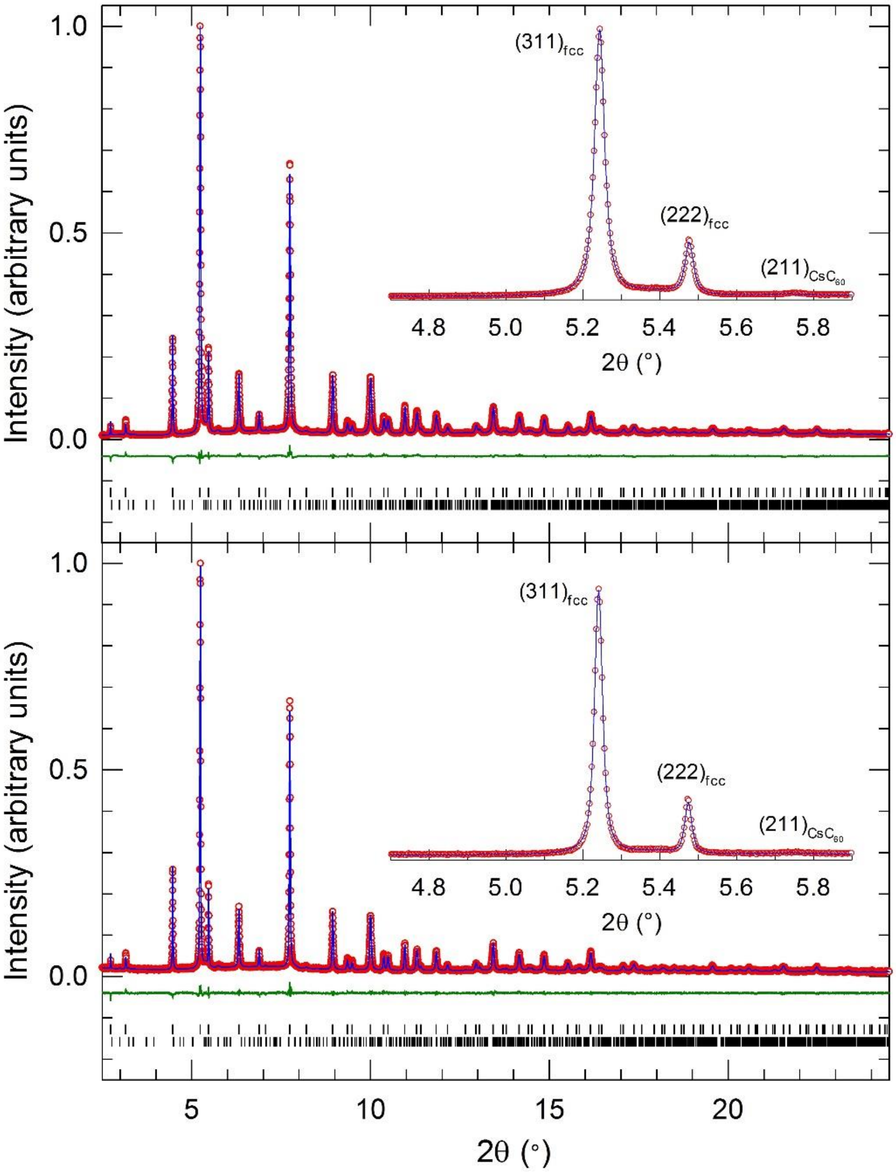

Figure A4: Rietveld fits to synchrotron PXRD data collected for *fcc*-rich $Rb_{1.5}Cs_{1.5}C_{60}$ samples at ambient temperature (upper panel: sample I, λ = 0.40006 Å; lower panel: sample II, λ = 0.39996 Å). Red circles, blue lines and green lines represent the observed, calculated and difference profiles. Bars mark the reflection positions, from top-to-bottom, of co-existing *fcc* and CsC_{60} phases. Insets: expanded region of the fits, with key reflections labelled.

Table A4: Refined *fcc* phase structural parameters for $Rb_{1.5}Cs_{1.5}C_{60}$, from Rietveld analysis of synchrotron PXRD data collected at ambient temperature for sample I (*fcc* phase fraction 94.04(1)%) and sample II (93.98(2)% *fcc*); see Tables 3.2 and 3.3 for further information. Values in parentheses are statistical errors from the least-squares fitting.

$Rb_{1.5}Cs_{1.5}C_{60}$ sample I, RT	x/a	y/b	z/c	N	B_{iso} (Å^2)
Rb	0.25	0.25	0.25	0.782(3)	1.67(2)
Cs(1)	0.25	0.25	0.25	0.218(3)	1.67(2)
Cs(2)	0.5	0.5	0.5	1.0	6.41(4)
C(1)	0	0.04902	0.23772	0.5	0.68(4)
C(2)	0.20750	0.07924	0.09783	0.5	0.68(4)
C(3)	0.17707	0.15832	0.04902	0.5	0.68(4)

$Rb_{1.5}Cs_{1.5}C_{60}$ sample II, RT	x/a	y/b	z/c	N	B_{iso} (Å^2)
Rb	0.25	0.25	0.25	0.743(5)	1.88(3)
Cs(1)	0.25	0.25	0.25	0.257(5)	1.88(3)
Cs(2)	0.5	0.5	0.5	1.0	6.83(6)
C(1)	0	0.04900	0.23762	0.5	0.95(6)
C(2)	0.20740	0.07920	0.09779	0.5	0.95(6)
C(3)	0.17699	0.15824	0.04900	0.5	0.95(6)

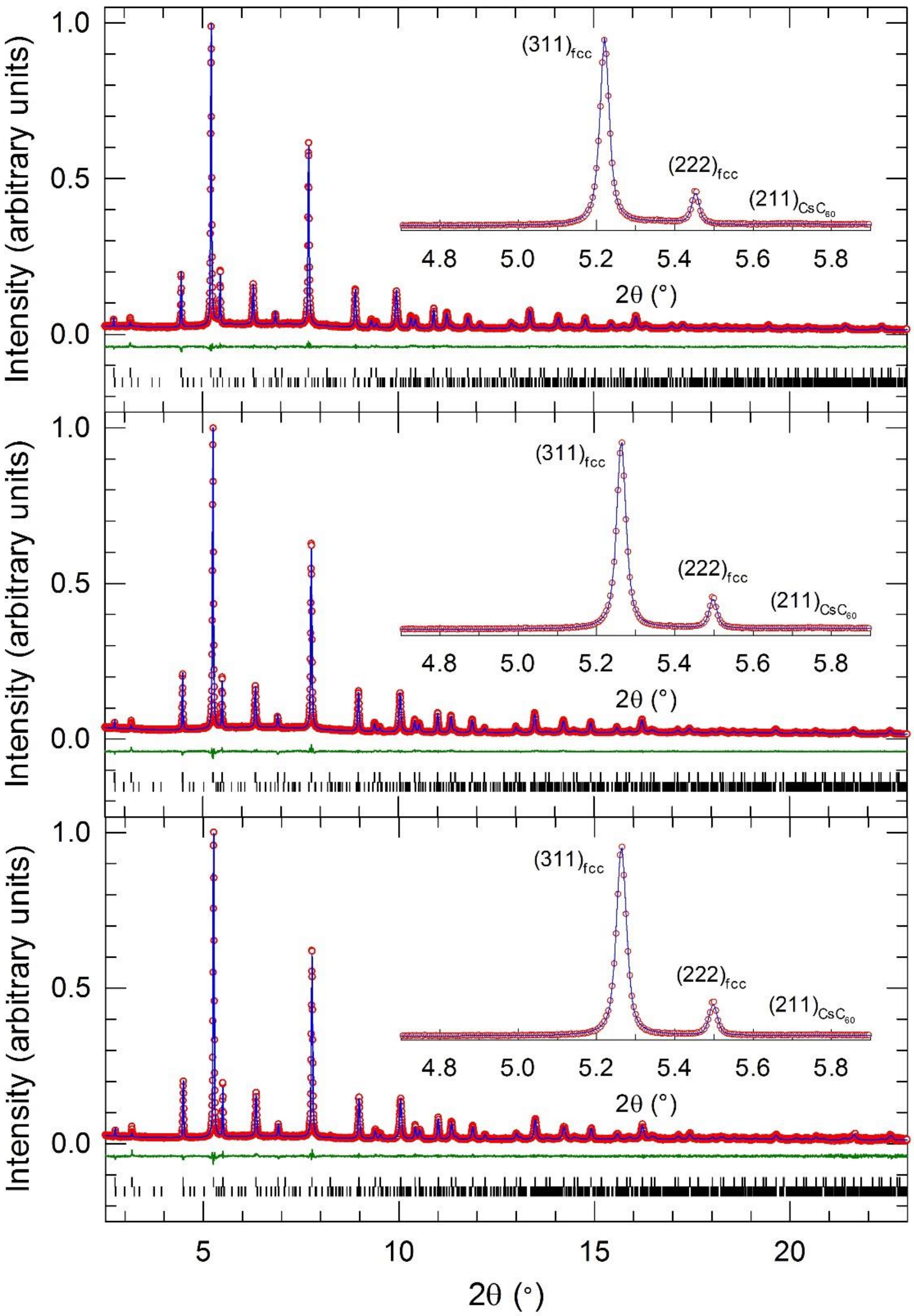

Figure A5: Rietveld fits to synchrotron PXRD data collected for *fcc*-rich Rb_2CsC_{60} samples at ambient temperature (upper panel: sample I, λ = 0.39620 Å; middle panel: sample II, λ = 0.40006 Å; lower panel: sample III, λ = 0.39996 Å). Red circles, blue lines and green lines represent the observed, calculated and difference profiles. Bars mark the reflection positions, from top-to-bottom, of co-existing *fcc* and CsC_{60} phases. Insets: expanded region of the fits, with key reflections labelled.

Table A5: Refined *fcc* phase structural parameters for Rb_2CsC_{60}, from Rietveld analysis of synchrotron PXRD data collected at ambient temperature for sample I (*fcc* phase fraction 91.71(2)%), sample II (98.184(4)% *fcc*) and sample 3 (99.137(2)% *fcc*); see Tables 3.2 and 3.3 for further information. Values in parentheses are statistical errors from the least-squares fitting.

Rb_2CsC_{60} sample I, RT	x/a	y/b	z/c	N	B_{iso} (Å^2)
Rb	0.25	0.25	0.25	1.0	1.41(2)
Cs	0.5	0.5	0.5	1.0	6.97(7)
C(1)	0	0.04919	0.23854	0.5	0.68(6)
C(2)	0.20821	0.07951	0.09817	0.5	0.68(6)
C(3)	0.17768	0.15886	0.04919	0.5	0.68(6)

Rb_2CsC_{60} sample II, RT	x/a	y/b	z/c	N	B_{iso} (Å^2)
Rb	0.25	0.25	0.25	1.0	1.38(2)
Cs	0.5	0.5	0.5	1.0	6.29(5)
C(1)	0	0.04921	0.23862	0.5	0.85(5)
C(2)	0.20828	0.07954	0.09820	0.5	0.85(5)
C(3)	0.17774	0.15891	0.04921	0.5	0.85(5)

Rb_2CsC_{60} sample III, RT	x/a	y/b	z/c	N	B_{iso} (Å^2)
Rb	0.25	0.25	0.25	1.0	0.97(4)
Cs	0.5	0.5	0.5	1.0	6.33(8)
C(1)	0	0.04921	0.23862	0.5	0.060
C(2)	0.20828	0.07954	0.09820	0.5	0.060
C(3)	0.17774	0.15891	0.04921	0.5	0.060

Low-temperature high-pressure synchrotron X-ray powder diffraction of *fcc*-rich $Rb_xCs_{3-x}C_{60}$ (x = 0.5, 1 and 1.5)

The evolution of PXRD profiles collected at low temperatures and high pressures for *fcc*-rich $Rb_{0.5}Cs_{2.5}C_{60}$, $RbCs_2C_{60}$ and $Rb_{1.5}Cs_{1.5}C_{60}$ is illustrated in Fig. A6. Observed and calculated PXRD profiles for measurements undertaken at two arbitrary pressures (at the lower and higher end of the measured ranges) are shown in Figs. A7, A8 and A9, respectively. Structural parameters for the majority *fcc* phases are presented in Tables A6, A7 and A8, respectively. Corresponding data for compositions x = 0.35 and x = 2 were presented in Chapter 3.

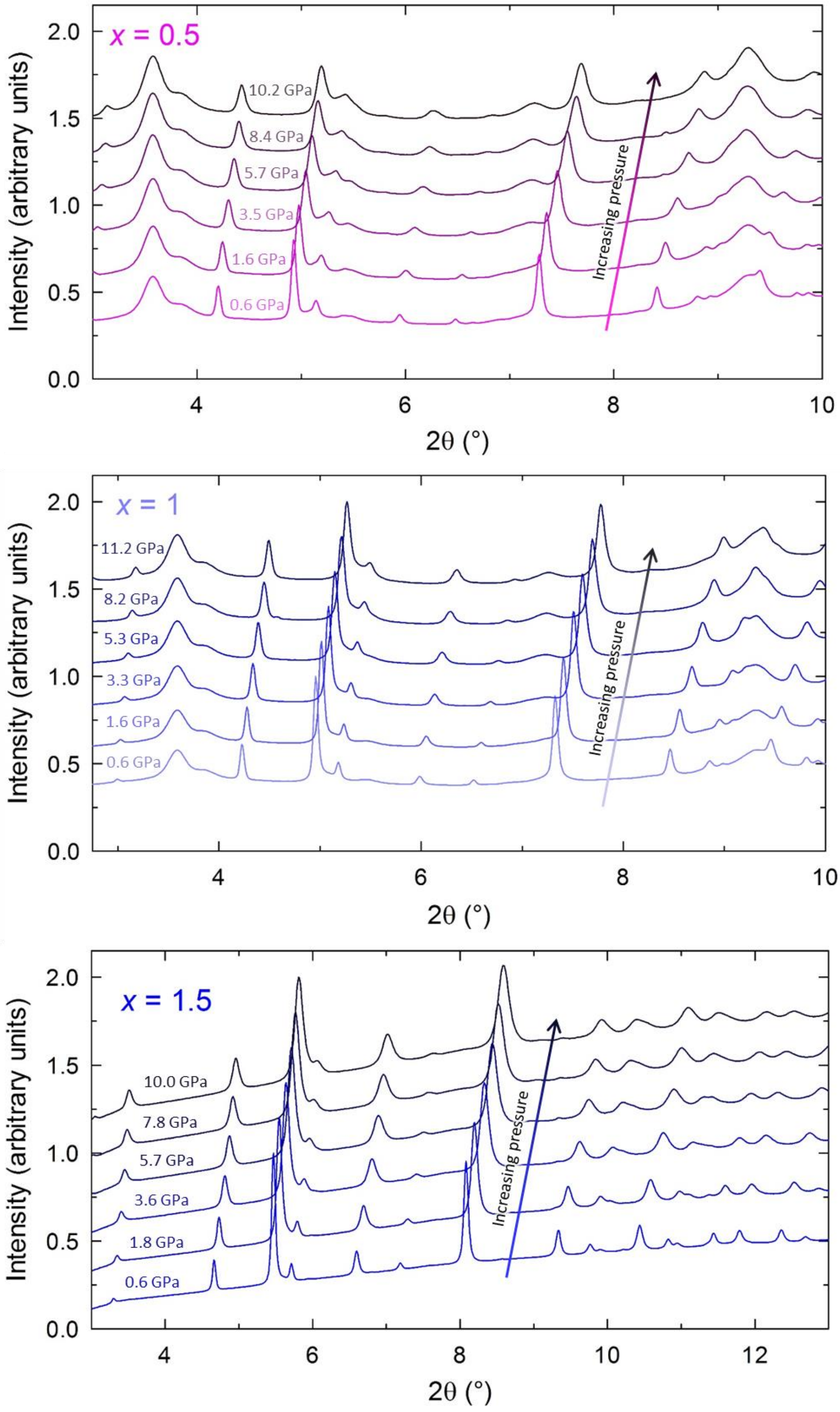

Figure A6: The evolution of synchrotron PXRD profiles with pressure for fcc-rich $Rb_xCs_{3-x}C_{60}$, collected at 20 K (x = 0.5, upper panel, λ = 0.3738 Å and x = 1, middle panel, λ = 0.3738 Å) and at 7 K (x = 1.5, sample I, lower panel, λ = 0.41238 Å). Intensities have been normalized and offset for visual clarity. For compositions where x = 0.5 and 1 (*i.e.* data collected at beamline ID27, ESRF), large broad cryostat contributions are visible *e.g.* at ~3.6° and ~9.2°; these 2θ regions were excluded from structural refinements.

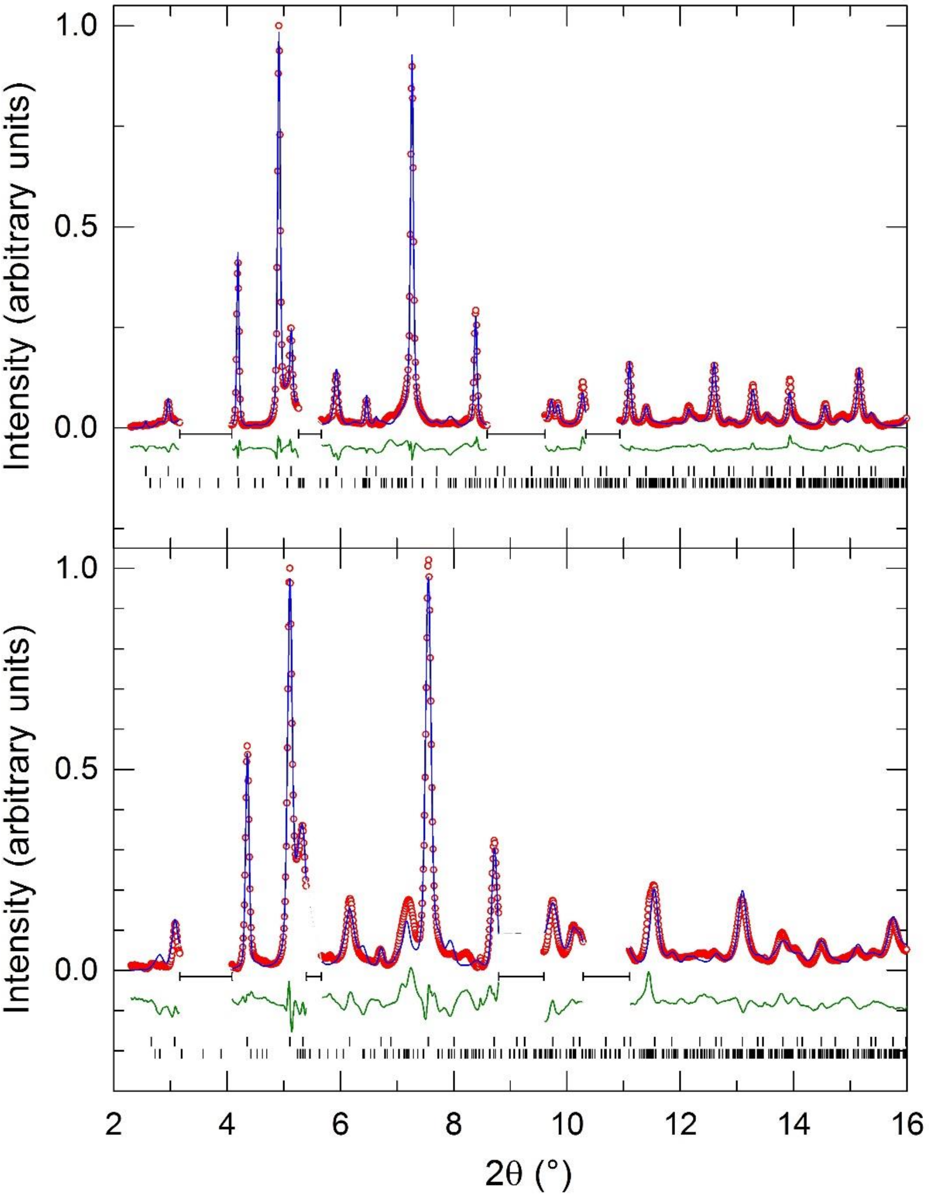

Figure A7: High-pressure synchrotron X-ray powder diffraction data for *fcc*-rich $Rb_{0.5}Cs_{2.5}C_{60}$ (20 K, λ = 0.3738 Å). Final observed (o) and calculated (blue line) diffraction profiles at 0.42 GPa (top) and at 5.75 GPa (bottom) from Rietveld refinement. Green lines show the difference profiles, with bars representing reflection positions from *fcc* $Rb_{0.5}Cs_{2.5}C_{60}$ (upper) and CsC_{60} (lower). The background contributions as obtained from fitting were subtracted for visual clarity. Several broad background peaks arising from the cryostat could not be fitted satisfactorily with a background polynomial function, so these regions were excluded from the fits.

Table A6: *Fcc* phase structural parameters for *fcc*-rich $Rb_{0.5}Cs_{2.5}C_{60}$, employed in Rietveld analysis of synchrotron PXRD data collected at 20 K and under elevated pressures (0.42 GPa and 5.75 GPa). The fractional cation occupancies, *N* of the tetrahedral interstitial site were fixed to values refined from the 5 K (highest statistics) ambient pressure data for the same sample, as described in Chapter 3. Thermal displacement parameters were fixed to values of appropriate magnitude as a best approximation, as with the data quality available these could not be meaningfully refined together with the profile shape parameters necessary to describe the pressure-induced peak broadening (the effect of pressure on isotropic thermal displacement parameters should be relatively small [**2**]). This is also applicable to the high pressure PXRD data analysis for the other compositions (although for $Rb_{1.5}Cs_{1.5}C_{60}$, where data quality was excellent, no 2θ regions needed to be excluded due to a smooth background and peak overlap was very minimal due to higher *fcc* phase purity, thermal displacement parameters for the tetrahedral and octahedral interstitial sites could be meaningfully refined).

x = 0.5 0.42 GPa	x/a	y/b	z/c	N	B_{iso} (Å^2)
Rb	0.25	0.25	0.25	0.2125	0.250
Cs(1)	0.25	0.25	0.25	0.7875	0.250
Cs(2)	0.5	0.5	0.5	1.0	1.126
C(1)	0	0.04921	0.23863	0.5	0.083
C(2)	0.20829	0.07954	0.09821	0.5	0.083
C(3)	0.17775	0.15892	0.04921	0.5	0.083

x = 0.5 5.75 GPa	x/a	y/b	z/c	N	B_{iso} (Å^2)
Rb	0.25	0.25	0.25	0.2125	0.250
Cs(1)	0.25	0.25	0.25	0.7875	0.250
Cs(2)	0.5	0.5	0.5	1.0	1.126
C(1)	0	0.05116	0.24810	0.5	0.083
C(2)	0.21655	0.08270	0.10210	0.5	0.083
C(3)	0.18480	0.16523	0.05116	0.5	0.083

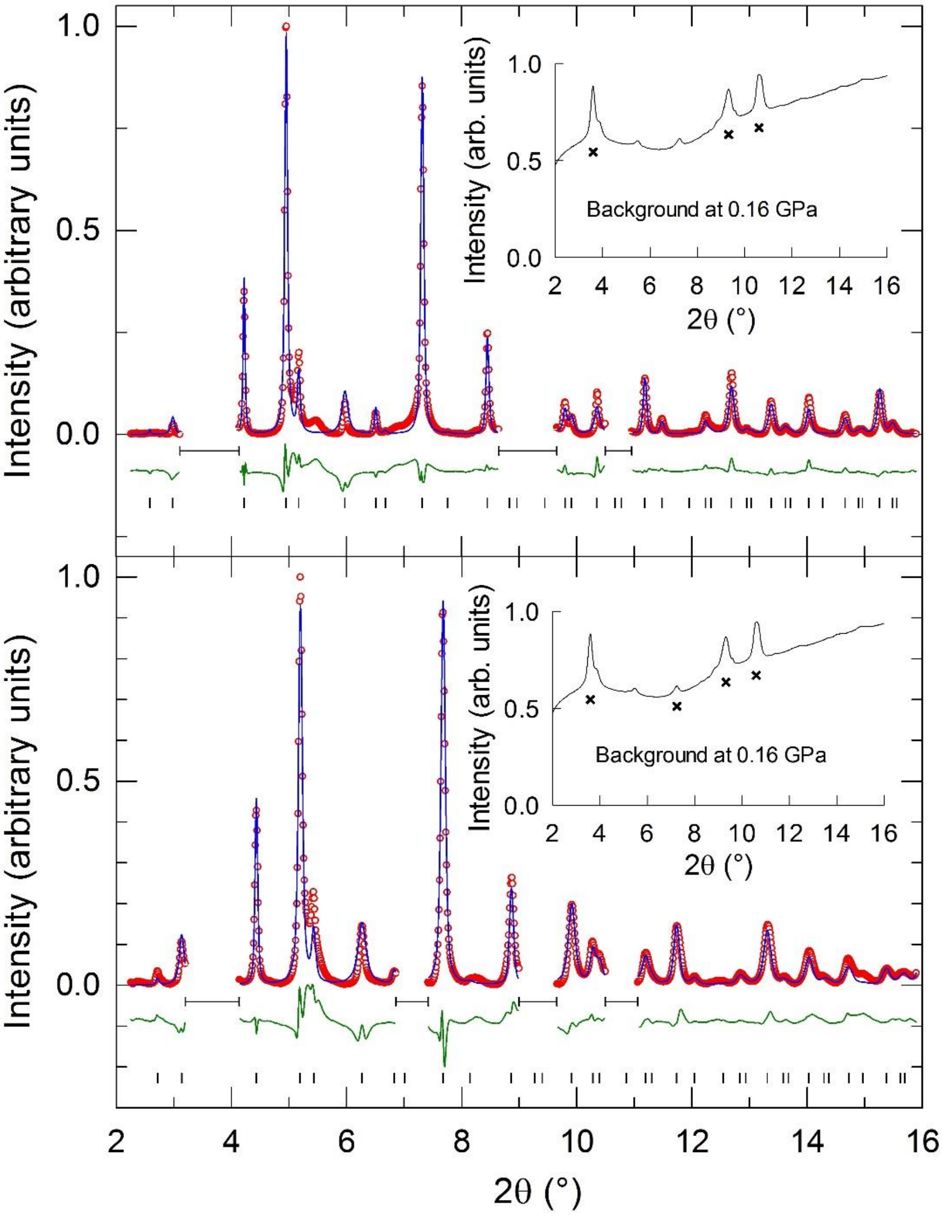

Figure A8: High-pressure synchrotron X-ray powder diffraction for *fcc* $RbCs_2C_{60}$ (20 K, λ = 0.3738 Å). Final observed (o) and calculated (blue line) diffraction profiles at 0.43 GPa (top) and at 7.42 GPa (bottom) from Rietveld refinement. Green lines show the difference profiles, with bars representing reflection positions from *fcc* $RbCs_2C_{60}$. The background contributions as obtained from fitting were subtracted for visual clarity. Several broad background peaks arising from the cryostat could not be fitted satisfactorily with a background polynomial function, so these regions were excluded from the fits. The inset plots show data collected at 0.16 GPa with the X-ray beam focused on an area of the DAC containing no sample, to indicate the approximate background contribution; background peaks excluded from the respective refinements are labelled with asterisks.

Table A7: *Fcc* phase structural parameters for *fcc*-rich $RbCs_2C_{60}$, employed in Rietveld analysis of synchrotron PXRD data collected at 20 K and under elevated pressures (0.43 GPa and 7.42 GPa). The fractional cation occupancies, *N* of the tetrahedral interstitial site were fixed to values refined from the 10 K (highest statistics) ambient pressure data for the same sample, as described in Chapter 3.

$x = 1$ 0.43 GPa	x/a	y/b	z/c	N	B_{iso} (Å^2)
Rb	0.25	0.25	0.25	0.4857	2.242
Cs(1)	0.25	0.25	0.25	0.5143	2.242
Cs(2)	0.5	0.5	0.5	1.0	1.713
C(1)	0	0.04957	0.24037	0.5	0.684
C(2)	0.20980	0.08012	0.09892	0.5	0.684
C(3)	0.17904	0.16008	0.04957	0.5	0.684

$x = 1$ 7.42 GPa	x/a	y/b	z/c	N	B_{iso} (Å^2)
Rb	0.25	0.25	0.25	0.4857	2.519
Cs(1)	0.25	0.25	0.25	0.5143	2.519
Cs(2)	0.5	0.5	0.5	1.0	1.376
C(1)	0	0.05195	0.25194	0.5	0.829
C(2)	0.21991	0.08398	0.10368	0.5	0.829
C(3)	0.18766	0.16778	0.05195	0.5	0.829

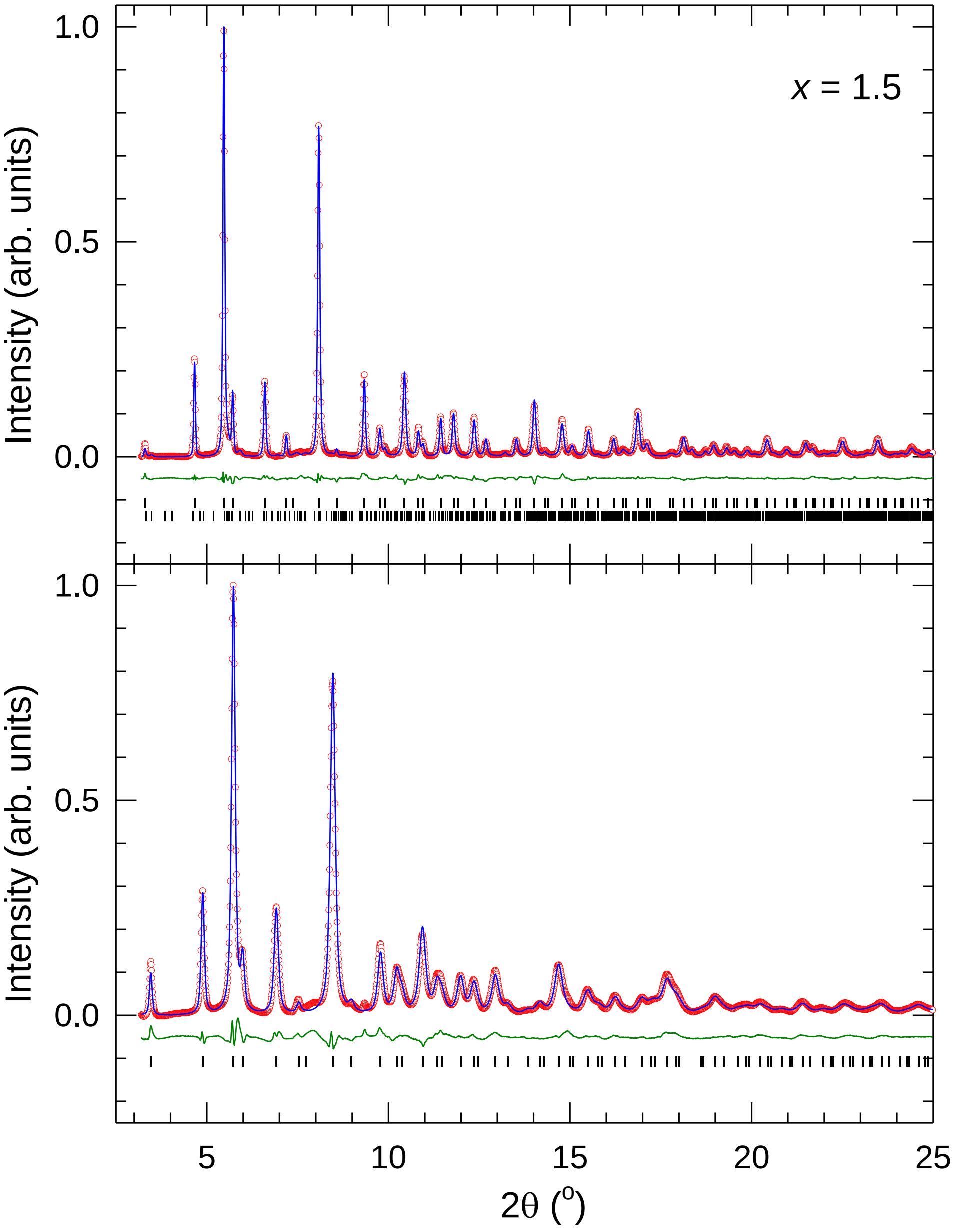

Figure A9: High-pressure synchrotron X-ray powder diffraction for *fcc*-rich $Rb_{1.5}Cs_{1.5}C_{60}$ (7 K, λ = 0.41238 Å, sample I). Final observed (o) and calculated (blue line) diffraction profiles at 0.55 GPa (top) and at 6.47 GPa (bottom) from Rietveld refinement. Green lines show the difference profiles, with bars representing reflection positions from *fcc* $Rb_{0.5}Cs_{2.5}C_{60}$ (upper) and CsC_{60} (lower); however, no contributions from CsC_{60} could be well-defined in the 6.47 GPa dataset, so only the *fcc* phase was included in the refinement. The background contributions as obtained from fitting were subtracted for visual clarity.

Table A8: *Fcc* phase structural parameters for *fcc*-rich $Rb_{1.5}Cs_{1.5}C_{60}$ (sample I), employed in Rietveld analysis of synchrotron PXRD data collected at 7 K and under elevated pressures (0.55 GPa and 6.47 GPa). The fractional cation occupancies, *N* of the tetrahedral interstitial site were fixed to values refined from the 10 K (highest statistics) ambient pressure data for the same sample, as described in Chapter 3; values in parentheses are statistical errors from the least-squares fitting.

x = 1.5 0.55 GPa	x/a	y/b	z/c	N	B_{iso} (Å^2)
Rb	0.25	0.25	0.25	0.8210	1.13(5)
Cs(1)	0.25	0.25	0.25	0.1790	1.13(5)
Cs(2)	0.5	0.5	0.5	1.0	0.55(5)
C(1)	0	0.04994	0.25111	0.5	0.395
C(2)	0.21581	0.07803	0.10125	0.5	0.395
C(3)	0.17515	0.15265	0.05002	0.5	0.395

x = 1.5 6.47 GPa	x/a	y/b	z/c	N	B_{iso} (Å^2)
Rb	0.25	0.25	0.25	0.8210	1.79(8)
Cs(1)	0.25	0.25	0.25	0.1790	1.79(8)
Cs(2)	0.5	0.5	0.5	1.0	1.9(1)
C(1)	0	0.05232	0.26304	0.5	0.395
C(2)	0.22607	0.08173	0.10606	0.5	0.395
C(3)	0.18347	0.15990	0.05239	0.5	0.395

References

1. O. Zhou and D.E. Cox, *Journal of Physics and Chemistry of Solids*, 1992. **53**(11): p. 1373-1390.
2. R.M. Hazen, R.T. Downs, and C.T. Prewitt, *High-Temperature and High-Pressure Crystal Chemistry*, 2000. **41**: p. 1-33.